National Library of Canada
Acquisitions and Bibliographic Services Branch
395 Wellington Street
Ottawa, Ontario
K1A 0N4

Bibliothèque nationale du Canada
Direction des acquisitions et des services bibliographiques
395, rue Wellington
Ottawa (Ontario)
K1A 0N4

Your file Votre référence

Our file Notre référence

NOTICE

The quality of this microform is heavily dependent upon the quality of the original thesis submitted for microfilming. Every effort has been made to ensure the highest quality of reproduction possible.

If pages are missing, contact the university which granted the degree.

Some pages may have indistinct print especially if the original pages were typed with a poor typewriter ribbon or if the university sent us an inferior photocopy.

Reproduction in full or in part of this microform is governed by the Canadian Copyright Act, R.S.C. 1970, c. C-30, and subsequent amendments.

AVIS

La qualité de cette microforme dépend grandement de la qualité de la thèse soumise au microfilmage. Nous avons tout fait pour assurer une qualité supérieure de reproduction.

S'il manque des pages, veuillez communiquer avec l'université qui a conféré le grade.

La qualité d'impression de certaines pages peut laisser à désirer, surtout si les pages originales ont été dactylographiées à l'aide d'un ruban usé ou si l'université nous a fait parvenir une photocopie de qualité inférieure.

La reproduction, même partielle, de cette microforme est soumise à la Loi canadienne sur le droit d'auteur, SRC 1970, c. C-30, et ses amendements subséquents.

Canada

Studies on the Mechanisms of Heterogeneous Nucleation of Grains and Pores in Aluminum Castings

by

Pravansu Sekhar Mohanty

Department of Mining and Metallurgical Engineering
McGill University, Montreal, Canada.

A thesis submitted to the Faculty of Graduate Studies and Research
in partial fulfilment of the requirements for the degree of
Doctor of Philosophy

February 15, 1994

National Library of Canada
Acquisitions and Bibliographic Services Branch
395 Wellington Street
Ottawa, Ontario
K1A 0N4

Bibliothèque nationale du Canada
Direction des acquisitions et des services bibliographiques
395, rue Wellington
Ottawa (Ontario)
K1A 0N4

Your file Votre référence

Our file Notre référence

ISBN 0-315-94688-1

Mechanisms of Nucleation of Grains and Pores in Aluminum Castings

by

Pravansu Sekhar Mohanty

Department of Mining and Metallurgical Engineering
McGill University, Montreal, Canada.

A thesis submitted to the Faculty of Graduate Studies and Research
in partial fulfilment of the requirements for the degree of
Doctor of Philosophy

February 15, 1994

Abstract

In the present study, a fundamental theoretical and experimental investigation has been carried out on the mechanisms of heterogeneous nucleation of grains and pores in aluminum castings. A direct addition technique has been developed to introduce known types and quantities of inoculants into liquid aluminum alloys, irrespective of their wettability and chemical reactivity while preserving the surface characteristics and melt chemistry. Many different types of inoculants such as: Al_2O_3, SiC, MgO, Mg_2AlO_4, TiB_2, TiC, SrO and $Sr(OH)_2$ have been successfully added into liquid aluminum alloys, yielding single particulate distributions while avoiding incorporation of naturally occuring oxide films.

The commercial grain refining practice of Al and its alloys has been experimentally simulated by introducing synthetic TiB_2 and TiC crystals into melts containing dissolved Ti. Experimental findings indicate that in the absence of dissolved Ti, TiB_2 crystallites alone do not nucleate α-Al. TiC particles which are generally believed to be the nucleating substrate are unstable and form various complex carbides. In the presence of dissolved Ti even below the peritectic level, an interfacial layer of $TiAl_3$ is formed at the TiB_2/melt interface which subsequently nucleates the α-Al. A 'duplex' nucleation mechanism is proposed based on the solute segregation phenomenon to the substrate/melt interface. In the case of hypoeutectic Al-Si alloy, this interfacial layer was found to be a ternary compound of Al-Si-Ti, however, a drastic drop in the peritectic solidification temperature presumably reduces its grain refining potency at higher Si content.

Particles which do not nucleate the solid phase and/or do not get engulfed by the growing solid, are continuously rejected by the solid/liquid (S/L) interface until the end of local solidification. These substrates act as a barrier to the fluid flow as well as to the diffusion field at the S/L interface, giving rise to enhanced gas segregation and viscous pressure drop. A novel theoretical mechanism for the heterogeneous nucleation of pores has been proposed, based on this behaviour of foreign particles at the advancing S/L interface. Mathematical analyses have been employed to predict the gas segregation and pressure drop in the gap between the particle and the S/L interface. An order of magnitude analysis is done, and it is shown that pressures in the range of the activation barrier can be obtained in normal castings. To substantiate the mechanism further, experimental studies were carried out by introducing various possible inclusions into liquid aluminum. The experimental findings are in line with the theoretical predictions.

Résumé

Dans la présente étude, une investigation fondamentale, théorique et expérimentale a été conduite sur les mécanismes de germination hétérogène des grains et des pores dans les pièces coulées d´aluminium. Une technique d´addition directe a été développée pour introduire des types et des quantités connus d´inoculants dans les alliages liquides d´aluminium, indépendamment de leur mouillabilité et de leur réactivité chimique mais en conservant les mêmes caractéristiques de surface et la chimie de la coulée. De nombreux inoculants de différents types tels que: Al_2O_3, SiC, MgO, Mg_2AlO_4, TiB_2, TiC, SrO and $Sr(OH)_2$ ont été ajoutés avec succès dans les alliages liquides d´aluminium, avec une distribution particulaire simple et en évitant l´introduction de films d´oxide qui se forment naturellement.

La pratique commerciale d´affinage des grains de l´aluminium et de ses alliages a été simulée expérimentalement en introduisant des cristaux synthétiques de TiB_2 et de TiC dans les coulées contenant du Ti dissous. Les conclusions expérimentales indiquent qu´en l´absence de Ti dissous, les cristallites de TiB_2 seuls ne germinent pas α-Al. Les particules de TiC qui sont généralement considérées comme le substrat germinant, sont instables et forment des carbures complexes variés. En présence de Ti dissous, même sous le niveau péritectique, une couche interfaciale de $TiAl_3$ est formée à l´interface TiB_2/coulée qui germine par la suite α-Al. Un mécanisme de germination 'duplex' basé sur le phénomène de ségrégation du soluté à l´interface substrat/coulée a été proposé. Dans le cas de l´alliage Al-Si hypoeutectique, cette couche interfaciale est un composé ternaire d´Al-Si-Ti; cependant une baisse drastique de la température de solidification péritectique réduit probablement son potentiel d´affinement de grain pour des teneurs de Si plus élevées.

Les particules qui ne germinent pas la phase solide et/ou ne sont pas englouties par la phase solide en croissance, sont continuellement rejetées à l´interface solide/liquide (S/L) jusqu´à la fin de la solidification locale. Ces substrats agissent comme une barrière pour l´écoulement du fluide ainsi que pour le champ de diffusion à l´interface S/L, donnant lieu à une ségrégation de gaz rehaussée et à une baisse de la pression visqueuse. Un nouveau mécanisme théorique pour la germination hétérogène des pores, basé sur ce comportement des particules étrangères à l´interface S/L en progression, a été proposé. Des analyses mathématiques ont été employées pour prédire la ségrégation de gaz et la baisse de pression dans l´espace entre la particule et l´interface S/L. Une analyse d´ordre de grandeur a été faite et a montré que des pressions de l´ordre de celle de la barrière d´activation peuvent être obtenues dans des pièces coulées normales. Pour consolider le mécanisme davantage, des études expérimentales ont été faites en introduisant des inclusions possibles variées dans l´aluminium liquide. Les résultats expérimentaux s´enlignent avec les prédictions théoriques.

Claim of Originality

The author sincerely believes that all aspects addressed in this thesis constitute distinct contributions to knowledge and claims the originality of the items listed below:

- A novel technique has been developed for direct addition of known types and quantities of inoculants into liquid metal irrespective of their chemical reactivity and wettability, while preserving the surface characteristics and the melt chemistry. This is the first successful case of direct addition of reactive synthetic crystals such as: TiB_2, TiC, SrO and $Sr(OH)_2$, into liquid aluminum.

- This thesis presents direct experimental proof that TiB_2 crystals alone do not nucleate α-Al and invalidates the so called 'boride theory'.

- A 'duplex' nucleation mechanism for grain refinement by Al-Ti-B master alloys is proposed. Experimental evidence in favour of the proposed mechanism has been presented. Unlike the existing hypotheses, this mechanism can successfully explain all the observed phenomena in grain refining practice.

- This study clearly demonstrates that under normal aluminum foundry operating conditions, TiC is unstable in the melt and proposes that the so called 'carbide theory' is an inappropriate concept in its original form. Even when TiC is directly introduced into an aluminum melt, interfacial layers of Al_4C_3 and Ti_xAlC are prone to form, leading to poisoning of the nuclei.

- This thesis proposes that Al-Si alloys cannot be grain refined by TiC. TiC crystals decompose completely giving rise to aluminum carbide and complex carbides immediately after introduction into Al-Si melts.

- This study also shows that TiB_2 crystals alone do not grain refine hypoeutectic Al-Si alloys. Grain refinement in hypoeutectic Al-Si alloys by Al-Ti and Al-5Ti-1B master alloys occurs by a peritectic reaction involving liquid aluminum and a ternary aluminide (Al-Ti-Si) which nucleates α-Al.

- The grain refinement mechanism by Al-Ti-B master alloys in hypoeutectic Al-Si alloys is also 'duplex' in nature. When the Ti/B ratio is higher than the stoichiometry of TiB_2 (2.22), a ternary Al-Ti-Si aluminide precipitates on TiB_2 particles. This aluminide subsequently undergoes the peritectic reaction and nucleates α-Al.

- This study demonstrates that the enhanced performance of Al-3Ti-3B master alloy in hypoeutectic Al-Si alloys is possibly related to the presence of boron in excess of TiB_2 stoichiometry, rather than the hypothesized heterogeneous nucleation on the $(Al,Ti)B_2$ phase (metastable boride theory). In the presence of excess boron, precipitation of AlB_2 presumably occurs on TiB_2 which nucleates α-Al via a eutectic reaction.

- Inclusions which do not nucleate the solid and/or do not become engulfed within the solid, are pushed by the S/L interface. A novel mechanism for pore nucleation at heterogeneous sites is proposed based on the interaction of inclusion particles with the S/L interface.

- Mathematical analysis shows that the activation barrier to bubble nucleation can be reached in a normal casting. The model identifies the inclusions and casting conditions which are responsible for pore nucleation.

- A systematic experimental study on the effect of different inclusions on pore nucleation is presented in this thesis.

- This study also shows that the TiB_2 inclusions which are added for the beneficial effect of grain refinement can act as a pore nucleant.

- Further, the thesis also presents experimental evidence indicating that SrO and $Sr(OH)_2$ cannot exist in aluminum melts, and the proposed hypothesis of enhanced porosity due to Sr-related inclusions in modified castings seems to be inappropriate.

Acknowledgements

It is with great apprehension that I have taken up the task of acknowledging all those who were of great help and were involved directly or indirectly in making this work a success. This is because of the fact, that mere words do not represent thoughts very well; everything immediately becomes a little different, a little distorted, a little foolish, and yet it also pleases me and seems right that what is of value and wisdom to one individual seems nonsense to another.

Knowing fully well the limitations language has imposed upon me, I take it as a pleasure to convey my sincere thanks to my supervisors Prof. J. E. Gruzleski and Prof. F. H. Samuel for their invaluable guidance. Each stage of my thesis was closely monitored by them. John! you never failed to be hopeful in 'Chicoutimi days'. That's history! Your patience and words of encouragement went a long way in completing this work. I enjoyed so much the monthly dinners, discussions on scientific ethics and philosophy of life and friendship.

I neither believe nor claim that this document is absolutely free from flaws. Comments from many researchers, however, contributed to the existing degree of accuracy. The comments were not necessarily pleasant and encouraging everytime, but they paid off in the long run by motivating me to change the course of action and to improve my scientific understanding of the topic. I take it as a pleasure to convey my thanks to Prof. R. I. L. Guthrie, Dept. of Mining and Metallurgical Engineering, McGill University, Dr. F. J. Major, Alcan International, Kingston, Ontario, Mr. T. J. Kosto, Milward Alloys Inc., New York and the reviewers of my papers.

Prof. Jacques Carrignan, the director of the Dept. des Sciences Appliquées, Université du Québec à Chicoutimi, Québec, has been very helpful and supportive. He always extended his help and encouragement upto the last day. Thank you so much.

Regis! you were always suppportive and patient irrespective of difficulties of language and communication we had. Certainly your help was a key factor in conducting the experiments successfully. Thank you very much. Gilles Lemire! thanks a lot for your help.

I wish to acknowledge the financial assistance of the Natural Sciences and Engineering Research Council of Canada (NSERC), the Fondation Sagamie de l'Université du Québec à Chicoutimi (FUQAC) and the Société d'électrolyse et de chimie Alcan (SECAL). The support of KB Alloys Inc. in supplying Al-Ti master alloys, Norton Ceramics Co, Timinco Metals, MSM Alabama, and Duralcan Canada (usine Dubuc), in providing the raw materials, is gratefully acknowledged. The support of the Center for Intelligent Machines (CIM), McGill University, for computation and word processing is also acknowledged.

I am thankful to Prof. Dipak Mazumdar, Visiting Professor, Dept. of Mining and Metallurgical Engineering, for his personal interest in me, friendship, encouragement and suggestions. Many thanks to Prof. Ranjit Kumar Ray, IIT Kanpur (India), who motivated me to join McGill and has been a constant source of encouragement. I am also thankful to Prof. N. Chakraborty, Prof. A. K. Jena and Prof. G. S. Murty of IIT Kanpur (India) and Prof. T. Sundararajan of IIT Madras (India) for their encouragement.

My family members particularly my parents who always wanted me to come abroad for higher education, have been very patient and supportive and never failed to encourage me. My sister in law Padmaja has been very special always. Sumitadi, thank you so much for good company and care. I am thankful to Florence Parray for French translation of the abstract. Santanu and Raju, my room mates, thanks for adding fun(?) to life. Last but not least I am also thankful to my friends in Montreal: Bobby, Eddy, Ganesh, Mamata, Bala and others. Any omission is not intentional. I thank you all once again for making my three years' stay at McGill a memorable one.

Dedicated to

My Father, (Could you not wait another two months to see it?)

Introduction to the Thesis

In recent years, a trend towards aluminum castings has been fuelled by a growing demand for stronger, lighter and corrosion resistant components, especially in the aerospace and automotive industries. The current push for greater fuel efficiency, coupled with the continuous need for pollution control and safety regulations necessitates the development of more lighter weight components. Aluminum alloy castings are one of the most viable alternatives because of their excellent castability, strength to weight ratio and physical properties. As is well known, the properties of a cast component are greatly influenced by its internal structure such as: grain size and type, internal voids, the various phases present and their shape, size and distribution. Among these, grain structure is an important and readily observable feature in aluminum alloy castings. Depending on the constitutional and heat flow conditions in a solidifying aluminum alloy, three different grain morphologies are possible, namely, equiaxed, columnar and twinned columnar (TCG). The formation of a fine equiaxed grain structure is almost always desired due to its inherent uniform mechanical properties, reduced ingot cracking, improved feeding, distribution of second phases on a fine scale, improved machinability and cosmetic features. The conversion of liquids into different solid grain structures is also accompanied by the formation of casting defects called pores or internal voids. The origin of these voids in castings is generally attributed to the cooperative effects of hydrogen rejection and volumetric shrinkage associated with the phase change. This inevitable casting defect deteriorates the soundness of castings resulting in decreased mechanical properties.

The evolution of solid grains and pores from solidifying melts is considered to be formally similar, *i.e.*, they involve a nucleation problem or an activation barrier as shown in Fig. 0.1.[1] As the temperature falls, the thermal agitation of the atoms of the liquid reduces, allowing small random aggregations of atoms into crystalline regions. Once a small cluster is formed the net energy to form this phase is reduced in proportion to its volume. At the same time, however, the creation of new surface area involves extra interfacial energy. When the total energy is plotted against the size of the cluster, the net energy to grow the embryo increases at first, reaches a maximum and then decreases. This maximum is known as the activation barrier for homogeneous nucleation. Embryos which do not reach the maximum require more energy to grow, so normally they will shrink and be redissolved back into the liquid. Only when the temperature is sufficiently low (*i.e.*, melt is undercooled), so that the net energy overcomes the barrier, will the embryo reach the critical size and grow into a solid. On the other hand, when the melt contains suitable foreign substrates, the interfacial energy component can be reduced or

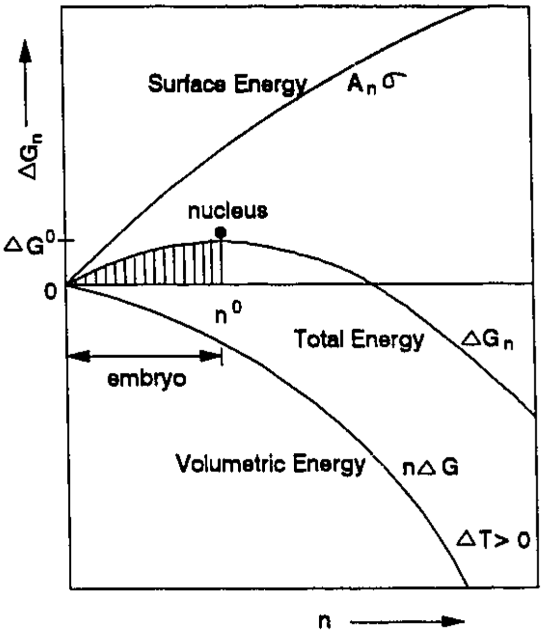

Fig. 0.1 Energetics of a Typical Nucleation Process.[1]

even eliminated and the new crystal will form heterogeneously on them.

Similarly, as solidification progresses, dissolved hydrogen is continuously rejected from the solid into the remaining liquid due to the sharp solubility difference of hydrogen between solid and liquid as shown in Fig. 0.2.[2] As a result, a stage is reached when the hydrogen content in the liquid goes above its solubility limit and the hydrogen will have a tendency to evolve as gas bubbles. The shrinkage usually associated with solidification will have an additive effect and will facilitate the formation of these bubbles. A bubble or pore cannot begin at zero size, as the surface tension pressure becomes infinite at this radius. Hence, there is a critical radius of the bubble, r^*, below which it is not capable of surviving and above which it will tend to grow. It has been recognized that nucleation of pores in liquid aluminum would require extremely high gas contents and shrinkage pressures of the order of 30,000 atm.[3] Unlike the case of solid nucleation, this activation barrier is too high to be reached simply by gas and shrinkage pressure drop in a normal casting. Thus, homogeneous nucleation of pores is extremely difficult and is unlikely to occur in practice. Nevertheless, as is well known, pores in castings are more the rule than the exception, and in castings, nucleation of pores can be expected to occur primarily at heterogeneous sites.

Heterogeneous sites are inherent in almost all normal castings, with inclusions forming the most important category of such sites in the melt. Inclusions are nonmetallic and intermetallic phases present as solids, or sometimes liquids, in the bulk melt. In most

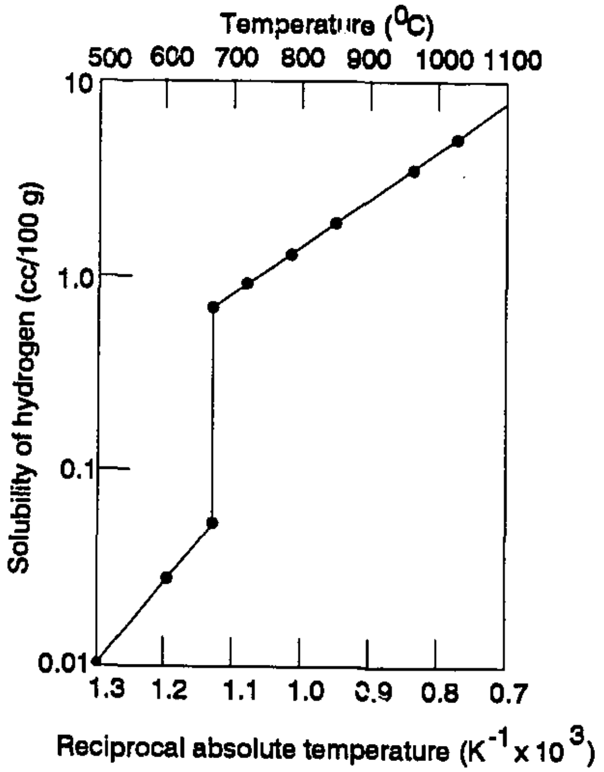

Fig. 0.2 Solubility of Hydrogen in Solid and Liquid Aluminum.[2]

metal casting operations, inclusions are considered to be detrimental to the performance of the cast components. To cite an example, mechanical properties can be adversely influenced by inclusions, which act as stress raisers. There is no set pattern for the effect, but some properties are more sensitive to the presence of inclusions than others. It has been demonstrated that the presence of such substrates greatly enhances the porosity formation in aluminum alloys.[4–9] On the other hand, when inclusions are removed by filtration, the porosity level is significantly reduced.[10,11] However, the mechanism by which such inclusions operate to facilitate pore formation is not well understood.

Inclusions are not, however, always prejudicial. Their intentional introduction can lead to significant improvement in properties as in the case of grain refinement. The deliberate suppression of columnar or TCG growth in aluminum alloy ingots and castings and the formation of an equiaxed solidification structure throughout is termed grain refinement which is most usually brought about by the addition of inoculants to the melt before casting. The grain refining inoculants commonly used in the aluminum industry are master alloys of titanium or titanium plus boron. In principle, the mechanism of grain refinement is quite straight forward. Numerous potent heterogeneous nuclei are dispersed in the melt, and a large number of these sites become active during solidification and nucleate the grains. Exactly which particles are released, their physical and chemical characteristics and their subsequent reaction with the melt are still disputed.

There can be several types of nonmetallic and intermetallic phases present in an aluminum melt. Though a strict classification of inclusions is rather difficult, two categories of inclusions are usually recognized, namely; exogenous, those derived from external sources *e.g.*, dross, entrapped mold materials and refractories, and indigenous, those that are native, innate, or inherent in the molten metal treatment process *e.g.*, oxides, borides and carbides. Table 0.1 presents the possible types of inclusions and their characteristics in aluminum melts.[12]

Table 0.1 Typical Inclusions in Aluminum Melts.[12]

Phase	Shape	Size Range in μm	Characteristics (light microscopy, no etching)
Al_2O_3	films or clusters polygonal particles	t = 0.1 to 5 d = 10 to 1000 d = 0.2 to 30	Dark grey or black
MgO	polygonal particles	d = 0.2 to 1	Black
Al_2MgO_4	truncated pyramidical thick films or lumps	d = 0.1 to 5 d = 1 to 6 t = 10 to 1000	light grey
Al_4C_3 & Al_4O_4C	rectangular or hexagonal discs	t < 1 d = 0.5 to 25	Grey
Na_3AlF_6	spheres	d = 2 to 60	medium grey
AlB_{12}	irregular polygonal	d = 1 to 20	Grey
AlB_2	hexagonal	d = 20 to 50 t < 1	Dark brown
TiB_2	clusters of hexagonal discs	d = 1 to 50	Beige or light grey
VB_2	clusters of hexagonal discs	d = 1 to 20	Medium grey
ZrB_2	clusters of hexagonal discs	d = 1 to 10	Brownish grey
$TiAl_3$	rods or blocky	d = 10 to 1000	Light grey
$ZrAl_3$	polyhedral clusters of rods	d = 1 to 100	Light grey

d - diameter   t - thickness

It is important to realize that not all foreign substrates present in liquids are favourable nuclei for the solid phase, nor do all of them nucleate pores. In fact it is likely that each nucleation process (*i.e.*, grain or pore) is indifferent to the presence of many of these inclusions. As in the case of grain refinement, the fact that a small addition is beneficial does not necessarily mean that additions beyond an optimum quantity, or additions that lead to formation of undesirable by-products will provide greater rewards. Diborides, Al_4C_3 and other complex carbides produced during grain refining practice can become undesirable inclusions. Therefore, to maximize their benefits as a grain nucleant and minimize their negative impact as a pore nucleant, it is essential to identify the respective nuclei and to understand the mechanisms by which they operate.

Studies on the mechanisms of grain nucleation and pore nucleation as well, at heterogeneous sites, are not new. They form classic research topics in solidification processing, and substantial theoretical and experimental information is available in the literature. Despite the commercial importance and volume of scientific study on this topic over the years, it still remains unclear how nucleation of these phases occurs at heterogeneous sites. Careful analysis of the theories hypothesized as of today, shows that none is fully satisfactory. Many anomalies can be found between these postulations and experimental observations. These anomalies have tempted the present author to carry out a theoretical and experimental investigation, as reported in this thesis, to address the fundamental aspects of heterogeneous nucleation of grains and pores with special emphasis on:

- the identification of the respective nuclei,
- the mechanisms of heterogeneous nucleation in each case,
- the metallurgical parameters that affect the nucleation phenomena.

The main body of this work has been divided into three chapters (1-3) according to the logical progession of: development of a technique for introducing synthetic crystals into molten metal, understanding the mechanism of grain nucleation under simulated grain refinement practice using synthetic TiB_2 and TiC, and determining the effect of many synthetic inclusions (*e.g.*, Al_2O_3, MgO and SrO etc.) on pore formation and the mechanism by which they operate.

In the case of ordinary melting conditions, a wide variety of inclusions is usually found in an aluminum melt. The simultaneous occurence of these inclusions complicates any systematic study of their behaviour. A systematic study necessitates the controlled addition of known types of inclusions into the melt while avoiding incorporation of those which are easily formed during the melt processing stage. For this purpose, a novel inclusion addition technique has been developed to introduce many types of inclusions into liquid aluminum, irrespective of their wettability and chemical reactivity while preserving their surface characteristics and the melt chemistry. The state of the art of particulate addition techniques, fabrication and principle of operation, and novelty of the present inclusion addition set-up forms Chapter 1 of the thesis.

Chapter 2 deals with the mechanisms of grain refinement by inoculant addition into the melt. A critical review of earlier experimental studies and theories is presented. Experiments are conducted by introducing synthetic inoculants (TiB_2 and TiC) to aluminum melts in order to verify their nucleation potential. To simulate grain refining practice, the behaviour of these inoculants is studied with the presence of dissolved Ti, and the mechanism of nucleation is made clearer. A 'duplex' nucleation mechanism is proposed based on these experimental findings and observations made in the grain refining practice.

Chapter 3 begins with a bibliographic survey of studies on the mechanisms of pore nucleation, emphasizing the limitations of models presented to date. A theoretical model of the mechanism of heterogeneous nucleation of pores in metallic systems is presented. The proposed mechanism is based on the behaviour of foreign particles at the advancing solid/liquid interface. Foreign substrates which are pushed by the solid/liquid interface act as a barrier to the fluid flow as well as to the diffusion field at the solid/liquid interface, giving rise to enhanced gas segregation and viscous pressure drop. Mathematical analyses have been employed to predict the gas segregation and pressure drop in the gap between the inclusion and the solid/liquid interface, and it is shown that pressures in the range of the activation barrier can be obtained in normal castings. To consolidate the mechanism, further experimental verifications have been carried out with different types of inclusions and the results are compared with the theoretical predictions.

The thesis ends with general conclusions and industrial implications of the study, including some suggestions for future work, which are presented in Chapter 4.

Major parts of this thesis are either published in journals and conferences or submitted for publication, the present author being the principal writer.[13-17] On many occasions, the text presented in this thesis has been taken directly from these publications. The present format conforms to the McGill University guidelines concerning thesis preparation.

Contents

List of Figures

List of Tables

Chapter 1

Inoculant Addition Technique

1.1 Introduction

Inclusions find their way into the melt from various sources. In aluminum alloys a wide variety of inclusions are found. Some of them occur naturally in the system, *e.g.*, Al_2O_3, MgO, spinel, SiC etc., and some are intentionally added as grain refiners, *e.g.*, TiC and TiB_2. Many of these inclusions occur simultaneously in the melt, complicating the systematic study of their behaviour. For example, in the case of grain refinement by the use of Al-Ti-B master alloys, the crystallites that are commonly believed to nucleate grains are TiB_2,[18] which form as the reaction product of K_2TiF_6 and KBF_4 salts.[19] However, in addition to the production of TiB_2, (Al, Ti)B_2, $TiAl_3$ and dissolved Ti also enter into the melt and complicate the detailed analysis of grain refinement.

Over the last four decades, several investigations[19] have been carried out to identify the nucleating crystals in this complex system and the mechanism by which they operate. A detailed discussion is presented in Chapter 2. These attempts have met with little success for several reasons. Firstly, the presence of dissolved Ti and $TiAl_3$ may alter the behaviour of TiB_2 significantly.[20] Secondly, control of particle size and chemistry is very difficult from the salt reaction, and subsequent metallographic identification of the particles is uncertain. In the context of enhanced porosity in strontium modified alloys, it is often mentioned that the presence of SrO and $Sr(OH)_2$ inclusions may nucleate pores.[9] There is, however, no experimental evidence indicating that such inclusions can exist in an aluminum melt in the first place. This implies that the first logical step in the systematic study of inoculant behaviour during solidification (*i.e.*, their role on the nucleation of grains and pores) should be the development of a suitable technique for the controlled addition of known types of inclusions into the melt while preserving their characteristics, and avoiding incorporation of those inclusions which are naturally formed during the processing stage such as oxide films and gas bubbles.

Efforts to introduce solid particles into molten metal in a controlled way are not new. From time to time various attempts have been made in this direction, with different degrees of success or failure. In the following section, a brief review of the state of the art of this technology is presented.

1.2 Literature Review

Several approaches have been adopted for introducing solid particles into molten alloys. They can be classified into two broad categories; namely, (a) production of solid particles in the melt through a chemical reaction, and (b) mechanical introduction of pre-processed particles into the melt.

The principles on which the first category is based have been widely used in the area of grain refinement. Cibula[21] utilized KBF_4 salt at high temperature($\sim$ 1100^0C) to produce AlB_2 particles in molten Al. TiB_2 particles were produced either by reacting Al-Ti hardner and Al-B master alloy through cryolite flux, or by adding boron directly into Al-Ti master alloys. Commercial Al-Ti-B grain refiner master alloy production is based on the principle of salt reactions in which salt mixtures of K_2TiB_6 and KBF_4 are added to a molten alloy and mixed by mechanical paddles until the reaction is complete.[22]

Several attempts have been made[21] to add carbon in the form of graphite powder or rod, carbon tetrachloride, CO, acetylene and high carbon steel to Al-Ti melts to create TiC particles. Carbon has also been added together with potassium halide flux, and potassium titanofluride was reacted with graphite[23] for the same purpose. All of these trials failed to introduce any appreciable amount of carbon and no useful results were obtained owing to the difficulties in forming and dispersing the carbides.

Subsequent attempts to produce TiC in Al-Ti alloys either did not succeed at all or generated too few carbides. These include work by Mondolfo *et al.*,[24,25] Lihl *et al.*,[26] Nakao *et al.*,[27,28] and Thury.[29] The major problem encountered in synthesizing these alloys is the poor wettability of carbon with molten Al. Recently, Banerji *et al.*,[30,31,32] have succeeded in generating substantial amounts of TiC in Al-Ti alloys using a vortex method or by electromagnetic stirring for introducing graphite powders into superheated Al-Ti alloys. In another attempt, Sahoo *et al.*,[33,34] also succeeded in *in-situ* production of TiC by blowing carbonaceous gas into a superheated Al-Ti melt.

Although considerable success has been achieved in creating solid particles in the melt through chemical reaction, the control of the chemistry of the products and particle size is difficult. In addition, the chemistry of the alloy also changes. It is also well known that the presence of small amounts of certain elements can completely change the behaviour of the inclusions. In the case of TiB_2 production from a salt reaction, a whole range of compositions from AlB_2 to TiB_2 may form.[35] Similarly, in the case of TiC production, Al_4C_3 and other complex carbides form.[31]

Other approaches involve mechanical introduction of pre-processed particles into the melt. This group of techniques has gained popularity for the synthesis of composites. Since most of the inclusions are non-wettable, their incorporation into the melt is facilitated by promoting wettability and/or by using some mechanical means of introducing them and holding them in the melt. There is a wide variety of techniques available to promote wetting between the non-wettable particles and metallic melts such as the use of Ni and Cu coatings[36,37] and the addition of reactive elements such as Mg, Ca, Ti Zr and P.[37] Clearly in the study of inoculant behaviour in a melt, any kind of surface treatment is not useful as it imposes an artificial surface on the particle.

Based on the principle of mechanical introduction of non-wettable particles, the vortex method has been extensively used in synthesizing metal matrix composites. In this method, the melt is agitated by an impeller to create a vortex force which draws

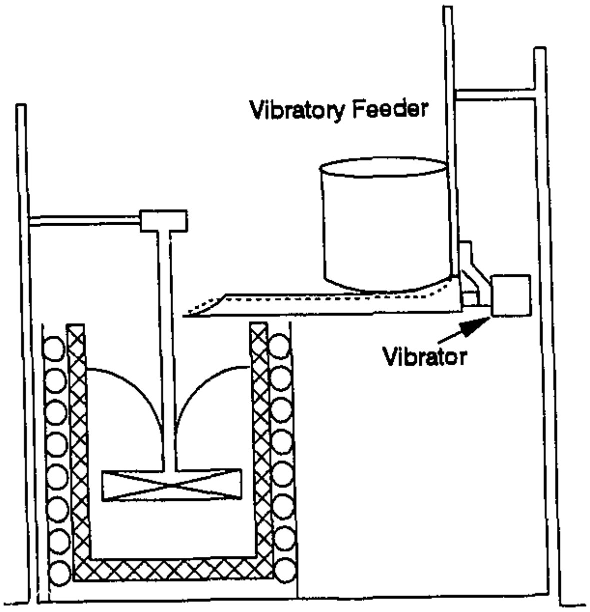

Fig. 1.1 Schematic of Vortex Method with Vibratory Feeder.

the particles from the surface of the melt into the metal as shown in Fig. 1.1. The vortex, while drawing the particles into the melt, also incorporates surface oxides and gas bubbles. The particles, before entering into the melt, spend some time in the vortex and this time is usually sufficient to oxidize and nitride reactive powders such as TiB_2 and TiC. Even though the particles may be stable in the melt, their surface characteristics can be completely altered during the residence time in the vortex at high temperature. As far back as 1950, Cibula[21] mixed TiC powder with aluminum powder and compressed the mixture into pellets which were subsequently stirred into aluminum melts. In all of their attempts, no appreciable amount of TiC was introduced into the melt as the carbide merely oxidized and mixed with the dross. To avoid surface oxidation, an inert gas shield can be maintained over the melt, but this makes the process complex and expensive. Another problem associated with the vortex method is cluster formation in the melt, particularly at a low volume fraction of addition of fine particles in the range of 2-5 μm. Clusters may form due to:

- flocculation of particles in the original powder

- flocculation and segregation of particles during and after injection into the melt
- movement of particles in the melt
- segregation of particles during solidification.

The first three phenomena are specific to the method of addition while the fourth one depends on the particle characteristics, the melt and the solidification process. Fine particles in the range of 5μm or below normally flocculate in the original powder. Moisture content plays a vital role in the flocculation tendency of the powder, and therefore, the powders are normally preheated, and mechanical feeders are used to break the clusters to supply powders uniformly into the vortex. It is, however, extremely difficult to break up all the clusters into individual particles and to maintain a free flow into the vortex, particularly in the lower size fractions.

From this review of the state of the art over the past three to four decades, it is clear that to satisfy the requirements of the present study on inoculant behaviour there is a need for a methodology to introduce inclusions into liquid metal to meet the following objectives:

(i) the introduction of all types of inclusions into metallic melts, irrespective of their wettability and chemical reactivity, while preserving their surface characteristics and the melt chemistry

(ii) the avoidance of incorporation of undesirable surface oxides and gas bubbles during the addition

(iii) the formation of a uniform particle distribution at low volume fraction of addition and fine particle size($\sim$ 2-3μm).

1.3 Experimental

The principle of the method described here is to heat a bed of sized particles in an inert atmosphere and then to blow a continuous stream of these particles by means of an inert gas into the melt. In the melt, the particles are uniformly distributed by breaking up the bubbles carrying the particles with the help of an impeller.

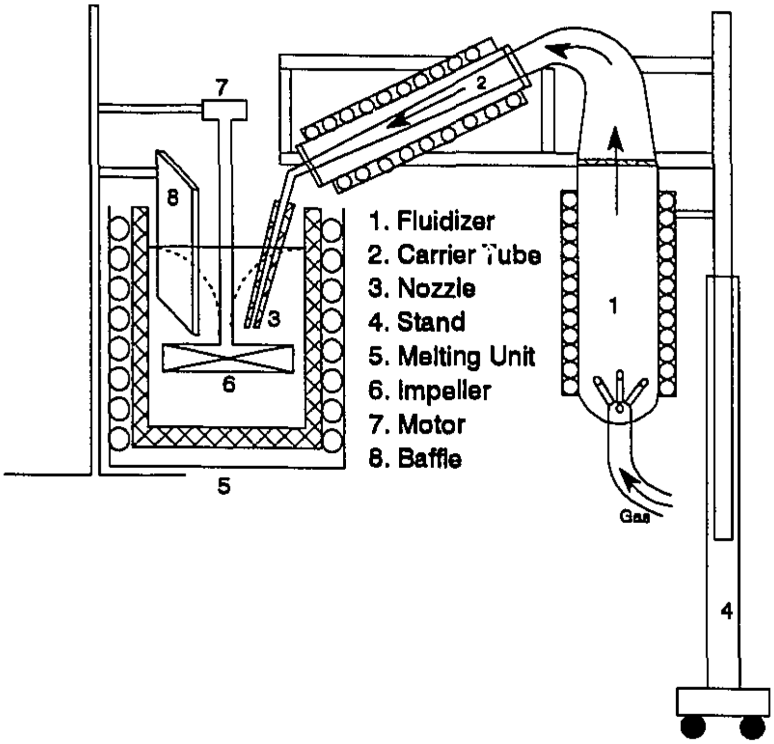

Fig. 1.2 Schematic of the Inclusion Addition Apparatus.

A schematic of the inclusion addition apparatus is shown in Fig. 1.2. It consists of (a) fluidizer tube, (b) carrier tube and nozzle, (c) heating coils and control, (d) adjustable stand, (e) melting unit, (f) impeller with reversible motor, and (g) flow diversion baffles. The fluidizer unit is a cylindrical quartz tube ($\sim$ 4.5 cm dia. × 30 cm high) with an inlet gas injection nozzle system in one end and a conical outlet fitted to the carrier tube on the other end. The inlet gas tube has four nozzles (1 mm dia.) positioned on a hemispherical dome. Three of these are placed on the base circle of the dome at 120^0 to each other with an inclination of 30^0 to the vertical centre line. The fourth nozzle is positioned in the centre of the dome at a right angle to the base circle. This arrangement avoids dead zone formation during fluidization and maintains a uniform particle cloud. The carrier tube, which is heated by resistance coils to compensate for heat loss during blowing, converges uniformly into an immersion nozzle of 2 mm dia. The immersion nozzle is covered with an alumina tube sheathing to protect the quartz nozzle from the stress exerted by the agitation of the melt. A resistance heating coil surrounds the fluidizer tube for preheating the powder. The entire set-up is mounted on a movable and adjustable stand so that the position of the nozzle can be altered accordingly.

Melting was done using an electric resistance furnace and cylindrical alumina crucibles. The impeller stock was constructed of alumina coated stainless steel with four graphite blades (~6 cm dia.) inclined at an angle of 45^0 to the stock.

To make an inclusion addition, a measured quantity of powder was filled into the fluidizer tube. These powders were normally heated for 2 to 3 hours depending on the particle size and chemistry. The prolonged heating was necessary to ensure that the powder was uniformly heated and moisture free before injection started. During preheating, a slow stream of argon gas was continuously maintained through the powder bed at a flow rate insufficient to lift the powder out of the tube. The flow of argon gas maintained an inert atmosphere inside the tube, helped in the drying process, and avoided lump formation. The preheating temperature depended on the type of the powder. For stable ceramic powders (*e.g.,* Al_2O_3, SiC etc.) a preheating temperature of $\sim 700^0C$ was employed, while reactive powders (*e.g.,* TiB_2, TiC etc.) were preheated to a lower temperature ($\sim 250^0C$).

The aluminum alloy melts used were approximately 20 cm in depth and 8 cm in diameter. Once the melt was ready, the impeller was lowered into the melt and kept at 5 cm above the bottom surface of the crucible. The nozzle was preheated before immersion to avoid thermal shock. It was then immersed into the liquid and the position was adjusted through the adjustable stand. The position of the nozzle in the melt was very crucial for efficient recovery of the particles since, on blowing, the gas bubbles carrying the inclusions must be delivered directly onto the blades of the impeller. The direction of rotation was maintained so that the impeller blade pushed the liquid down. Rotation speeds of about 300 rpm were necessary to break up the bubbles efficiently. At such speeds a strong vortex is expected, and to avoid vortex formation two ceramic baffles were immersed into the melt opposite each other as shown in Fig. 1.2. The dimensions of these baffles were 15 × 2 × 0.4 centimeter and they were positioned at an angle of 45^0 to the flow direction. Thus, high agitation was maintained while avoiding vortex formation, and a greater shearing action was provided which was useful for better mixing.

With the impeller operating as described, the gas flow rate was increased to fluidize the powder bed. The particles were separated from each other and became suspended in the gas. The flow level was maintained such that only the separated particles escaped from the cloud into the carrier tube. As they entered the carrier tube their velocity increased gradually and they were delivered onto the impeller at high speed. The impeller broke down the carrier gas bubbles, and in the process, particles were transferred into the melt. Some particles did escape from the melt and they became trapped below the dross formed on the surface.

At the end of blowing, the nozzle was removed from the melt while agitation was still maintained. At this moment, the rotation direction was adjusted according to the melt/particle density ratio. During blowing the effective density of the particle was always lower than the melt irrespective of the melt/particle density ratio, since particles were suspended in the carrier gas. A downward force was therefore essential. At the cessation of blowing, the melt was lifted up (by reversing the direction of rotation) if the particles were heavier than the melt (*e.g.,* SiC and TiB_2 etc.) and pushed down if the particles were lighter(*e.g.,* γ-Al_2O_3). Agitation was maintained for about 30 minutes after blowing, and the melt was then cast into chill molds. On some occasions (*e.g.,* TiC) the melt was cast immediately after addition to study the interfacial reactions of the particles. These inclusion containing ingots were then remelted and used in experiments designed to study the role of inclusions during solidification *i.e.,* in pore nucleation[25] and grain refinement etc. The inclusion recovery and distribution were studied by metallographic means, and the chemical composition of the particles after addition was verified by electron probe micro analyser (EPMA).

$Sr(OH)_2$ inclusions could not be added using the injection system described above due to the low fusion point of the hydroxide. Molten hydroxide stuck to the hot nozzle wall and choked the nozzle after a few minutes of addition. For the addition of

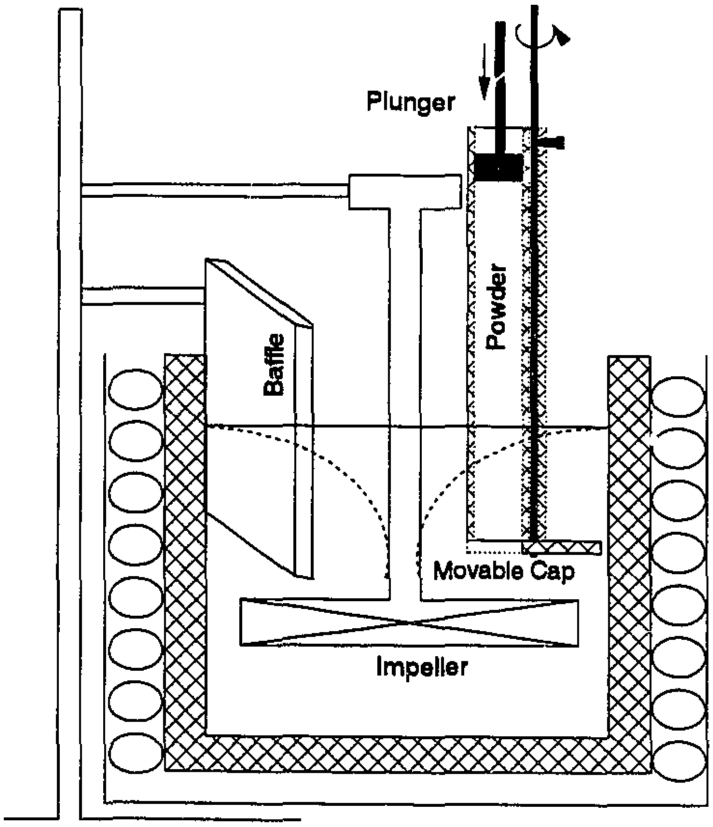

Fig. 1.3 Schematic of the Liquid Inclusion Addition Apparatus.

such inclusions which become liquid at temperatures below the melt temperature, the simple arrangement shown in Fig. 1.3 was used. It consisted of a graphite tube with a revolving cap at one end, and a plunger at the other end. The powder specimen was filled and both ends of the tube were closed. After the tube was immersed in the liquid melt with the bottom end opened adjacent to the impeller, the plunger was pushed downward manually to release the powder into the melt. By this means $Sr(OH)_2$ could be added successfully.

1.3.1 Metallography

The polishing procedure is particularly critical in such a study since a poor surface polish showing diamond pick-up, relief, scratches, particles break out etc., will alter the true contour of the ceramic particles and of the pores. This will affect the precision of the micro-analytical examinations and image analysis for the evaluation of the true areas that the phases occupy on the plane of polish. Though there are some techniques developed (Dural-A-90)[38] for polishing metal matrix composites, these do not work well for all kinds of particles, especially for samples containing only a few particles. Samples with very few inclusions pose special problems due to the irregular regions of soft aluminum matrix and hard particles. Though there were variations depending upon the type of particles, a typical polishing schedule which was established on a trial and error basis, to avoid particle loss, polishing compound residue at the particle/matrix interface, and scratches, is presented in Table 1.1. A Buehler^{TM} automatic polishing machine was utilized for this purpose.

Table 1.1 Typical Polishing Schedule.

Disc	Lubricant	Abrasive Mesh	Time (min)	Pressure (lb/sample)	RPM	Rotation (ccw/cw)
Grinding						
SiC	water	120	2:00	3	120	ccw
SiC	water	240	2:30	2	120	ccw
SiC	water	320	3:00	1	120	ccw
Polishing						
METLAP #4	oil	6 μ	2:00	5	120	ccw
TexMet	oil	4 μ	7:00‡	5	120	ccw/cw
TexMet	Ethyl alcohol	1 μ	7:00‡	5	120	ccw/cw
Final Polishing						
Mastertex	water	Mastermet 0.05μ	2:30	5	70	ccw

‡:- 3:30 min. counter clockwise and 3:30 min. clockwise.

1.3.2 Image Analysis

LECO 2000^{TM} and 2001^{TM} optical image analysers were employed for the evaluation of area fraction of different phases, number densities, size distributions etc. The basic difference between the 2000 and the 2001 series is that the latter has automatic scanning and focusing facilities while the former is manually scanned and focused. The most important function of the image analyser is its capability to discriminate various phases based on their grey levels.[39] The precision of the analysis therefore, primarily depends on the appropriate setting of the threshold limits that discriminate the phases. In the present study, the threshold limits were set to discriminate the particles and the porosity from the metal matrix. Threshold interference was the most serious problem faced during the present study. Depending on the particle and alloy composition, quite often it was difficult to distinguish between particles and pores due to the narrow grey level difference *e.g.,* Al_2O_3 particles. When this happened, certain types of particles were interpreted as pores. To circumvent this problem, the sample surface was coated with a thin layer of gold by plasma sputtering. This thin coating improved the contrast between Al_2O_3, MgO, spinel particles and pores, since the grey level of pores remained unchanged while the grey level of the particles was drastically altered. On the other hand, when the grey level of the particles was close to that of the matrix, it was almost impossible to resolve them *e.g.,* TiB_2. Preferential etching of the matrix resolved the particulate boundary to some extent by an artificial contrast due to defocusing, which was sufficient for optical photography, however, image analysis could not be successfully carried out. To make the analysis even more difficult, the constituent silicon particles in Si containing alloys, which are also not preferentially dissolved by etching, interfered with the particles.

Though image analysis appears to be quite simple and useful, there are many limitations of this method, and the reliability of the test results presented in this thesis is subject to them. Therefore, a brief mention of the scope of the image analysis results becomes imperative at this stage. The accuracy of the technique cannot be determined since the method is essentially empirical. The precision of the method is defined by the term repeatability *i.e.,* the variability between independent test results. The repeatability is affected by several factors such as: threshold calibration against reference sample, magnification, number of fields and scanning procedure. The reference samples for many particulate samples are not available. Threshold corrections were made by comparing the view through the eye piece and the view on the image screen such that shading covered all the particles that were viewed through the microscope. For fixing the number of fields and magnification, a series of tests was carried out on the same sample and the results

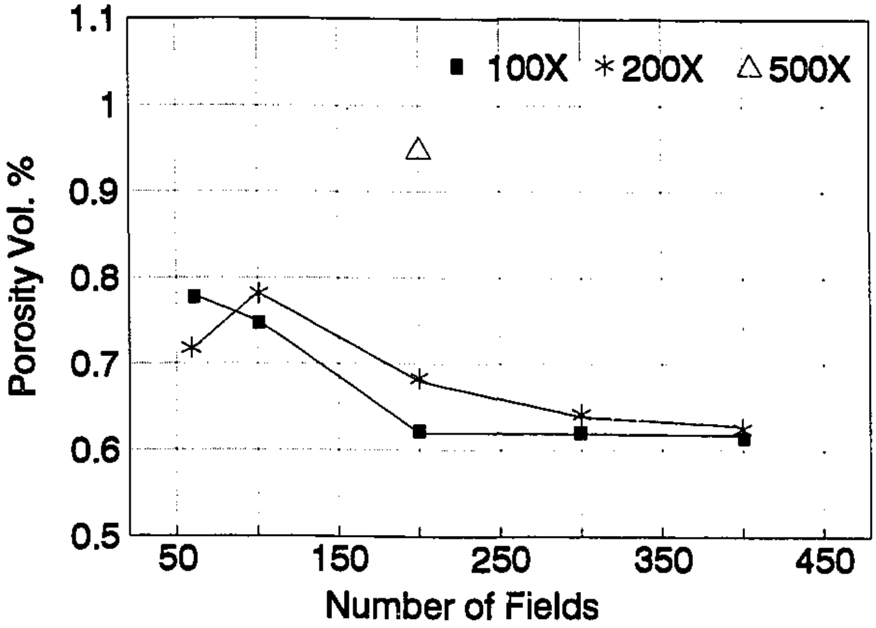

Fig. 1.4 Volume Percent of Porosity vs Number of Fields at Different Magnifications.

are presented in Fig. 1.4. It is evident that the repeatability of the test result is quite satisfactory at a magnification of 100X and at 200 fields. Therefore these values were set for the measurements. The scanning mode which was followed is shown in Fig. 1.5.

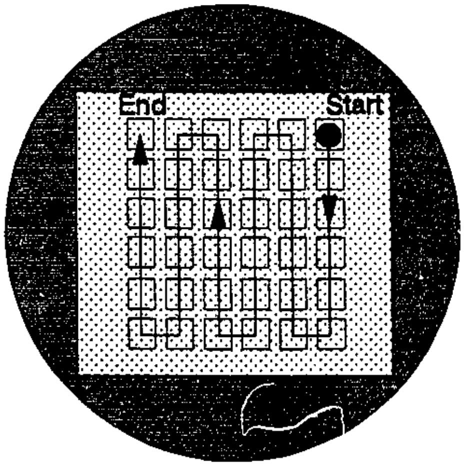

Fig. 1.5 Scanning Mode Used in Image Analysis.

1.4 Results and Discussion

As mentioned earlier, the objective of developing this apparatus was to successfully introduce various inoculants for the systematic study of their behaviour during solidification *i.e.*, their nucleation potential. These aspects constitute separate chapters in the latter part of this thesis. In this section, results and discussions which are only relevant to the addition process will be presented.

In the early stages of the present study, trials were made to add inclusions by the vortex method using a vibratory feeder as shown in Fig. 1.1. Preheated powders ($\sim$ 700^0C) were transferred into an insulated chamber to which a vibrator was attached to maintain a continuous stream of particles into the vortex and to break up the clusters before they entered the vortex. It proved to be extremely difficult to break up all the clusters into individual particles and maintain a free flow into the vortex, particularly in the lower size fractions ($\sim$2-5μm). In addition, the particles tended to reform clusters once again in the vortex. When these clusters which formed in the vortex entered into the melt their disintegration appeared to be virtually impossible.

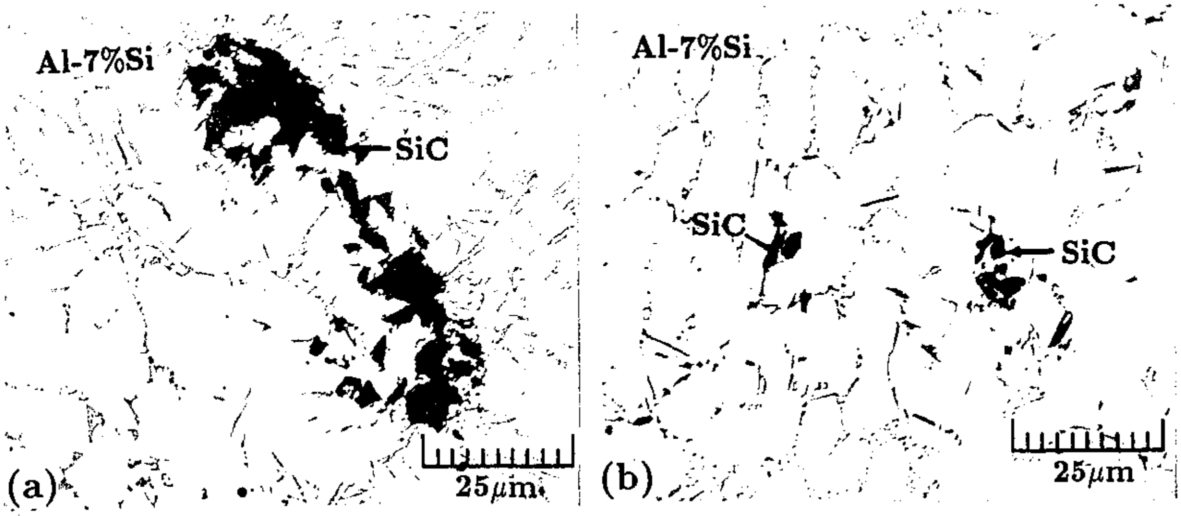

Fig. 1.6 Particle Distribution Obtained from the Vortex Method; (a) Normal Distribution and (b) Best Distribution.

Table 1.2 Chemical Composition and Source of Supply of Inoculants.

Inclusions Type	Chemical Analysis (wt.%)	Source of Supply
α-Al_2O_3	Al_2O_3=99, ¶=1	Norton Co, USA
γ-Al_2O_3	Al_2O_3=98, ¶=1-2	Condea, Germany
SiC	SiC=99, ¶~1	Norton Co, USA
MgO	MgO>95, CaO=1-4, ¶<1	MSM, USA
Spinel	$MgAl_2O_4$=95, CaO=2-3, ¶ ~2	Alcan Int., Canada
SrO	SrO=99-100, BaO=0.1-1	Timinco Metals, Canada
$Sr(OH)_2$	$Sr(OH)_2$>95, CaO=1-4, ¶<1	Timinco Metals, Canada
TiB_2	Ti=68-69, B=30-31, C=0.25, O=0.5, N=0.15	Union Carbide, USA
TiC	Ti=80.0, C=19.8, O=0.1, Fe=0.05, Si=0.01	Kennametal, Canada

¶:- Other elements such as: Si, Fe, Ca, O, N etc.

The results obtained from these initial attempts are shown in Fig. 1.6. Clusters were frequently observed (Fig. 1.6(a)), and the best distribution that was obtained is shown in Fig. 1.6(b). Reactive particles such as TiC and TiB_2 etc., could not be added by this method due to oxidation and sintering. On the other hand, different particles irrespective of their wettability and chemical reactivity (see Tables 1.2 & 1.3) could be successfully added into aluminum melts using the injection technique developed for the present study.

The volume percent retained in the melt, as expected, showed a strong dependence on the particle size and chemistry as indicated in Table 1.3. The percent retained was calculated from the known amount added to the fluidizer tube and the amount measured by image analysis in the final ingot. For some particulate systems the volume percent retained in the melt could not be determined by the image analyser because the inclusions either decomposed in the melt (*e.g.*, SrO and TiC), or the contrast between the matrix and the particle was insufficient (*e.g.*, TiB_2) as discussed earlier. Among all the particles, γ-Al_2O_3 was the most difficult to retain in the melt because of its low wettability and low density. Only large particles were used (~75μm), and these tended to float immediately after agitation was stopped.

The distribution of α-Al_2O_3, TiB_2 and SiC particles in an Al-7%Si alloy is shown in Fig. 1.7. It can be seen that even very fine (~ 2-5μm) Al_2O_3 particles could

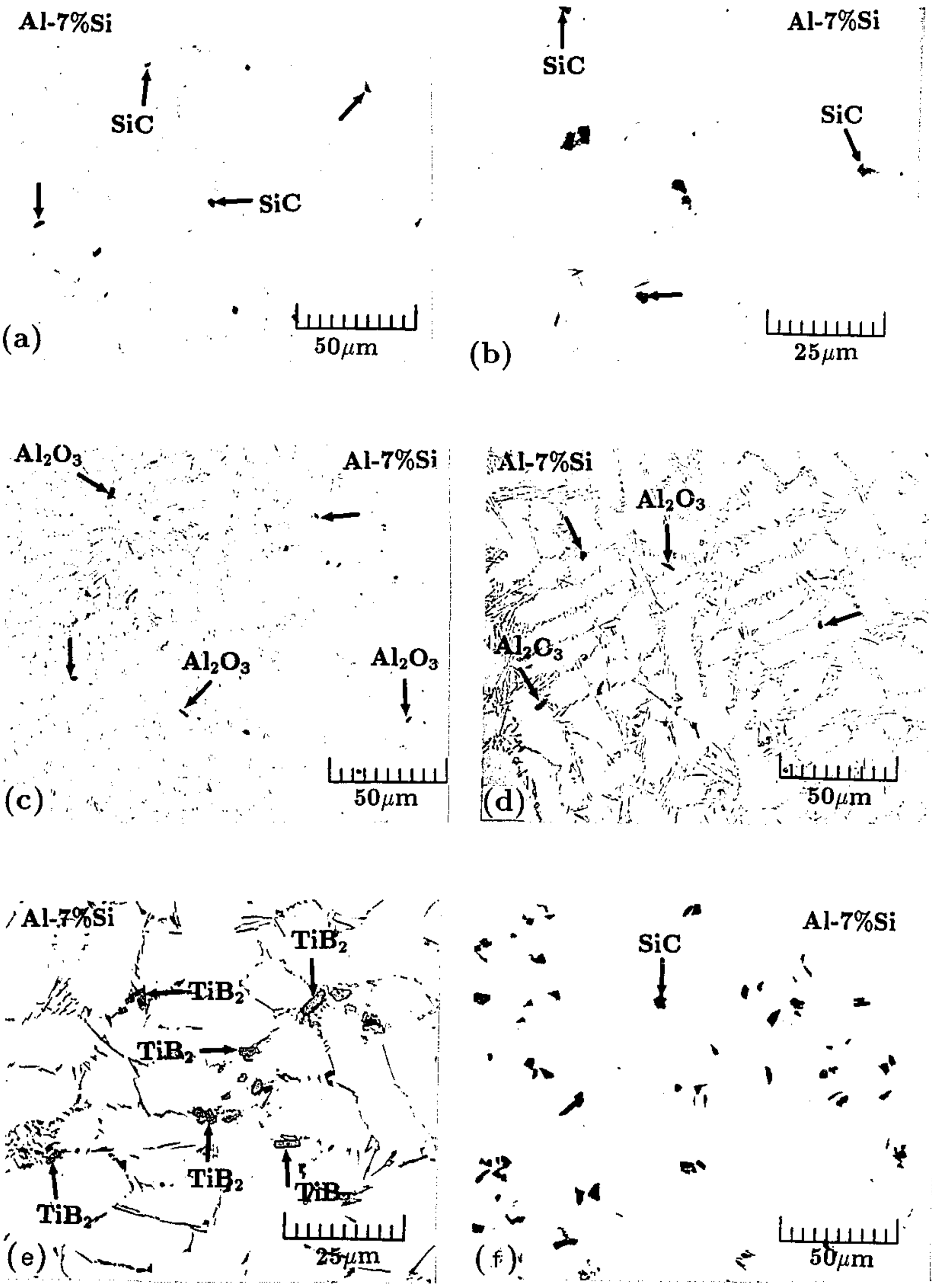

Fig. 1.7 Distribution of Various Particles in Al-7%Si Alloys; (a) 5 μm SiC, (b) 5 μm SiC Showing Worst Distribution, (c) 2-5 μm Al_2O_3, (d) 5 μm Al_2O_3, (e) 5 μm TiB_2 and (f) 2 vol. % SiC (10 μm).

Table 1.3 Physical Characteristics of Inoculants[37,40−42] and Volume Percent Retained in the Melt.

Inclusions Type	Size Range μm	Preheat Temp. ^{0}C	Melting Point ^{0}C	Contact Angle	Density g/cm^3	Vol. % Retained
α-Al_2O_3	5 - 40	700	$\sim$2050	$\sim$ 148[43]	3.98^t	60 - 85
γ-Al_2O_3	$\sim$75	700	N. A.	N. A.	3.2^t	$\sim$ 30
SiC	5 - 100	600	$\sim$2825†	$\sim$ 134[44]	3.2	70 - 95
MgO	10 - 40	700	$\sim$2900	N. A.	3.58	70 -85
Spinel	10 - 40	600	N. A.	N. A.	N. A.	$\sim$ 90
SrO^r	15- 40	200	$\sim$2430	N. A.	4.7	N.A.
$Sr(OH)_2{}^r$	15- 40	100	$\sim$375	N. A	3.6	N.A.
$TiB_2{}^r$	5 - 10	250	$\sim$3225	$\sim$ 90[45]	4.52^t	N. A.
TiC^r	5 - 10	250	$\sim$3150	$\sim$ 90[45]	4.93^t	N. A.

N. A.:- Not Available r:- reactive t:-theoretical †:- decomposition

be added without significant cluster formation (Fig. 1.7(c)). The distribution of 10μm Al_2O_3 particles over the entire surface of a polished sample was analysed by the image analyser and the resulting distribution is shown in Fig. 1.8. It is evident that even at a low level of addition ($\sim$ 1.2 vol. %), the distribution is quite uniform.

As mentioned earlier, clusters may form due to the characteristics of the particles and the solidification process. In Fig. 1.7, it can be seen that the particles are pushed into the interdendritic regions. When the particle number density is low (Fig. 1.7(a-d)), cluster formation due to particle pushing is not observed, but when the particle number density is increased (Fig. 1.7(e & f)), some clusters do appear in the microstructure. These are believed to be due to particle pushing during solidification rather than clustering in the liquid. Inclusions of spinel, MgO and γ-Al_2O_3 were also pushed by the α-dendrites into the interdendritic regions. A detailed discussion on these aspects is given in Chapter 3.

Badia and Rohatgi[46] confirmed that non-wettable particles could not be introduced into molten alloys by injection below the bath surface through an inert gas stream. They utilized a hand gun for this purpose. During the injection of a gas stream, powder particles encapsulated within a bubble (Fig. 1.9) can be transferred into the melt only, if (i) they come in contact with the melt by replacing solid/gas and gas/liquid

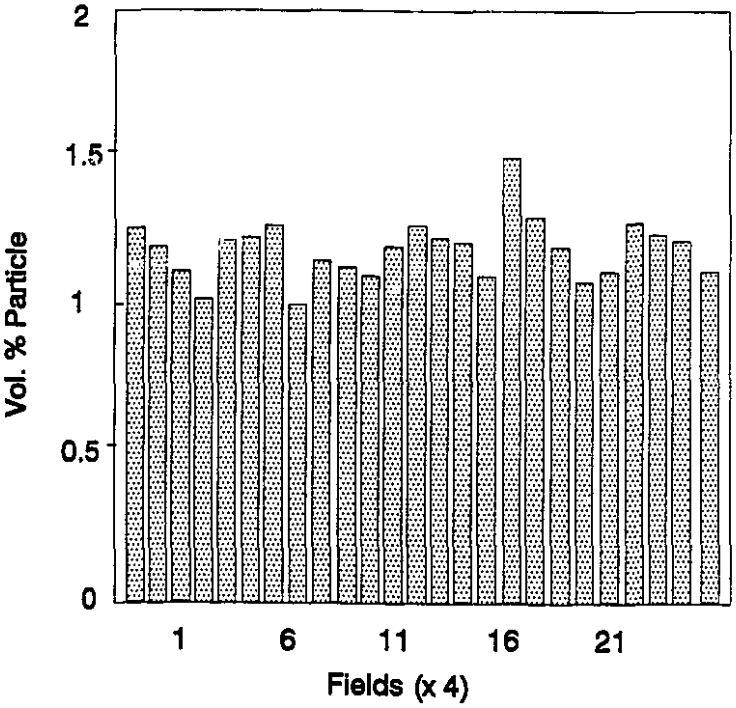

Fig. 1.8 Distribution of 10 μm Al_2O_3 Particles on Whole Sample Surface.

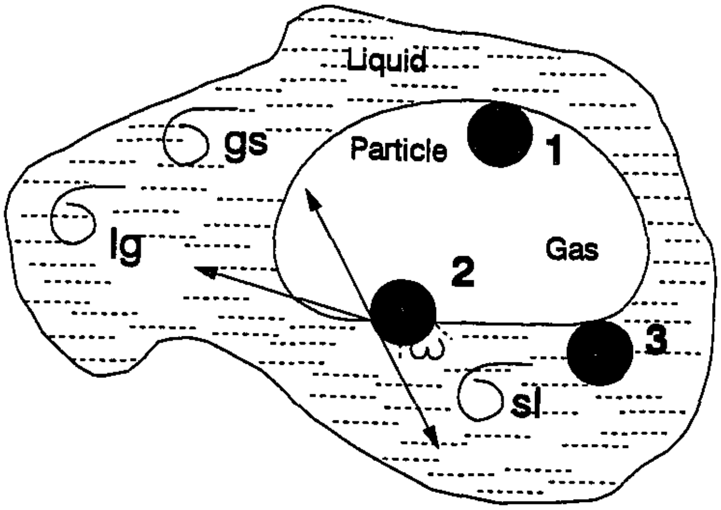

Fig. 1.9 Schematic of Particle Transfer Process From Bubble to Melt.

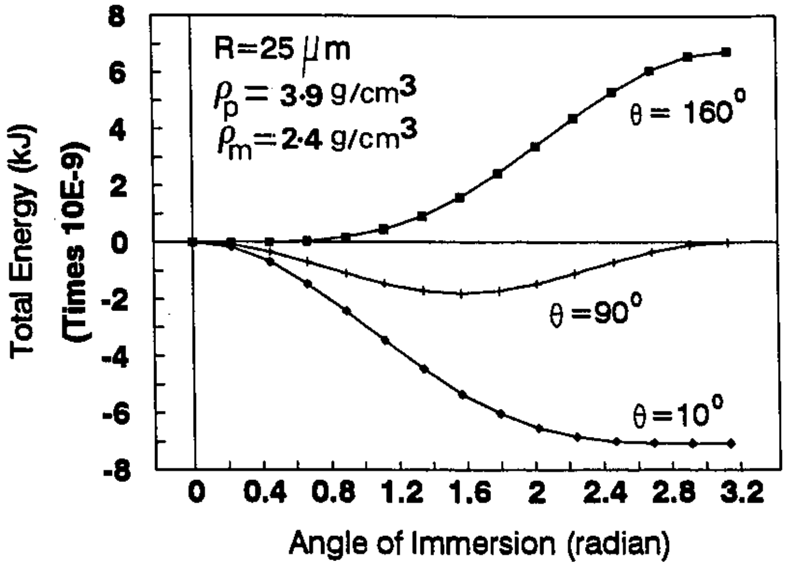

Fig. 1.10 Variation of Total Energy with Angle of Immersion for Wettable and Non-wettable Particles.

interfaces with an equivalent solid/liquid interface, and (ii) the transfer is energetically favourable *i.e.*, the particles are wettable. The total energy change of the system can be expressed as

$$\Delta E_t = \sum_{i=1}^{n} \Delta E_i \tag{1.1}$$

where the ΔE_i's are the contributions due to changes in the surface, potential, kinetic, and thermal energies. Neglecting kinetic and thermal effects, the various energy contributions can be expressed as[47]

$$\Delta E_{surf} = \pi R^2 \sigma_{LG}[2(cos\omega - 1)cos\theta - sin^2\omega] \tag{1.2}$$

$$\Delta E_{pot} = -\frac{4}{3}\pi R^4 \rho_p g(1 - cos\omega) \tag{1.3}$$

$$\Delta E_{buoy} = -\frac{\pi R^4}{48}\rho_l g[108\ln(\frac{2+cos\omega}{3}) + 39 - 40cos\omega + cos^4\omega] \tag{1.4}$$

where σ_{LG} is the surface tension, ρ is the density, θ is the contact angle between the particle and the melt, g is the acceleration due to gravity, R is the radius of the particle and ω is the semi-epical angle of immersion. The variation of the total energy at different stages of immersion is shown in Fig. 1.10, where it is suggested that in the case of $\theta \leq 10^0$ (theoretically $\theta \leq 90^0$), i.e., wettable particles, the particles should enter the melt spontaneously as the total value of ΔE_t is negative.

TiB_2 and TiC particles whose contact angle is believed to be low[45,48] should, therefore, enter the melt easily. No such particles could be retained in practice by simple injection into the bath, and even particles which readily react with the melt (*e.g.*, TiC and SrO) could not be retained in this way. The implication is, therefore, that the kinetics of the process more than the thermodynamics determine the ease of particle transfer from the gas phase to the liquid phase.

Up to 2 volume percent of particles could be easily added. Additions above this level were limited partly by the size of the unit used and partly by the process dynamics. When the fluidizer tube was filled to more than one third of its height it was difficult to achieve a steady state fluidization. At these higher loads, it was necessary to increase the gas flow rate with the result that clusters of particles were released into the carrier tube. These ultimately, resulted in a non-uniform distribution in the melt as illustrated in Fig. 1.7(f). If the gas flow rate was too large, excessive bubbling occured in the melt, and as a result some bubbles escaped without interacting with the impeller. This excessive bubbling could also float out particles which were already in the melt and could decrease the recovery. Under ordinary melting conditions inclusion levels as high as 35/500 mm^2 may be found in an aluminum melt.[9] When operated properly the present technique was able to introduce inclusion levels much higher than this and thus was able to facilitate research on inoculant behaviour in liquid aluminum.

1.5 Summary

Considerable initiatives have often been taken to introduce specific solid particles directly into molten metals in a desirable quantity, but little success has been acheived particularly in the case of reactive particles. Therefore, alternative routes such as production of solid particles through chemical reactions within the melt are often used. While these methods are capable of producing solid particles within the melt, the chemistry of the melt changes and control of particle size and chemistry is difficult. In the present study, a direct addition technique has been utilized to introduce many types of inclusions into liquid aluminum and Al-Si alloys, irrespective of their wettability and chemical reactivity while preserving the surface characteristics and melt chemistry. It has been shown that a wide variety of inclusions can be added to aluminum and aluminum alloy melts using this technique of injection. Uniform distributions can be obtained in the melt even with particle sizes of the order of 2-5 μm, and particle recoveries are in the range of 30-90 percent depending on the inclusion type. It has been demonstrated that the kinetics, more than the thermodynamics, determine the ease of particle transfer from the gas phase to the liquid phase. Inclusions with melting points below the melt temperature can also be added by a simple modification to the apparatus.

Chapter 2

Mechanisms of Grain Refinement

2.1 Introduction

In solidifying aluminium alloy castings three different grain morphologies are possible, namely, equiaxed, columnar and twinned columnar (TCG). The deliberate suppression of columnar or TCG in aluminium alloy ingots and shaped castings, and the formation of an equiaxed solidification structure by the addition of inoculants to the melt before casting is a common industrial practice. There are several reasons why the control of grain size and structure is important in castings. Equiaxed grain structure ensures uniform mechanical properties, reduced ingot cracking, improved feeding to eliminate shrinkage porosity, distribution of second phases and microporosity on a fine scale, improved machinability and cosmetic features. The grain refining inoculants commonly used in the aluminium industry are usually master alloys of Al-Ti or Al-Ti-B. Despite the commercial importance of grain refinement and the volume of scientific study on this topic over the years, it still remains unclear how Al-Ti-B grain refiners operate.

In principle, the mechanism of grain refinement is quite straight forward. Numerous potent heterogeneous nuclei are dispersed in the melt, and a large number of these sites become active during solidification and nucleate the solid. It is agreed that when master alloys are added, the aluminium matrix dissolves and releases intermetallic particles into the melt to subsequently act as nucleants. Exactly which particles are released, their physical and chemical characteristics, and their subsequent reaction with the melt are still disputed.

With the aim of putting recent studies on the grain refinement mechanism and the importance of the present experimental investigation into proper context, earlier experimental studies and theories will be reviewed briefly.

2.2 Literature Review

The literature on the topic of grain refinement is voluminous and intriguing. Several theories have been hypothesized and many have been contradicted. Interestingly, some of those postulations which were discarded reappeared over the course of time as research advanced. To cite an example, as far back as 1951 Cibula[21] suggested TiB_2 particles to be the nucleant in melts treated with Al-Ti-B master alloys. Later, in 1987, Sigworth and co-workers,[49] made a critical argument against the so called 'boride' theory based on the observation of TiB_2 particles in the grain boundaries of Al-Ti-B master alloys, suggesting that they are poor nucleants. More recently, in 1993, Sigworth and co-workers[18] using a sensitive thermal analysis technique reported TiB_2 to be the most active nucleant. Detailed discussion of this broad literature is beyond the scope of the present thesis, and the reader is referred to the recent review by McCartney.[19] Only the major schools of thought and experimental findings will be dealt with here.

2.2.1 Phase Diagram Theories

The first attempt to hypothesize the mechanism of grain refinement dates as far back as 1951. Crossley and Mondolfo[24] proposed the peritectic theory based on the peritectic reaction in the Al-Ti phase diagram (Fig. 2.1) as:

$$L + TiAl_3 = \alpha\text{-}Al \tag{2.1}$$

The titanium aluminide crystals, added through the master alloy, dissolve slowly in molten aluminium giving a grain refinement, the effect of which fades away with time. It is reasonably clear that $TiAl_3$ crystals are active nucleants since they have planes of low disregistry and surface energy with α-Al.[35,50–51] Davies, Denis and Hellawell,[50]

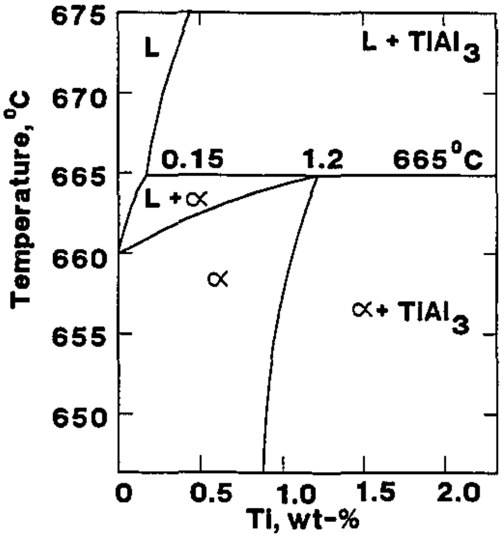

Fig. 2.1 Aluminum Rich Corner of Al-Ti Phase Diagram.[24]

and Maxwell and Hellawell[53] have observed $TiAl_3$ particles in the centre of α-Al grains. These particles promote the peritectic reaction, and fading is observed because they dissolve with time. Careful etching reveals a titanium rich 'halo' around $TiAl_3$ particles suggesting a peritectic type of reaction.[49] Cooling curves published by Arnberg, Bäckerud and Klang[35] also support the sequence of nucleation *i.e.*, they show no nucleation undercooling and a nucleation temperature (T_n) above the melting point (T_m) of aluminum. This observation implies that nucleation occurs through a peritectic reaction around the peritectic temperature (665^0 C) which is higher than the melting point of pure aluminium.

Despite the fact that most commercial grain refiners contain both Ti and B, no clear concensus has emerged as to how and why commercial grain refiners containing boron work. Careful analysis of the theories hypothesized shows that none is fully satisfactory. The proponents of the peritectic theory[24] suggest that the improved performance of boron containing master alloys is due to the displacement of the peritectic composition from 0.15 % Ti towards the aluminium end of the phase diagram thus ensuring the thermodynamic stability of $TiAl_3$ at low levels of Ti addition (~0.02%). This proposition, however, appears to be incompatible with the Al-Ti-B phase diagram predicted by Maxwell and Hellawell,[54,55] Moriceau,[56] Jones and Pearson,[57] Sigworth,[58] Abdel-Hamid and Durand[59] as well as the segregation experiments of Finch.[60] All of the calculated phase relations show that the surface separating the liquid Al from the liquid plus the TiB_2 region is sharply nosed into the pure aluminium corner. It is also suggested that there is a ternary peritectic reaction virtually identical to the binary peritectic and of the form:

$$L + TiAl_3(+TiB_2) = \alpha\text{-}Al(+TiB_2) \tag{2.2}$$

This reaction occurs at liquid compositions of about 10^{-4} wt.%B and 0.15 wt.%Ti. In other words, the solubility of $TiAl_3$ is virtually unaffected by the presence of boron. However, contrary to these thermodynamic predictions, Mondolfo and co-workers[61] claim to have obtained experimental data indicating the effect of boron in displacing the peritectic towards the Al-rich end. It has also been suggested that when all the boron reacts to form TiB_2, its effect disappears and grain refinement fades away. The general acceptability of these propositions is questionable since little experimental support exists.

Marcantonio and Mondolfo[25] have proposed a ternary eutectic reaction nucleating the solid phase as:

$$L = \alpha\text{-}Al + TiAl_3 + (Al, Ti)B_2 \tag{2.3}$$

It is, however, unclear whether a ternary eutectic of this form exists at low Ti levels, and experimental studies do not support such a reaction.[55]

2.2.2 Particle Theories

Cibula[21,23] and others[57] postulated the 'carbide-boride' particle theory which suggests that nominal addition of Al-Ti master alloy promotes TiC formation by reaction with the residual carbon present in the aluminium melt. With the addition of Ti-Al-B master alloy, TiB_2 particles are dispersed in the melt, and TiB_2 and TiC being virtually insoluble in molten aluminium, act as heterogeneous nucleation sites. The observed fading behaviour is merely a result of particle settling and/or agglomeration.

While theoretical and experimental investigations concerning borides are quite extensive, not much information is available regarding the behaviour of TiC. To prove the so called carbide theory experimentally, several attempts have been made[21,23–29] to form appreciable amounts of TiC in titanium containing aluminium melts with little success as mentioned in Chapter 1. Banerji *et al.*,[30–31] claimed to have succeeded in generating substantial amounts of TiC in Al-Ti alloys by introducing preheated graphite powders into superheated melts, using the vortex method or electromagnetic stirring. It was also claimed that the master alloy so prepared can be used to grain refine aluminum and its alloys, and thus it was concluded that the 'carbide' theory is a valid mechanism for grain refinement. Cissé *et al.*,[62] suggested that, for TiC particles, epitaxy occurs on all faces giving a single aluminium grain having a single orientation. Though the existence of epitaxy makes the nucleation process feasible from the crystallographic point of view, it is not clear whether TiC is, in fact, stable in an aluminium melt and much controversy has emerged over this point.[63–65]

The relative stabilities of Al_4C_3 and TiC in aluminium are not yet clearly established. Studies[31,63–69] on the thermodynamic stability of these compounds are contradictory and somewhat inconclusive. The feasible reaction in an Al-Ti melt containing carbon is[67,68]

$$13Al(l) + 3TiC(s) \rightleftharpoons Al_4C_3(s) + 3TiAl_3(s) \tag{2.4}$$

which can be broken down to the following sub-reactions:

$$4Al(l) + 3C(s) \rightleftharpoons Al_4C_3(s) \tag{2.5}$$

$$Ti(l) + C(s) \rightleftharpoons TiC(s) \tag{2.6}$$

$$Ti(l) + 3Al(l) \rightleftharpoons TiAl_3(s) \tag{2.7}$$

The last reaction (Eqn. [2.7]) is feasible when the Ti concentration exceeds the peritectic composition (~0.15%). In addition to the binary compounds, the complex carbides Ti_3AlC and Ti_2AlC are also reported to form in this ternary system. Banerji *et al.*,[31] considered Eqns. [2.5] and [2.6] for thermodynamic calculations and concluded that below 1450 K, TiC is unstable and leads to the formation of Al_4C_3. Fine and

Conley[63] suggested that it is necessary to compare the free energy of formation of Al_4C_3 and TiC on a per mole basis of C as illustrated in the Ellingham diagram for carbides where TiC shows a much higher stability than Al_4C_3. However, these calculations on the free energy of formation are based on pure solid Ti as the standard state, and, therefore, use of these data for grain refining systems can be erroneous. Later, Rapp and Zheng[64] considered Gibbs energies of formation of Al_4C_3 and TiC based on equilibria involving C (dissolved or pure), dissolved Ti, and liquid Al. Their calculations showed that only for a very low concentration of dissolved Ti($C_{\underline{Ti}} < 0.5$ wt pct.), does Al_4C_3 become thermodynamically more stable than TiC in the temperature range of 1150 to 1800 K. It was suggested that since there is only a negligible difference in the temperature dependence of phase stability for the TiC and Al_4C_3 phases, in normal grain refinement of aluminium alloys, TiC is thermodynamically more stable than Al_4C_3.

The complete phase diagram for the Al-Ti-C system is not available, but useful information can be obtained from partial diagrams. Fig. 2.2(a) and (b) presents isothermal sections of the ternary phase diagram (at 750^0C) and chemical potential diagrams respectively for the Al-Ti-C system.[65,66] Clearly, at equilibrium only three phases may be present except at the ternary eutectic. These are suggested to be Al, $TiAl_3$ and Al_4C_3 or $TiAl_3$, TiC and Al_4C_3. According to Yokokawa *et al.*,[65] at 973 K, Al(l) does not have an equilibrium contact with TiC, whereas at 1273 K, Al(l), TiC and $TiAl_3$ can coexist. Therefore, Al_4C_3 is most prone to form in the Al-Ti-C system below a melt temperature of 1273 K and most of the aluminum foundry operations are carried out well below this temperature. In other words, the carbide theory is highly suspect.

Numerous problems can also be found with the boride theory. Commonly, three boride phases are discussed in the context of grain refinement; namely, TiB_2, AlB_2 and $(Al,Ti)B_2$. Marcantonio and Mondolfo,[25] and Cibula[23] have shown that AlB_2 is a weak grain refiner in pure aluminium and is active only at hypereutectic compositions. If TiB_2 is the nucleating phase, then the grain refining curves would suggest TiB_2 to be a more effective nucleant than $TiAl_3$ (*i.e.*, $T_n \leq T_m$), but there is evidence to the contrary ($T_n > T_m$).[35] It has been established both in laboratory and industrial experience that the Ti/B ratio ($X_{Ti} > 0.5\ X_B$), and in particular the TiB_2 stoichiometric ratio (2.22),

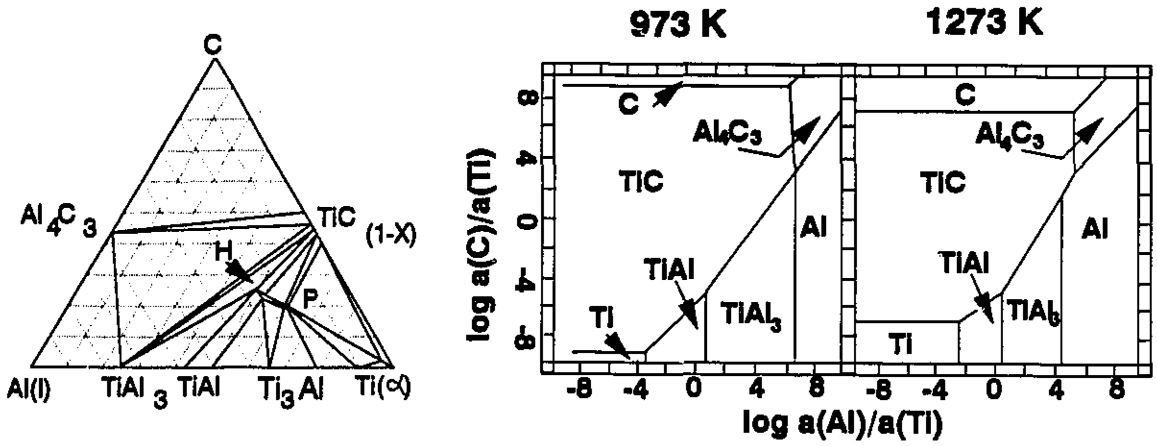

(a) (b)

Fig. 2.2 Phase Relations in Al-Ti-C System; (a)Isothermal Section of Phase Diagram at 1023 K[66] and (b) Chemical Potential Diagrams at 973 K and 1273 K[65].

has a critical significance in grain refinement. Ti in excess of the stoichiometry of TiB_2 is a must for efficient refinement.[70]

The observation of a complex (Al, Ti)B_2 phase led researchers to propose another theory known as the 'metastable' boride theory.[56,70,71] The (Al,Ti)B_2 phase has been thought to be a metastable boride, since it may disappear with long holding time.[71] It has been proposed that the (Al, Ti)B_2 phase assists grain refinement either by acting directly as a nucleant or by nucleating $TiAl_3$ crystals during cooling.

The metastable boride theory is also not free from problems. Both AlB_2 and TiB_2 have hexagonal and isomorphous structures (see Fig. 2.3).[72,73] Unless very precise measurements are made it is not possible to differentiate clearly between the X-ray spectra of the two phases. Though it is well known that TiB_2 and AlB_2 are stable equilibrium phases, it is not clear whether (Al, Ti)B_2 is stable or metastable.

Sigworth *et al.*,[58] claims that AlB_2 and TiB_2 form a continuous solid solution series, while Abdel-Hamid and Durand[59] state that they exist as separate phases.

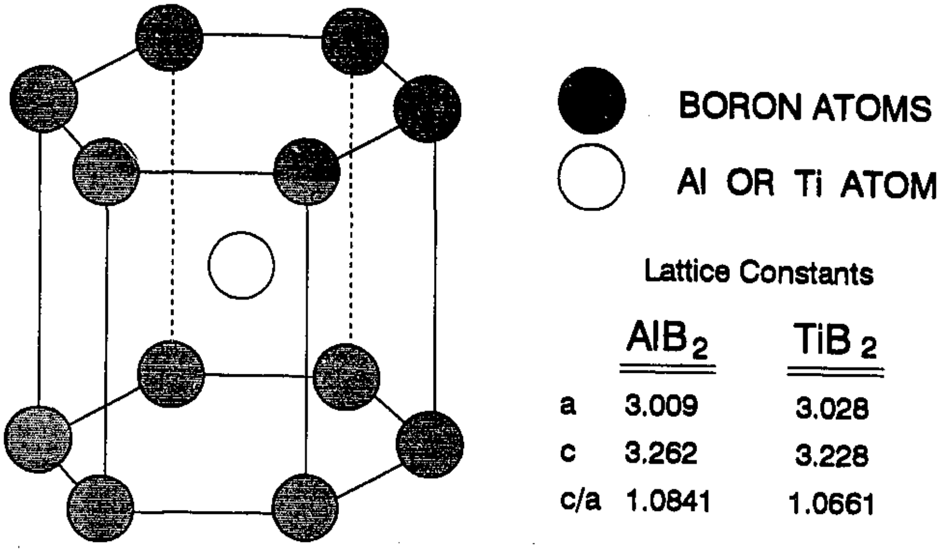

	AlB_2	TiB_2
a	3.009	3.028
c	3.262	3.228
c/a	1.0841	1.0661

Fig. 2.3 The Unit Cell for AlB_2 and TiB_2.[72,73]

Kiusalaas and Bäckerud[72,74] carried out an extensive study on the nature of these crystals and concluded that the initial composition of the boride phase (Al, Ti)B_2 is determined by the processing route for the master alloy, and a whole range of compositions from AlB_2 to TiB_2 may form. During holding of the master alloy in the liquid state a transformation occurs in the direction of (Al, Ti)$B_2 \Rightarrow TiB_2$ which seems to stop before the pure TiB_2 composition is reached. While the exact nature of the boride phases is not resolved, in view of their similarity to AlB_2 and TiB_2, the nucleating potential of (Al, Ti)B_2 may be expected to be similar. In other words, since AlB_2 and TiB_2 are weak refiners, (Al, Ti)B_2 is expected to behave in a similar manner. Kiusalaas and Bäckerud[72] reported that the grain refining efficiency increases as transformation occurs in the direction of (Al, Ti)$B_2 \Rightarrow TiB_2$. It has also been established that in master alloys in the form of rods, boride particles which were extracted onto a carbon replica, proved to be essentially TiB_2 having an Al content less than 1 %.[75] It is well known that rod master alloys are very efficient grain refiners and whether or not (Al, Ti)B_2 is stable or metastable does not bear much significance as far as the grain refinement mechanism is concerned.

2.2.3 Theories Based on Combined Effect of Phase Diagram and Boride Particles

Jones[76–78] hypothesized the concept of hypernucleation at the TiB_2/melt interface. By caculating the activities of Ti in the melt and in TiB_2, he showed that Ti atoms will segregate to the TiB_2/melt interface providing a stabilised layer of atoms on the TiB_2 crystal surface. This layer, being a solid solution of Ti and Al, was predicted to remain stable above the melting point of pure Al *i.e.*, exist in the melt before casting. On cooling, such a layer will permit the ready growth of primary α-Al from the bulk with virtually no undercooling. Though this concept sounds the most promising there is no experimental evidence to support it and it is not clear whether or not the volume influenced around the boride particles by adsorption is sufficient to cause a high $T_n(>T_m)$.

More recently, Bäckerud *et al.,*[79] and others[80,81] have proposed the peritectic 'hulk' theory. The mechanism consists of several sequential steps (Fig. 2.4). The essential step of this theory is based on the concept of duplex crystal formation which has been discussed by many researchers.[49,72,74,82,83] It was suggested that the dissolution of master alloy leads to the formation of a protective boride sheathing (presumably TiB_2) at the interface of α-Al/$TiAl_3$ crystals which effectively prevents the aluminide from dissolving. Simultaneous dissolution of these duplex crystals will give rise to fine peritectic cells. Titanium and aluminium atoms will counter flow through this passive layer of TiB_2 on the peritectic cells, creating a layer of Ti rich liquid called the peritectic 'hulk'. As the temperature falls, nucleation of α-Al begins in the liquid in the hulk and dendrites form with subsequent piercing of the passive layer. Though the proponents[80,81] of this theory claim it to be the most viable mechanism, several arguments can be levelled against it.

Recently, Mayes *et al.,*[83] observed the presence of TiB_2 crystals within $TiAl_3$ crystals using TEM on thin foils. Johnsson *et al.,*[18] performed experiments with repeated melting and solidification cycles on a 0.03% Ti (Ti/B = 4.8/1) alloy. After five repeated cycles at 775°C no difference in T_n and grain size was noticed. According to the peritectic 'hulk' theory, once a peritectic cell is activated, its higher Ti concentration

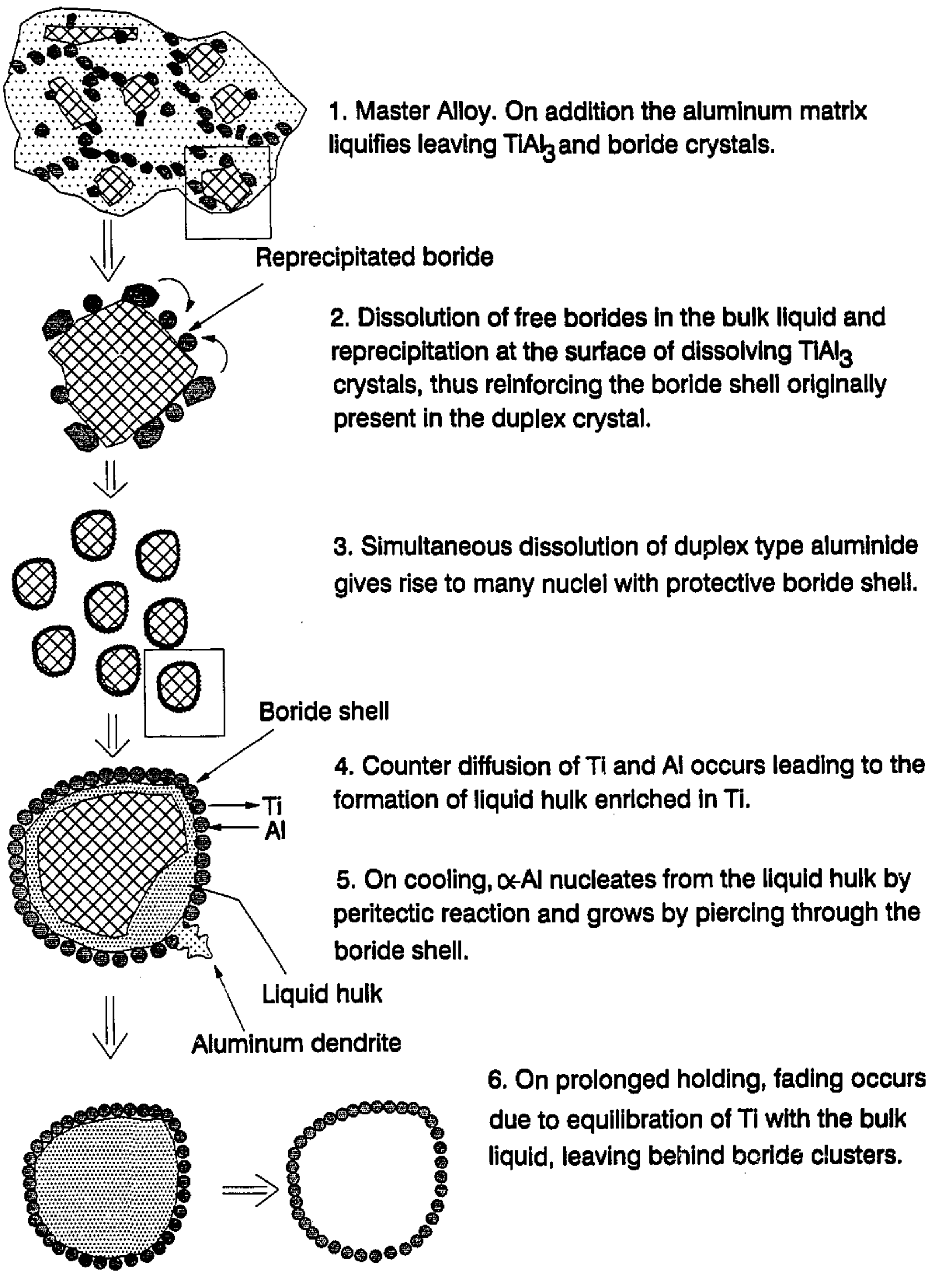

Fig. 2.4 Schematic Sequence of Peritectic Hulk Theory.[79,80,81]

should be equilibrated with the melt and dissipated by repeated melting and solidification. Further, the phenomenon of recovery of fade on stirring a melt grain refined by Al-Ti-B master alloy after long holding time, as observed by Birch *et al.*,[84] cannot be explained by this theory.

Although much work has been done to establish the grain refining mechanism and the influence of various parameters such as Ti-content, Ti/B ratio, contact time, and temperature on the grain refining efficiency in aluminum and its wrought alloys, research on grain refinement of foundry alloys is scanty. Aluminum-silicon alloys are currently the most important aluminum based foundry alloys because of their excellent castability, mechanical and physical properties. The Al-Si alloys form a simple eutectic system. The commercial procedure for grain refinement in hypoeutectic Al-Si alloys seems to be borrowed wholly from grain refining practice in wrought alloys without a consideration of the influence of the silicon content. As a result, Al-Ti-B master alloys form the standard grain refiner in the industry. Lu and co-workers[85] have demonstrated that AlB_2 is a powerful grain refiner in Al-5%Si and Al-7%Si alloys, contrary to their behaviour in pure aluminum. Sigworth *et al.*,[86] confirmed that the presence of dissolved Si has a most remarkable effect on the AlB_2 type Al-3%B master alloy, making it a powerful refiner in Al-Si alloys. Sigworth and Guzowski[22] have also reported work on the development of an Al-3Ti-3B master alloy specifically formulated for use in hypoeutectic Al-Si casting alloys. Their results show that such an alloy performs much better than conventional Al-5Ti-1B master alloys in Al-7%Si alloys. Recently, a different class of grain refiners based on the binary Al-B system has been developed and found to be efficient in hypoeutectic Al-Si alloys.[87]

As far as the mechanism of grain refinement by Al-Ti and Al-Ti-B master alloys in Al-Si alloys is concerned, not much has been accomplished in this direction. The general concept of grain refinement mechanism in Al-Si alloys has been adopted from that in wrought alloys. It was deemed that the inefficient grain refinement by Al-Ti master alloys in casting alloys was presumably due to some kind of interference that Si has with the grain refining effect of titanium. Considering the binary Si-Ti system, Sigworth *et al.*,[86] suggested that possibly the titanium silicide coats the surface of $TiAl_3$

and thus poisons the effectiveness of the nuclei present in Al-Ti master alloy. On the other hand, when Al-B is the grain refiner, it is the AlB_2 phase which acts as the nucleant and the presence of Si enhances its nucleation potential. From the cooling curve obtained from an Al-7%Si alloy grain refined by Al-B master alloy, they also suggested that AlB_2 appears to decompose during solidification, probably by a peritectic reaction. However, it is well known that Al-B forms a eutectic system at about 0.022 wt % B, at 659.7^{0}C. The enhanced performance of Al-3Ti-3B master alloys was thought to be due to the formation of (Al, Ti)B_2 phase, which is isomorphous with AlB_2, and grain refines in the same manner. Sigworth *et al.*,[86] claimed that Al-3Ti-3B master alloy is better than Al-B master alloy, since the mixed boride (Al, Ti)B_2 formed in the former has a lower solubility in liquid Al than AlB_2, but the structure is close enough to the AlB_2 phase to grain refine Al-Si casting alloys. As a result, the B consumption will be less and the associated disadvantages of Al-B master alloy in alloys with residual Ti, such as TiB_2 sludge formation, can be avoided.

In a study on the effect of various grain refiners in hypoeutectic Al-Si alloys, Apelian[89] also concluded that in the Al-3Ti-3B master alloy, the nucleating agent is clearly the metastable (Al,Ti)B_2 particles, and this master alloy has superior performance over the Al-5Ti-1B master alloy. In another study[90] on the performance of different classes of grain refiners in A356 and 319 alloys it was concluded that a small (0.022%) Ti residual will increase the grain refining performance of the classes of grain refining master alloys *i.e.,* Al-Ti-B with excess Ti, or boron, or straight Al-B. Increasing the titanium residual to above the peritectic value generally produces a further small improvement. At the 0.022% Ti residual, the Al-B product is superior to the other master alloy products in A356, and equivalent or better in 319. All products perform comparably in 319 and A356 with high titanium residual. A slight advantage in grain size was noted for the Al-2.5Ti-2.5B master alloy in most cases. Interestingly, Al-5Ti-1B showed no fade for up to thirty minutes. From these observations, it is clear that in Al-Si alloys, residual Ti has a significant impact on the refining efficiency as in the case of pure aluminum. As far as the existence of epitaxy is concerned, AlB_2 and (Al,Ti)B_2 crystals should not have any special advantage compared to TiB_2, since they are isomorphous. The existence of a eutectic at 659.7^0 C in the Al-B system,[58] which is close to the melting point of pure Al, clearly indicates why AlB_2 is a weak refiner in pure Al. However, there is no ternary experimental data on the possible role of Si, on the eutectic in the Al-B system to explain the enhanced grain refinement in Al-Si alloys. Thus, it can be concluded that the knowledge on the mechanism of grain refinement in Al-Si alloys by Al-Ti-B master alloys is limited and incomplete.

From this brief discussion, it is clear that no completely satisfactory model exists. At the heart of the grain refining problem there is the basic need to identify the nuclei. Clearly, any nuclei which are potent enough to nucleate the α phase should be present at the centre of the grains. In most of the studies to date, master alloys or chemical reaction techniques have been used for the introduction of the crystallites into the melt; however, the chemistry of the products, particle sizes and the melt chemistry are all difficult to control by these methods.

Any detailed analysis of grain refinement in these complex systems poses numerous difficulties. The substrates are submicron in size and, therefore, cannot be optically observed, and it may be almost impossible to distinguish the nuclei from other intermetallic phases in the alloy. There are only a few reports of direct metallographic studies, and the results are somewhat inconclusive. Studies involving techniques such as TEM on thin foils[74], replica extraction[91] and EPMA with neutron activated boron radiography[70], identified traces of borides and aluminides. Interaction with the background precludes the determination of the exact chemical nature of submicron nuclei, and in the case of extraction methods there is no conclusive proof that the extracted particle actually took part in a nucleation event.

An ideal way to prove the nature of the nuclei would be to establish whether or not TiC and TiB_2 alone nucleate α-Al, and then to study their behaviour in the presence of dissolved Ti. The simplest way of doing this would be to introduce moderately large (~5-10μm) synthetic crystallites whose compositions are known into the melt, and to observe their behaviour in the microstructure. The size of the crystal in such an experiment would be important since relatively large particles can be seen optically and

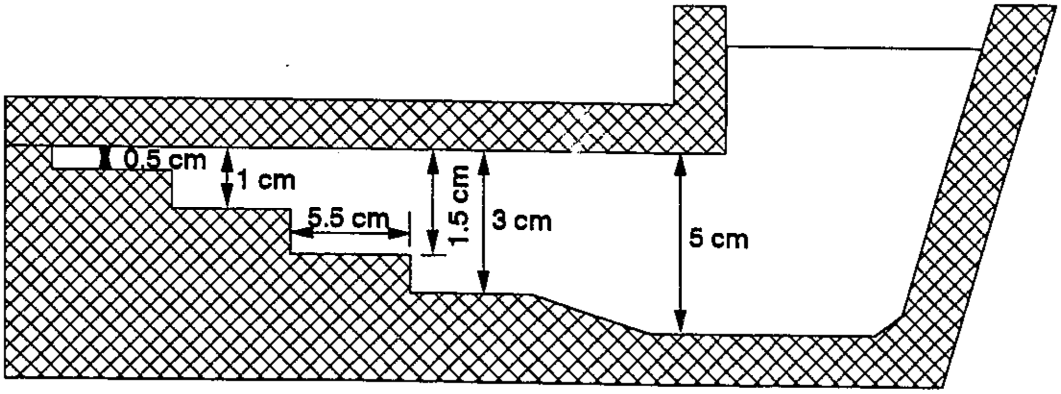

Fig. 2.5 Schematic Step Mold Used to Study the Effect of Cooling Rate.

chemically analysed in the post solidification stage. There are, however, many complexities involved in placing synthetic crystallites into an aluminum melt without changing their surface properties as discussed in Chapter 1, and little success has been achieved to date. Having developed a technique to introduce particles into an aluminum melt while preserving their physical and chemical characteristics, the behaviour of synthetic TiB_2 and TiC crystallites was studied with and without the presence of dissolved Ti, and the mechanism of nucleation is clarified in this chapter of the thesis.

2.3 Experimental

The aluminum melts (pure as well as Al-Si alloys) used were approximately 20 cm in depth and 8 cm in diameter. Inoculant were added using the technique described in Chapter 1. After the inoculant addition process was completed, the melt was cast into chill molds. The inoculant containing ingots were remelted to study the effect of holding time and alloying addition on the behaviour of the particles. During remelting, a slow agitation was maintained to keep the particles suspended in the melt. Alloying additions were done through Al-Ti and Al-Si master alloys. The melt was cast into a step mould as shown in Fig. 2.5. The mold preheat temperature was also varied from room temperature to 450^0C to study the effect of cooling rate. Cooling curves were obtained from each step at different preheating temperatures. Cooling rates were estimated from the curves, as the slope between the start of liquidus and eutectic solidification. The cooling rates were obtained for A356 alloys only. Although the cooling rates will be slightly different, the cooling rates for each step obtained from A356 alloys are considered to be same in the case of pure aluminum and hypereutectic alloys. The procedure for sample preparation has already been discussed earlier. A combination of metallographic (optical and SEM) and micro-analytical (EPMA) techniques was employed to study the behaviour of the inoculants in the solidified samples.

2.4 Results

By using the injection method described in Chapter 1, TiC and TiB_2 could be successfully added into aluminum melts without bringing the particles into contact with the atmosphere. Uniform inoculant distributions were achieved even in the case of low volume fraction additions and finer sizes. The chemical compositions of several TiB_2 particles as verified by EPMA matched the supplier specifications (*i.e.*, Ti ~69.49 wt % and B ~30.51 wt %). No trace of oxygen or nitrogen was detected, suggesting that the chemistry of the particles was not altered during the addition process.

2.4.1 Behaviour of TiB_2 Inoculant

Figs. 2.6(a) and (b) show the distribution of single and clustered TiB_2 particles in a pure Al matrix solidified at a cooling rate of $\sim 3^0$C/s. The distribution of TiB_2 particles in an Al-7%Si alloy is shown in Figs. 2.7(a) and (b) solidified at cooling rates of $\sim 3^0$C/s and $\sim 10^0$C/s respectively. It is evident from Figs. 2.6 and 2.7 that TiB_2 particles are pushed into the interdendritic region by the α-Al dendrites suggesting that they do not nucleate α-Al. The TiB_2 particles are continually rejected by the solid/liquid interface and are mechanically trapped at the grain boundaries at the end of local solidification. Etching the polished sample with modified Keller's reagent (2 ml. HF, 3 ml. HCL and 20 ml. HNO_3) caused preferential dissolution to occur along the particle/matrix boundary, indicating a high energy interface. Fig. 2.8 shows a SEM photomicrograph (at 2000X) of a TiB_2 particle cluster at the grain boundary in pure aluminum. The purely mechanical nature of the entrapment is quite clear in the

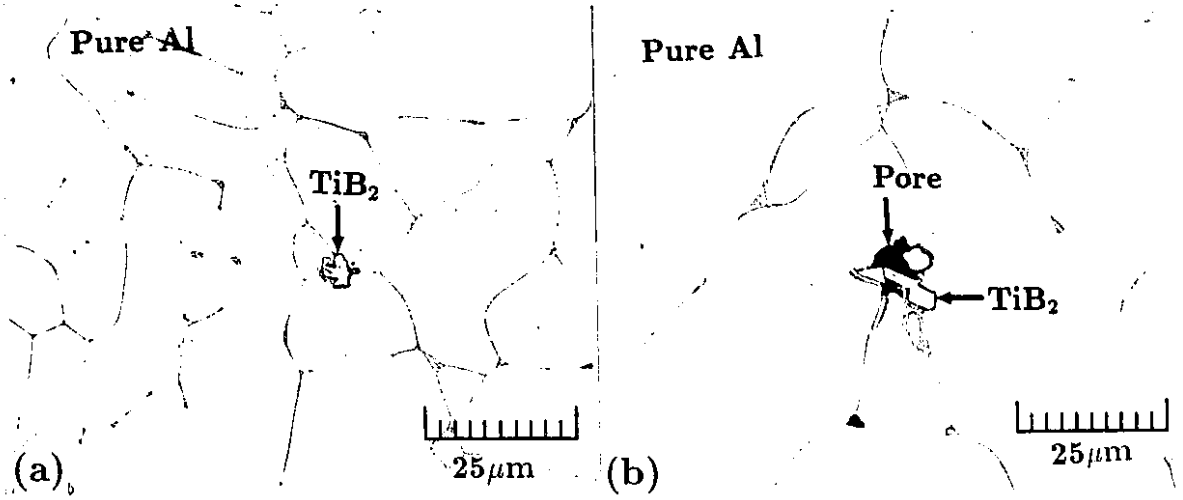

Fig. 2.6 Distribution of TiB$_2$ Particles in Pure Aluminium Matrix in the Absence of Solute Ti; (a) Single Particle and (b) Particle Cluster.

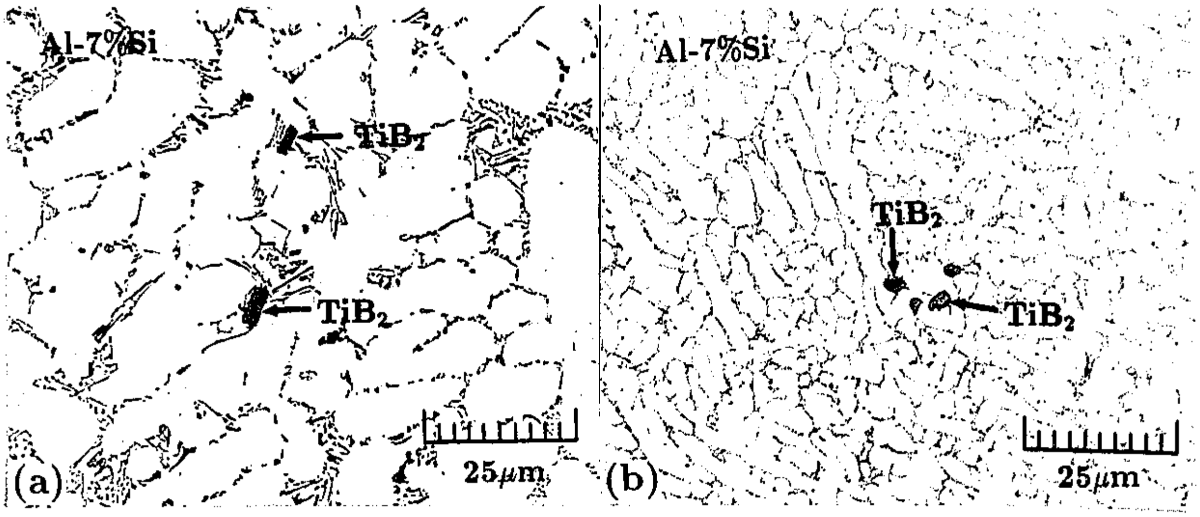

Fig. 2.7 Distribution of TiB$_2$ Particles in Al-7%Si Alloy Matrix in the Absence of Solute Ti; (a) Cooling Rate ~ 3^0 C/s and (b) Cooling Rate ~ 10^0 C/s.

Fig. 2.8 SEM Image Showing Preferential Dissolution by Etchant at the Particle/Matrix Boundary.

photograph.

Fig. 2.9 presents the microstructure of an Al-7%Si alloy, remelted and held for 6 hours at 750°C after addition of TiB_2 particles. The particle number density by manual counting was found to be approximately $43/cm^2$ before remelting. Image analysis could not be carried out on these samples due to poor contrast between the particles and the matrix as discussed in Chapter 1. In order to test the stability of the particles in these melts a slow agitation was maintained throughout the holding period to keep the particles suspended in the melt and to facilitate dissolution, if it occurs at all. The particle number density remained almost the same after a holding period of 6 hours and no change in particle chemistry was observed. Electron probe analysis (WDS) indicated no trace of aluminum within these particles and no significant amount of boron was detected in the aluminum matrix, confirming that TiB_2 particles once introduced into the melts were very stable, or at the most had very low solubility.

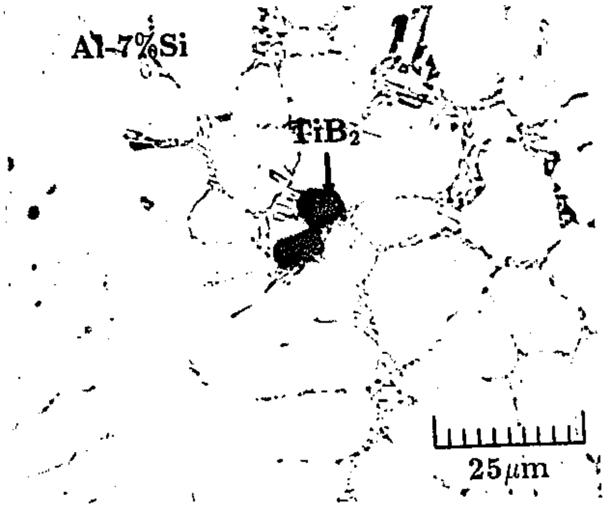

Fig. 2.9 TiB_2 Particles in Al-7%Si Alloy Matrix After 6 Hours Holding Time.

2.4.2 Behaviour of TiB_2 Inoculant with Dissolved Ti

To simulate grain refinement practice by Al-Ti-B master alloys, Al-6%Ti binary master alloy was added to provide dissolved Ti in melts to which TiB_2 had already been introduced. When excess Ti was present, most of the TiB_2 particles were found to occur within the grains. Fig. 2.10(a) presents the typical microstructure of a TiB_2 inoculated melt. The base melt was the same as that used to obtain Figs. 2.6(a) and (b). Clearly, any substrate which nucleates the grains should be engulfed by the growing crystal, provided growth is non faceted as is the case with aluminum. It is evident that with the addition of 0.01 wt pct. Ti, nucleation now occurred on the particles.

As seen from Fig. 2.10(b), a thin layer of $TiAl_3$ is present between the Al matrix and the TiB_2 crystal. It was possible to see this only at higher concentrations of Ti *e.g.*, at 0.05%, which is much lower than the peritectic composition, but it is reasonable to suppose that a similar but much thinner layer also forms at the normal Ti levels used in grain refining practice ($\sim$ 0.01%). Such a hypothesis is supported by the observation that TiB_2 clearly nucleates α-grains at 0.01% Ti level (Fig. 2.10(a)). From Fig. 2.10(b), it is evident that titanium has a specific affinity to segregate onto the TiB_2 surface forming $TiAl_3$ crystals. The $TiAl_3$ layer formed only on some parts of

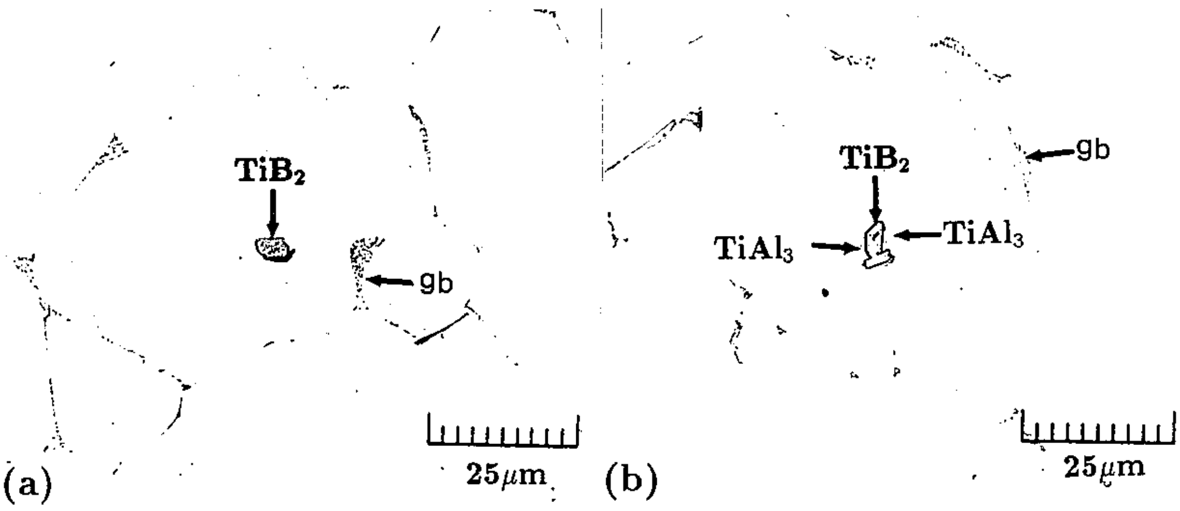

Fig. 2.10 Distribution of TiB_2 Particles in Pure Aluminum Matrix in the Presence of Solute Ti; (a) 0.01% Ti and (b) 0.05%Ti.

the TiB_2 surface and exhibited faceted growth. At higher Ti levels all particles were associated with $TiAl_3$ crystals, and particle clusters were frequently present within grains (Fig. 2.11). Particle morphology also affected the engulfment tendency significantly. Spherical particles (Fig. 2.11) invariably exhibited association with $TiAl_3$ crystals and were present within the grains, whereas elongated particles having fewer exposed crystallographic planes were occasionally pushed to the grain boundaries even in the presence of dissolved Ti. Figs. 2.12(a) and (b) clearly show that the $TiAl_3$ particles preferentially nucleate on TiB_2 particles, even at higher concentrations of Ti ($0.5\% \gg Ti_{peritectic}$) where homogeneous nucleation in the bulk melt is thermodynamically feasible. Although the TiB_2 particles were not completely covered by $TiAl_3$ crystals, almost all TiB_2 particles were found to be associated with $TiAl_3$ crystals at this composition. At 2 % Ti, TiB_2 particles were found at both the exterior surface and the interior of $TiAl_3$ as shown in Fig. 2.13.

Grain refinement of hypoeutectic Al-Si alloy by Al-Ti-B master alloy was simulated by adding various amounts of silicon to melts already containing synthetic TiB_2 crystals and solute titanium. Silicon addition was achieved by adding binary Al-Si master alloys. Figs. 2.14(a) and (b) show the microstructure of alloys containing 0.5

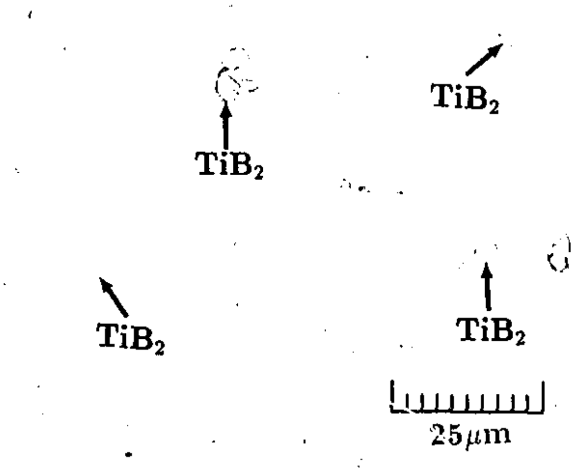

Fig. 2.11 Sperical Shape TiB$_2$ Particles in the Presence of Solute Ti.

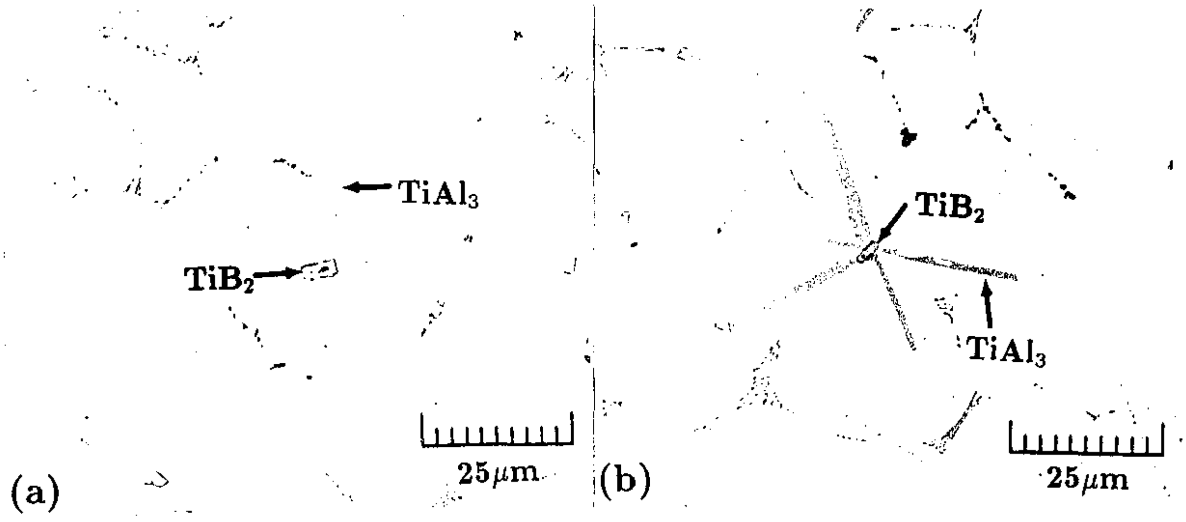

Fig. 2.12 Nucleation of TiAl$_3$ on TiB$_2$ (Ti= 0.5 wt. %); (a) Single Nucleation and (b) Multiple Nucleation.

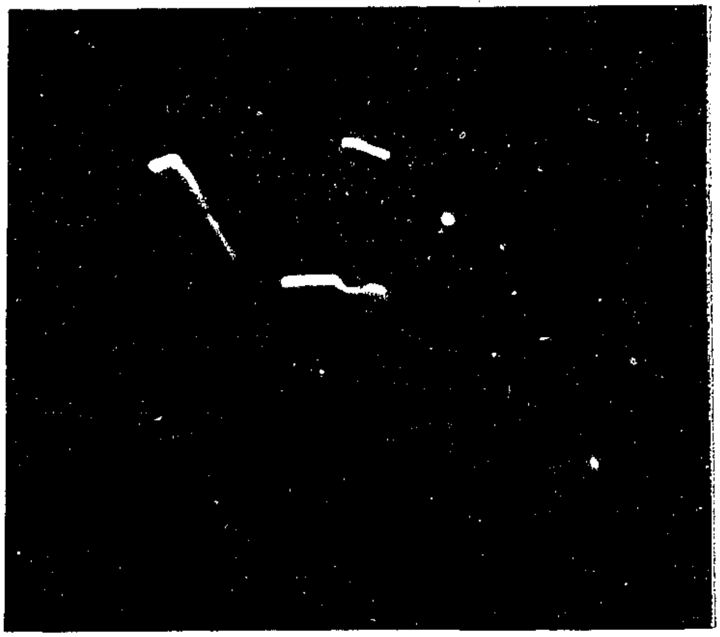

Fig. 2.13 SEM Image Showing Engulfment of TiB_2 Particles by $TiAl_3$.

% and 3% Si respectively. It is evident from Fig. 2.14(b) that the aluminide crystals preferentially nucleated on the TiB_2 crystals. Subsequently, the aluminide nucleated the α aluminum. This proposition is supported by Figs. 2.7 and 2.9, where the boride particles are pushed to the grain boundary in the absence of any dissolved Ti in Al-Si alloy.

Electron microprobe analysis revealed that these aluminides are essentially ternary compounds of Al-Ti-Si, with varying Ti and Si content. The Si content varied from 5 to 11 wt.% whereas the Ti content varied from 21 to 25 wt.%. Due to their variable composition having a non-integer stoichiometry, these phases have been indicated as $Ti_xSi_yAl_{1-(x+y)}$ in the present study. Although the number of Al and Si atoms per Ti atom do not add up to 3, the stoichiometric formula resembles a $TiAl_3$-like compound containing Si. The composition and morphology of these phases were dependent to a large extent on the cooling rate. It is interesting to note that at a moderately high cooling rate ($\sim 4^0C/s$), the ternary phase forms a ladder like morphology (see Fig. 2.14(a)). Fig. 2.15 shows a clear view of such a morphology observed when a commercial Al-5Ti-

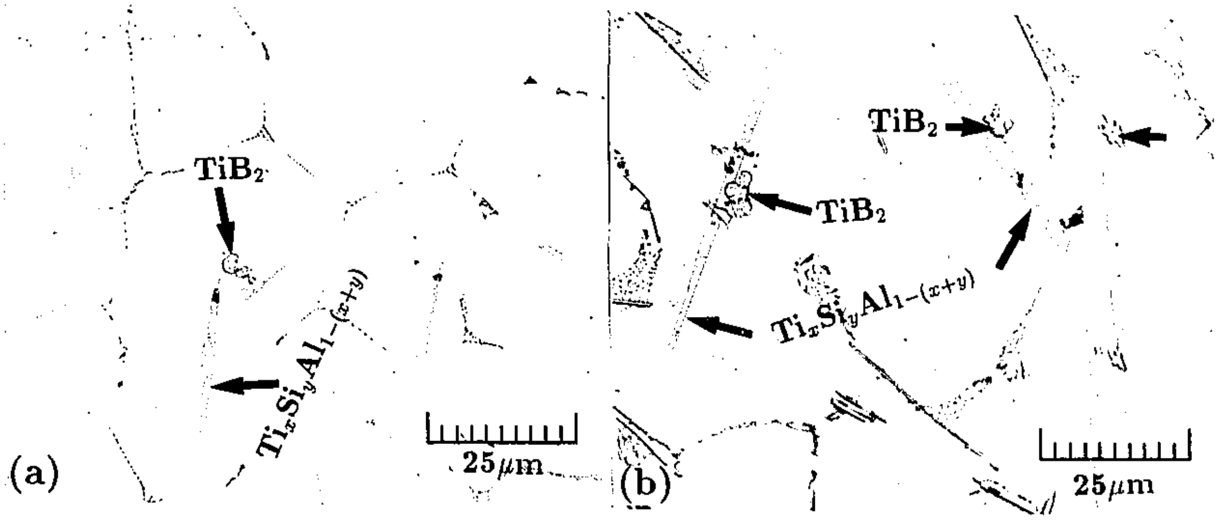

Fig. 2.14 Microstructure of Alloys Containing TiB$_2$, Solute Ti(0.5%) and Si; (a) 0.5%Si and (b) 3%Si.

1B master alloy was added to A356 alloy at a nominal Ti level of 0.3 wt. %. The silicon composition in these phases was detected to be in the range of 5-7 wt. %. This phase was found to be a very efficient nucleus as is evident from Fig. 2.16(b).

Figs. 2.16 (a) and (b) show the microstructures of pure Al and A356 alloy grain refined by Al-5Ti-1B at a nominal Ti level of 0.3 wt.%. It is seen that in the case of A356 alloy the ladder like Ti$_x$Si$_y$Al$_{1-(x+y)}$ crystallites are invariably found within the α-phase whereas in the case of pure aluminum the nuclei are blocky TiAl$_3$ crystals. Fig. 2.17 shows the microstructure of Al-9%Si base alloy after addition of synthetic TiB$_2$ crystals and 2 wt. % Ti. The cooling rate was approximately 0.1 ^{0} C/s. Clearly, the TiB$_2$ crystals are present within as well as on the boundary of the faceted Ti$_x$Si$_y$Al$_{1-(x+y)}$ crystals suggesting that the ternary aluminide nucleates on the borides. The Si and Ti compositions of these blocky crystals were found to be ~ 11 wt. % Si and ~ 25 % Ti. It is clear (Fig. 2.14, 2.16 and 2.17) that the cooling rate plays an important role in the evolution of the morphology and composition of the ternary aluminide.

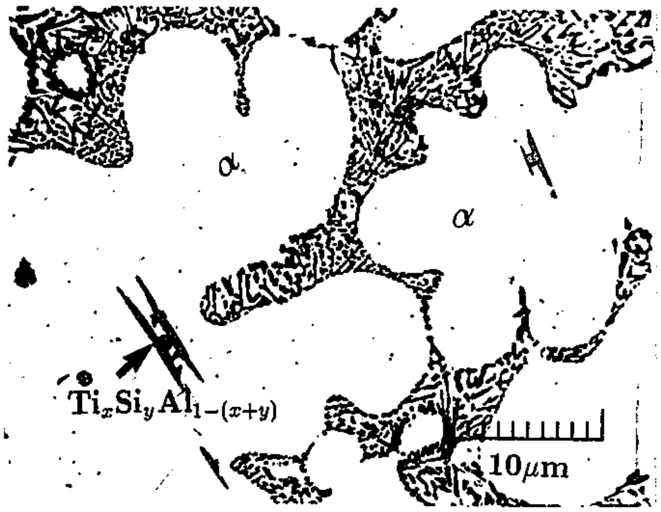

Fig. 2.15 Microstructure of A356 Alloy on Addition of Al-5Ti-1B Master Alloy (0.3 wt. % Ti).

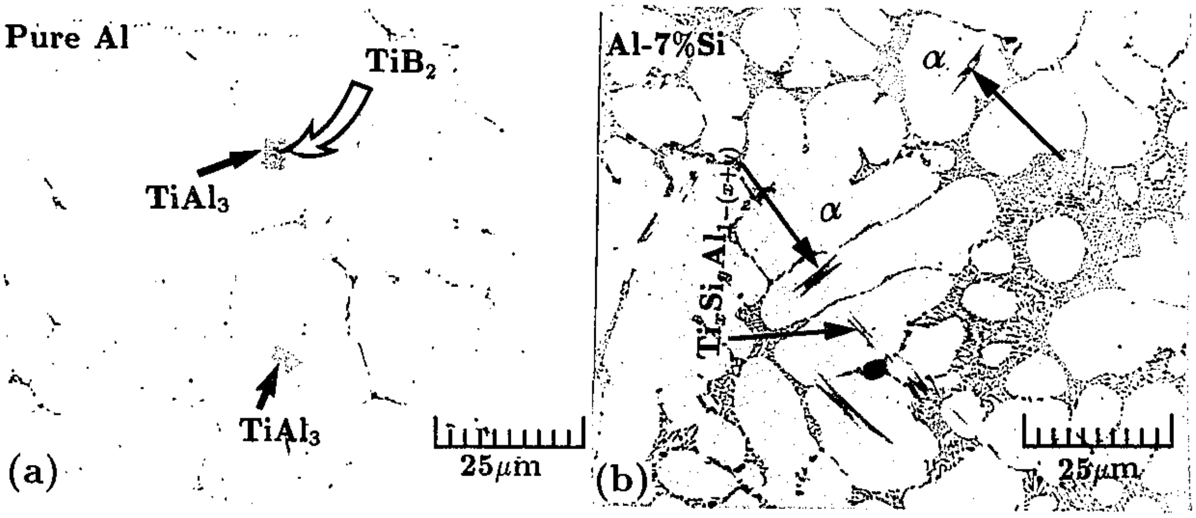

Fig. 2.16 Microstructure of Pure Al and A356 Alloy on Addition of Al-5Ti-1B Master Alloy (0.3 wt. % Ti, Cooling Rate~ $4^0C/s$); (a) Pure Al and (b) A356.

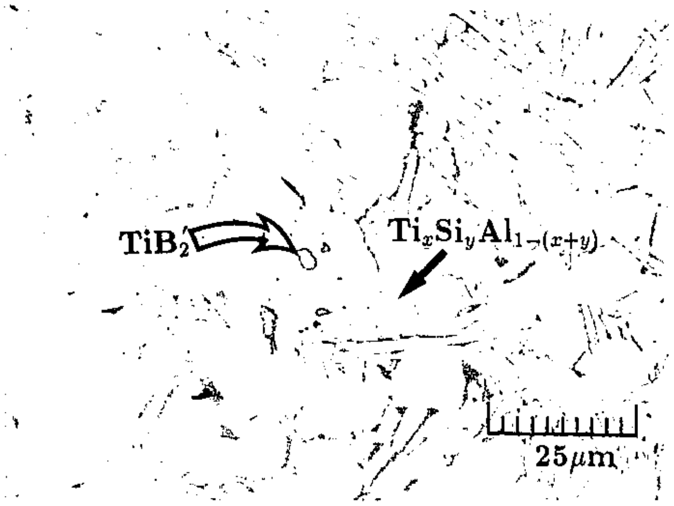

Fig. 2.17 Microstructure of Al-9%Si Alloy on Addition of TiB$_2$ Inoculant and 2 wt.% Ti (Cooling Rate~ 0.1^{0}C/s).

2.4.3 Behaviour of TiC

Fig. 2.18 shows the microstructure of pure Al cast within 5 minutes of addition of TiC particles. TiC crystals were distributed within the grains indicating that they nucleate α-Al. It can be seen that TiC particles react with the melt to form Al_4C_3 and complex carbides in pure Al. The compositions of these carbides varied from Al_4C_3 to Ti_3AlC. In the case of an Al-7%Si alloy (Fig. 2.19), TiC particles decomposed completely to form a complex compound of Al-Ti-Si and various aluminum carbides. The composition of the complex compound of Al-Ti-Si matched with that of the ternary aluminide discussed earlier except that approximately one percent carbon was detected in it. Some Al-Ti-Si crystals which were covered with fine crystals of Al_4C_3 and other complex carbides were pushed to the grain boundaries suggesting that their nucleation potential was lost (Fig. 2.19). Different morphologies of the ternary compound of Al-Ti-Si were also observed in this case. Fig. 2.20 shows the ladder-like or the needle-like structure which occurs at moderately high cooling rates after addition of TiC particles. A fully developed needle of $Ti_xSi_yAl_{1-(x+y)}$ can be seen in Fig. 2.20(b). From Fig. 2.20(a), it is clear that the carbide clusters do not promote nucleation of the α phase since they are rejected to the interdendritic space by the growing primary solid. The blocky structures

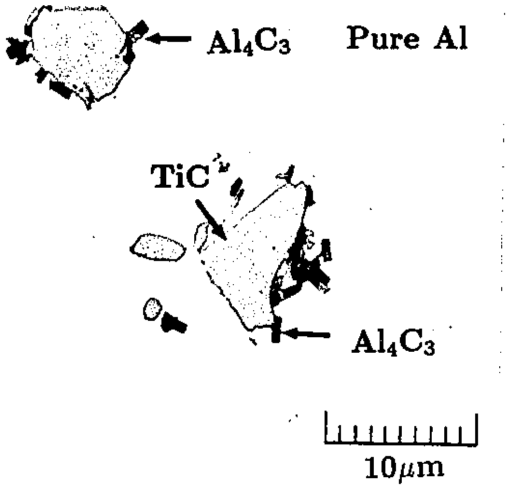

Fig. 2.18 Formation of Al_4C_3 and Complex Carbides at TiC Interface in Pure Aluminum Matrix.

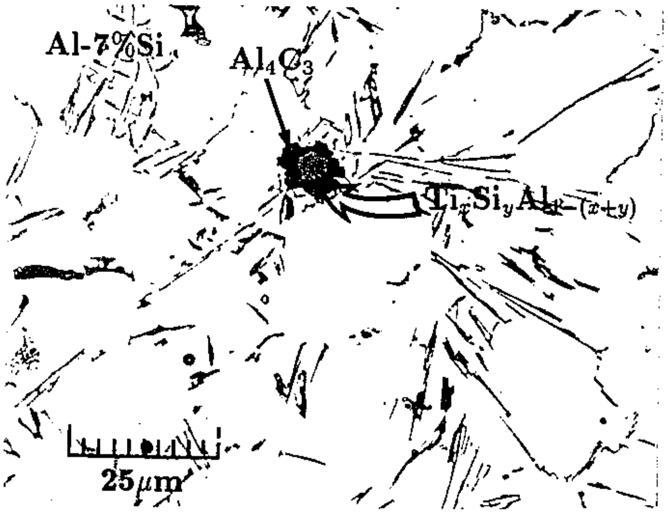

Fig. 2.19 Decomposition of TiC into Al-Ti-Si Compound, Al_4C_3 and Complex Carbides in Al-7%Si Alloy Matrix.

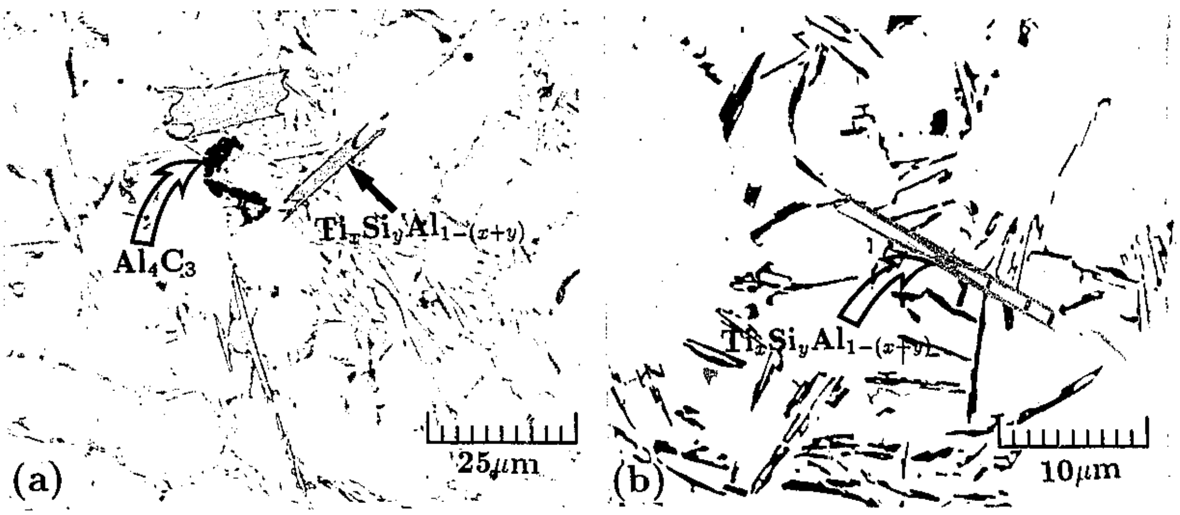

Fig. 2.20 Decomposition of TiC into Needle Like Al-Ti-Si Compound, Al_4C_3 and Complex Carbides in Al-7%Si Alloy Matrix; (a) Aluminum Carbides in the Interdendritic Eutectic and (b) Fully Developed Needle.

which formed at moderately slow cooling after decomposition of TiC crystals are shown in Fig. 2.21.

2.5 Discussion

2.5.1 Grain Refinement by Al-Ti-B Master Alloys

Heterogeneous nucleation can be regarded as a geometrically modified case of homogeneous nucleation by which the activation barrier is decreased by the presence of a foreign substrate. A purely geometrical calculation[1] shows that when the solid/liquid interface of the substance is partly replaced by an area of low energy solid/solid interface between the crystal and a foreign solid, nucleation can be greatly facilitated. Normally, the potential of the foreign substrate in facilitating the nucleation process is estimated from the following relation

$$f(\theta) = \frac{(2 + cos\theta)(1 - cos\theta)}{4} \qquad (2.8)$$

where θ is the wetting angle between the growing crystal and the foreign substrate within the melt.

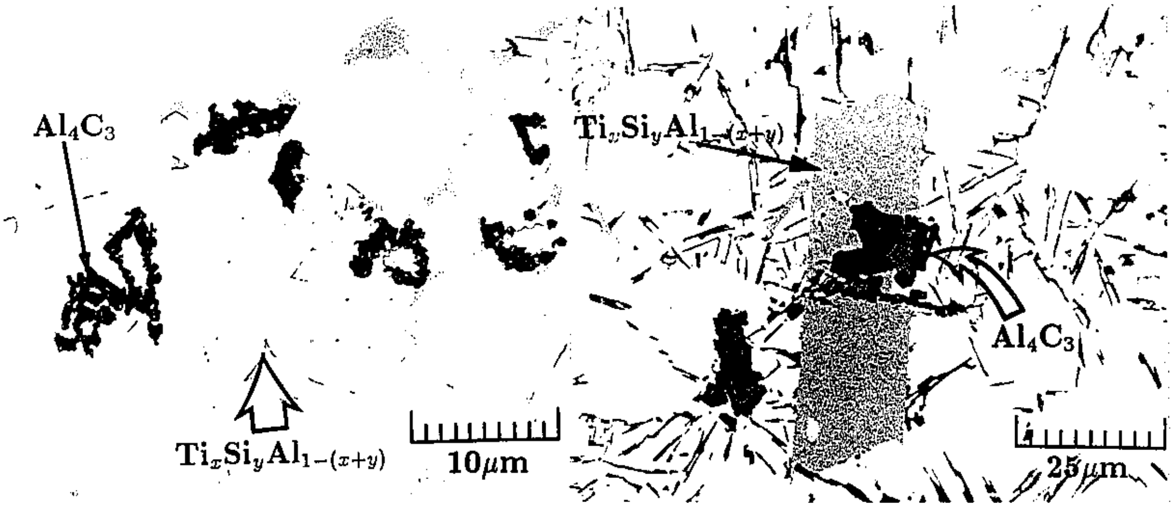

Fig. 2.21 Decomposition of TiC into Blocky Al-Ti-Si Compound, Al_4C_3 and Complex Carbides in Al-7%Si Alloy Matrix.

Under conditions of good solid/solid wetting *i.e.*, small θ, the foreign substrate can have a dramatic effect on the nucleation process. Unfortunately the solid/solid interfacial energy of a TiB_2 crystal on an α-Al crystal is not known. Good solid/solid wetting is expected when there are planes of low lattice disregistry between the foreign substrate and the growing crystal. Therefore, the need for near-perfect epitaxy of α-Al on at least one of the crystal faces of the substrate has been mooted as essential for effective nucleation. Cissé *et al.*,[62] have shown epitaxy to occur for some faces of $TiAl_3$, giving aluminum grains with different orientations according to the faces involved, while for TiC epitaxy occurs on all faces. The factor conducive to this epitaxy has generally been considered to be favourable matching of the lattice spacing of the nucleants to the lattice of α-Al. Unlike TiC and $TiAl_3$, no attempt has been made to study the epitaxy between Al and TiB_2; however, a qualitative analysis can be made from the phenomena of particle pushing and engulfment during solidification.

In a solidifying melt, the thermodynamic feasibility of a solid particle being pushed by the solidifying interface is determined by the net interfacial energy ($\Delta\sigma_0$), which can be represented as[92,93]

$$\Delta\sigma_0 = \sigma_{ps} - \sigma_{pl} \tag{2.9}$$

where σ_{pl} is the interfacial energy between the particle and the liquid, and σ_{ps} is the interfacial energy between the particle and the growing solid. When the net interfacial energy, $\Delta\sigma_0$, is negative, the presence of the particle within the solid is thermodynamically favourable and vice versa. Since the boride particles are pushed to the grain boundaries by the S/L interface even at high cooling rates ($\sim 10^0$C/s), it is evident that the net interfacial energy between α-Al, Al liquid and TiB_2 is positive *i.e.,* σ_{ps} is much higher than σ_{pl}.[92] In other words, the lattice mismatch between α-Al and TiB_2 is large suggesting that nucleation of α-Al grains on TiB_2 is not favourable. This conclusion is contrary to many published opinions.[18,21]

As mentioned earlier, there has been considerable debate regarding the exact nature of the boride phase. Jones and Pearson[57] suggested that at 1020 K an aluminum melt which is grain refined by addition of Al-5%Ti-1%B master alloy at a level equivalent to 0.005 pct Ti, should dissolve about 9 pct of the pre-existing TiB_2 added in the master alloy. However, in the present work, TiB_2 crystals did not show any significant solubility in aluminum melts even in the absence of any dissolved Ti (Fig. 2.6). Even under conditions of prolonged holding as shown in Fig. 2.9, it is evident that the TiB_2 particles once formed, are very stable within the melt.

2.5.1.1 Pure Aluminum

The observed pushing of TiB_2 particles does not necessarily rule out their contribution to the grain refinement process. The behaviour of TiB_2 particles changes dramatically in the presence of dissolved Ti as shown in Figs. 2.10 - 2.13. It is also established, both in laboratory and industrial experience, that Ti in excess of the stoichiometry of TiB_2 (Ti/B = 2.22) is a must for efficient grain refinement, but the role of dissolved Ti in the mechanism of grain refinement is not yet clearly set out.

Maxwell and Hellawell[53] presented an elegant model to demonstrate heterogeneous nucleation and the growth restricting effect of solute Ti. The rate of growth is inversely proportional to the quantity, $mC_0(k-1)$, where m is the slope of the liquidus, k is the partition coefficient and C_0 is the bulk alloy composition. In other words, the growth factor is determined by the characteristics of the phase diagram. For Ti, Zr and Cr, this quantity is estimated to be 35, 5 and 0.5 respectively, demonstrating that Ti is a growth restricting element. Though this model explains many experimentally observed phenomena, the basic question of identity of the nucleating substrate remains unresolved.

Maxwell and Hellawell[55] had no proof of nucleation of $TiAl_3$ on TiB_2, but they proposed a monovariant reaction of the form

$$L + TiB_2 \rightleftharpoons TiAl_3 \tag{2.10}$$

Bäckerud[94] did observe a thin coating of $TiAl_3$ on TiB_2, and based on this observation a mechanism for the formation of $TiAl_3$ was proposed to be

$$\begin{aligned} TiB_2 + Al &= (Ti, Al)B_2 + Ti \\ Ti + 3Al &= TiAl_3 \\ TiAl_3 + L &= \alpha\text{-}Al \end{aligned} \tag{2.11}$$

From the present experimental findings, no such mechanism is evident with pure TiB_2 particles which are stable in the melt and play no direct role in the nucleation process.

From the formation of $TiAl_3$ crystals at a composition much below the peritectic level on the TiB_2 particles (Fig. 2.10(b)), it is clear that titanium has a specific affinity to segregate onto the TiB_2 surface. It is well known that a layer of a few atoms in thickness can completely alter the behaviour of the substrate. A similar segregation of Ti to the interface of ZrB_2 particles was observed by Naess and Berg[95] in a melt inoculated with 0.03% excess Ti and Al-Zr-B master alloy. At the time, it was suggested that borides of Ti and Zr should behave similarly since they belong to the same subgroup in the periodic table. Studies involving techniques such as TEM on thin foils[74], replica extraction[91] and EPMA with neutron activated boron radiography[70], identified traces of borides and aluminides in the grain centre.

Segregation of certain solutes from within the grains to concentrate at matrix/precipitate boundaries as well as at the grain boundaries is known to occur in steel, and the thickness of the segregated solute atoms can sometimes amount to more than one atomic layer.[96] Solute segregation is also known to occur at liquid/solid interfaces.[97] Unfortunately, for aluminum, there are no data on the relative degrees of segregation of various solutes to interfaces. Jones[77] has recently presented a theoretical explanation of Ti segregation to the inoculant surface based on the activity gradient of Ti in the melt and TiB_2 inoculant.

In a melt saturated with TiB_2, the concentration of Ti is determined by the bulk solubility product $[Ti][B]^2$. Since TiB_2 is the most stable boride phase,[72] the mean chemical potentials of Ti and B within its crystal lattice are virtually invariant. Depending on the Ti/B ratio in the master alloy, the concentration and the activity of Ti in the melt can be either below or above the value in the substrate, so that at the melt/substrate interface the activity values of both Ti and B will change considerably. The partial molar free energy of solute Ti at this balance point is approximately −152.350 kJ/mole.,[78] about half that of the free energy of formation of the inoculant TiB_2 (−319.65 kJ/mole.).[40] Since excess Ti is a pre-requisite for efficient grain refinement, it is reasonable to suppose that in an inoculated melt $a_{Ti(melt)}$ exceeds $a_{Ti(TiB_2)}$. Whenever an element is exposed to an activity gradient, there will be a tendency for that element to undergo net transport by diffusion. Thus, relative to the melt, the melt solute interface should have a markedly raised titanium content, which on thermodynamic grounds can reach up to 2%.[78]

Based on this segregation behaviour, Jones[76–78] postulated the 'hypernucleation' theory which suggests that material of 2 %Ti would remain solid at temperatures below about 690°C, and would provide the substrate with a thin solid coating of α-Al capable of existing as a pre-nucleus well above melt freezing temperatures. These conclusions were derived from a hypothetical phase diagram in which the "liquid + α" region was projected in the direction of increasing temperatures providing an imaginary metastable region of α-Al (Fig. 2.22). Normally, metastable regions in a phase diagram are observed in decreasing temperature directions due to kinetic factors. It is, therefore, difficult to see how a phase diagram such as that shown in Fig. 2.22 could arise.

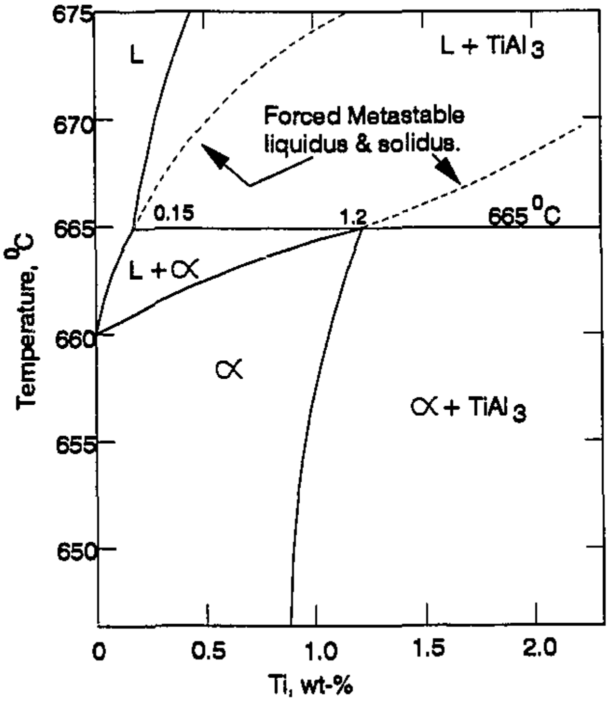

Fig. 2.22 Hypothetical Metastable Phase Diagram According to Hypernucleation Theory.[77]

Presumably Jones' idea of a forced metastable solidus and liquidus at the substrate up to 2% Ti arose from the fact that $TiAl_3$ crystals dissolve rapidly in aluminum melts below the peritectic composition, as predicted by the phase diagram. Therefore, although segregation of Ti up to 2% at the melt/substrate interface is argued to be thermodynamically feasible, the formation of $TiAl_3$ crystals seems to be an apparent contradiction to the phase diagram. The dissolution of $TiAl_3$ on the addition of master alloys leads to an equilibrium of dissolved Ti in the bulk melt. This results in the establishment of the activity gradient which leads to solute segregation, and the well known contact time in grain refining practice is a result of this process.

The observed dissolution of $TiAl_3$ crystals on the addition of master alloy does not necessarily rule out the formation of $TiAl_3$ on TiB_2 crystals. Since the bulk melt and interfacial regions of the inoculated system have different concentrations of Ti, they can be expected to have different intrinsic properties (see Fig. 2.23). Therefore, $TiAl_3$ at the interface would be thermodynamically stable for the same reasons that segregation up to 2% Ti is possible against the predictions of the phase diagram *i.e.*,

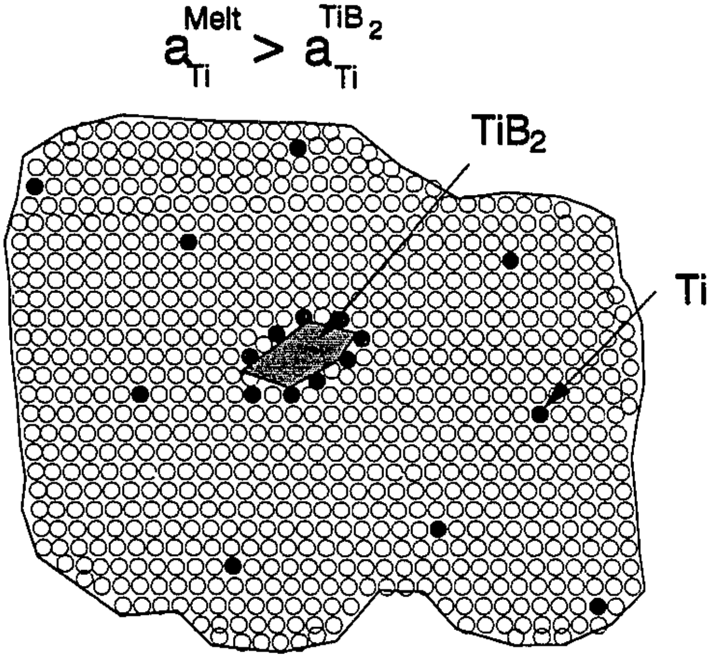

Fig. 2.23 Schematic of Inoculated System with Solute Ti .

the intrinsic difference in the properties of the bulk melt and the substrate interface. Equilibrium phase diagrams are based on a highly idealized situation of homogeneous solutions having no localized effect of contaminants. Since the local activity gradient can create a segregation level up to 2 % Ti under equilibrium conditions, $TiAl_3$ crystals, while unstable in the bulk melt, can be locally stable, and on cooling can provide a peritectic cell. It is worth noting that the molar free energy of formation of $TiAl_3$ is of the same order of magnitude (~ -143 kJ/mole)[40] as that predicted for solute Ti by Jones.[77] Formation of $TiAl_3$ on the interface is quite clear from Fig. 2.10(b). Even at higher concentrations of Ti where $TiAl_3$ is thermodynamically stable in the bulk melt, precipitation occurs predominantly on the TiB_2 particles (Figs. 2.11 - 2.13), a clear indication that growth of $TiAl_3$ is favourable on certain planes of the TiB_2 crystals. At this stage there is no proof for the existence of epitaxy between $TiAl_3$ and TiB_2, but from the growth pattern of $TiAl_3$ crystals, some crystallographic matching can be expected.

In commercial Al-Ti-B master alloys, TiB_2 crystals appear to be associated with $TiAl_3$ crystals. In general, it has been thought that TiB_2 crystals are present at the

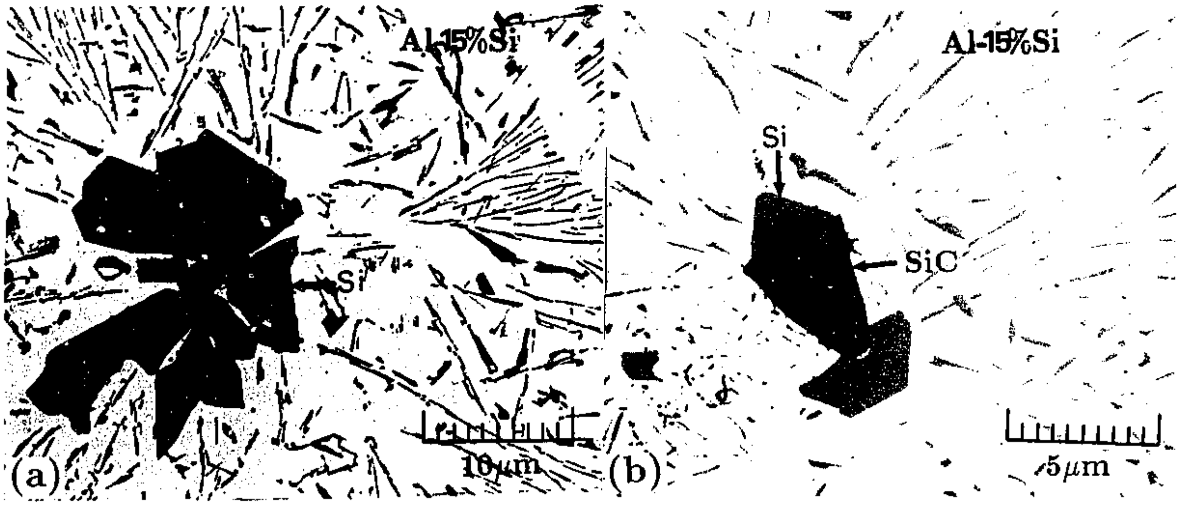

Fig. 2.24 Faceted Growth of Si Crystal; (a) On Al_2O_3 and (b) On SiC.

α-Al/$TiAl_3$ interface, and several mechanisms have been proposed for the formation of such crystals.[18,72,74] As mentioned earlier, the peritectic 'hulk' theory is based mainly on the formation of a TiB_2 passive layer on $TiAl_3$. It has been suggested, on the basis of the Al-Ti-B phase diagram, that the $TiAl_3$ and (Ti, Al)B_2 particles are dissolved on addition of master alloy yielding B and Ti in solution. Further dissolution of pure $TiAl_3$, subsequently reprecipitates a TiB_2 layer with a thickness of several nanometers on the $TiAl_3$ crystals, as governed by the solubility product of B in solution. Recently Lee and Terry[82] and Mayes *et al.*,[75] have reported the presence of TiB_2 within $TiAl_3$ crystals and a mechanism involving coprecipitation of $TiAl_3$ and TiB_2 was suggested;[75] however, from Fig. 2.13, it is clearly seen that $TiAl_3$ nulceates on the TiB_2 crystals. Since $TiAl_3$ crystals are faceted, their growth pattern will be strongly crystallographic in nature, and they will not completely cover the TiB_2 resulting in encapsulated pools of liquid aluminum. The observation of such regions has been thought to be the result of hindered diffusion of Ti out of $TiAl_3$ due to the presence of the boride, from which the concept of peritectic 'hulk' arose. From the present study, it is clear that these regions are merely the result of the faceted growth of $TiAl_3$. Similar growth patterns have also been observed (Figs. 2.24(a) and (b)) in a separate study by the author[16] on the heterogeneous growth of faceted silicon crystals on Al_2O_3 and SiC. Further, it is also

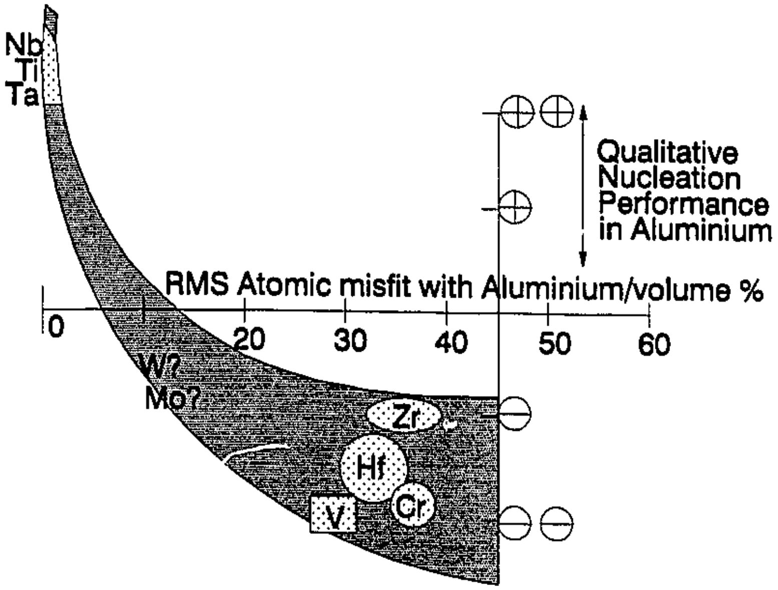

Fig. 2.25 Qualitative Picture of Grain Refining Ability of Transition Metals on the Basis of Atomic Misfit with Solvent Al.[77]

seen that the TiB_2 particles (predominant boride phase in master alloys) do not dissolve even in the absence of dissoved Ti and B. Therefore, the so called peritectic 'hulk' theory apparently seems to be an invalid proposition.

Nucleation of $TiAl_3$ on the TiB_2 surface should be affected by the exposed crystallographic planes of TiB_2 and the associated interfacial attachment kinetics. Atomic attachment becomes favourable only when the segregated atoms are of similar size. Such similarity leads to a packing with minimum lattice distortion and an interface to provide higher nearest neighbour binding. The solvent/solute atomic size ratio will therefore dictate whether or not precipitation of a crystal layer is favourable. If atomic misfit is significant, even though segregation is thermodynamically favourable, stabilization of a crystal layer may not be feasible. Fig. 2.25 presents the qualitative index of the performance of various solute elements as nucleants for aluminum when added as borides, in relation to their atomic size match/mismatch with aluminum. When the solvent/solute size ratio is close to unity the probability of providing a well ordered crystal is greatly enhanced, and efficient grain refinement is achieved, as is experimentally verified with Nb,

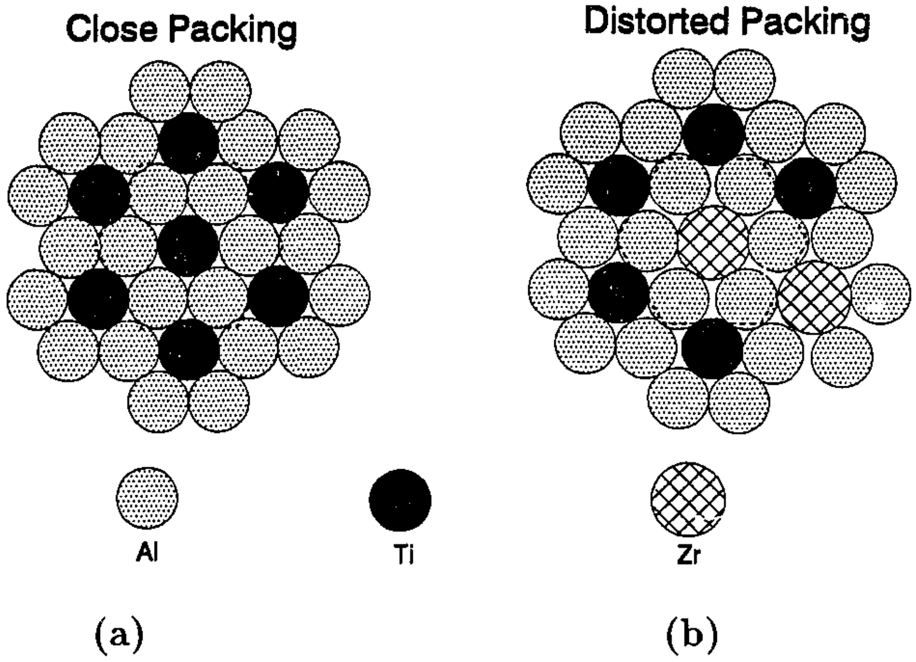

Fig. 2.26 Schematic Representation of Ordering of Aluminide; (a) Close Packing in the Presence of Ti and (b) Distortion in the Presence of Zr.

Ti and Ta (Fig. 2.26(a)).[77] On the other hand, significant mismatch leads to poisoning by hindering the precipitation of a stable crystal layer (*e.g.,* Zr and Cr)(Fig. 2.26(b)). Similarly, boride particles with spherical morphology presumably would enhance the chance of exposing a suitable crystallographic plane for precipitation, whereas an elongated particle morphology may limit the probability and thus may prove to be a redundant site. In such a situation, even under a very strong activity gradient, attachment and formation of a crystal will not be possible. It is also possible that in the presence of many suitable sites in a close vicinity, the precipitation of $TiAl_3$ may not occur on all particles. This is because, once precipitation starts at one centre, atomic attachment on another centre just adjacent to it may not be favourable compared to the further growth of the already existing nucleus. In other words, in the presence of many suitable sites in a close vicinity, precipitation of $TiAl_3$ will randomly occur on one. As a result, while one site being an effective nucleus, the others will be redundant and will be pushed into the grain boundary. In reality, this phenomenon is widely observed in grain refinement practice. However, when the bulk Ti concentration is high, presumably close to the peritectic, precipitation of $TiAl_3$ should be favourable on many nearby sites, and as a result more than one particle can be found within the grain. This is clearly evident from Fig. 2.11 (Ti $\sim$ 0.5).

To explain the observed distribution of TiB_2 particles in the grain boundaries, Maxwell and Hellawell[53] applied their model on heterogeneous nucleation and growth showing a correlation between number of particles and number of grains. They considered TiB_2 particles to be the nucleant. Nuclei beyond an optimum number are not necessary for nucleation and will be pushed into the grain boundary by already growing solid. However, Fig. 2.11 is contrary to this proposition, showing the presence of many particles within the same grain. The argument of Maxwell and Hellawell[53] regarding the competition between growth and the nucleation event is quite justified, but the fundamental assumption of TiB_2 being well wetted by liquid aluminum and nucleating α-Al is incorrect. If the intrinsic property of all particles is the same *i.e.,* the wettability, while solid nucleates on one particle, the engulfment of others within the solid will be thermodynamically feasible.[92] What makes the distinction between two particles, is the first nucleation phenomena *i.e.,* the precipitation of $TiAl_3$. In other words, the particle on which precipitation occurs, will be the nucleus, and the particle on which no precipitation occurs will be rejected by the growing solid. In Fig. 2.11, the alloy contains high Ti ($\sim$0.5), and it is reasonable to assume that precipitation of $TiAl_3$ will be possible on many particles. As a result more than one particle is present within the same grain. Recalling the concept of hypernucleation,[77] if a solid layer is formed on all TiB_2 particles according to the hypothetical phase diagram, then all of them should be engulfed by the growing solid. In reality the situation is very different.

For the precipitation of $TiAl_3$ on a TiB_2 crystal, the particles must be well wetted. The wetting behaviour is affected by preferential migration of atoms from, or to, the interface when the solid substrate is brought into contact with the liquid. When specific migration (or chemical reaction) is either absent or only slight, the surface of the particle is not wetted by molten metal *i.e.,* the contact angle is greater than 90^0. Measurements on a TiB_2 surface indicate a contact angle greater than 100^0.[45] Since TiB_2 is very stable within Al melts, this behaviour is expected. In the case where there is preferential migration of atoms from the molten metal into the solid substrate, wetting is observed. In other words, the wetting of a substrate by molten metal can be influenced by introducing elements which intensify the migration of atoms in the required direction. Since dissolved Ti in the melt is segregated to the TiB_2/melt interface, the wettability is expected to improve.

2.5.1.2 Hypoeutectic Al-Si Alloys

It was mentioned earlier that the industrial practice of grain refinement of hypoeutectic Al-Si alloys by Al-Ti-B master alloys has been directly adopted from the grain refinement practice in the wrought aluminum industry. As a result, the proposed mechanisms of grain refinement[22,86,89] in these alloys have been simply an extension of the theories proposed for pure aluminum with little attention paid to the possible role of Si on the refining mechanism of these ternary master alloys. In fact, only a few attempts[86,89] have been made towards an understanding of the mechanism of grain refinement in these alloys. Despite the development of a special class of master alloys more suitable for Al-Si alloys, very little progress has been made as to why they perform better.

From a glance at Figs. 2.14 - 2.17, it appears that grain refinement in hypoeutectic Al-Si alloys follows the same sequence as in pure aluminum. However, there is a fundamental difference in the nature of the nucleating crystal *i.e.,* the aluminide in the case of Al-Si alloys is a ternary compound whereas it is binary in the case of pure aluminum. The presence of solute Si in the aluminide necessitates a discussion of the phase relations in the Al-Ti-Si ternary system and their implication for grain refinement practice.

Information on the ternary Al-Ti-Si system is limited. The Al-rich corner of the Al-Ti-Si ternary phase diagram is presented in Fig. 2.27. Ramon and Schubert[98] obtained a $Ti(Al,Si)_3$ phase after a lengthy high temperature anneal (7 days at 700^0C) of the solidified alloy. However, in the present experiments, carried out under non-equilibrium conditions similar to industrial practice, no evidence was found for the $TiAl_3$-

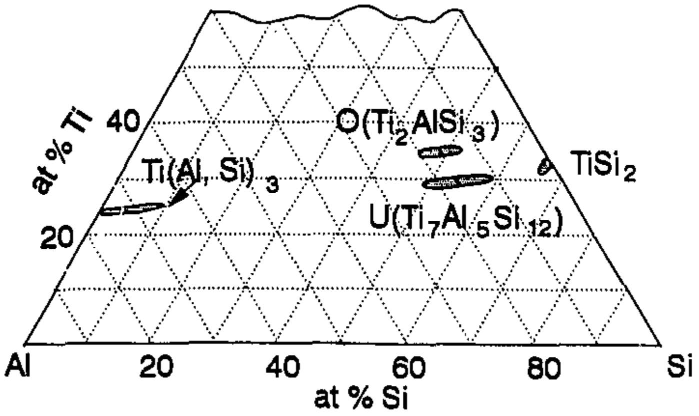

Fig. 2.27 Partial Al-Ti-Si Phase Diagram.[98]

like structure containing Si *i.e.,* Ti(Al,Si)$_3$. Similar observations were also made by Hoffmeyer *et al.,*[99] and Youdelis *et al.,*[103,104] in the Al-Ti-Si ternary system.

As discussed earlier from the fundamental aspects of nucleation theory and grain refinement, solid nucleation is promoted when the interfacial energy between the inoculant and the solid phase is small or when there is a phase reaction between the liquid and the inoculant, resulting in the formation of the solid phase *e.g.,* a peritectic reaction. However, the effectiveness of grain refining additions are not only controlled by the potency of the added particles, but are also influenced by local equilibrium and the alloy constitution. The importance of localized solute redistribution has been demonstrated in the previous section (2.5.1.1). Presumably, addition of silicon results in a constitutional effect on the Al-Ti system and/or increases the nucleation rate of the peritectic compound when Si is dissolved in TiAl$_3$. This is a kinetic effect due to increased nucleation entropy in the presence of impurities.[102]

Of particular importance is the peritectic composition ($C_p{}^l$) and temperature. If the shift in C_p^l to lower Ti concentration is significant with a given impurity addition, the possibility for only partial dissolution of the inoculant addition exists, after which the particle may become stable in the liquid. Although experimentally unproven and

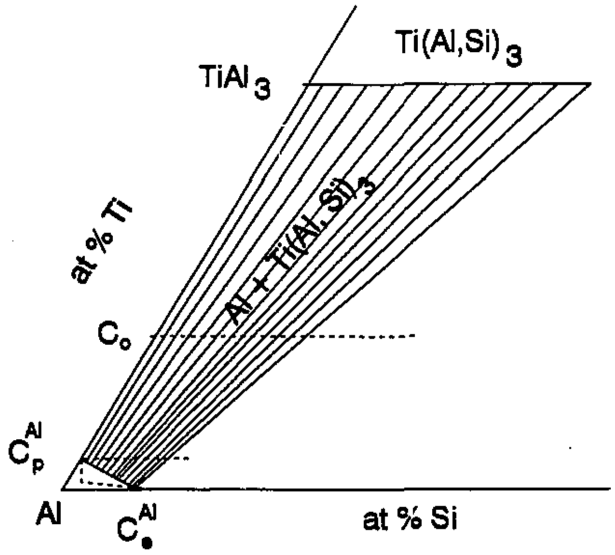

Fig. 2.28 Tie Line construction Between Al and Ti(Al, Si)$_3$ in Al-Ti-Si Phase Diagram.[99]

abandoned, the mechanism of enhanced grain refinement in the presence of boron was conceived from the supposed shift of C_p^l to lower Ti concentration. The present study shows that there exists a fairly large compositional range over which the $Ti_xSi_yAl_{1-(x+y)}$ phase can form, and similar observations have been made by others.[99,104] Since Si substitutes directly into the TiAl$_3$ lattice, the amount of the aluminide phase, for a given concentration of Ti, must increase with Si addition, in accordance with the lever rule (see Fig. 2.28).[99] This suggests that the solubility of Ti in Al decreases resulting in a shift in the peritectic composition to lower Ti levels. This is also indicated in Fig. 2.16, where the number of aluminide crystals in A356 alloy is higher than that in pure aluminum with the same Ti level.

In addition to this shift in peritectic composition, there is also a shift in the peritectic solidification temperature range with Si addition. In the binary Al-TiAl$_3$ system the peritectic occurs at 665^{0}C. In a differential thermal analysis (DTA) study on the melting behaviour of Al-Ti-Si alloys,[99] it was confirmed that with approximately 0.20%Si the peritectic reaction occurs in the range of 665-672^0 C. With further increase

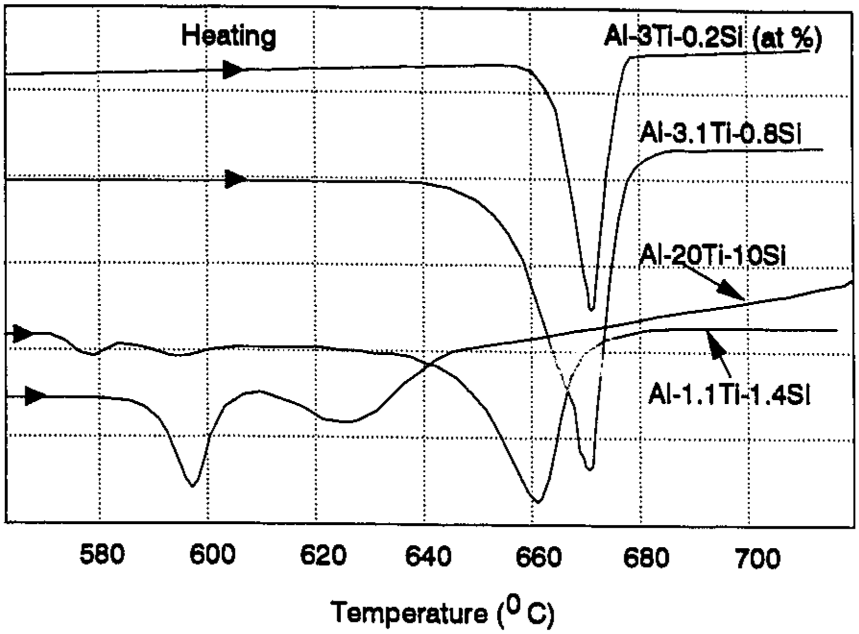

Fig. 2.29 DTA Thermograms Showing the Melting Behaviour of Al-Ti-Si Alloys with Increasing Si Content.[99]

in Si, it was observed that there is a drastic drop in temperature for maximum extent of the peritectic solidification range (see Fig. 2.29). The temperature range also broadened with increased Si.

These considerations reveal that the number of aluminide particles increases with nominal Si additions for a given bulk Ti concentration. In other words, in the presence of silicon, the effective Ti level is increased. More importantly, since Ti solubility in Al is reduced with Si addition, inoculant particles that contain Si may not dissolve when added to an aluminum melt in concentration levels normally used for grain refinement operations. Thermodynamic calculations in the Al-Ti-Si system also predict an enhanced resistance to aluminide dissolution in Al melts containing Si.[101] In fact, experiments performed by Reif and Schneider[105] have shown that the addition of Si to Al melts prior to the addition of an Al-Ti-B master alloy results in enhanced grain refinement. Youdelis and Grekul[104] have also observed improved grain refinement when low level of Si additions are made to Al-Ti and Al-Ti-B master alloys.

From the phase diagram and the available experimental evidence, it is clear that Si is a key addition for improving the effectiveness of Al grain refinement. The role of boron added through the master alloy, however, remains unexplained at this point. The possible role of B on the ternary Al-Ti-Si phase diagram is unknown. Considering the discussion on the role of B in the binary Al-Ti phase diagram and the stability of TiB_2 particles in Al-Si alloy (Fig. 2.9) and in Al-Ti-Si alloy (Figs. 2.14 and 2.17), it appears that B has no other role than to form borides. In a master alloy with Ti/B ratio higher than 2.22, these borides are predominantly TiB_2.[83] When TiB_2 particles are present in a melt having titanium in excess of stoichiometry, the titanium would segregate to the TiB_2 substrate for the same reasons as discussed in the case of pure Al. Unlike the case of pure aluminum, however, Si will also concentrate close to the inoculant surface, thereby forming the ternary $Ti_xSi_yAl_{1-(x+y)}$ aluminide. Thus, in the presence of Si, the ternary aluminide can be stable at the TiB_2/melt interface even at lower Ti concentrations than in the case of pure aluminum due to the shift of the peritectic composition towards lower Ti.

As can be seen from Fig. 2.30, the ordering and close packing is not distorted in the presence of Si due to its smaller size. The preferential nucleation of the ternary aluminide on TiB_2 crystal is quite evident from the present study (Figs. 2.14 and 2.17). Due to the faceted nature of these crystals, the growth pattern will be similar to that of the binary aluminide discussed in Section 2.5.1.1. Fig. 2.31 presents the growth pattern of ternary crystals. The boride particles are distributed along the boundary of the ternary aluminide crystals. Observation of these duplex crystals has tempted researchers to propose several hypotheses for the mechanism of grain refinement *e.g.,* the peritectic hulk theory. However, as in the case of the binary aluminides discussed earlier, the ternary aluminide crystals nucleate on the TiB_2 particles as is clear from the presence of boride within them (Figs. 2.17 and 2.32). The nature of the inoculant substrate plays a very significant role on the precipitation process. Fig. 2.33 presents the microstructure of an Al-Ti-Si ternary alloy in the presence of Al_2O_3 particles. Unlike the case of preferred nucleation on TiB_2, the ternary aluminides nucleated independent of the alumina particles, confirming that even if excess Ti is present, in the absence of a

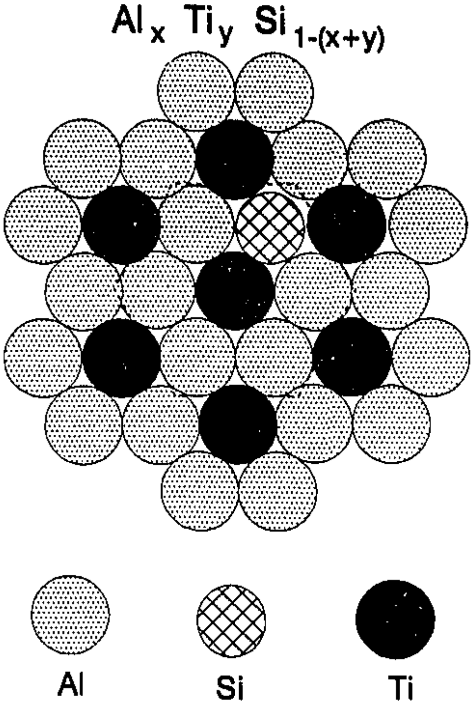

Fig. 2.30 Schematic Representation of Ordering of Ternary Aluminide of Al-Ti-Si.

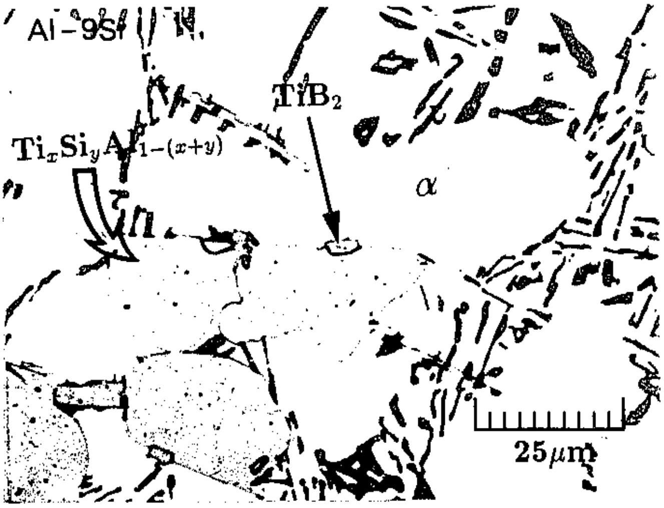

Fig. 2.31 Growth of Faceted $Ti_xS_yAl_{1-(x+y)}$ Crystals on TiB_2.

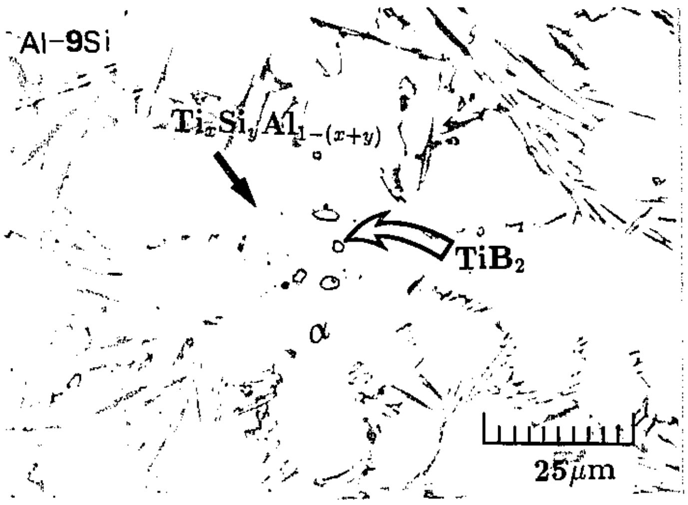

Fig. 2.32 Growth of Faceted $Ti_xS_yAl_{1-(x+y)}$ Crystals Showing Presence of TiB_2 Within.

suitable substrate, the precipitation of the aluminides will not be favourable. Therefore, the presence of boride is essential for efficient grain refinement.

Considering the crystallographic disregistry between Al//$TiAl_3$ and Al//Ti(Al, Si)$_3$, Hoffmeyer *et al.,*[99] reported that the increase in disregistry between various planes of Al//$TiAl_3$ due to Si addition was limited to ~ 1% at the maximum extent of Si solubility. Although it is difficult to judge the exact nature of atomic interaction at the interface between Al and the aluminide particles, their calculation suggests that Si addition to $TiAl_3$ does not detrimentally alter the crystallographic misfit.

From this discussion on the role of boron in the master alloy, it is clear that master alloys containing boron will produce better results than the binary Al-Ti master alloy in Al-Si alloys. This has been verified by many researchers.[85,86,89,90] Fig 2.34 presents the performance of three master alloys in A356 (~7% Si) alloy. Aluminum casting alloys containing high levels of Si are known to be more difficult to grain refine than pure aluminum using conventional Al-5Ti-1B master alloy. It can be seen from Fig. 2.34, that although Al-5Ti-B works better than Al-5Ti, significant grain refinement occurs only at high Ti content (~ 0.1%). This value is higher than the Ti content used for pure Al (~ 0.01-0.02 %). Considering the beneficial effect of Si as an impurity

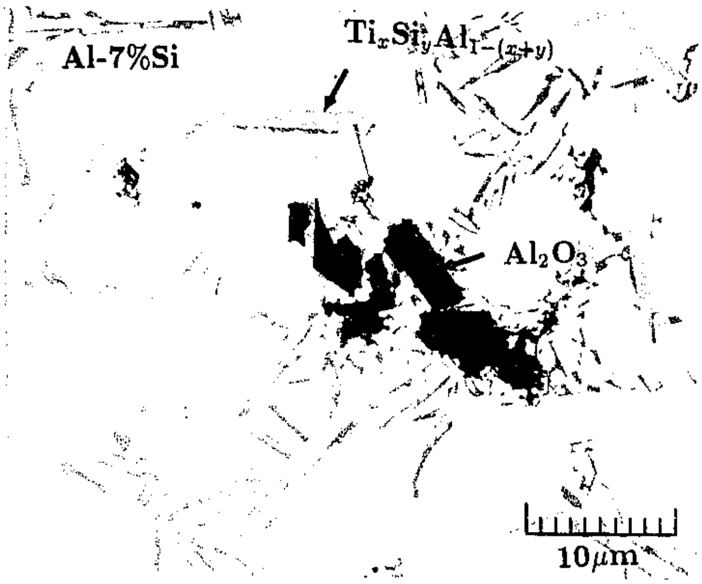

Fig. 2.33 Nucleation of $Ti_xS_yAl_{1-(x+y)}$ Crystals in the Presence of Al_2O_3.

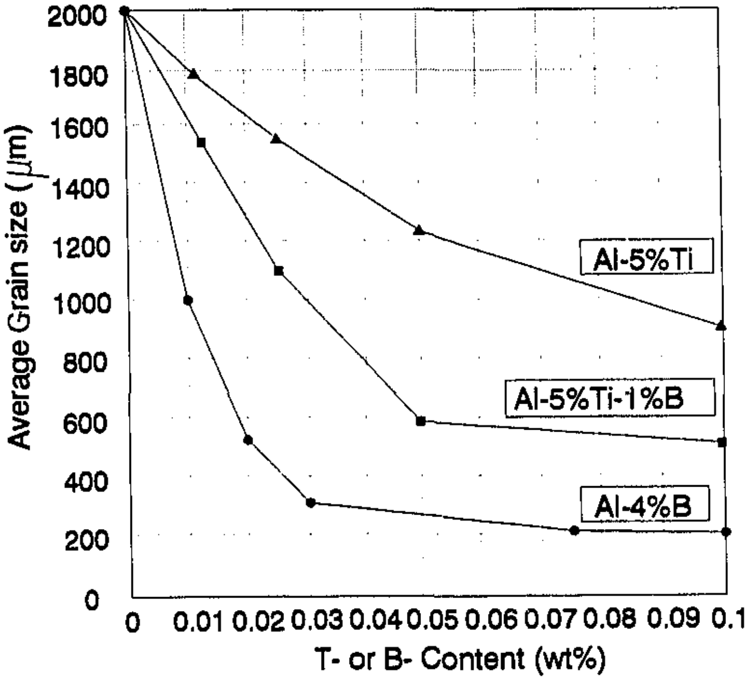

Fig. 2.34 Grain Refinement of A356 Alloy with Al-Ti, Al-5Ti-B and Al-B Master Alloys.[87]

in the performance of conventional master alloys in grain refinement of Al, its failure in Al-Si alloys is quite puzzling. Though this point has not been resolved, alternative master alloys specifically suitable for Al-Si casting alloys have been developed having excess boron over the TiB_2 stoichiometry (Ti/B =2.22/1) such as: Al-3Ti-3B and Al-2.5Ti-2.5B etc. Interestingly, this class of master alloys does not grain refine pure Al efficiently.

In an attempt to explain the reason for the failure of Al-5Ti-1B master alloy in Al-Si alloys, Jones[76] applied the concept of hypernucleation suggesting that Si together with Ti will also segregate near the surface of TiB_2 particles. As a result, the local solidification temperature will reduce below the bulk melt liquidus because of the eutectic nature of the Al-Si system, decreasing the tendency for adjacent melt layers to be ordered and solidify. The effect of the ternary Al-Ti-Si system was completely ignored in his analysis and the experimentally observed enhanced grain refinement due to the presence of silicon impurity is contrary to this proposition. Jones[76] went on to explain the effectiveness of the Al-3Ti-3B master alloy on similar grounds. It was suggested that when B is present in excess it will segregate to the TiB_2/melt interface, and the energy sequence would attract the solvent atom *i.e.,* Al next to B. This layer now will have a lower solute (Si) content relative to the bulk melt, thereby the liquidus will be raised and the system will become hypernucleative (see Fig. 2.22).

Some insight can be gained into the failure of Al-5Ti-1B in Al-Si alloys by looking back at the effect of Si on the peritectic solidification temperature. As mentioned earlier, a DTA study on the melting behaviour of Al-Ti-Si alloys,[99] (see Fig. 2.29) indicated that with Si being present, the peritectic temperature range first increased and with a further increase in Si caused a drastic drop in temperature for the peritectic solidification. It then appears that a critical Si level is necessary for optimum benefits due to the shift of the peritectic. As Si alloy addition levels are increased, a significant temperature drop is required for the onset of peritectic solidification in the ternary system. This temperature drop is quite drastic in that a 1.5 wt% Si addition to an alloy with a Ti concentration comparable to alloys used in grain refinement operation (6 wt %) produces an onset to peritectic solidification well below the melting point of pure Al.

At higher concentrations of silicon the onset of the peritectic solidification range is too low to produce effective refinement. The failure of Al-5Ti and Al-5Ti-1B master alloys to grain refine Al-7%Si alloys efficiently, seems to be a direct consequence of this change in the peritectic solidification temperature.

It should be noted that depending on the cooling rate, the morphology and composition of the ternary phases varies, showing a non-integer stoichiometry. It then appears that an increase in the cooling rate will yield a ternary aluminide having low silicon content, so that the peritectic will be above the equilibrium melting point of the alloy to be refined. In this case higher Si levels can be tolerated and the grain refiner will be effective. This has been experimentally verified in the case of A356 and 319 alloys where grain refinement by Al-5Ti-1B was significantly influenced by the solidification rate.[90] At low solidification rates, the performance was inferior to other grain refiners, but as the solidification rate increased it performed equivalent to the efficient grain refiners developed for Al-Si alloys *i.e.,* Al-2.5Ti-2.5B and Al-B master alloys.

A trend towards the use of Al-B master alloys for grain refinement of Al-Si foundry alloys is now being set, due to its powerful refining ability over a broad range of Si content. Fig. 2.34 clearly shows that Al-Si alloys can be efficiently grain refined by Al-4%B master alloys. A class of commercial grain refiners based on the binary Al-B system has already appeared on the market. It has been suggested that the grain refinement mechanism is heterogeneous nucleation of aluminum crystals on intermetallic AlB_2 particles in the melt, combined with the more common growth restriction process due to segregation of silicon during solidification.[86,87]

Recalling the discussion on the heterogeneous nucleation on foreign substrates (Section 2.5.1), it can be inferred that for aluminum to nucleate heterogeneously on AlB_2, there must exist near-perfect epitaxy of α-Al on at least one of the crystal faces of AlB_2. Information on the existence of epitaxy between α-Al and AlB_2 is not available in the literature; however, an indirect analysis can be made from the behaviour of AlB_2 in pure Al and the similarity of crystal structure between TiB_2 and AlB_2. It has been well demonstrated that AlB_2 does not grain refine pure Al.[23,49] Si having no special role

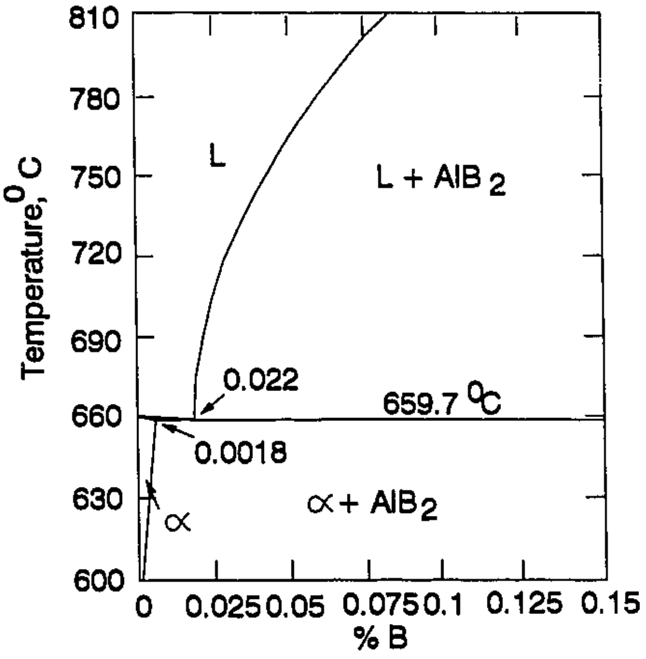

Fig. 2.35 The Al-rich Side of the Al-B Phase Diagram.[22]

on the substrate behaviour except its growth restricting ability, AlB_2 should become a nucleus in pure aluminum as well. In addition, AlB_2 and TiB_2 are isomorphous having negligibly small difference in lattice parameter (see Fig. 2.3), and they should behave in a similar fashion. From Figs. 2.7 and 2.9, it is evident that TiB_2 crystals do not nucleate aluminum in Al-Si alloys. It then appears that the idea of simple heterogeneous nucleation (*i.e.*, by epitaxial growth) of Al on AlB_2 in Al-Si alloys is highly doubtful.

The above discussion, however, does not rule out the possibility of AlB_2 being the nucleant. It was mentioned earlier, that nucleation can occur either directly on the substrate by epitaxial growth, or by some phase reaction involving α-Al *e.g.*, peritectic reaction. Unlike the Al-Ti system there is no evidence showing the existence of a peritectic reaction in the Al-B system. The accepted phase diagram (see Fig. 2.35) of the Al-B system has a eutectic at about 0.022 wt % B, at 659.7°C as shown below:[22]

$$L = \alpha Al + AlB_2 \tag{2.12}$$

The liquidus temperature of A356 alloy (~7%Si) being 614°C, a eutectic reaction occuring at about 659^{0}C should grain refine the alloy efficiently. In other words, in the presence of AlB_2 particles, α-Al will exist well before the onset of the liquidus, and as the temperature reaches the vicinity of the liquidus, the solid will grow readily from it without any undercooling. This proposition is in line with the observed cooling curve by Sigworth *et al.,*[86] showing no undercooling and a temperature rise of about 4^0 C in the first thermal arrest in an Al-7%Si alloy grain refined by 0.02%B. If heterogeneous nucleation occurs directly on AlB_2, then the thermal arrest should be observed at the liquidus temperature of the alloy. In fact the system will be efficient even for alloys with lower Si levels. It has been proven that boron grain refines well even at 5% Si.[87] On the other hand, when boron is added to pure Al, the liquidus (~660^{0}C), being above the eutectic, there will be no pre-existing α-Al at this point. The eutectic reaction itself will need an undercooling (ΔT) of several degrees to begin. As a result, the liquid will be forced to solidify in a similar manner to that occurs in an unrefined melt. Thus, AlB_2 will not grain refine pure aluminum whereas it is proved to be efficient for Al-Si alloys.

There is no ternary Al-Si-B phase diagram available in the literature. However, calculated phase diagrams are available[87] and some basic ideas on the phase relations in the Al-rich corner of Al-Si-B system can be derived from these. The binary eutectic reaction is expected to continue inside the ternary system (see Fig. 2.36). The effect of silicon is reported to shift the phase boundary towards lower boron content *i.e.*, the eutectic point is shifted from 220 ppm B to about 100 ppm B. The calculated line shows the expected qualitative behaviour, but the exact position has not yet been determined.

The improved performance of Al-3Ti-3B master alloys over Al-5Ti-1B in Al-Si alloys led researchers[86,89] to believe that the so called metastable boride theory based on the (Al,Ti)B_2 nucleus is a valid mechanism for grain refinement. Based on the observed grain refinement of Al-Si alloys by AlB_2, Sigworth *et al.*,[86] suggested that the mixed boride (Al, Ti)B_2 structure is close enough to AlB_2 phase to grain refine Al-Si casting alloys. However, the very existence of the metastable boride phase is questionable and the arguments against this hypothesis have already been discussed. It has also been confirmed in the present study that TiB_2 crystals are very stable in Al-Si melts (Fig. 2.9).

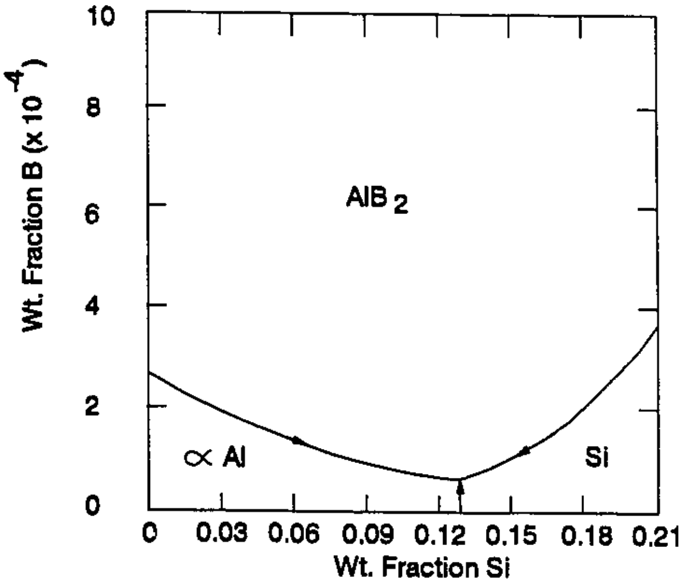

Fig. 2.36 The Al-rich Corner of the Calculated Al-Si-B Liquidus Surface.[87]

The improved performance of Al-3Ti-3B master alloys in Al-Si alloys is presumably due to the grain refining effect of excess B. When Al-3Ti-3B master alloy is added, the excess B over the TiB_2 stoichiometry will remain essentially as solute B. In the presence of TiB_2 particles, the excess B will segregate to the TiB_2/melt interface as in the case of excess Ti discussed earlier. As a result the effective B concentration at the interface will be raised above the eutectic composition causing precipitation of AlB_2. The preferential growth of AlB_2 on the TiB_2 particle should be feasible considering their isomorphous structure (see Fig. 2.3). On cooling the interfacial layer of AlB_2 is expected to undergo a eutectic reaction, nucleating α-Al well above the liquidus temperature of an Al-7%Si alloy. Interestingly, this process will not grain refine pure aluminum, since the eutectic reaction occurs below the liquidus of pure aluminum. It has been well demonstrated in laboratory as well as in industrial tests that Al-3Ti-3B master alloy does not grain refine pure aluminum.[70]

2.5.2 Grain Refinement by TiC

The inherent thermodynamic instability of TiC in aluminum melts is quite clear from Fig. 2.18 through Fig. 2.21. The present experimental observation does not support the idea of spontaneous formation of TiC, on the addition of Al-Ti master alloys to aluminum melts according to the original postulation of the 'carbide theory'. Even if pre-prepared TiC is introduced into the melt, interfacial reactions leading to the formation of aluminum carbides and complex carbides are likely to occur almost instantaneously.

The present observation has an important industrial implication concerning the recent trend to develop grain refiners and metal matrix composites by *in-situ* production of TiC, either by introducing graphite powders[30−32] or by blowing carbonaceous gas[33,34] into Al-Ti melts. As mentioned earlier (Section 2.2.2), considering the ternary Al-Ti-C phase diagram, aluminum carbides are most prone to form in Al-Ti melts containing carbon below a melt temperature of 1273 K. Even under the conditions when formation of Al_4C_3 is thermodynamically feasible, the wetting behaviour of liquid Al on carbon (graphite) particles may act as a kinetic barrier and cause the reaction to cease.

There are many contradicting views regarding the wettability of carbon in liquid aluminum. According to the chemical theory of wetting, the work of adhesion at interfacial boundaries is determined by the free energy loss, (ΔG), through the liquid metal/wetted body interaction. Therefore, it should be possible to determine the wettability of carbon with a liquid metal by considering the free energy of formation of the metal carbide. It has been suggested[106] that aluminum should wet carbon at all temperatures above its melting point, since the free energy change for aluminum carbide formation is negative ($\Delta G_{933K} = -191$ kg/mole) at the melting point of aluminum. However, it has been extensively observed that liquid aluminum does not wet carbon up to a temperature of about 1273 K.[106−110] Presumably, this is because of the presence of an aluminum oxide film in the melt which can exist even in a vacuum of 10^{-3} Pa[106] and which is believed to break down above 1273 K. It has also been found that above 1273 K the contact angle decreases with increasing temperature and reaches values below

90 deg (*i.e.*, wetting) at temperatures exceeding 1373 K.[107] Simultaneously, interfacial reactions result in the formation of Al_4C_3 at the carbon/melt interface. By adopting a capillary method to remove the oxide film, Naidich *et al.*,[108] observed contact angles below 90 deg at 1223 K, and Kostikov *et al.*,[109] reported a contact angle of 75 deg at 973 K.

By considering the wetting behaviour of liquid Al on C, Banerji *et al.*,[31] presumed that graphite would not react with aluminum below 1273 K, and hence in their experiments for the production of Al-Ti-C master alloys, reaction temperatures were chosen in the range of 1023 K to 1273 K, in order to prevent any direct reaction of carbon with aluminum, even though it is thermodynamically impossible. The reaction to produce TiC in the temperature range of 1023 K to 1273 K was proposed to be Eqn. [2.6] and

$$TiAl_3(s) + C(s) \rightleftharpoons TiC(s) + 3Al(l) \tag{2.13}$$

It has been reported that the presence of Ti has no effect on the surface tension of liquid aluminum, even though it increases the viscosity sharply.[111] When all other conditions remain the same, wettability is a function of the surface tension of the liquid phase, becoming less as surface tension increases. Therefore, graphite is not likely to be wetted by Al-Ti alloy melts below 1273 K, unless some chemical reactions take place. While these authors[31] presumed that reaction between Al and C can be suppressed by choosing a reaction temperature below 1273 K, it is unclear how such a temperature can promote preferential reaction between Ti and C to form TiC. If wetting is the kinetic barrier for the formation of Al_4C_3 in an Al-Ti alloy melt, then it should also be a barrier for TiC formation. To accomplish the supposed reaction between Ti and C, the Ti in solution must bypass the non wettable interface and contact the C. Since Al-Ti melts do not wet graphite particles either, it is not clear how this can be accomplished. If a chemical reaction occurs to improve the wettability of the graphite particles in this melt, the probability of C reacting with Al is equivalent or higher than with Ti since the former is the major constituent of the melt and has the proper thermodynamic potential at the chosen temperature.

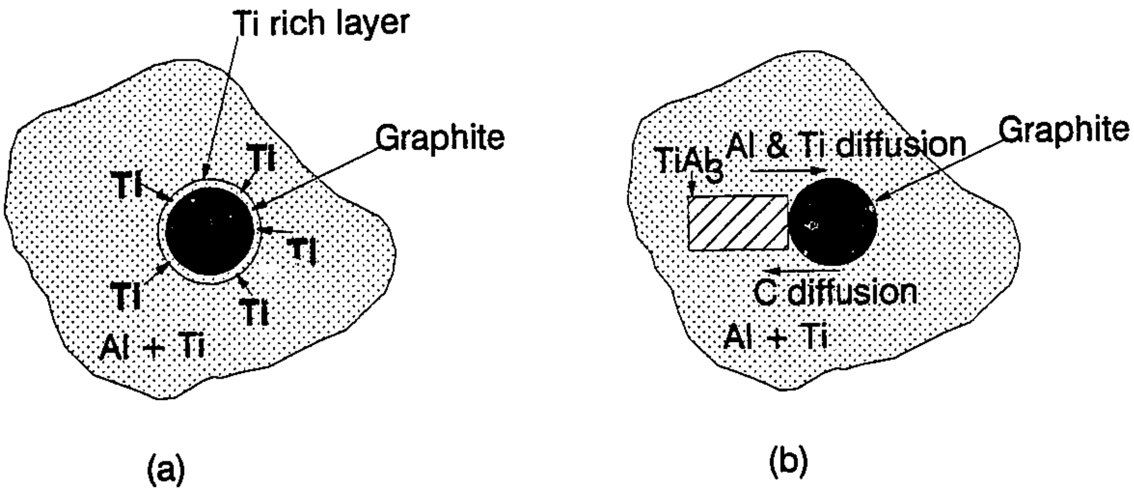

Fig. 2.37 Schematic of Preferential Reaction of Graphite Particle in Al-Ti Melt; (a) Reaction with Solute Ti and (b) Reaction with $TiAl_3$ Particles.

Preferential reaction between Ti and C in the system under consideration can only occur if some mechanism operates such that Ti is concentrated around carbon particles, and thus reduces the local activity of Al (Fig. 2.37(a)). Sahoo *et al.*,[33] suggested that Ti diffuses in liquid aluminum to the carbon source and reacts to form TiC as in Fig. 2.37(a). There is no reason why preferential migration or segregation of Ti should occur around the non wettable graphite particles. Even if such segregation of Ti were to occur, it will increase the local melting point of the system resulting in higher non wettability. It is thus difficult to see why, as claimed by Banerji *et al.*,[31] there is a preferential reaction between Ti and C rather than between Al and C.

Stable $TiAl_3$ crystals will be present within the melt when the Ti concentrations are high (> 0.15 %). The formation of TiC according to Eqn. [2.13] is essentially a solid state reaction. As such, diffusive mass transfer of Ti and C will be the controlling mechanism of the reaction (Fig. 2.37(b)). If contact between $TiAl_3$ and C ($\sim 20\mu$m) particles were to be established, the carbon atom, because of its size, should diffuse into the $TiAl_3$ crystal resulting in complex carbides of the type Ti_xAlC. The reverse process *i.e.*, diffusion of Ti into carbon is unlikely to occur. Another possible solid state reaction mechanism might involve Ti from $TiAl_3$ and C from graphite diffusing to the interface and reacting there. Since the atomic sizes of Ti and Al are very similar,[78] the probability of Al diffusion to the interface is equivalent to Ti, and Ti_xAlC, not pure TiC, would form. Jarfors *et al.*,[69] observed formation of complex carbides in direct contact with $TiAl_3$. From the above discussion it is quite evident that it is almost impossible to avoid formation of Al_4C_3 and Ti_xAlC by direct reaction of graphite powder with an Al-Ti melt at temperatures below 1273 K.

Aluminum carbides and complex carbides of Ti and Al were in fact observed by Banerji *et al.*[30,31] According to them, since the TiC in their experiments was freshly formed *in-situ*, it would be well wetted and would react with Al forming aluminum carbide and Ti_xAlC. The contact angle is affected by preferential migration of atoms, a process which depends on the character of chemical reactions at the contacting materials.[45] Wetting is not observed when there is preferential migration of elements from the solid compound into the melt. It is well known[112] that TiC is generally prone to carbon depletion when in contact with liquid Al, and must therefore be subject to dissolution in which carbon reacts much faster with Al than it does with Ti. This is quite evident in Fig.2.18(a) where fine crystals of Al_4C_3 and Ti_xAlC are formed on the surface of TiC.

Measurements made on a TiC surface indicate that the contact angle is greater than 90 deg below 973 K and decreases rapidly with temperature (at 1200^0C, $\theta \sim 30$-40^0).[45] A rise in temperature, therefore, activates the diffusion of elements from the melt into the solid compound resulting in improved wettability. Thus, the claim[31] of improved wettability of TiC at the operating temperature range of 1023-1273 K is quite justified. Wettability is, however, an interfacial phenomenon, and a layer of the order of nanometers can alter the surface characteristics. Particles of the order of 20μm in size are not converted to TiC instantaneously, and evidence for this is presented by Banerji *et al.*,[31] showing the sequence of the reaction. As soon as the first layer of TiC is formed, the graphite particle is effectively wetted by the Al. For the reaction to proceed, C atoms must diffuse through the TiC layer, but since the particle is now wetted it will react with Al to form aluminum carbide. Sahoo *et al.*,[33] suggested that as soon as a stable size TiC particle forms, it breaks off from the parent graphite particle and is dispersed in the aluminum melt. By the time the whole particle is converted to TiC, a significant amount of TiC formed at the beginning will be converted to Al_4C_3 and Ti_xAlC. Thus Al_4C_3 and Ti_xAlC must form either directly in the melt or through TiC decomposition. From the discussion on thermodynamics and kinetics it is most likely that the former process is predominant.

The entire carbide theory was based on the spontaneous formation of TiC by reaction of Ti with the residual carbon in the melt. Theromodynamic considerations (Fig. 2.2) do not predict that this reaction occurs at temperatures normally used in Al foundry operations, and carbon present *in-situ* should not have the kind of wettability kinetic barrier for the formation of Al_4C_3 discussed by Banerji *et al.*[31] Production of TiC on the addition of Al-Ti master alloy does not, therefore, seem to be a feasible proposition.

Cissé *et al.*,[62] studied solidification of Al on a TiC surface using electron beam melting and forcing the solidification to start and continue preferentially from the substrate. It was observed that the initial orientation of Al on the TiC was completely epitaxial as $(001)_{Al}//(001)_{TiC}$; $[001]_{Al}//[001]_{TiC}$. This certainly makes nucleation of Al on TiC feasible from the crystallographic point of view, but the very existence of TiC in its virgin form within Al melts must be questioned.

It is well known that even a monoatomic layer adsorbed on the surface of a nucleus can completely destroy the nucleation potential. Cissé *et al.*,[62] observed Al_4C_3 formation in their study, but it was presumed that this did not have any effect on the nucleation process. From Fig. 2.19 it is clear that clusters of carbides of Al, do affect the nucleation of Al on $Ti_xSi_yAl_{1-(x+y)}$. $Ti_xSi_yAl_{1-(x+y)}$ is a potent nucleus for the nucleation of the α phase in Al-Si alloy as demonstrated earlier (Section 2.5.1.2). Al_4C_3 and complex carbide clusters cover the crystal and the particle is pushed into the interdendritic region by the solidification front rather than acting as an active nucleus for α-Al. From Fig. 2.18 it is quite evident that a significant amount of Al_4C_3 and complex carbides have formed at the interface of TiC within five minutes of addition. The whole melting and freezing sequence, in the study carried out by Cissé *et al.*, [62] was very short because of electron beam melting. Though little or no interdiffusion of Ti and Al was revealed in either

TiC or Al, surprisingly, Al_4C_3 was formed at the TiC/Al interface indicating the rapid kinetics of aluminum carbide formation.

The carbide theory has been contradicted before.[24,25,27] Crossley and Mondolfo[25] found that low carbon additions did not affect the grain size of aluminum castings, and higher amounts increased the grain size, particularly at hyperperitectic Ti-levels. This was attributed to the eventual reduction in number of active $TiAl_3$ particles available in the melt as a result of TiC formation. Banerji *et al.*,[31] argued that, if Crossley and co-workers[25] had TiC dispersions, it was most likely that these particles were poisoned during grain refiner preparation due to prolonged holding time. The usual Ti level in a grain refined melt is approximately 0.01 %. At this level of addition of Al-Ti master alloy into Al melts under normal melting conditions, TiC formation is not thermodynamically favourable,[64] and even if it is introduced into the melt by any other means, Al_4C_3 and complex carbides are prone to form on TiC particles and destroy their nucleation potential. This is clear from the close resemblance of fade properties of Al-Ti-C master alloy with boron free Al-Ti master alloys.[113] The efficiency of Al-Ti-C master alloys is also susceptible to process temperature.[114]

2.6 Summary

There are several theories as to how and why commercial grain refiners (Al-Ti and Al-Ti-B) work, but careful analysis shows that no clear consensus has yet emerged. The crystallites that are commonly believed to nucleate grains are $TiAl_3$, TiC, TiB_2 and (Al, Ti)B_2, which come either from the master alloy or form in the melt after addition. While the behaviour of $TiAl_3$ is rather clear, the role of TiC, TiB_2 and (Al, Ti)B_2 is most puzzling. Most of the studies in this regard have been carried out by adding master alloys of Al-Ti or Al-Ti-B into aluminum melts. Clearly, addition of master alloy changes the melt chemistry in terms of dissolved Ti, and causes a dispersion of extremely fine crystallites in the melt. Identification of the physical and chemical nature of these crystallites in this complex system is difficult and an understanding of their behaviour has never been conclusive.

In the present study, experiments have been carried out by introducing synthetic TiB_2 and TiC crystallites ($\sim$5-10μm) into melts by the specially developed technique. The addition methodology is critical for subsequent study of the behaviour of these particles during solidification. The role of excess Ti (hypo and hyperperitectic compositions) on the behaviour of TiB_2 crystallites has been investigated. The mechanisms of grain refinement of pure Al and hypoeutectic Al-Si alloys by Al-Ti-B and Al-Ti-C master alloys have been made clearer.

From the present study, one can develop a sequence for grain refinement of Al by Al-Ti-B master alloys (see Fig. 2.38). On addition of master alloys, TiB_2 crystals are dispersed throughout the melt while simultaneously $TiAl_3$ crystals dissolve to provide excess solute Ti. At the same time any $(Al, Ti)B_2$ if present may react to form the stable boride phase, TiB_2. When sufficient Ti is dissolved in the melt, an activity gradient is established between the melt and substrate, and as a result Ti is segregated to the interface to form a thin coating of $TiAl_3$ on TiB_2. On cooling this $TiAl_3$ layer undergoes a peritectic reaction and nucleates α-Al. Thus, the nucleation mechanism, in the case of Al-Ti-B master alloys is a two step process *i.e.*, duplex in nature. The entire process leading to the formation of $TiAl_3$ on TiB_2 is completed within the contact time for the grain refiner which is affected by the distribution of the boride phase in the master alloy. The microstructures of waffle and rod master alloys are presented in Figs. 2.39(a) and (b) respectively. The borides are distributed uniformly on a finer scale in rod master alloys, and hence the observed contact time is generally very short. On prolonged holding, the boride particles settle and cause loss of grain refinement which can be reversed by agitation of the melt. In the presence of impurities such as Zr, specific segregation of Zr will also take place on the TiB_2 substrate and its atomic size mismatch will hinder $TiAl_3$ formation and lead to poisoning of the seeds.

In the case of Al-Si alloy, unlike pure Al, a ternary aluminide (Al-Ti-Si) is formed at the TiB_2/melt interface by similar processes to those described for Al. However, due to the drastic reduction in peritectic solidification temperature of the ternary system at higher Si content, refinement by Al-5Ti-1B is inefficient. At higher cooling rates the non-equilibrium ternary aluminide may be an effective nucleant. The

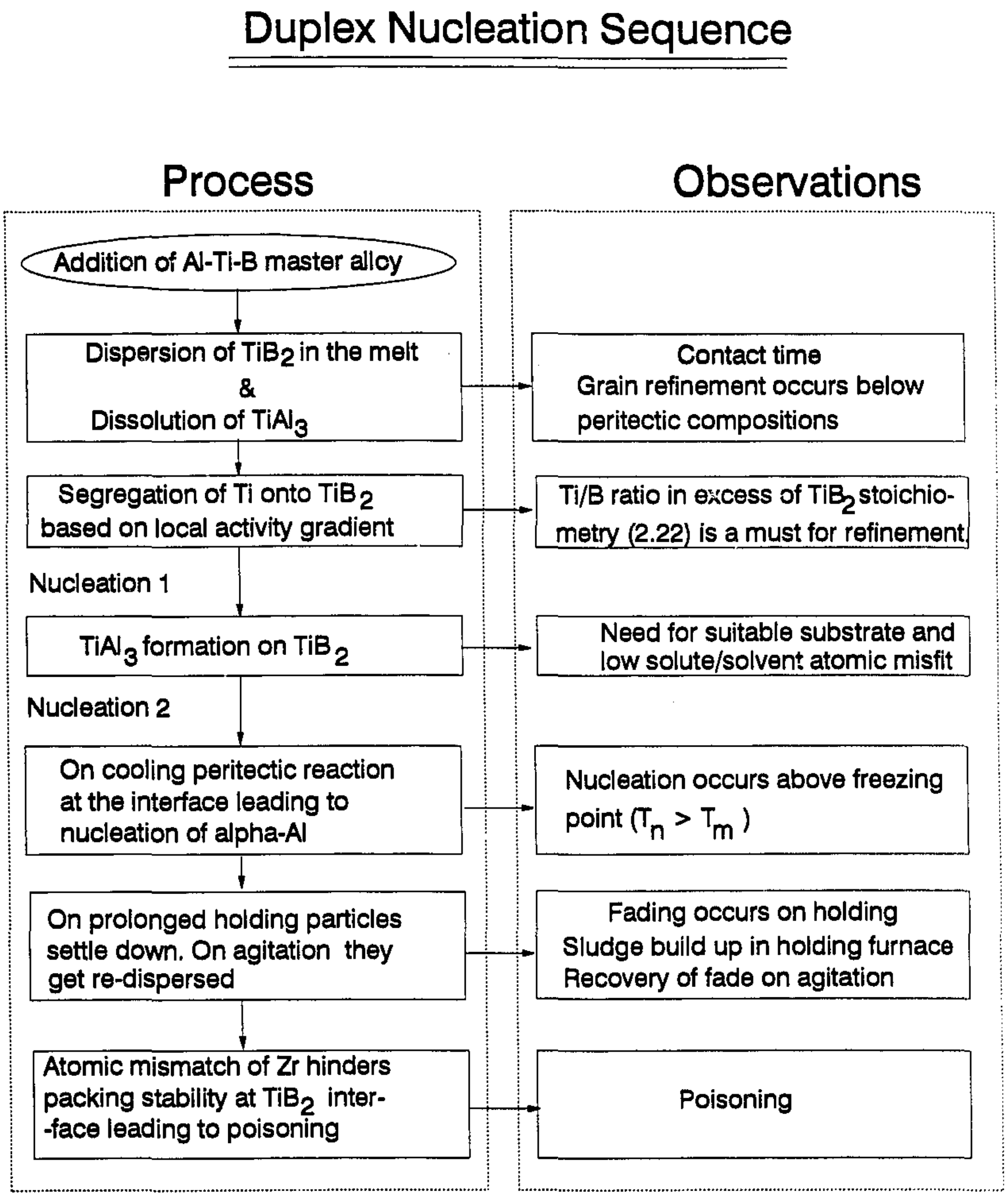

Fig. 2.38 Schematic Presentation of Processes in Grain Refinement Practice and Their Implication on Experimental Observations.

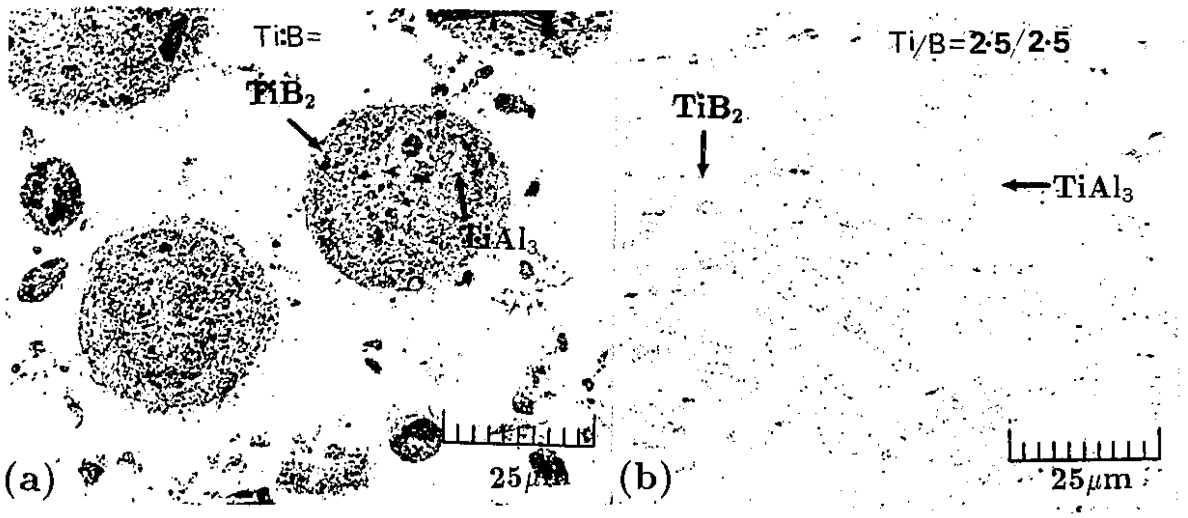

Fig. 2.39 Typical Microstructure of Master Alloys; (a) Waffle Al-2.5Ti-2.5B and (b) Rod Al-5Ti-1B.

nature of the solid substrates decides the aluminide nucleation potential. The improved performance of Al-3Ti-3B is presumably due to excess B present in solution, which forms a layer of AlB_2 at the TiB_2/melt interface. On cooling, this interfacial layer nucleates α-Al in a similar manner to that which occurs in the Al-B system *i.e.*, possibly via a eutectic reaction.

The mechanism of grain refinement by TiC is much more straight forward *i.e.*, α-Al nucleates directly on TiC particles. The existence of epitaxy on the surface of TiC enables direct nucleation, but the thermodynamic stability of TiC within liquid aluminum limits its potential as a grain refiner. When TiC is present in liquid aluminum, depletion of carbon and aluminum carbide formation occurs. According to the theory of chemical wetting, the wettability of TiC will be affected significantly due to the undesirable chemical reaction which destroys the nucleation potential. In the case of Al-Si alloys, TiC proves to be even more disasterous, since it decomposes completely.

Chapter 3

Mechanism of Pore Nucleation

3.1 Introduction

Probably the most serious problem the casting industry faces today is the fact that internal voids are usually associated with cast structures. This inevitable casting defect deteriorates the soundness of castings, resulting in decreased mechanical properties, poor surface finish and leakage in castings. The production of castings free from porosity is a serious challenge to the foundry industry. It would appear that in a commercial foundry, fifty to seventy five percent of all scrap castings are due to the factors related, directly or indirectly, to porosity.[115]

Pores in cast metal are not always prejudicial. Well dispersed pores can balance solidification contraction and thereby prevent the more damaging effect of localized shrinkage cavities in poorly fed castings. In general, however, they are unwanted. Depending on the application, the tolerence level, distribution and type will vary. For example, even in very small amounts, porosity can markedly reduce mechanical properties, whereas, low levels may not affect the leaktightness of pressure castings and hence may be tolerated.

3.2 Pore Formation

The problem of porosity formation is quite complex and interesting. Significant effort has been put forth in the past to understand the factors responsible for pore formation and the mechanisms by which they form. Pores in a casting may appear due to several reasons. Pore formation by mold reactions, high temperature oxidation, blow holes and entrapped gas are undoubtedly one of the most important sources of porosity in castings. The origin of such pores is fairly well understood and the methods of control are well established. On the other hand, the process by which pores are formed during freezing of a casting is one of the most difficult phenomena to understand and control. Over the last fifty years, this subject has been studied in detail, and as a result a significant amount of literature has appeared, but surprisingly, there appears to be no clear cut agreement as to the important mechanisms which control the formation of such porosity.

Traditionally, the origin of porosity during soildification of aluminum and its alloys is attributed to the rejection of hydrogen from the growing solid into the adjacent liquid, and/or the inability of the liquid to feed the interdendritic regions to compensate for the volume shrinkage associated with the phase change. Thus, the gas porosity which is similar to shrinkage porosity, usually occurs in the mushy zone. Quite often, gas porosity and shrinkage porosity are discussed under separate headings in the literature[10,116–119] but in reality the formation of shrinkage pores and gas pores in separate locations is rare, unless, the casting process has been specifically designed to minimize one of them (Figs. 3.1(a) and (b)). Normally, they occur simultaneously, interacting with each other to develop the resulting porosity, and it is difficult to separate their behaviour. The relative effect of each is not known, except in a qualitative way which comes from years of experience in producing castings. The same fundamental nucleation principles are also applicable for both and in the present study, the general term 'porosity', will be used, independent of its origin. A comprehensive picture of pore formation is presented in Fig. 3.2.

Factors affecting porosity as indicated in the literature, can be identified as:

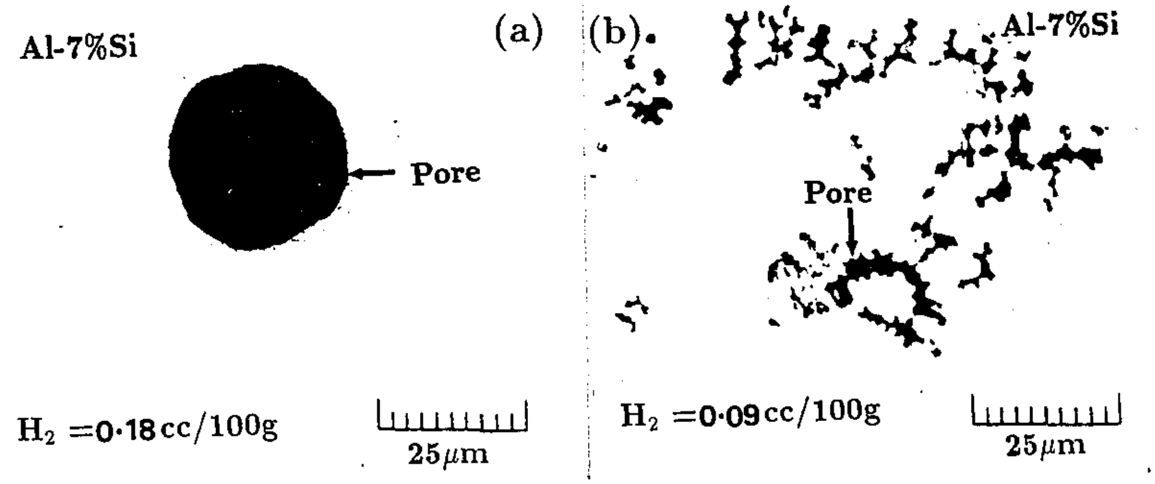

Fig. 3.1 Types of Porosity; (a) Gas Pores Formed During Directional Solidification and (b) Shrinkage Pores.

- hydrogen content,[2,3,115–127]
- process variables such as:
  - cooling rate,[5,11,120–122]
  - superheat,[123–127]
  - external pressure,[2,129,130]
  - casting design,[131–138] and
  - heat extraction mode (unidirectional or isotropic),[136–140]
- grain structure, including grain size and grain morphology,[141–149]
- alloy chemistry, which influences hydrogen solubility, solidification range and intermetallic constituent formation,[123–128] and
- inclusion content.[2,4,10,13,16]

3.2.1 Fundamentals of Pore Nucleation

As mentioned earlier, the problem of pore nucleation is regarded as formally similar to the nucleation of dense phases such as solids from liquid.[150] However, there

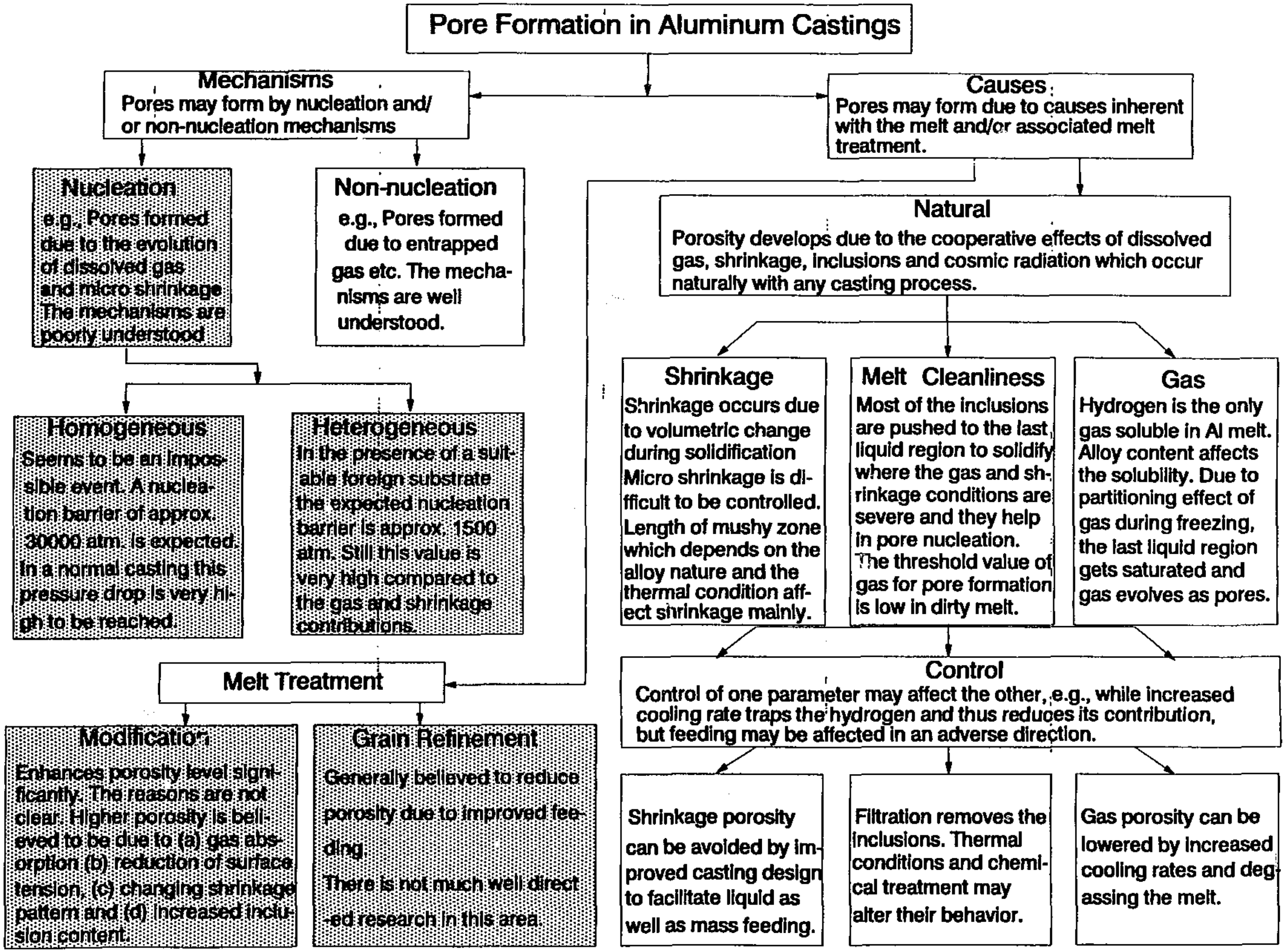

Fig. 3.2 A Comprehensive Picture of Pore Formation in Castings.

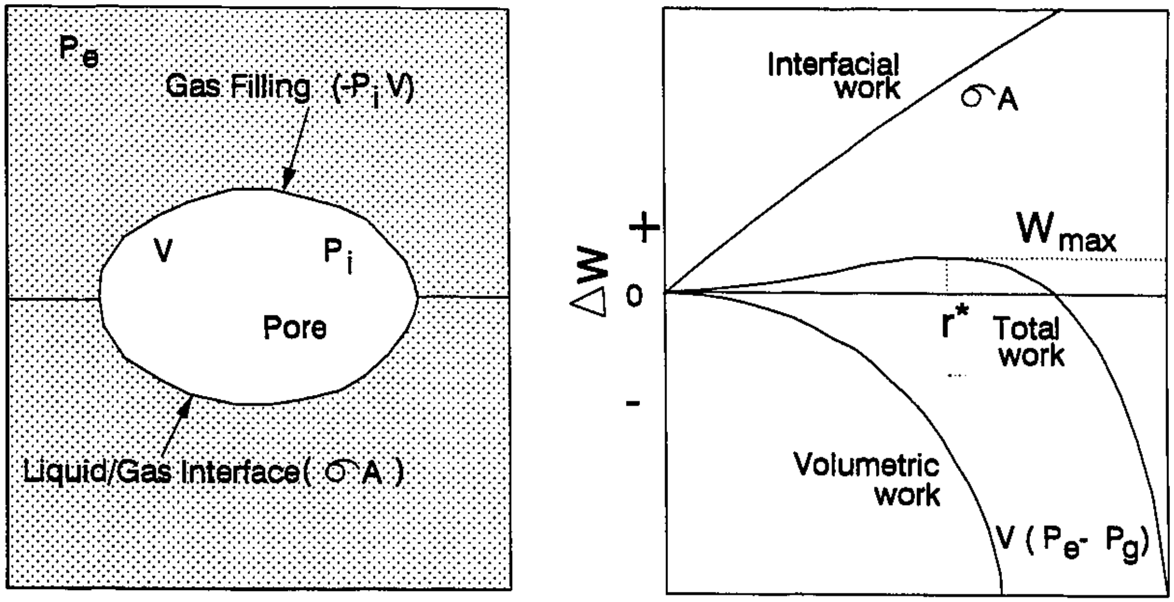

(a) (b)

Fig. 3.3 Work Done to Nucleate a Void in a Liquid Continuum; (a) Schematic Bubble Formation and (b) Work Done vs Radius of the Bubble.

are differences which make it worthwhile to deal with the problem separately in some detail.

The total work associated with the formation of a bubble in the interior of the liquid (see Fig. 3.3(a)) can be computed from the contribution of three factors as:[151]

- the work required to push back the liquid far enough to create a bubble of volume, V, expressed as P_eV, where P_e is the existing pressure in the liquid,
- the work required to create and stretch out the new liquid-gas interface of area A, σA, where σ is the interfacial energy per unit area, and
- the work required to fill the bubble with vapour or gas at pressure, P_i, expressed as $-P_iV$. This work is negative because pressure inside the bubble clearly helps the formation of the bubble as opposed to other work requirements.

For a spherical bubble of radius, r, the total work can be expressed as:

$$\begin{aligned} W &= \sigma A + P_e V - P_i V \\ &= 4\pi r^2 \sigma + (\frac{4}{3})\pi r^3 (P_e - P_i) \end{aligned} \qquad (3.1)$$

The internal gas pressure, P_i, is expected to be the result of gases in solution in the melt. The pressure acting on the outside of the bubble, P_e, is:

$$P_e = P_h + P_a + P_s \qquad (3.2)$$

where, P_h is the hydrostatic head, P_a is the applied pressure on the surface of the liquid and, P_s, is the tensile force arising by various mechanisms because of volumetric shrinkage during solidification. Among these, P_s is most dominant under normal casting conditions and is considered as a negative pressure because of its tensile nature.

A bubble cannot develop progressively from zero size, but must spring into being at some finite size, because the surface tension pressure becomes infinite at zero radius. Hence, there is a critical radius, r^*, below which it is not capable of surviving, and above which it will tend to grow. The plot of W vs r (Fig. 3.3(b)), shows a maximum, W_{max}, which constitutes the energy barrier to nucleation and can be represented as:

$$W_{max} = \frac{16\pi\sigma^3}{3(P_e - P_i)^2} \qquad (3.3)$$

The critical radius, r^*, can now be expressed as:

$$r^* = \frac{-2\sigma}{(P_e - P_i)} \qquad (3.4)$$

The above expression (Eqn. [3.4]) represents the condition of mechanical equilibrium for the existence of a bubble in the liquid.

3.2.2 Previous Work

Careful analysis of existing literature on porosity formation in castings reveals that studies fall into two classes. In one, various theoretical treatments and experimental studies are only concerned with the understanding of the fundamentals of the nucleation process *i.e.*, the mechanisms,[2,3,4,13,150–162] the applicability of classical nucleation theory to predict the activation barrier,[3,150–152,157] and the possibility of achieving it in a real casting.[6,8,121,163–165] It has been recognized that the activation barrier estimated from these analyses is well above the values that can be achieved in a real situation.[2,3] In the second category, research efforts are mainly concerned with experimental studies on various factors affecting porosity in real castings and their quantitative measurement.[5,9,131,166–168] Almost all of the theoretical treatments in this regard[169–194] deal with the quantitative prediction of shrinkage and gas porosity through mathematical models. As a result several empirical and semi-empirical rules have been established for foundry practice.[190–196] The fundamental question of the nucleation mechanism has, however, been disregarded, and all the mathematical developments[170–175,180–188] are based on the concept of mechanical equilibrium required for the existence of a bubble in the liquid as described by Eqn. [3.4]. Although significant advancement has been made in this area, little has been accomplished in an understanding of the nucleation mechanism itself.

Though the effects of gas and shrinkage are additive and encourage nucleation, two important processes which are specific to a gas free melt and an unconstrained melt respectively, must be recognized. Growth of bubbles in liquids under positive (compressive) hydrostatic stress is known as *bubble nucleation* whereas the corresponding process in liquids under negative (tensile) hydrostatic stress is termed *cavitation.* There are two important differences between bubble nucleation and cavitation; namely (i) growth of an embryonic bubble in cavitation generally occurs by transport of vacancies rather than transport of molecules as in the case of bubble nucleation, and (ii) a critical nucleus in bubble nucleation contains many molecules ($\sim 10^6$) while a critical nucleus in cavitation may contain only a few.[197]

Fisher[151] in his analysis for the prediction of activation barrier, considered the condition of cavitation only, by neglecting the work contribution by internal gas pressure (since $P_e \gg P_i$) in Eqn. [3.1]. His analysis on homogeneous nucleation of a pore leads to an expression for the activation barrier (or fracture pressure) in a liquid as follows:

$$P_f = [\frac{16\pi\sigma^3}{3\kappa T ln(N\kappa T/\hbar)}]^{1/2} \tag{3.5}$$

where N, κ and $\hbar$ are the Avogadro's, Boltzmann's and Planck's constants respectively. Later, Campbell[3] modified Fisher's analysis to include internal gas pressure, P_i, as well as the external pressure, P_e, to give the condition for homogeneous nucleation as:

$$P_i - P_e = P_f \tag{3.6}$$

Using values for liquid aluminum at its melting point in Fisher's expression (Eqn. [3.5]), the activation pressure is found to be approximately 30,500 atm.[3] However, there are some limitations in Fisher's analysis which were pointed out by Hirth and Pound[157]. The major assumption in Fisher's analysis is the existence of a constant pressure *i.e.,* somehow, the pressure is kept at P_e even after the first bubbles have begun to grow. Hirth and Pound[157] demonstrated the thermodynamic irregularity of following a constant pressure path and used instead an isothermal and constant volume approach to predict the activation barrier for pore nucleation as given below:[6,8,157,198]

$$\Delta F^* = \sqrt{\frac{16\pi\sigma^3}{3 \times 60\kappa T}} \tag{3.7}$$

where F is the Helmholtz free energy. For liquid aluminum, with a surface tension of 0.914 N/m,[8] this value is about 35,000 atm. Now, for homogeneous nucleation, this pressure requirement must be fulfilled by solidification shrinkage and gas evolution. Several investigations[163–165,170–175,179–189] have been made in the past for an estimation of the actual shrinkage pressure drop and gas pressure in castings.

3.2.2.1 Contribution of Solidification Shrinkage

Campbell[164,165] practically formulated the process of computation of the negative pressures associated with the volume change on solidification and the possibility for occurence of cavitation. Calculations based on an ideal case of an unfed solidifying sphere were carried out by Campbell, employing various approaches such as elastic-plastic[164] deformation and creep.[165] The spherical geometry (shown in Fig. 3.4) was

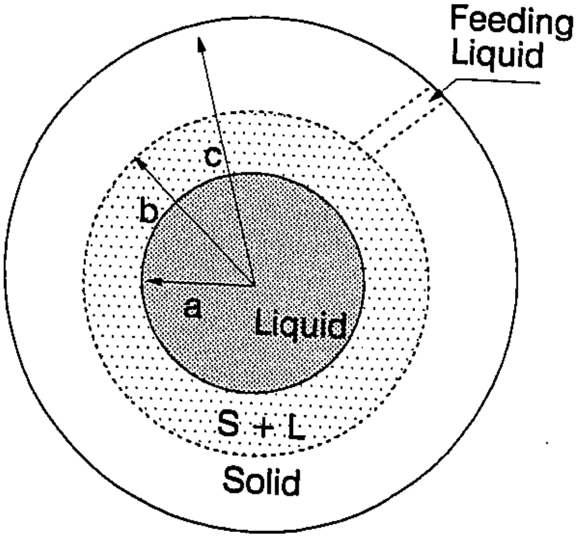

Fig. 3.4 The Solidification Model for an Unfed Sphere.[164]

chosen because the highest shrinkage pressures would be developed in such a system. Furthermore, small regions of confined liquid in a large solidified volume of a casting approximate reasonably well to a spherical geometry. The elastic-plastic model analysis was based on the assumption that yield stress is independent of strain rate, whereas in the actual solidification process cast metals and alloys are at their melting points, and the yield stress is strongly dependent upon strain rate. In a subsequent attempt, Campbell[165] assumed that deformation of a solid metal at its melting point is best described by creep and his analysis led to the conclusion that the maximum hydrostatic tensions are limited by the collapse of the casting, and are in the region of -1500 to -4200 atm. for aluminum, copper, nickel and iron.

In the case of well fed castings, pressure drop occurs due to viscous flow of the residual liquid through the mushy zone, a phenomenon known as 'interdendritic feeding'. This aspect has been widely discussed and mathematically modelled by many researchers.[121,132,163–165,170–175,179–189] Allen [199] made the first attempt to provide a quantitative theory. An estimate of the pressure gradient involved can be obtained simply by use of the well known equation by Poisseuille[2] which describes the pressure gradient required to cause fluid flow along a capillary:

$$\frac{dP}{dx} = \frac{8v\eta}{\pi r^4 n} \tag{3.8}$$

where, v is the volume flowing per second, η is the viscosity, r is the radius of the capillary and n is the number of capillaries. Piwonka and Flemings[172] considered the effect of simultaneous solidification and developed a more realistic model. Subsequently, several refinements have been introduced to their original equation by many researchers,[144,147,184] the details of which have been discussed by Campbell[2] and by Sigworth *et al.*,[121,132] The pressure drop by viscous flow through the mushy zone can be expressed as:[121]

$$\Delta P = \frac{\eta\beta\xi}{(1-\beta)} 8n\pi\tau^3 \frac{V_x \Delta T}{G_x} ln \frac{\phi}{1-g_s} \tag{3.9}$$

where β is the coefficient of volumetric shrinkage, ξ is the correction factor for the nonlinear dependence of solid fraction on temperature, V_x is the solidification velocity, G_x is the thermal gradient along the mushy zone, g_s is the volume fraction solid at the point of consideration and τ is the tortuosity factor. $\phi = \lambda/l$, where λ is the portion of the mushy zone where dendrites are coherent and liquid filters through, and l is the length of the mushy zone.

This solution reveals that the pressure drop by viscous flow through the mushy zone is controlled by a number of important factors such as viscosity, solidification shrinkage, the rate of freezing, the length of the mushy zone and the dendrite arm spacing. Calculations[121,132] show that the viscous pressure drop is of the order of only a few atmospheres. However, viscous flow does not occur till the end of solidification. The pressure drop is most sensitive to the size of the flow channels. The overriding effect of the radius of the flow channels leads to ΔP becoming extremely high towards the end of solidification. The high hydrostatic stress near the end of freezing will be limited by the inward collapse of the solid by creep flow described earlier. The natural progression of interdendritic feeding followed by solid feeding is confirmed by more recent models.[205]

Liquids have been known to be able to withstand tension for many years. Early work[200–203] on the determination of the tensile strengths of liquids held in various containers gave notoriously scattered results due to different degrees of cleanliness and presence of microscopic imperfections. Experiments to test the liquid away from the influence of walls have been carried out using ultrasonic waves focused in the centre of a volume of liquid. These experiments have been moderately successful, but impurities in the liquid have tended to obscure the results. Carlson[204] reflected shock waves through a thin film of mercury and recorded strengths of up to 30,000 atm. This result is one of the first to give strength values as high as that predicted by various theoretical approaches.

Negative pressures in solidifying aluminum were measured directly by Ohsasa *et al.*[205] Stainless steel discs were immersed into the top of a solidifying melt, such that the disc almost filled the top of the crucible containing the metal. On the arrival of the solidification front at the disc, a volume of liquid was effectively trapped underneath. As this volume solidified, the stress in the liquid was measured by a transducer connected to the disc. Stresses needed to cause pore formation were typically only about -0.1 atm, which is several orders of magnitude less than the theoretically predicted values.

3.2.2.2 Contribution of Dissolved Gas

A number of valuable rules and realtionships have been determined, that describe the role of dissolved gas (hydrogen in aluminum) in pore formation:

- Regardless of composition or solidification condition, a critical or threshold dissolved hydrogen level must be exceeded for hydrogen porosity to occur (order of 0.1 cc/100g),[195,196]
- For any specific cooling rate, the pore volume fraction and pore size decreases with decreased hydrogen content, however, this rule applies for hydrogen contents above the threshold value,[5,11] and
- For a given alloy and hydrogen content, pore volume fraction and pore size decrease with cooling rate.[5]

A quantitative estimation of gas pressure can be made by considering hydrogen enrichment in the residual liquid pool during solidification. Since hydrogen is continuously rejected by the solid to the residual liquid, the liquid will be enriched with gas as solidification progresses. The partial pressure of hydrogen gas which is in equilibrium with liquid metal having a dissolved hydrogen content, C_l, can be estimated by applying Sievert's law and published solubility data:[121]

$$P_{H_2} = C_P(\frac{f_H C_l}{S})^2 = C_P(\frac{f_H C_0}{S})^2(\frac{1}{1-g_s(1-k)})^2 \tag{3.10}$$

where C_0 is the initial gas concentration (cc/100g), C_P is the conversion constant, f_H is the activity coefficient of hydrogen, and S is the hydrogen solubility which can be expressed for pure aluminum as:

$$ln(S) = \frac{-5872}{T} + 6.033$$

Considering a normal gas level in a foundry melt, calculations[121] show that the estimated gas pressure, at the most, can reach a few atmoshperes, much lower than the required activation barrier.

Whether or not these figures are particularly accurate is a detail that need not concern us here. The important message here is that the pressure which is required for nucleation is extremely high, and reflects the apparently real difficulty of homogeneous nucleation. The required pressure is so high as to be perhaps unattainable. Moreover, the disparity between the theoretical predictions[2,8] and experimental observations[205] implies that there must be some mechanism which facilitates the nucleation process.

3.2.2.3 Heterogeneous Nucleation

In castings, nucleation of pores can be expected to occur primarily at heterogeneous sites. It has been experimentally shown in transparent systems that for rapid depressurization nearly all initial bubbles are nucleated on existing surfaces.[162] Heterogeneous sites are inherent in almost all normal castings with inclusions forming the most important category of such sites in the melt. Even when the best of corrective measures are taken some inclusions find their way into the liquid. In certain cases, their addition

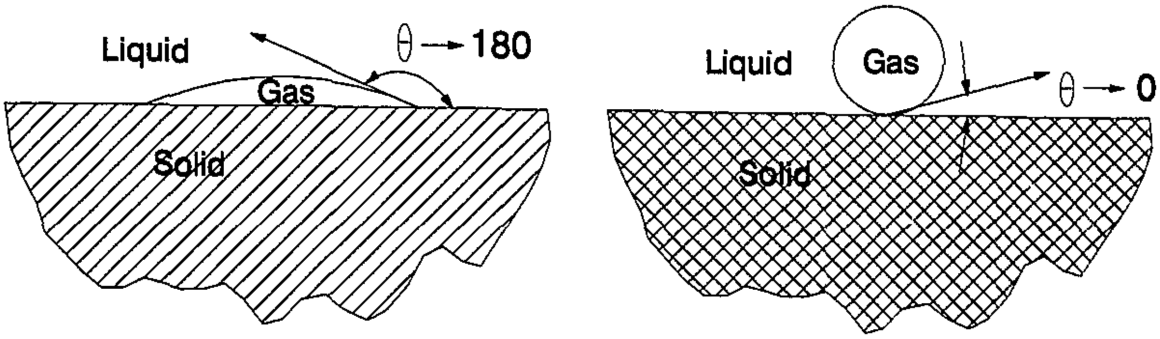

Fig. 3.5 Wetting Behaviour of Solids; (a) Non-Wettable and (b) Wettable.

is intentional *e.g.*, metal matrix composites and grain refinement discussed earlier. It has been well demonstrated that the presence of such substrates greatly enhances the porosity formation in aluminum alloys.[4,6,7,8,10] In one of these studies,[4] the deliberate addition of oxides skimmed from the melt surface shows their association with the pores. On the other hand, when inclusions are removed by filtration, the porosity level is significantly reduced.[10,11] However, the mechanism by which such inclusions operate to facilitate pore formation is not well understood. A theoretical analysis of nucleation on a foreign substrate shows that heterogeneous nucleation is more favourable in energy terms than homogeneous nucleation.[2,3,8] Fisher[151] suggested that nucleation at foreign substrates is easier by a factor:

$$P_{f,het} = 1.12 \times [\frac{(2 - cos\theta)(1 + cos\theta)^2}{4}]^{1/2} \times P_{f,hom} \tag{3.11}$$

where θ is the contact angle of the liquid with the solid substrate. A contact angle, θ=0^0, implies complete wetting, whereas, θ=180^0, is complete non-wetting as demonstrated in Fig. 3.5. The factor 1.12 arises because of the fewer sites for nucleation on a plane surface of atoms, compared to the greatly increased number of possibilities in the bulk liquid. The numerical value of the multiplying factor falls below one when θ is above 60^0, which implies that solids with higher contact angle than this value will be favourable nuclei.

The wetting considerations are still not sufficient for the interface to play a significant role in pore formation. Measurements of contact angles of liquid metal on various refractory solids indicate that a contact angle of 160^0 may be the maximum possible value for any liquid-solid combination.[2] This implies that, even with the most efficient substrate, the fracture pressure term is reduced approximately by a factor of 20 only *i.e.*, a pressure drop of the order of 1500 atm. is still required to nucleate a pore. Thus, although this makes heterogeneous nucleation more favourable than homogeneous nucleation in terms of the pressure requirement, it still does not make heterogeneous nucleation absolutely feasible.

A number of authors [161,175,176,179] are of the opinion that while the solid/liquid interface of a growing crystal can be a site for heterogeneous nucleation of pores, a plane solidification front is not suitable since it is completely wetted by the liquid. It is considered that the work of formation of an embryonic bubble is reduced on a concave substrate and becomes zero for perfectly sharp notches. Chalmers,[150] therefore, considers that a cellular or dendritic interface is a much more favourable nucleation site, partly because of the presence of grooves and partly due to the greater local gas concentration of the interdendritic liquid. It has also been experimentally observed that oxides skimmed from the surface of the melt contain numerous pores and cracks of radii ranging from 5-40μm.[4] Therefore, embryonic bubbles trapped in the crevices of these oxides may subsequently grow into pores.

3.2.3 The Present Study

Establishing a suitable mechanism of pore nucleation has been one of the major challenges in this field with the result that several mechanisms have been postulated.[2,3,4,150,161,175,176,179] However, none of these is capable of explaining how a pressure drop in excess of 1500 atm. can be achieved and how foreign substrates aid in this process. This is because little attention has been paid to the pressure drop and gas segregation behaviour in the film of liquid between an inclusion and a nearby growing S/L interface. In the present chapter, a theoretical analysis of the interaction phenomena between an inclusion and a S/L interface is made, and a mechanism of pore nucleation based on this interaction is proposed.

It was demonstrated in the previous chapter that particles whose presence within the solid is thermodynamically unfavourable are pushed by the solid/liquid interface to the grain boundary. The particle and S/L interface interaction phenomena are highly complex and are particular to specific particle/melt combinations. Depending on the particle/melt properties such as: surface energy, thermal conductivity, density, geometry and solidification characteristics of the alloy, the particles will either be pushed or be trapped by the interface. Particles which are pushed by the interface act as a barrier to the fluid flow and the diffusion field ahead of the interface. The kinetic considerations of the particle pushing process suggest that a finite separation must be maintained between the particle and the S/L interface and fluid must flow continuously into this region to compensate for the liquid that is exhausted in the solidification process. Consequently, the viscous pressure drop and gas segregation are enhanced in this thin film region. A mathematical analysis is presented here to predict the particle behaviour, the viscous pressure drop, and the gas segregation in the gap between the particle and the S/L interface. An order of magnitude analysis is carried out and compared with the fracture pressure requirement. A stability analysis for the existence of a bubble in the thin film region is also performed, and the effects of particle properties and solidification parameters on the nucleation process are discussed in order to identify the type of particles and casting conditions responsible for pore nucleation. Further, the proposed mechanism is verified experimentally with many types of particles and melt combinations. Finally, various implications of the proposed nucleation mechanism are discussed.

3.3 Theoretical Analysis

The mechanism of achieving the fracture pressure is based on the interaction of particles with the advancing S/L interface, and so it is necessary to develop a theoretical analysis of the process. With this objective in mind, the interaction behaviour will be discussed and the necessary mathematical expressions will be developed.

3.3.1 Interaction of Inclusions with an S/L Interface

Understanding the inclusion and S/L interface interaction is of great fundamental as well as technical importance, and has therefore been the subject of theoretical and experimental study over the past two decades. When a moving solidification front intercepts an insoluble particle, it can either *push* it or *engulf* it. For a specific melt and particle combination there exists a critical velocity below which the particle will be pushed and above which it will be engulfed. In the case of pushing, a driving force exists which tends to keep a finite separation between the growing solid and the particle, resulting in the particle being pushed. This driving force is a balance of the forces acting on the particle and is a function of several variables.

The main issues involved in modelling of the process are related to:

- The nature of the forces between the particle and the interface. These forces can be identified as: repulsive force, F_r, drag force, F_d, and buoyancy force, F_b.
- The mechanism involved in mass transfer into the gap between the particle and the solidification front by diffusive and/or viscous flow. The implication of both of these processes is discussed later.
- The influence of the interface shape on the process.

A number of theoretical models[44,92,93,206–210,212,213] have been developed, but detailed discussions of these models are not necessary here. An excellent review has been presented by Stefanescu *et al.* [213]

The critical interface velocity for particle pushing depends on many variables and can be expressed as:

$$V_c = f[\Delta\sigma_0, \eta, d, R, R_S, k_{pl}, \Delta\rho, g] \tag{3.12}$$

where V_c is the critical velocity for pushing, $\Delta\sigma_0$ is the net interfacial energy (see Glossary), η is the viscosity, d is the separation between the particle and the S/L interface, R is the radius of the particle, R_S is the radius of curvature of the S/L interface, k_{pl} is the ratio of the thermal conductivity of the particle to the matrix, $\Delta\rho$ is the difference in the densities of the particle and the liquid, and g is the acceleration due to gravity.

The models that are now used include numerous assumptions. The assumption of planar interface or limited morphological instability precludes model validation in practical cases. In metallurgical alloy systems, the behaviour is quite complex, and the critical velocity will depend to a large extent on the thermal gradient. None of the theoretical models available, gives a general solution which can be used, particularly for metal alloy systems. Similarly, experimental study in metallic systems is obstructed by the opaqueness of the material with the result that little experimental data is available at present. However, a qualitative picture can be obtained by analysing the dominating terms of Eqn. [3.12]. Stefanescu *et al.*, [212] have presented the behaviour map given in Fig. 3.6, for a foreign particle in front of a solidifying interface.

Table 3.1 Data Used for the Construction of Particle Behaviour Map.[212]

Symbols	Values
a_0	$2*10^{-10}$ m
η	0.005 Pa.s
k_{pl}	0.91
g	9.81 m/s^2
$\lvert\Delta\rho\rvert$	500 kg/m^3
$\Delta\sigma_0$	1.0 N/m

The particle behaviour map was developed on the basis of the following expressions:[212]

$$V_F = \frac{2}{9}\frac{R^2\Delta\rho g}{\eta} \tag{3.13}$$

and

$$V_c = \frac{a_0\Delta\sigma_0}{12\eta k_{pl}R} \tag{3.14}$$

where V_F is the velocity attained by the particle due to its buoyancy force, V_c is the critical velocity of the interface, $\Delta\rho = \rho_l - \rho_p$, and a_0 is the interatomic distance. Eqn. [3.13] determines whether the interface will ever encounter the particle, depending on the direction and magnitude of V_F relative to the growth velocity V, while Eqn. [3.14] determines whether the particle will be pushed or engulfed if the particle/interface interaction does

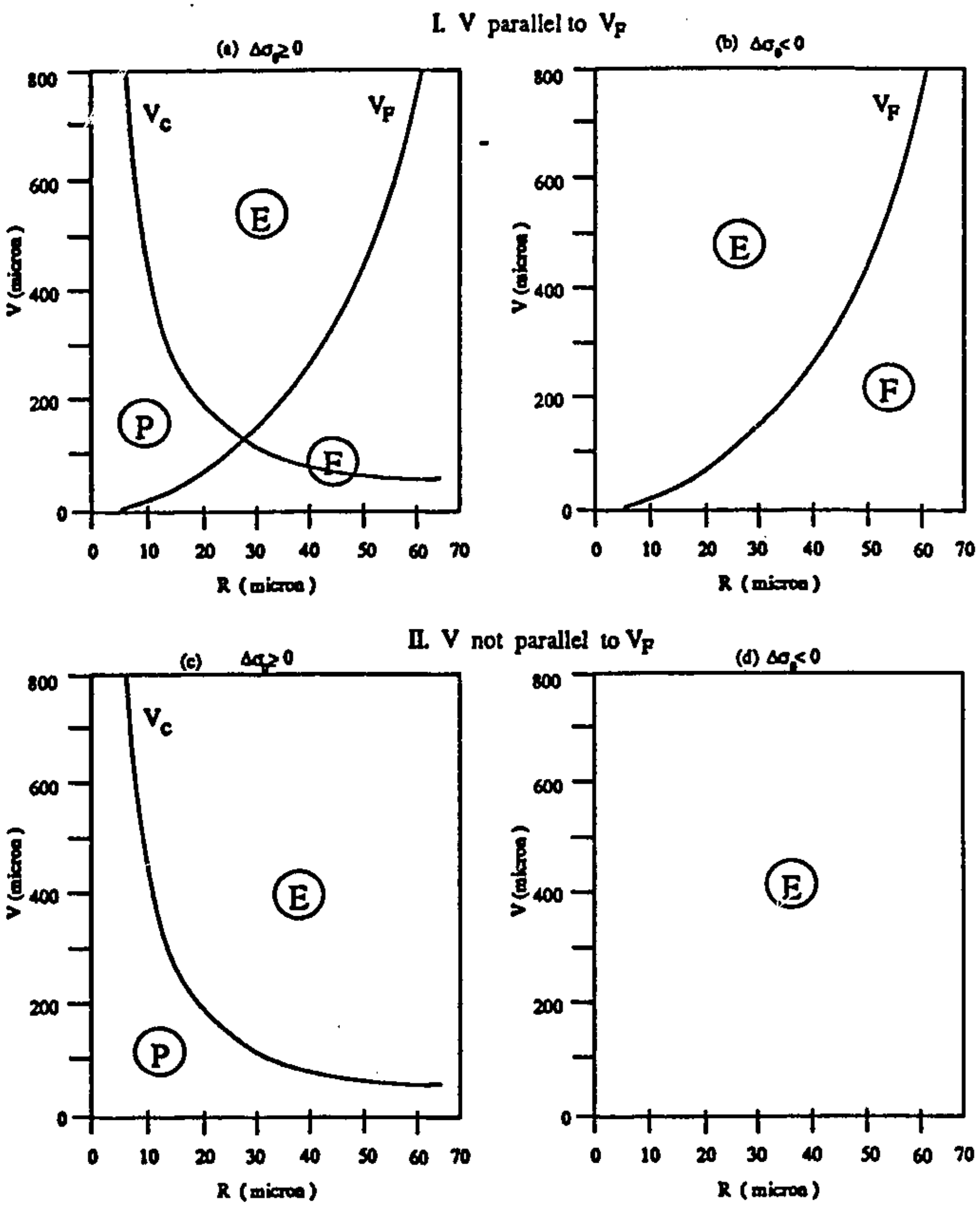

Fig. 3.6 Particle Behaviour Map, E=Engulfment, P=Pushing, and F=Floating (Reproduced from Reference [212]).

indeed occur, depending on the magnitude of V relative to V_c. The data used to construct the particle behaviour map are given in Table 3.1.

In Fig. 3.6, V and V_F, represent the growth velocity and the buoyancy contribution of the particle velocity respectively. It is interesting to note that, in the case of $\Delta\sigma_0 \geq 0$ *i.e.*, nonwetting substrates, there can be three possibilities as represented by Fig. 3.6(a), *i.e.*, engulfment, pushing or flotation. The majority of real inclusions fall into this category. In the case of $\Delta\sigma_0 < 0$, *i.e.*, wetting substrates, only engulfment or flotation are possible. Figs. 3.6(c) and (d) represent a situation where the growth direction is opposite to the buoyancy force. In a normal casting, both situations 3.6(a) and (c) and situations 3.6(b) and (d) may occur depending on the wettability and relative density of the particle and melt. Thus, the same type of particle may exhibit different behaviour within the same casting, depending upon the local direction of solidification. Those particles which are pushed by the interface develop an environment conducive to nucleation of pores as demonstrated later. To make matters more complicated, a given particle may interact with more than one interface, as in a normal casting the interface may approach the particles from different directions.

Table 3.2 Characteristics of Different Inclusions.

Particles	Contact Angle (Deg.)	$\lvert\Delta\rho\rvert$(kg/m^3)	$\Delta\sigma_0$ (N/m)	k_{PL}
SiC[212]	134.2	911	5.397	0.1422
Graphite[212]	151.75	309	$\Delta\sigma_0 > 0$	0.7899
Al_2O_3[43]	160	800	$\Delta\sigma_0 > 0$	0.1461
$TiAl_3$[35]	~0	N. A.	$\Delta\sigma_0 < 0$	N. A.

N. A. :- Not Available

The relevant properties of some typical inclusions in a pure aluminum melt are given in Table 3.2. For many materials, the value for $\Delta\sigma_0$ is not available and this precludes a detailed quantitative analysis of inclusions of these materials. The pushing/engulfment phenomena are specific to a specific particle and melt combination. For example, in the hypoeutectic Al-Si alloy/SiC particle combination where the wettability between the particle and the matrix is poor ($\Delta\sigma_0 > 0$), there exists a critical cooling rate for the particle pushing/engulfment transition.[214] On the other hand, in eutectic and hypereutectic Al-Si alloys, where the wettability is good ($\Delta\sigma_0 < 0$), particles are always engulfed.[214]

3.3.2 Transport Phenomena and Particle Pushing

During pushing of a particle by the S/L interface, a gap (or film) separates the particle from that interface. Fluid must then flow continuously from the region around the particle into this gap, otherwise the solid will grow around the particle and engulf it. Uhlmann *et al.*,[92] assumed a diffusion model of feeding, and had difficulty in rationalizing the apparently large rate of fluid movement into the gap at higher rates of solidification. The ratio of the diffusive flux to that of hydrodynamic flow is of the order of 1 for a gap width of $h = 2 \times 10^{-10}$ m which is approximately equivalent to the interatomic spacing.[209] The greatest critical distance, d_c, occurs at the smallest measured critical velocity, and numerical calculation over a broad range of data shows that the greatest critical separation is of the order of 10^{-8}m.[206] Therefore, a critical separation of $d_c = 1.3 \times 10^{-8}$ m is assumed and thus, mass transport occurs mainly by viscous flow. A simple simulation of the velocity distribution in the gap can be done by assuming parabolic flow between two plates as given in Fig. 3.7. Particles of radius R ($\sim 10^{-6}$ m), greater than the critical distance d_c ($\sim 10^{-8}$ m), are considered here for reasonable validity of the parallel plate analogy.

Then, the liquid velocity $U(z)$, can be expressed as:

$$U(z) = \frac{z(h-z)}{2\eta}\frac{dp}{dr} \tag{3.15}$$

where η is the viscosity and $\frac{dp}{dr}$ is the pressure gradient in the film. This equation is developed such that it conforms to the boundary conditions at the two solid surfaces as:

$$U(z) = 0 \qquad at \qquad z = 0$$

$$U(z) = 0 \qquad at \qquad z = h(r) \tag{3.16}$$

Further, it is assumed that the pressure gradient is uniform along the film width h, which is true for a film which does not change rapidly. Then the flux of the

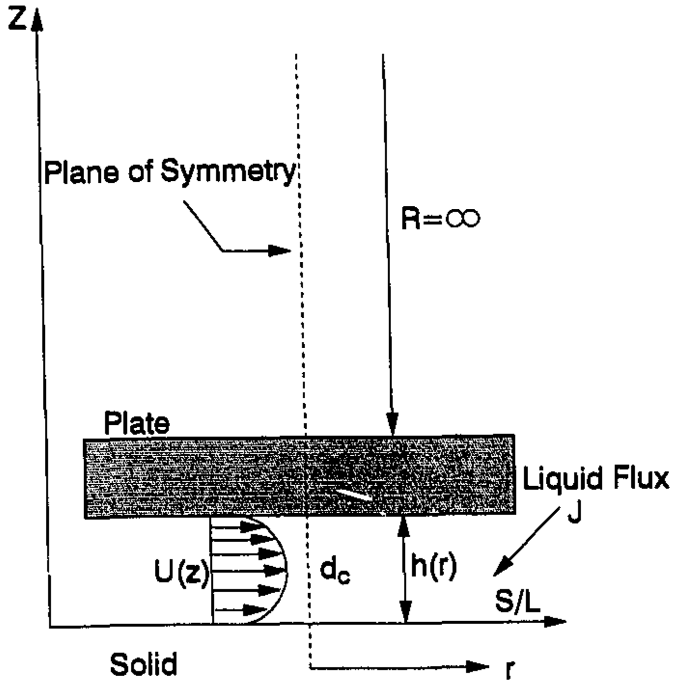

Fig. 3.7 Schematic Velocity Distribution Between Two Parallel Plates.

liquid, J, flowing per unit time into the gap can be written as:

$$J = \int_0^{h(r)} U(z) 2\pi r dz \tag{3.17}$$

Under steady state, the volume of material solidified per unit time is equal to the flux of the liquid coming into the film region and is expressed as:

$$J = \pi r^2 V \tag{3.18}$$

where V is the growth velocity. Equating both of these flux values and rearranging, the expression for the pressure drop can be written as:

$$\frac{dp}{dr} = \frac{6\eta V r}{h(r)^3} \tag{3.19}$$

The above expression (Eqn. [3.19]) was developed for the case of parallel plates; however, the S/L interface as well as the inclusions usually deviate from planarity. If this is the case, the distance between the inclusion and the S/L interface $h(r)$, will not be constant and will be a function of the S/L interface geometry as well as the inclusion shape. Therefore, it is necessary to modify Eqn. [3.19] to take into account the

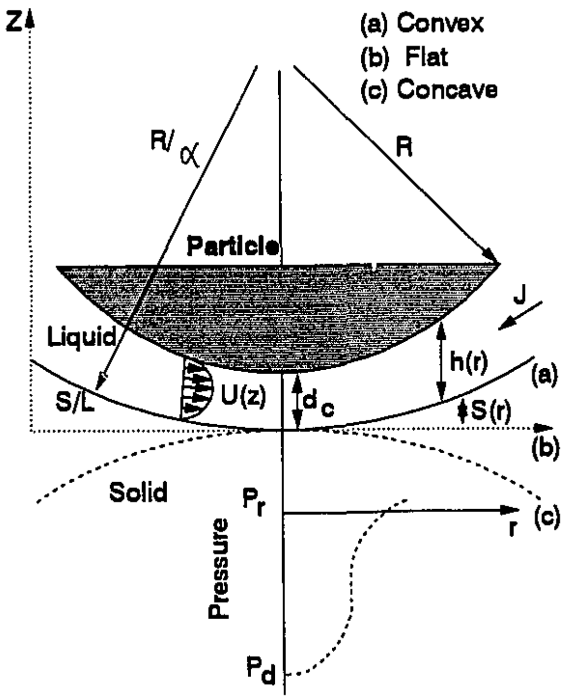

Fig. 3.8 Schematic Nature of the Interface.

curvatures. Considering spherical inclusion particles, h(r) can be expressed as:[208]

$$h = d + R - (R^2 - r^2)^{1/2} + S(r)$$

$$\cong d + \frac{r^2}{2R} + S(r); \qquad r \ll R \tag{3.20}$$

where $S(r)$ is the function which represents the dependence of $h(r)$ on the shape of the interface.

Eqn. [3.19] cannot be integrated without knowing the function $S(r)$; but to obtain an outer bound, it is possible to find a limit for this function that yields a maximum pressure. At the limit, $r = 0$, the close contact region between the interface and the particle, the S/L interface must approximate a sphere, and thus, $S(r)$ has a maximum value when it is in contact with a sphere of radius $R/\bar{\alpha}$, where $\bar{\alpha} = \frac{R}{R_S}$, and $|\bar{\alpha}| \leq 1$. R_S is the radius of curvature of the S/L interface and is a function of concentration and local thermal gradient. Now, the outer bound can be obtained using $S(r) \sim \bar{\alpha}r^2/2R$ and the difference between the reference pressure and the pressure in the film at $r = 0$ (see Fig. 3.8), can be expressed as:

$$\int_{P_d}^{P_r} dp = 6\eta V \int_0^R \frac{r\,dr}{\left[d + \frac{r^2}{2R}(1+\bar{\alpha})\right]^3} \tag{3.21}$$

An analytical solution to Eqn. [3.21] can be developed assuming a constant film width, d_c. This assumption is valid when $\bar{\alpha}$ reaches a value of approximately -1, a condition reached in practice when an inclusion is present in the interdendritic space. In such a case, the pressure drop behind the particle can be expressed as:

$$(P_r - P_d) = \frac{3\eta V R^2}{d_c^3} \tag{3.22}$$

3.3.3 Effect of Thermal Conductivity and Impurity Segregation

Thermal conductivity and impurity segregation affect the interface shape considerably.[44,207,210] Since most of the inclusions of interest are less conductive than the matrix, the case of $k_p < k_l$ is considered here. Here, k_p and k_l are the thermal conductivities of the particle and the liquid respectively. When the solidification front approaches the particle, because of the difference in thermal conductivities, there will be a different rate of heat transfer in the liquid ahead of the interface. However, the rate of heat extraction at the S/L interface is uniform, and as a result the temperature gradient along the symmetry plane of the gap will fall to G_h from G_l; the gradient in the liquid at the unaffected area (see Fig. 3.9). This will lead to the formation of a bump on the interface behind the particle.

Now, the width of film can be written as:[210]

$$d^* = d\frac{k_p}{k_l} \tag{3.23}$$

where d^* is the new width of the film. However, the bump cannot grow continuously, and will begin to push the particle ahead with fresh liquid from the surrounding region flowing into the gap. The temperature gradient there will reach a quasi-steady value because of convective heat transfer as shown in Fig. 3.10. Since the particle creates a diffusion barrier to the solute concentration field ahead of the growing interface, the

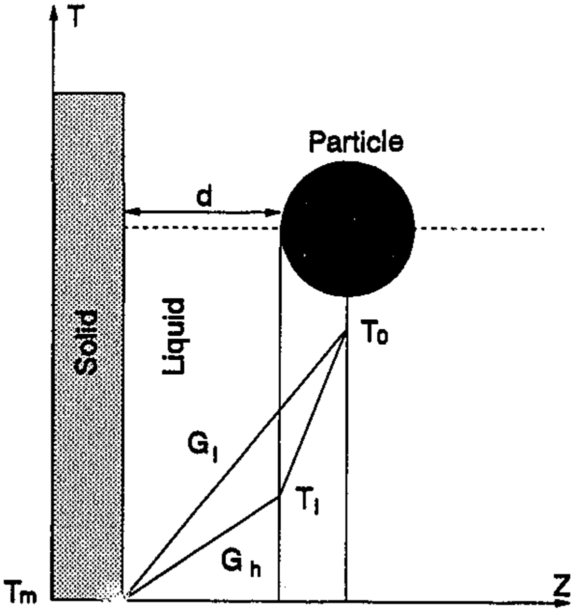

Fig. 3.9 Temperature Profile as Interface Approaches the Inclusion.

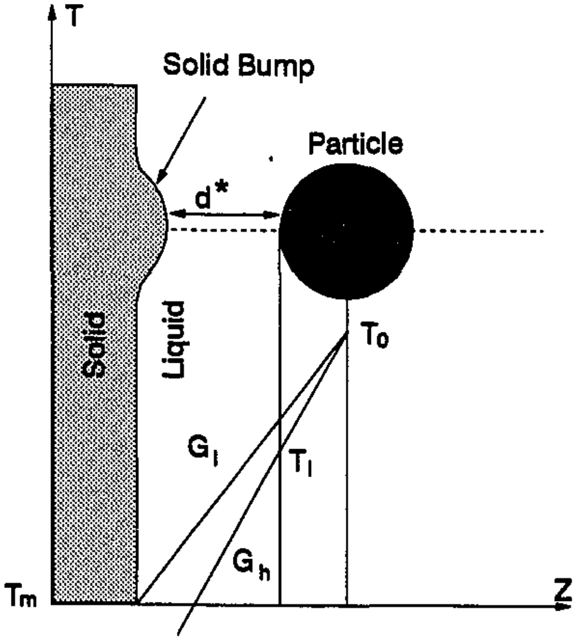

Fig. 3.10 Temperature Profile at Quasi-Steady State ($k_p < k_l$).

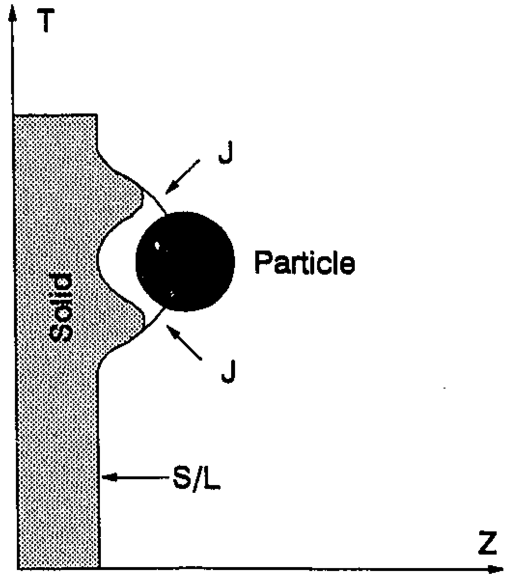

Fig. 3.11 Depression Formed on the Bump Due to Reduction in Concentration Gradient and Impurity Segregation ($k_p < k_l$).

concentration gradient behind the particle will be significantly reduced leading to a decrease in the interface velocity as compared to the interface velocity of the unaffected area. The equilibrium freezing temperature of the alloy behind the particle will also decrease because of impurity segregation and a depression will form on the bump as shown in Fig. 3.11. The viscous pressure drop may also cause pressure melting of the bump.

Since hydrogen is the only gas which is soluble in liquid aluminum, balancing the hydrogen penetrating into the gap, $h(r)$, per unit time, and the portion disappearing as a result of solidification (see Fig. 3.12), the differential equation for hydrogen distribution along the film can be written as:[208]

$$\frac{dC_H}{d\theta} = \frac{(R+h)^2 V sin\theta(\bar{C}_H k_e - C_H)}{2D_H h} \tag{3.24}$$

where k_e is the equilibrium partition coefficient of hydrogen between solid and liquid, C_H is the hydrogen concentration in the film, and $\bar{C}_H$ is the integral mean of the con-

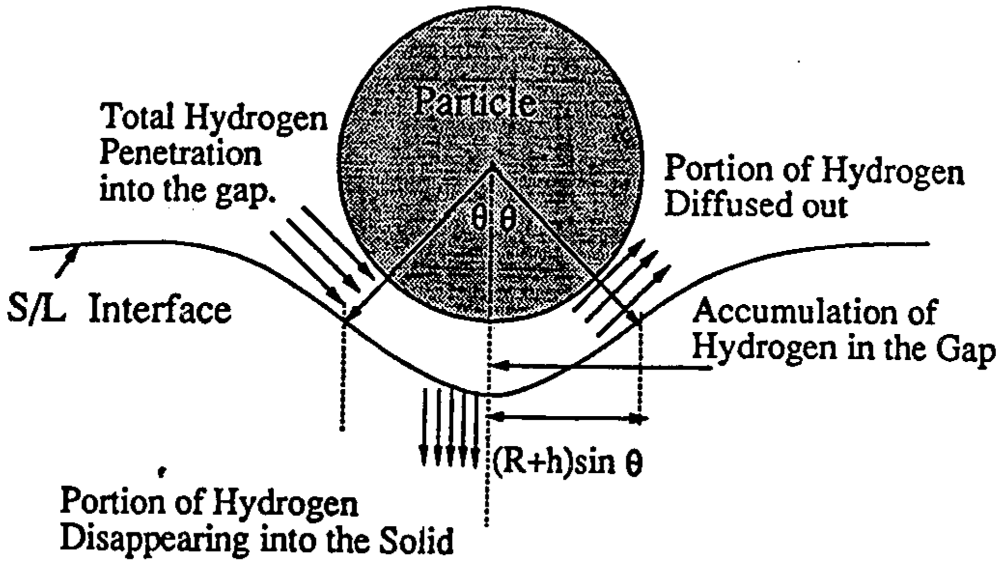

Fig. 3.12 Schematic Hydrogen Balance in the Gap.

centrations over the gap width, which is defined as:

$$\bar{C}_H = \frac{\int_0^\theta h(1+\frac{h}{R}+\frac{h^2}{3R^2})C_H sin\theta d\theta}{\int_0^\theta h(1+\frac{h}{R}+\frac{h^2}{3R^2}) sin\theta d\theta} \tag{3.25}$$

The details of the derivation are given in the appendix. The boundary conditions applicable to this equation are, $\theta = 0^0$, $\frac{dC_H}{d\theta} = 0$ and $\theta = \frac{\pi}{2}$, $C_H = C_{ref}$. Eqn. [3.24], can be solved numerically; however, the approximate analytical solution given below can be obtained assuming a constant film thickness, d_c, and uniform concentration across the film:

$$\frac{C_{ref}}{C_d} = \exp[\frac{(R+d_c)^2 V(k_e-1)}{2D_H d_c}] \tag{3.26}$$

It can be noted that, in Eqn. [3.26], all terms except $(k_e - 1)$ are positive. Therefore, the concentration of gas in the film region will increase exponentially, and the equilibrium gas pressure there can be predicted by Sievert's law [121,169] as described earlier (Section 3.2.2).

3.4 Experimental Study

Experiments using the apparatus described in Chapter 1, have been conducted for several possible types of inclusions introduced into pure aluminum and Al-Si alloy melts.

3.4.1 Selection of Inclusions

As mentioned earlier, a variety of inclusions can be present in aluminum alloys and they come from many different sources. A list of inclusions that are common in aluminium alloys is given in Table-0.1. In the present study, α-Al_2O_3, γ-Al_2O_3, MgO, $MgAl_2O_4$, SiC, SrO, $Sr(OH)_2$ and TiB_2 inclusions were considered. A brief discussion of their nature and their origin in the melt is given below.

The most important category of inclusions in aluminum alloys is oxides. It is nearly impossible to prevent dross formation during the melting of aluminum alloys. The fact that Al_2O_3 forms is not surprising, because the free energy of formation of Al_2O_3 is very low.[215] Furthermore, the specific gravity of Al_2O_3 is not greatly different from that of molten aluminum alloys.[215] The tenacious skin that forms on the top of the melt floats unless it is broken up into small particles, which when formed neither float nor sink, but become suspended in the melt. During mold filling larger dross particles also enter the mold. Several morphological forms of Al_2O_3, *e.g.,* α-Al_2O_3 and γ-Al_2O_3 exist. Other elements in the aluminum may react with oxygen and produce complex oxides with Al_2O_3 as one of the components. This is the case in magnesium containing alloys in which the spinel, $MgAl_2O_4$, may form. Here MgO has a lower free energy of formation than Al_2O_3[216] and the spinel results when they form together.

SiC which is considered as an inclusion here, normally does not occur in aluminum alloys; however, it has an important industrial application since SiC forms one of the major reinforcements in metal-matrix/particulate composites. It also may enter into the melt from the melting crucible which is quite frequently made of SiC.

SrO and $Sr(OH)_2$ inclusions are considered owing to their relevance to the modification practice. Modification is a common method used in the foundry for changing the morphology of the silicon phase in the Al-Si eutectic. When a modifier is added to the alloy in the correct amount, the silicon solidifies with a fine, interconnected fibrous morphology.[217] The fineness and overall roundness of this structure reduce the stress raising capability of the silicon, resulting an alloy having a significant increase in both ductility and impact resistance.

Probably the greatest problem associated with modification of aluminum-silicon casting alloys is the fact that modified castings are often more porous than their unmodified counterparts.[218] Sr is one of the common modifiers used in the casting industry today.[219] While it is fairly well accepted by the industry that porosity is a definite danger associated with modification, the origin of the problem is not well understood, and until the origin is clear and definite the solution will remain evasive. Several reasons have been hypothesized to explain the porosity behaviour of modified castings.[5,9,218,220–223] It has been proposed that when Sr is the modifier, it increases the inclusion content of the melt and pores are nucleated at these inclusions.[5,9] An electron mocroprobe study[9] on inclusions in Sr modified castings has indicated the presence of Sr and oxygen; however, the exact nature of these Sr containing inclusions is not yet known. Therefore, SrO and $Sr(OH)_2$ particles were considered in this thesis work to verify their effect.

As is demonstrated in Chapter 2, TiB_2 particles which enter into the melt via grain refiner master alloys do not nucleate α-Al alone. Further, the morphology of these particles and the melt chemistry play a significant role in deciding whether or not they take part in 'duplex' nucleation. Poisoning of the crystal in the presence of Zr may also spoil their nucleation potential. This implies that diborides can become undesirable inclusions if the chemistry of the melt is not properly controlled during grain refinement. Such diborides will be rejected by the solid/liquid interface and may act as nucleants for pores in the later stages of solidification.

3.4.2 Procedure

The controlled addition technique by fluidized nozzle injection is described in Chapter 1. Under normal melting conditions inclusion levels of as high as 35/500 mm^2 are found.[9] In the present study, the inclusion levels were maintained in the range of 0.3-1.0 area percent, a value higher than the normal level. The most important reason for this was to enhance the chance of encountering inclusions in the metallographic samples. An inclusion level higher than 1.0 percent is undesirable or it will tend to form clusters.

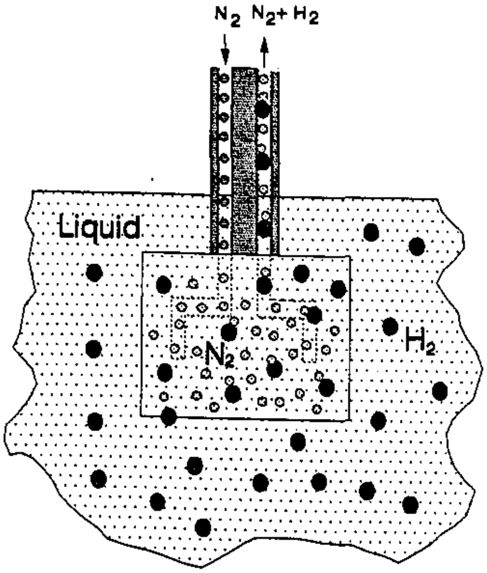

Fig. 3.13 Schematic of AlSCAN Probe.

Much higher densities will result in inclusions associated with pores even if they are not nucleated on them.

After injection of the inclusions, the melt was cast into ingots and then remelted for controlled experiments. This was done to avoid the retention of any pre-existing gas bubbles in the melt. After remelting a low agitation was also maintained to keep the particles suspended in the melt.

An AlSCAN^{TM} hydrogen analyser was used for on-line hydrogen measurement. This instrument operates on the principle of monitoring the hydrogen activity developed in a small quantity of nitrogen continuously recirculated through the molten metal under test until the gaseous hydrogen which diffuses into the nitrogen is in equilibrium with the solute hydrogen in the molten metal. A schematic of the AlSCAN probe is given in Fig. 3.13. The hydrogen content (cc/100g) is obtained by measuring the thermal conductivity of the gas mixture with a katharometer. In the present study three measurements were taken consecutively for a duration of 10 minutes to obtain a reliable measure of the dissolved gas concentration.

Hydrogen measurement in experiments with low hydrogen contents, *i.e.*, after degassing, was done by the LECO^{TM} sub-fusion method. A small quantity of the melt was solidified in a specially designed chill mold known as the Ransley mold to trap almost all hydrogen present in the liquid. A cylindrical sample of 10 mm diameter by 40 mm length was prepared from this casting. Special care was taken to avoid contamination during preparation of the sample. The method of hydrogen determination comprises the collection and measurement of hydrogen desorbed into an evacuated system from the specially prepared and heated solid sample. The sample is heated to a temperature below the eutectic or solidus but high enough to allow virtually all of the hydrogen to diffuse out of the sample during the extraction time which varies from 1-2.5 hrs depending on the heating temeperature. Gas levels ranging from $\sim$ 0.10 to 0.30 cc/100 g were considered in the present study.

The melt was cast into a preheated step mould as shown in Fig. 2.5. As described in Chapter 2, the mold preheat temperature was varied from room temperature to 450^{0}C to study the effect of cooling rate on the behaviour of the inclusions. Both hypoeutectic (Al-7%Si and A356) as well as hypereutectic (Al-15%Si) alloys were studied. Similarly, melts were prepared without any inclusion addition and filtered by 15 ppi ceramic filters before casting. The procedure for metallography has already been presented in Chapter 1 and porosity measurement was done by a LECO Image Analyser as discussed in Chapter 1. The experimental values presented in the following section (Sec. 3.5) are semi-quantitative in nature and their reliability falls within the framework of discussion presented in Chapter 1.

3.4.3 Directional Solidification

The mode of heat extraction affects porosity behaviour significantly. It is well known that shrinkage can be eliminated by the application of the principles of directional solidification. Similarly, with directional solidification gas can escape to the top of the melt, thereby reducing the occurence of gas porosity. Thus, directional solidification is an ideal way to minimize the possibility of pore nucleation.

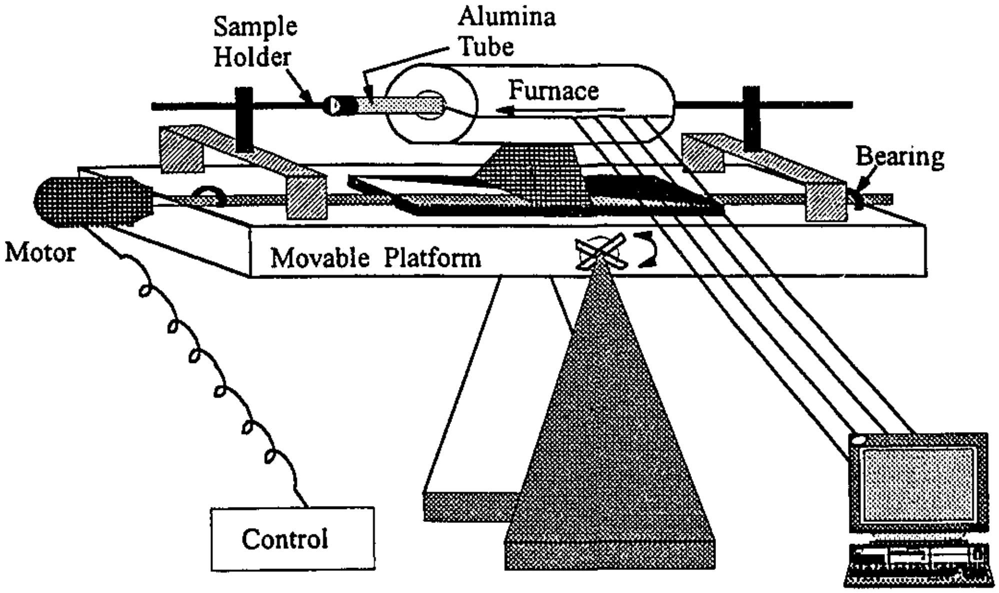

Fig. 3.14 Directional Solidification Unit with Adjustable Platform.

To verify the pore nucleating capability of the inclusions under this situation, an apparatus was fabricated as shown in Fig. 3.14. This was a Bridgman type of unit with stationary sample and movable furnace arrangement. Particle pushing behaviour is significantly influenced by gravity, and to change the direction of gravity with respect to the S/L interface the platform holding the sample and furnace track was mounted on an adjustable stand. Cylindrical samples with dimensions of 10 × 150 mm were machined from ingots containing inoculants and placed in alumina tubes. Both ends of the tube were supported by stainless steel cups as shown in Fig. 3.14. The variable speed of the motor allowed different solidification rates. Four thermocouples controlled by a digital controller determined the temperature gradient in the funace. The temperature fluctuations were within $\pm 1^0$ C. After solidification the rod was cut into two halves along the plane parallel to the direction of gravity. Three samples were studied, two from the ends after discarding 30 mm and one from the centre as shown by the cross-hatched areas in Fig. 3.15.

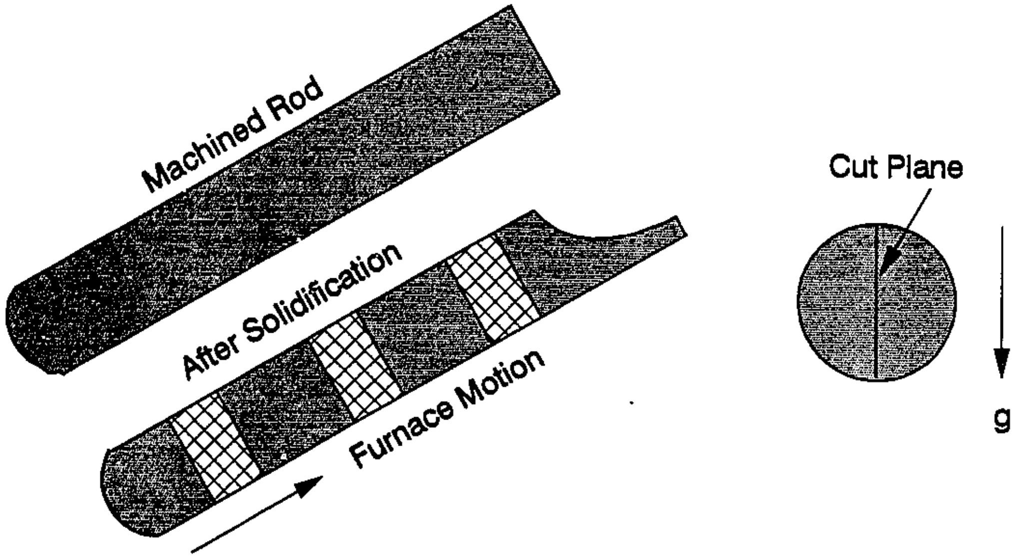

Fig. 3.15 Schematic of Sampling Procedure.

3.5 Results and Discussion

As mentioned earlier, data for the prediction of particle behaviour from the model equations developed in the previous sections, particularly for metallic systems of interest, are not readily available. However, with the aim of carrying out an order of magnitude analysis, the data given in Table 3.3 have been approximated from various sources.

For the prediction of pressure drop behind the particle, one must know the critical velocity, V_c, and the critical separation, d_c, between the particle and the interface. The models developed to date for the determination of critical velocity involve numerous assumptions and differ significantly from the experimental findings. Therefore, it would be appropriate to use the experimental range of critical velocity, rather than attempting to predict it from the models. Only limited data is available, and in the present study the experimental value reported in Reference [44] for SiC particles is used.

The absolute value of pressure drop will depend on the existing pressure in the liquid *i.e.*, the balance of the metallostatic pressure and the shrinkage pressure drop. The procedure for determination of shrinkage pressure is described earlier (Section 3.2.2). The shrinkage pressure variation at different solidification stages (solid fractions) is presented

Table 3.3 Data Used for Pressure and Impurity Segregation Calculation.

Symbols	Values	Reference
d_c	$1.3*10^{-8}$ (m)	[206]
V_c	100 (μ m)	[44]
η	0.002 (Pa.s)	[210]
D_H	$2.0*10^{-2}$ (cm^2/s)	[5]
T	893 (K)	
k_e	0.03	[5]
σ_{LV}	0.840 (N/m)	[210]
C_p	$1.0x10^5$ (N/m^2.atm.)	[119]
f_H	1.78	[121
S	0.40 (cc/100g.$atm^{1/2}$)	"
β	0.058	"
$8.\pi.\tau^3$	2700	"
γ	$1.15x10^{-04}$ ($m.^0C^{1/2}s^{-1/2}$)	"
ΔT	60 (^0C)	"
G	400 ($^0C/m$)	
$1 - f_s^c$	0.7	

in Fig. 3.16. The calculated viscous pressure drop behind the particle at different particle radii is presented in Fig. 3.17. It can be seen that the shrinkage pressure drop (Fig. 3.16) is almost negligible in comparison to the viscous pressure drop in the film.

The segregation behaviour of gas in the film region is shown in Fig. 3.18. The ratio of gas concentration in the bulk liquid to the gas concentration in the film region decreases exponentially as the particle size increases. The equilibrium gas pressure in the bulk interdendritic liquid and in the film region is plotted in Fig. 3.19, from which the importance of the particle in causing gas concentration is evident.

It is generally believed that pores are heterogeneously nucleated at non-wettable foreign substrates[4–11] and/or at the growing S/L interface.[150,161,175,176,179] Campbell[2,3] demonstrated that the classical nucleation theory simply cannot fulfill the fracture pressure requirement by taking into consideration the shrinkage pressure drop, the gas pressure and the presence of the most efficient foreign substrate in the bulk liquid. This anomaly has tempted researchers to develop some alternative nucleation mechanisms such as radiation damage by high energy particles.[2,3]

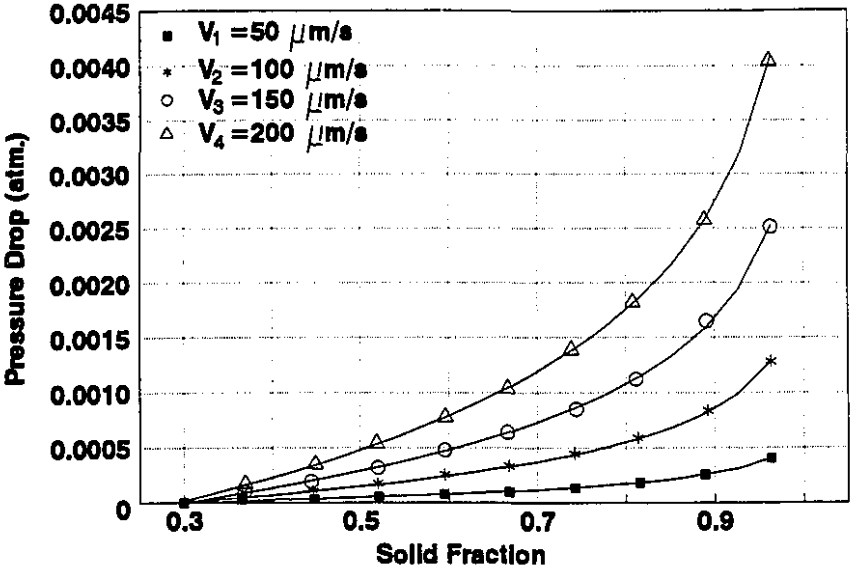

Fig. 3.16 Shrinkage Pressure Drop at Different Solid Fractions.

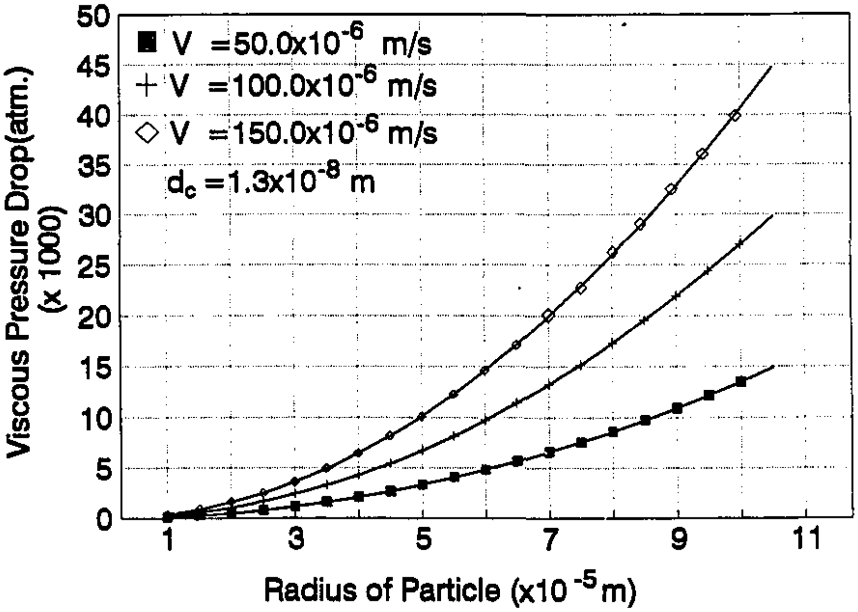

Fig. 3.17 Viscous Pressure Drop in the Film Region vs Particle Size.

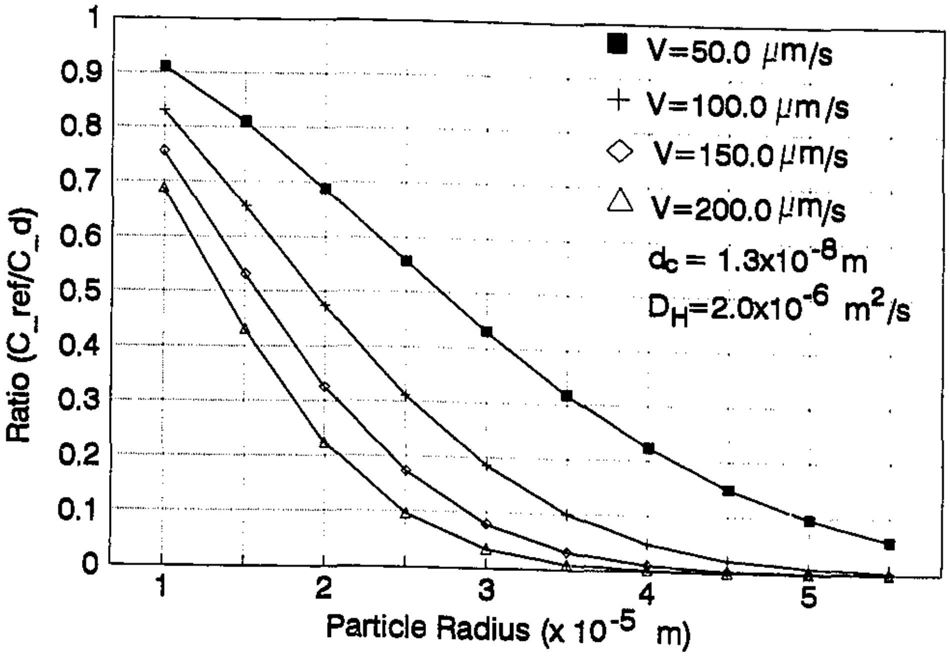

Fig. 3.18 Impurity Segregation Ratio in the Film at Different Particle Radii.

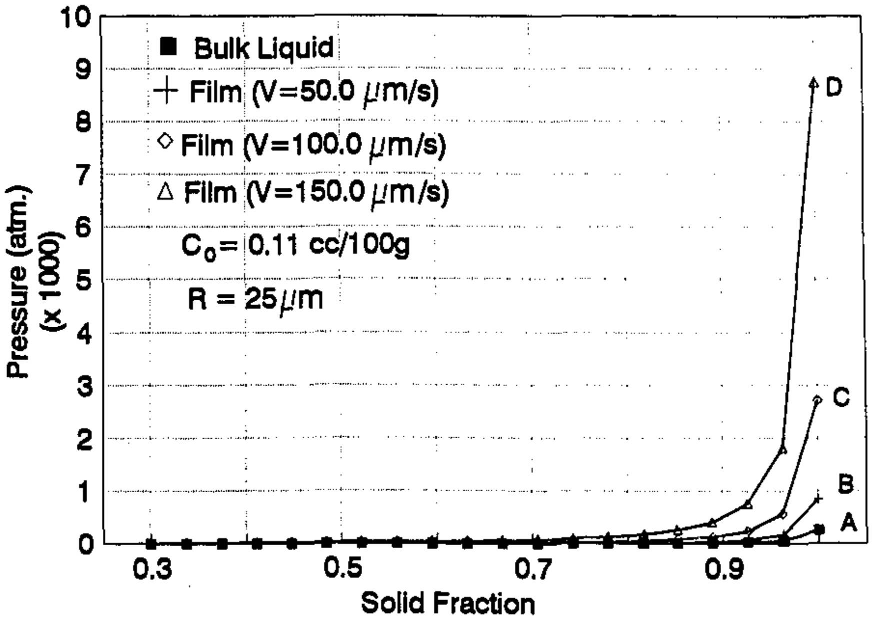

Fig. 3.19 Equilibrium Gas Pressure at Different Solid Fractions.

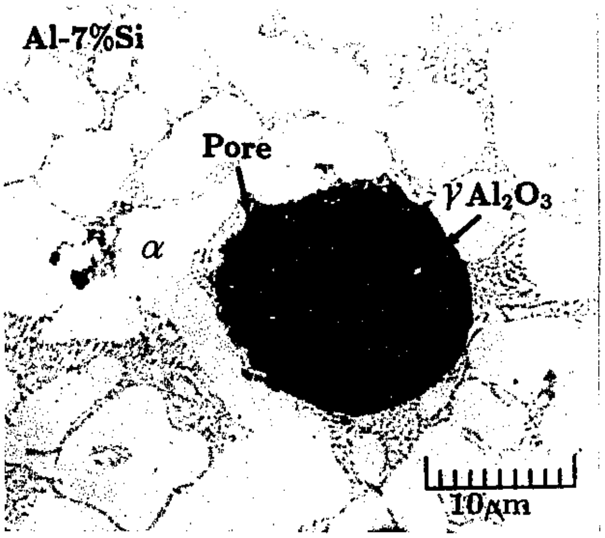

Fig. 3.20 Nucleation of Pores in the Film Region Between the S/L Interface and γ-Al_2O_3 Inclusion.

By considering the pressure drop and gas accumulation occuring in the thin liquid film separating an inclusion from the S/L interface, it is not necessary to resort to such alternative mechanisms to explain pore nucleation in solidifying liquid metals. From Fig. 3.17, it is evident that the viscous pressure drop in the film region can easily reach values of the order of 10^4 atm. In reality this pressure drop will however be limited by the creep resistence of the material, which is order of 10^3 atm.[164,165] In addition, according to Eqn. [3.26], there is an exponential increase in the gas content in the film, and the equilibrium gas pressure behind the particle can also be of the order of 10^3 atm. These two factors act cooperatively to overcome the fracture pressure requirement, and nucleation of a tiny gas bubble is feasible, the experimental evidence of which is shown in Fig. 3.20 and Fig. 3.21. Fig. 3.22, shows the effect of the presence of alumina inclusions in both hypoeutectic and hypereutectic Al-Si alloy. It is evident (see Fig. 3.22(a)) that the presence of alumina inclusions in A356 alloy significantly increases the porosity area fraction over the filtered base alloy solidified under similar conditions. On the other hand, it is interesting to note that in the case of hypereutectic Al-Si(15%) alloy the presence of alumina inclusions has no significant impact on the pore volume fraction (Fig. 3.22(b)). The same kind of inclusions exhibit a very different behaviour as the silicon content of the melt is increased.

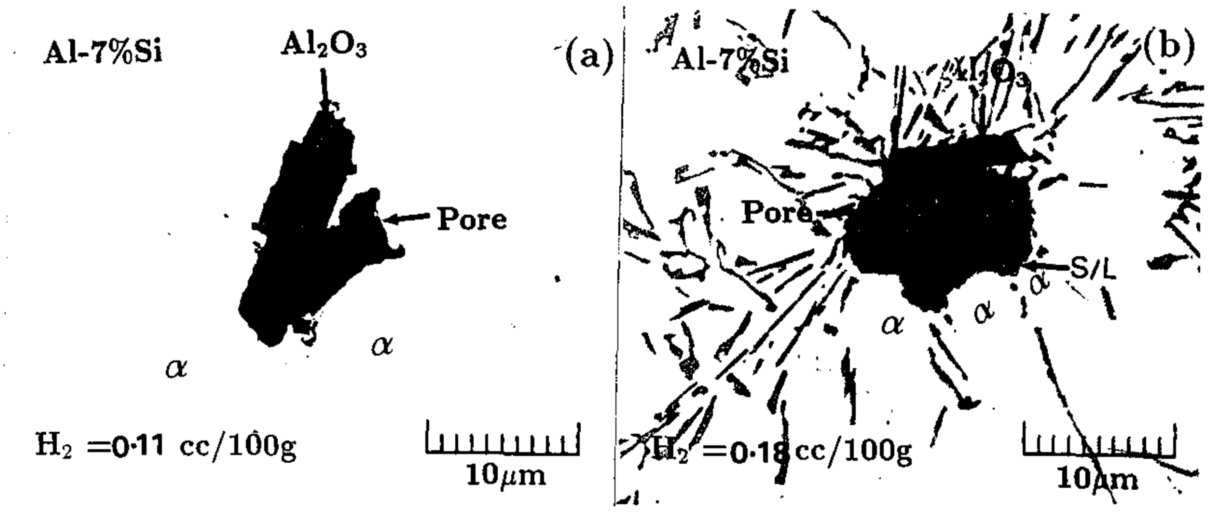

Fig. 3.21 Nucleation of Pores in the Film Region Between the S/L Interface and the Inclusion; (a) H_2= 0.11 cc/100g and (b) H_2= 0.18 cc/100g.

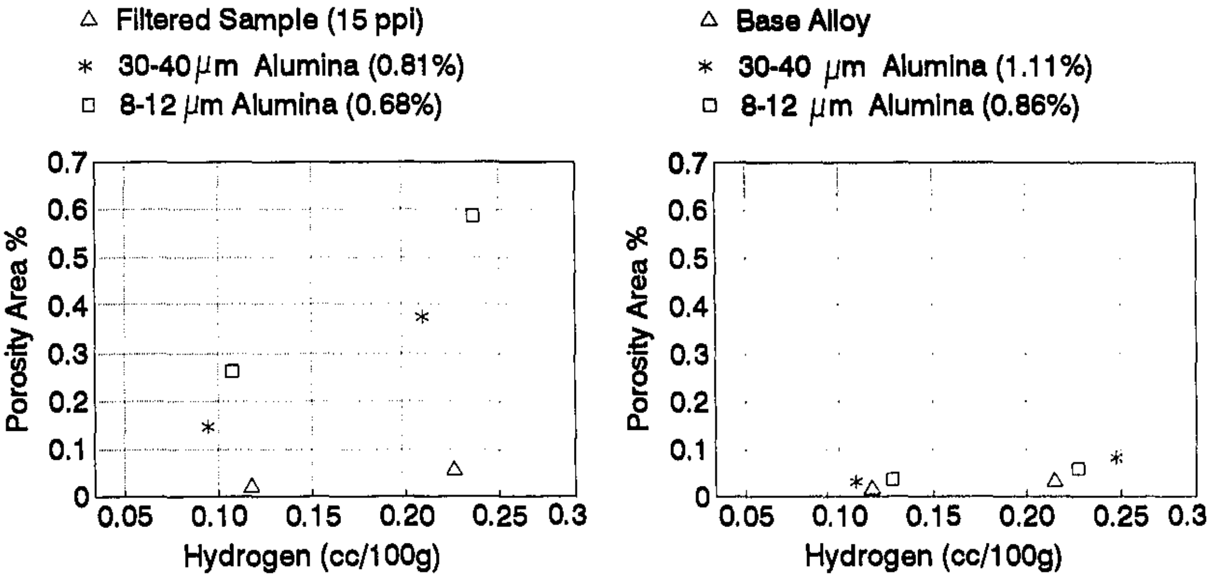

(a) (b)

Fig. 3.22 Porosity Area % at Different Gas Content in Castings With and Without Inclusions; (a) A356 and (b) Al-Si(15%) (Cooling Rate ~ 1 °C/s).

Though Fisher's[151] model of heterogeneous nucleation based on the contact angle (Eqn. [3.11]), can explain nucleation at heterogeneous sites due to lowering of the activation energy, it does not explain the different behaviour of the same kind of particles in the same system of alloys. It is well known that the surface energy of liquid aluminum is a function of silicon content *i.e.,* surface tension decreases as silicon content is increased (0.825 N/m for pure Al and 0.79 N/m for Al-7%Si alloy).[224,225] This decrease is not sufficient to completely alter the behaviour of the inclusions. It is evident from these experiments that the solidification characteristics and the related interaction of the S/L interface with inclusions significantly determine the pore nucleating capability of the inclusions. Considering the nucleation mechanism at the S/L interface proposed by Chalmers[150] and others[161,175,176,179], it can be infered that the contact angle of a solid with the liquid from which it is growing is close to zero degrees. Therefore, a fracture at the interface would necessarily require a pressure drop of a similar order of magnitude to that which is required in the bulk liquid. Contrary, therefore, to many published opinions, the interface is not a favoured site. Yet, paradoxically, pores will in any case nucleate there because of the other favourable conditions which prevail adjacent to the S/L interface. These include inclusions which are pushed by the S/L interface and become concentrated there, the enhanced gas segregation and viscous pressure drop resulting from the interaction of these inclusions with the S/L interface, and the low surface tension of the segregated liquid in the film region. Therefore, the accepted view of nucleation at the S/L interface is correct, but for reasons which are different from those normally proposed.

The number of pores in an inclusion containing alloy is much higher than the number of pores in alloys without any additions as shown in Fig. 3.23. However, though few in number, the sizes of pores in the latter case was much larger than in the former as seen in Fig. 3.23. When inclusions are present, due to the availability of many nucleation sites, the number of pores far exceeds the number of pores in alloys without any additions. In the former case, nucleation occurs at a lower threshold value of gas and shrinkage and the resultant pores are smaller in size. In alloys without any additions, there may be only a few sites available, and thus the gas accumulation and shrinkage

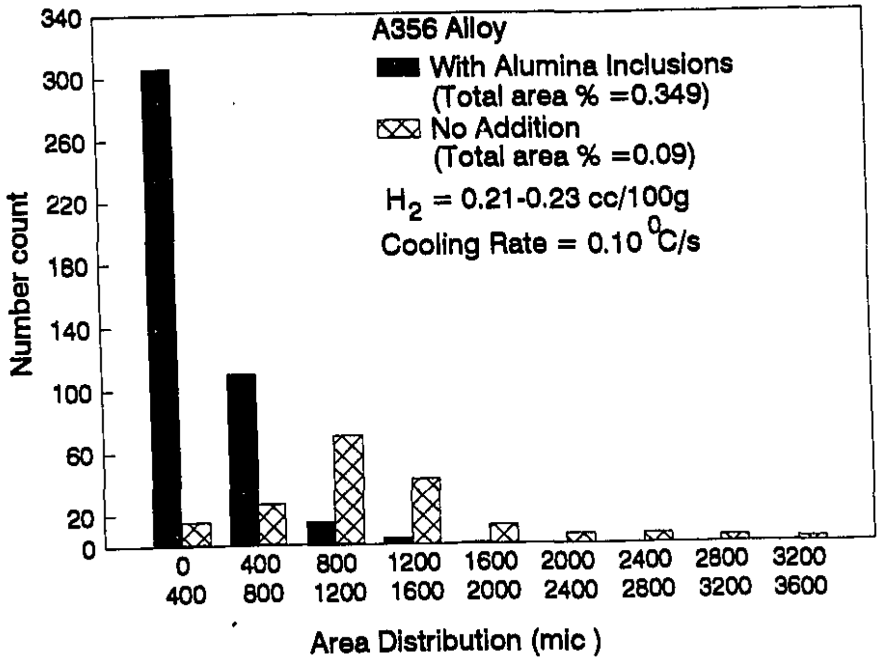

Fig. 3.23 Pore Number Count vs Area Distribution With and Without Inclusions in A356 Alloy (Cooling Rate ~ 0.1 ^{0}C/s).

pressure will build to a very high value, and the moment nucleation occurs, the pores expand rapidly to a large size.

Consideration must also be given to the stability criterion of a tiny bubble in the gap between the particle and the interface. The stability condition for the existence of an embryonic bubble in the bulk liquid dictates the following:

$$P_g - P_e = \sigma(\frac{1}{r_1} + \frac{1}{r_2}) \tag{3.27}$$

where P_g is the gas pressure, P_e is the pressure in the liquid, σ is the surface tension of the liquid, and r_1, r_2 are the principal radii of curvature of the bubble. However, since in the film an elongated shape would be favourable *i.e.*, $r_1 << r_2$ and $r_1 = \frac{d_c}{2}$, the condition can be written as:

$$P_g - P_e = \frac{2\sigma}{d_c} \tag{3.28}$$

From Fig. 3.19, it is evident that the gas pressure, P_g, in the film region (B and C) is much higher than in the bulk liquid (A). Again, it can be noted that

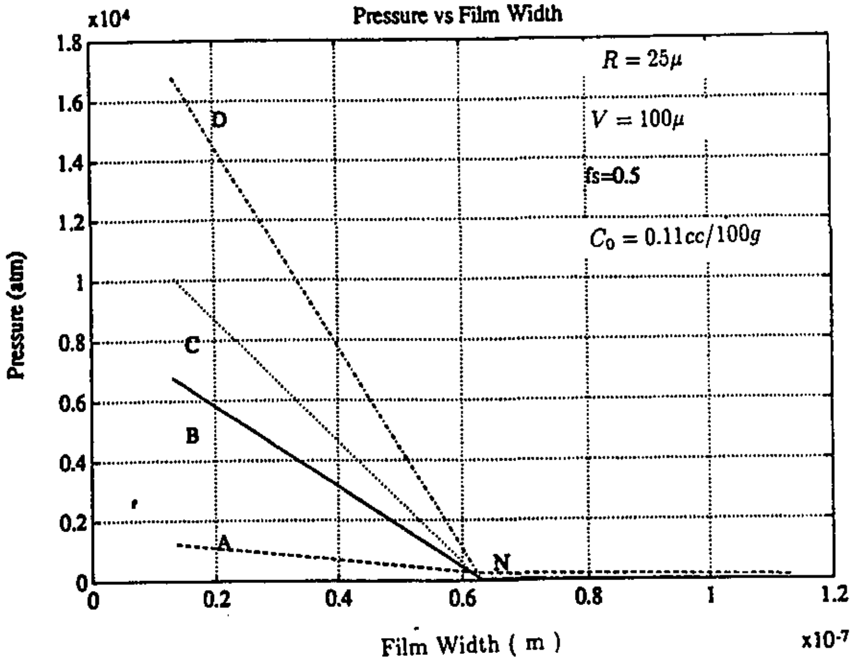

Fig. 3.24 Variation of Pressure Drop and Surface Tension Pressure With Film Width; A = Surface Tension Pressure, B = Gas Pressure, C = Viscous Pressure and D = Total Pressure (P_g-P_e).

P_e is a function of $\frac{1}{d_c^3}$, and the right hand term of Eqn. [3.28] *i.e.*, the surface tension pressure, is a function of $\frac{1}{d_c}$. When d_c is a very small number, the existence of such a bubble will certainly be favourable in the film region compared to the surrounding liquid. There will be a threshold size of the bubble, above which the existence will not be energetically favourable inside the gap. The relative magnitude of the different pressures is shown in Fig. 3.24. It is clear that at film widths smaller than N, the gas pressure and viscous pressure drop can overcome the surface tension force, and creation of an embryonic bubble is feasible in the film region. The value d_c, at point N, is the threshold value of the bubble radius above which it will tend to escape from region B provided the interaction phenomena are not affected significantly below this threshold value.

In reality, once the bubble starts growing in the gap, the kinetics of the interaction process will change, and the buoyancy contribution of the particle/bubble couple will begin to dominate. Again, the change in the separation and the presence of

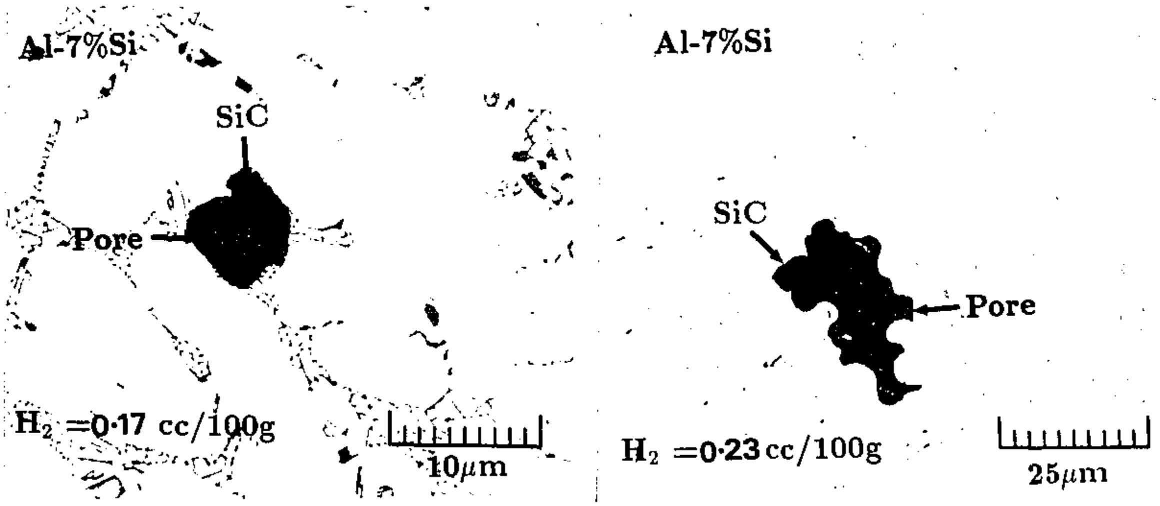

Fig. 3.25 Location of Large Pores With Respect to the Interface and the Inclusions.

a bubble will reduce the pressure gradient, which will reduce the drag on the particle. These changes will be additive to the repulsive force, and the particle will be further pushed ahead of the interface (Fig. 3.21(b)). Depending upon the local solidification time and gas availability, the bubble may be detached from the particle and become trapped in the interdendritic area, or it may be trapped together with the particle. The process starting from nucleation to entrapment together with the inclusion, can be viewed from Fig. 3.21 and Fig. 3.25. In Fig. 3.25(a) & (b), it is difficult to visualize the exact location of the nucleation site with respect to the S/L interface and the particle as in the case of Fig. 3.21. When the bubble nucleates in the film region, it too will interact with the interface and will be pushed into the interdendritic region by the primary dendrites. As a result porosity is rarely observed in the primary phase, but it may occasionally happen that tiny pores are engulfed into the primary phase. Evidence of this has been reported in Reference [7], where in a cast Al_2O_3/metal matrix composite, primary α-phase occasionally exhibited small pores.

It is also interesting to consider a heterogeneous mechanism that requires embryo bubbles to be retained in the pockets of the inclusions. Alumina skimmed from the melt surface contains cracks and pores with the latter varying from about 5 to 40 μ in radius.[4] Embryo in these structural features may grow and release gas bubbles in a

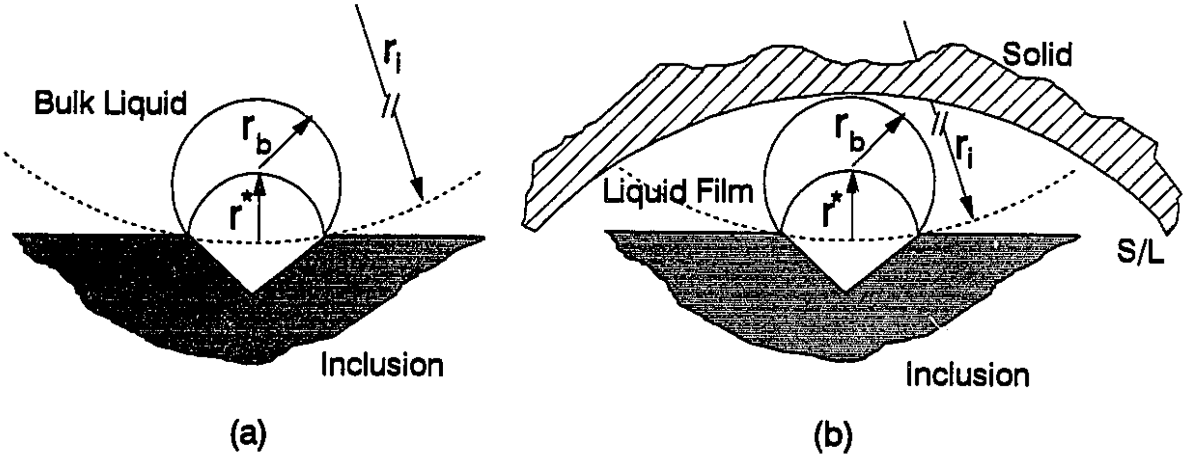

Fig. 3.26 Growth of an Embryonic Bubble from the Crevice; (a) Bulk Liquid and (b) Film Liquid.

manner similar to the formation of CO_2 gas bubbles in the crevices of the furnace linings during steelmaking.

Here, r_i (see Fig. 3.26(a)) is the initial radius of curvature of the entrained embryo. This embryo may grow as a result of reduction in the external pressure and ingress of rejected gas. For the embryo to mature into a bubble which will grow spontaneously and eventually be released as a gas bubble of radius r_b, r_i must change to the critical radius r^*. Now, at the critical size the condition of Eqn. [3.27], must be satisfied.

The variation of critical pressure drop with critical crevice radius is shown in Fig. 3.27. It can be seen that a pressure drop of the order of 2-5 atm. is required for the growth of these bubbles. In directional solidification this pressure drop cannot be attained by simple shrinkage (see Fig. 3.16), but when the crevice is in the gap between the inclusion and the S/L interface as shown in Fig. 3.26(b), growth of bubbles from it will be much easier. Thus, one crevice can release many bubbles before it becomes exhausted

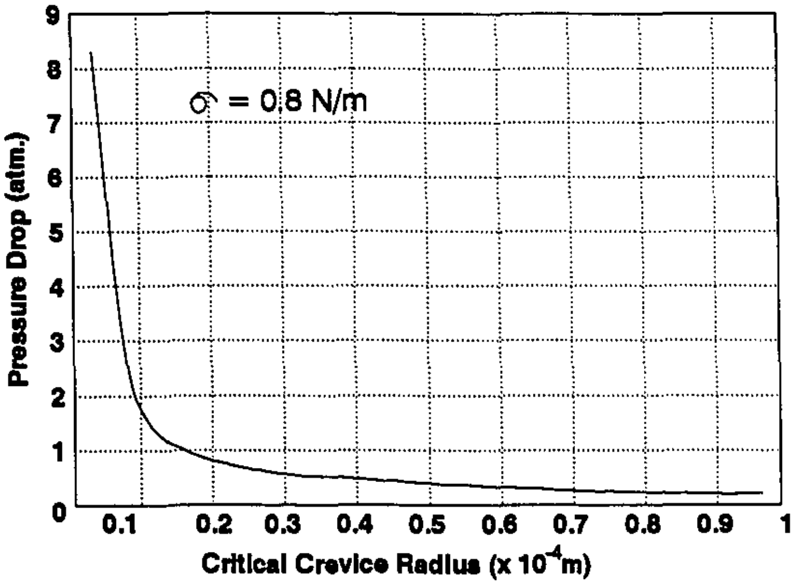

Fig. 3.27 Variation of Critical Pressure Drop with Critical Embryo Radius.

at the end of the local solidification time. This behaviour is evident in Fig. 3.28. Fig. 3.29 presents the porosity content of A356 alloy with different inclusions. While Al_2O_3, SiC and Spinel show similar behaviour, the porosity content is significantly enhanced with the presence of MgO inclusions. This is due to the presence of inherent structural defects as shown in Fig. 3.28(b).

The distribution and the volume fraction of the inclusions affect porosity behaviour significantly. Normally in casting alloys, the inclusion level is much less than a quarter of a volume percent and they are distributed quite randomly. In the case of addition levels of 0.5 vol. % or less (see the schematic Fig. 3.30), nearly all pores are associated with particles at moderately high gas content (~ 0.20 cc/100g) and only a small fraction of pores did not contain a related inclusion. The pore size as expected was larger in the case of a high gas level (see Fig. 3.25). At lower gas levels (~ 0.10 cc/100 g), however, all the pores were associated with particles, but some particles were not associated with pores.

The porosity content in any casting cannot increase infinitely in the pres-

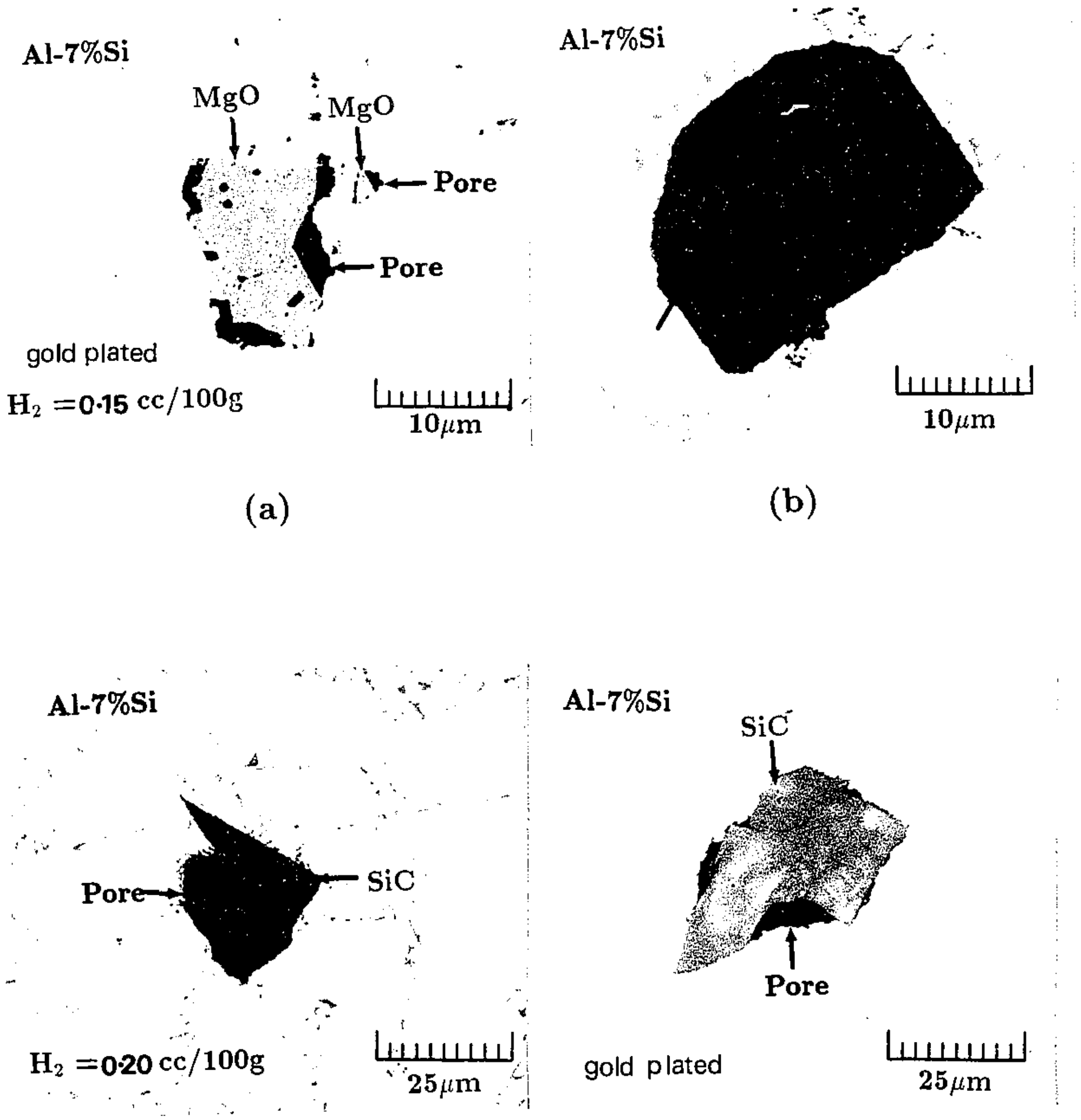

(a) (b)

(c) (d)

Fig. 3.28 Pores Nucleated at the Crevice Present in the Inclusions; (a) MgO, (b) Structural Defects in MgO and (c)&(d) SiC.

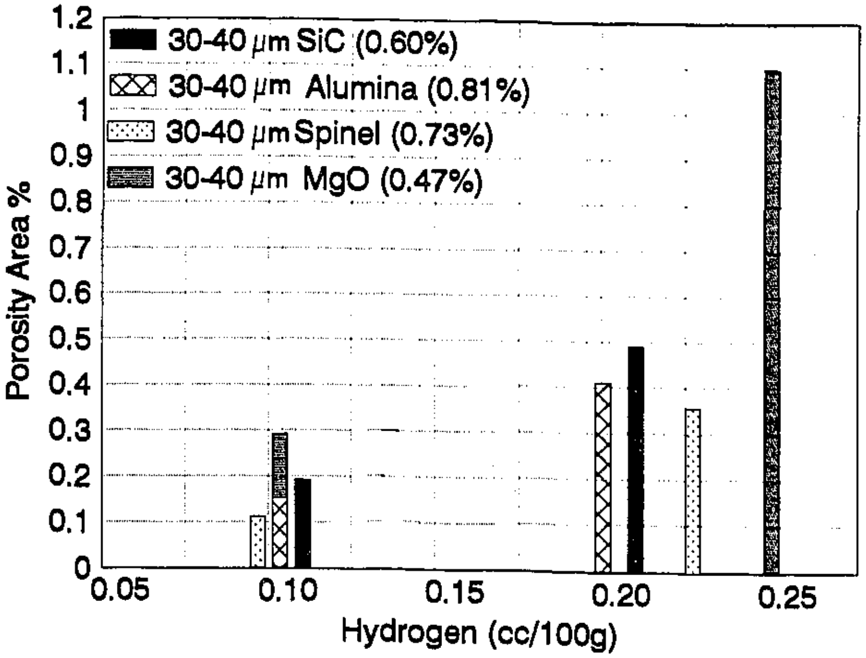

Fig. 3.29 Porosity Area % at Different Gas Content in Castings with Different Inclusions in A356 Alloy (Cooling Rate ~ 0.1 ^{0}C/s).

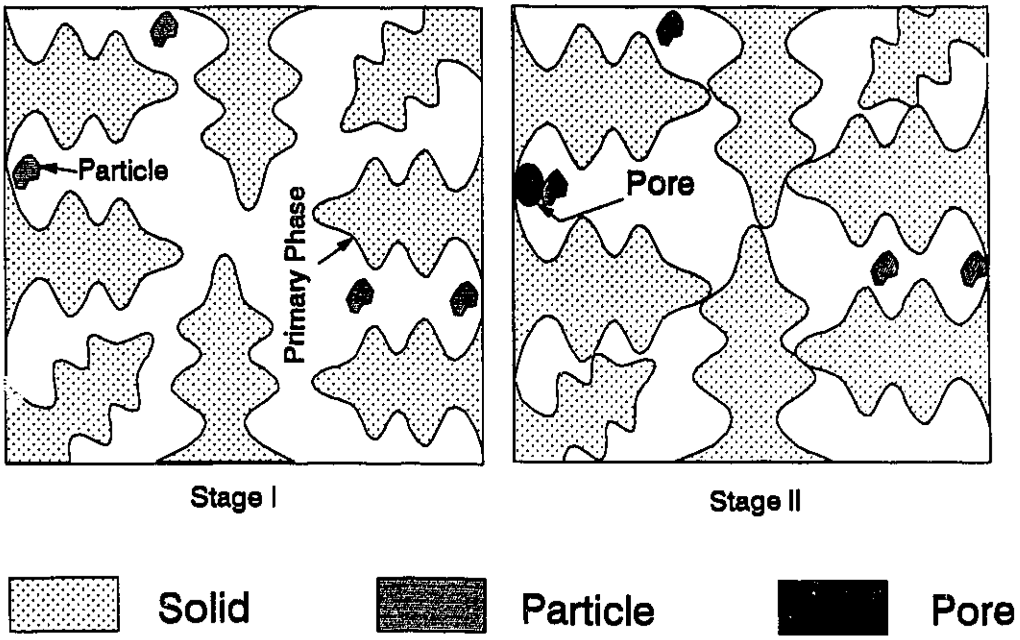

Fig. 3.30 Schematic Nature of Distribution of Inclusions at Low Volume Fraction.

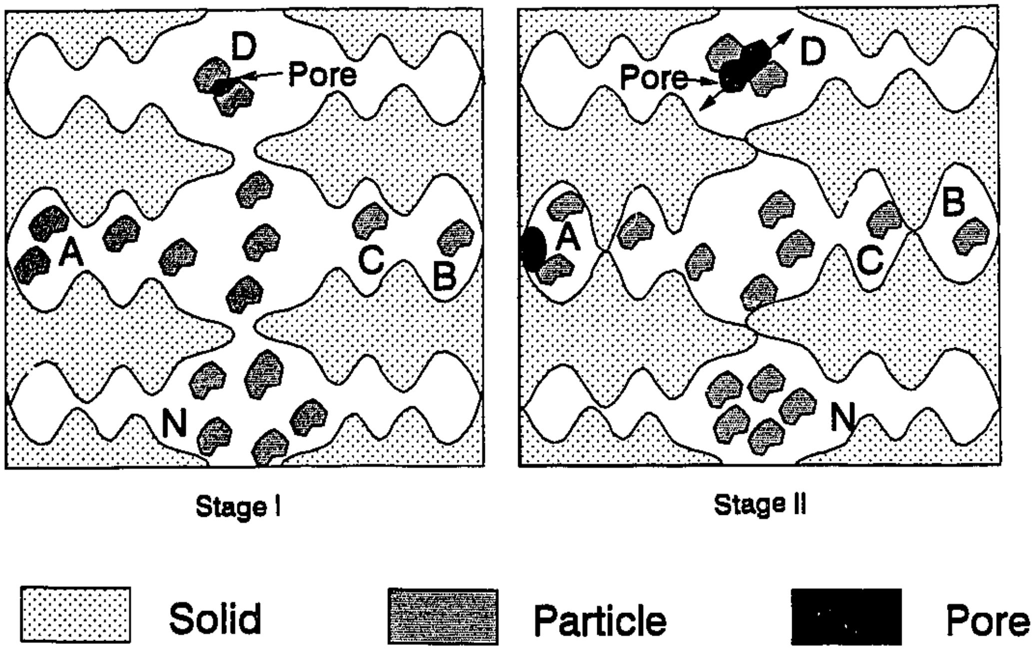

Fig. 3.31 Schematic Distribution of Inclusions at High Volume Fraction and Non-uniform Mixing.

ence of suitable nuclei. This value is limited by the availability of gas and associated shrinkage. In the absence of any suitable nuclei, pore evolution may be suppressed due to the nucleation difficulty. When inclusions are present, pores nucleate easily at a low threshold value of gas and shrinkage. The nucleation of one pore immediately adjacent to another is quite unlikely, since the gas content of the liquid must diminish rapidly in the neighbourhood of a growing cavity, and also the hydrostatic tension acting to induce nucleation will tend to develop a single nucleus in any one body of liquid. Once one pore is nucleated at one site, the presence of another site in the vicinity may become redundant and therefore, it is is not always possible to obtain a one-to-one association of pores particles when particles are distributed as schematically shown in Fig. 3.31. Nucleation may, however, occur at many localities in the same body of liquid due to an increase in gas concentration as shown in Fig. 3.32.

Cluster formation affects the porosity behaviour drastically. Clusters may arise in two ways. During the addition process clusters may form, or since the particles are pushed by the S/L interface they will tend to segregate in the last interdendritic

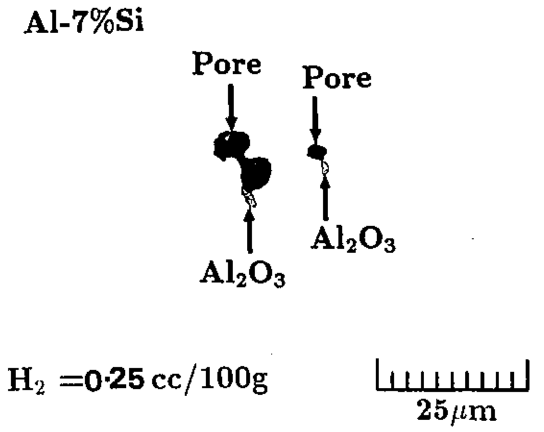

Fig. 3.32 Nucleation of Two Bubbles in the Same Locality.

liquid. All clusters were associated with pores. When two or more inclusions remain close to each other in an interdendritic space their interactions with the S/L interface will be very complex, and they will create severe localized feeding difficulties as described earlier in the case of a single particle. In addition the liquid film between the particles will experience additional feeding difficulties. Since the particles are non-wettable, there will be capillary rejection of liquid out of the channel as shown in Fig. 3.33. All of these factors will facilitate nucleation and depending upon the gas availability and local solidification time these pores may expand to a significant size. This situation is shown in Fig. 3.34.

3.5.1 Inclusion Behaviour at Dendritic S/L Interface

The foregoing theoretical analyses on the role of inclusions at the S/L interface, were carried out assuming a unidirectional plane front solidification or a planar interface having small perturbations. Of course, in real metal solidification the interface morphology is never so simple. Nevertheless, an intuitive analysis can be developed for the case of unidirectional dendritic solidification. Since most of the inclusions of interest are less thermally conductive than the matrix, once the dendrite approaches an inclusion a bump will form on it, as discussed earlier. This perturbation pushes the particle ahead

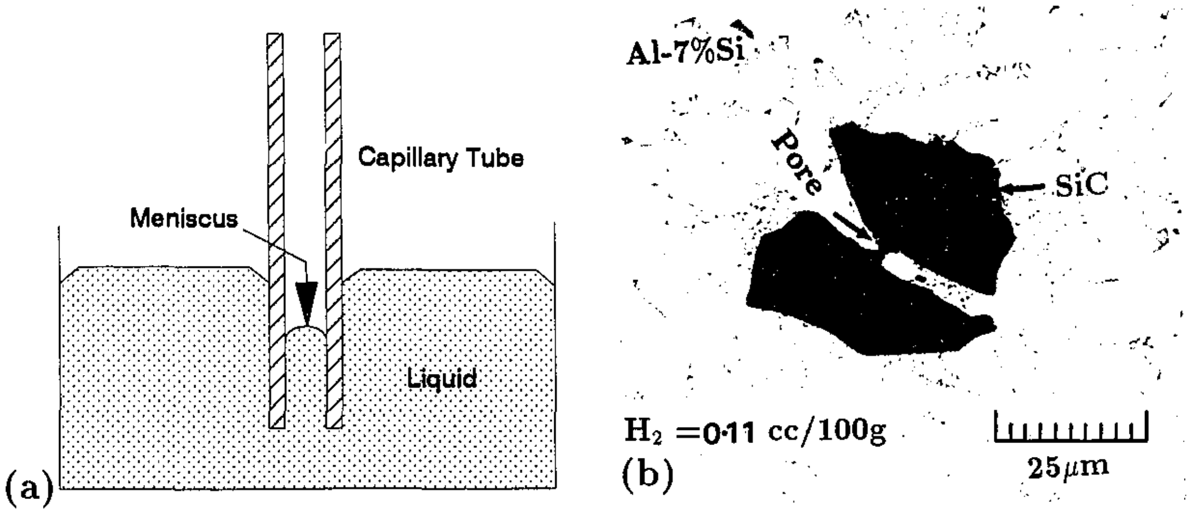

Fig. 3.33 Capillary Rejection of Liquid at Non-wettable Channel; (a) Schematic and (b) Experimental.

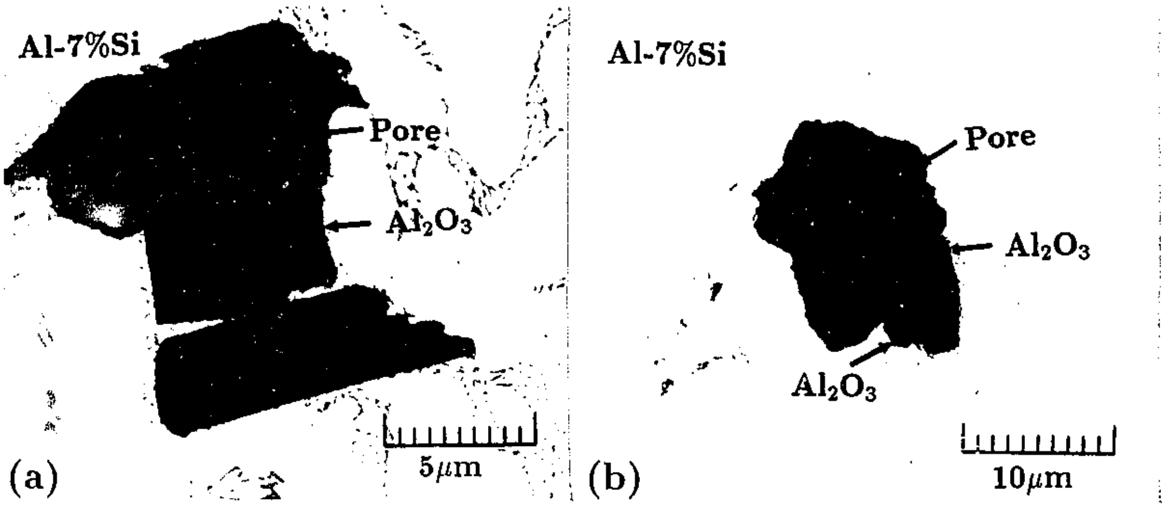

Fig. 3.34 Pore Formation at Clusters (Cooling Rate ~ $1^0C/s$); (a) H_2=0.11 cc/ 100 g and (b) H_2 = 0.20 cc/100 g.

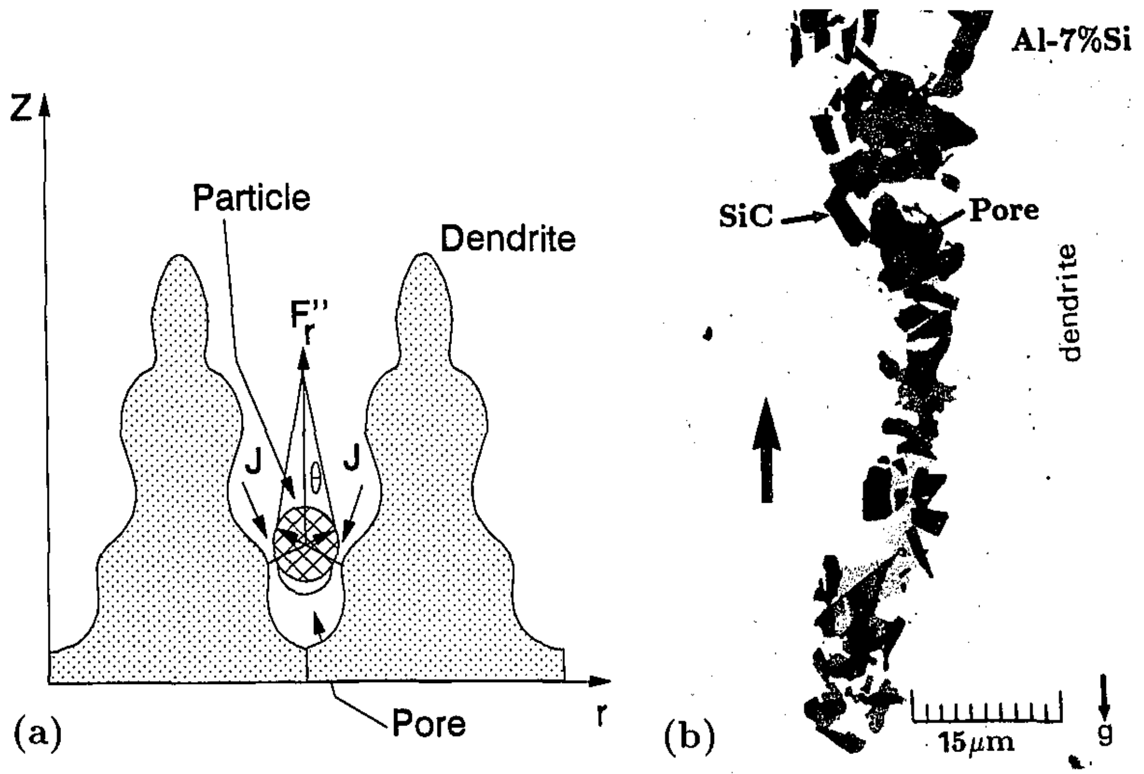

Fig. 3.35 Particle Interaction Within Interdendritic Channel; (a) Schematic and (b) Directionally Solidified A356 Alloy with SiC.

of the dendrite, but the particle motion is never quite steady, and the inclusion can roll down the bump into the interdendritic region (see Fig. 3.35). The bump on the dendrite tip then remelts. The pressure drop and gas segregation described in previous sections were predicted under the condition of steady motion of the particle. Due to the oscillatory motion of the inclusions as it shifts position the effects of pressure drop and gas segregation are lost in the dendrite tip region and pore nucleation will not occur here. Such oscillatory movement of particles has been observed in transparent systems,[211] and it is likely that convection in the melt will affect this behaviour considerably.

As inclusions become concentrated in the interdendritic region, their rolling motion will be restricted because of interaction with more than one interface as indicated in Fig. 3.35(a). The repulsive force is now reduced from that of a single planar interface due to surface energy considerations, [208] and is given by:

$$F_r' = \frac{F_r}{2} \tag{3.29}$$

The net force will be the resultant of the forces of the individual interfaces:

$$F_r'' = 2F_r' = F_r sin\theta < F_r \tag{3.30}$$

This is true for $0 < \theta < \frac{\pi}{2}$. The angle θ depends upon the size of the particle and the dendrite spacing which in turn depends upon the thermal gradient and freezing rate. The decrease in thermal gradient, G, which promotes interface instability coupled with narrow interdendritic channels result in higher entrapment as the repulsive force is reduced. This is in line with experimental findings.[44,210,211]

In the interdendritic channel, as the interfaces interact with the particle, they tend to push the particles together (see Fig. 3.35), and the inclusions create a barrier to the diffusion field and fluid flow in the interdendritic channel. Now, $|R_s|$, the radius of curvature of the S/L interface, is of the order of the radius of the particle. Recalling Eqn. [3.22], this situation will lead to a very high pressure drop and enhanced gas segregation behind the particle. The combined effect of each of these will be highly conducive to pore nucleation. In a study of the dendritic microstructure, Jacobi [226] concluded that the primary dendrites almost invariably align themselves such that adjacent arms have an interlocking type of arrangement as shown in Fig. 3.36. Once a particle moves to the mouth of this space and perturbations appear from all four sides there will be enormous resistance to the fluid flow and the situation will lead to severe gas segregation and a large viscous pressure drop.

The behaviour of inclusions will be significantly affected by their relative density *i.e.,* $\Delta\rho=\rho_m$-ρ_p, and the growth direction as described by the particle behaviour map (Fig. 3.6). When the inclusions are heavier than the melt, they will tend to settle down in the liquid. Interaction with the S/L interface is only possible if the growth direction is opposite to the motion of the particle in the liquid. Figs. 3.37, 3.38 and 3.39 show the effect of α-Al_2O_3 inclusions in directionally solidified rods. The growth directions were varied with respect to gravity by adjusting the movable platform shown in Fig. 3.14. It was not possible to maintain the platform perpendicular to the horizontal, but a maximum angle of 75-80^0 could easily be achieved.

Fig. 3.37 shows the general trend of pore number count along the width of

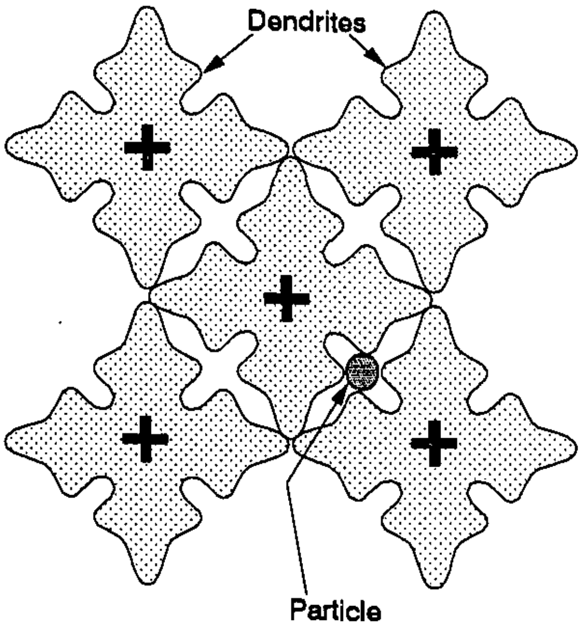

Fig. 3.36 Schematic Particle Interaction in Interdendritic Channel.

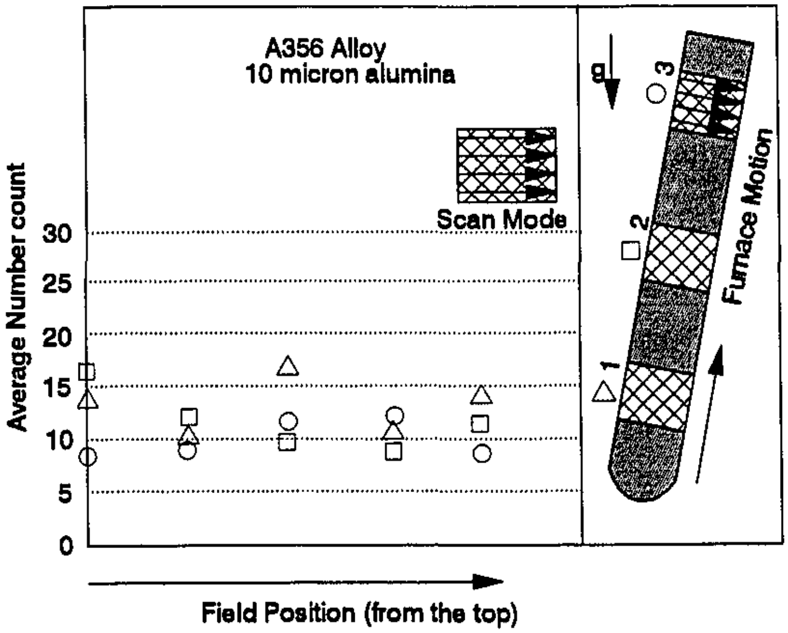

Fig. 3.37 Average Pore Number Count vs Field Position; $V \Uparrow g \Downarrow$.

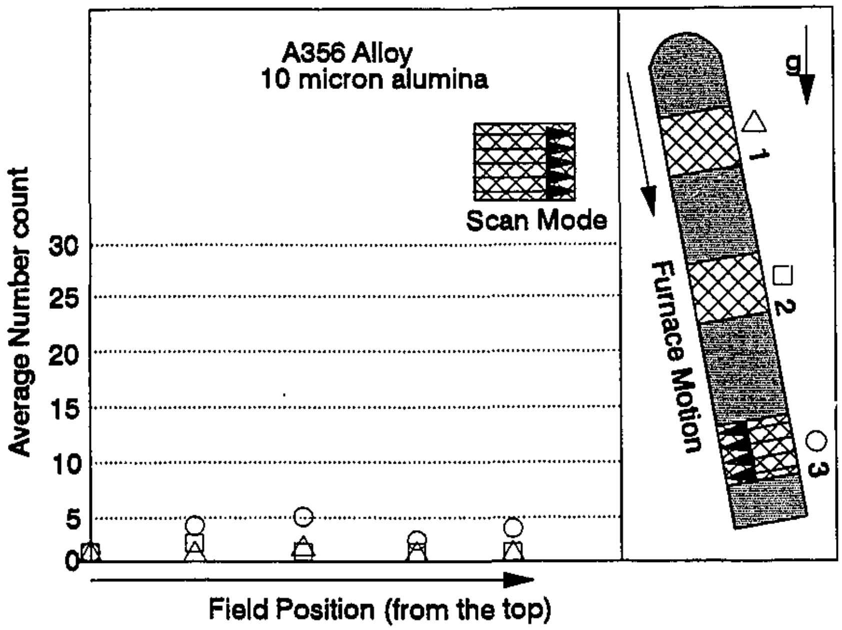

Fig. 3.38 Average Pore Number Count vs Field Position; $V \Downarrow g \Downarrow$.

the sample when the growth direction was opposite to the gravity. Though there was scatter in the number count which is probably statistical in nature, the number of pores remained almost the same across the sample. In this case the particles settled down the interdendritic channels (Fig. 3.35) and pore nucleation occured due to the associated feeding difficulty. When the growth direction was parallel to the gravity, interaction with the S/L interface was not possible. The particles settled to the bottom of the directionally frozen rod and only a few pores were detected as shown in Fig. 3.38. Particle settling is quite evident from Fig. 3.39, where the growth direction was kept perpendicular to the gravity. The top portion of the sample was devoid of inclusions, and no pores were detected there, whereas in the bottom portion many pores were detected.

In a conventional casting, solidification takes place multi-directionally and equiaxed dendritic or eutectic grains normally appear. It is believed that the concept of interaction should still apply. In this case, at an early stage of solidification the particle will interact with one dendrite, and in a later stage, it will be affected by the presence of several dendrites. The details of the resulting behaviour will depend on the local

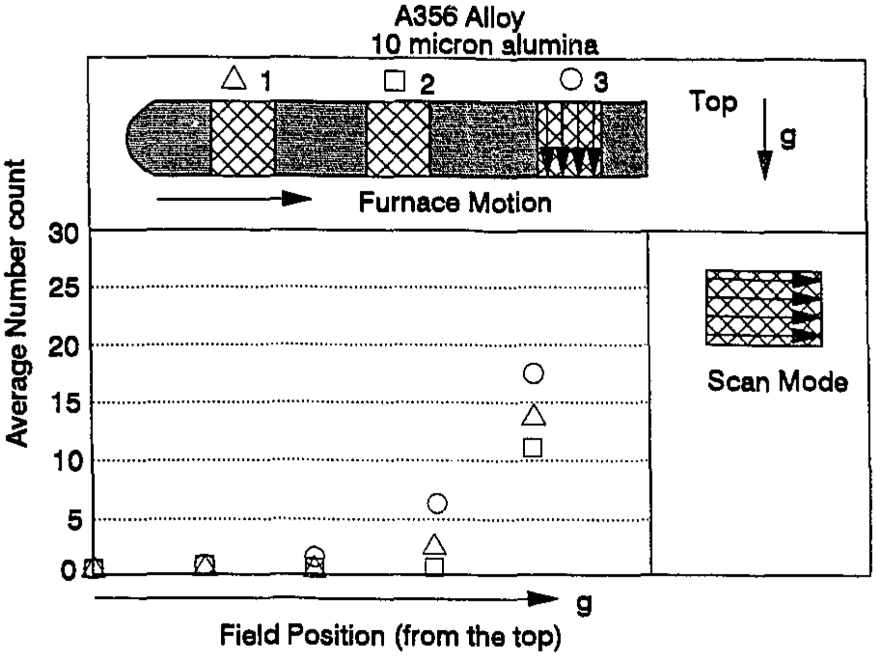

Fig. 3.39 Average Pore Number Count vs Field Position; $V \Rightarrow g \Downarrow$.

solidification phenomena and fluid flow conditions, but eventually significant viscous pressure drop and gas segregation will occur in a confined space between the inclusions and the interface, and favourable conditions for nucleation will result.

3.5.2 Proposed Mechanism of Pore Nucleation

Recalling the particle behaviour map (Fig. 3.6), it is noted that those particles which are easily engulfed would not lead to the enhanced pressure drop and gas segregation phenomena discussed here. The present experimental findings are in line with this hypothesis. Fig. 3.40 presents the behaviour of alumina and SiC inclusions in hypereutectic alloys. Their behaviour is contrary to the role of these inclusions in hypoeutectic alloys demonstrated in Figs. 3.21, 3.25 and 3.28. In the case of the hypoeutectic alloy, the Al_2O_3 and SiC inclusions are pushed by the α-dendrite interface and most of them are associated with pores (Figs. 3.21 & 3.25). On the other hand, in hypereutectic alloys primary silicon phases nucleate on, or engulf the Al_2O_3 and SiC inclusions (Fig. 3.40).

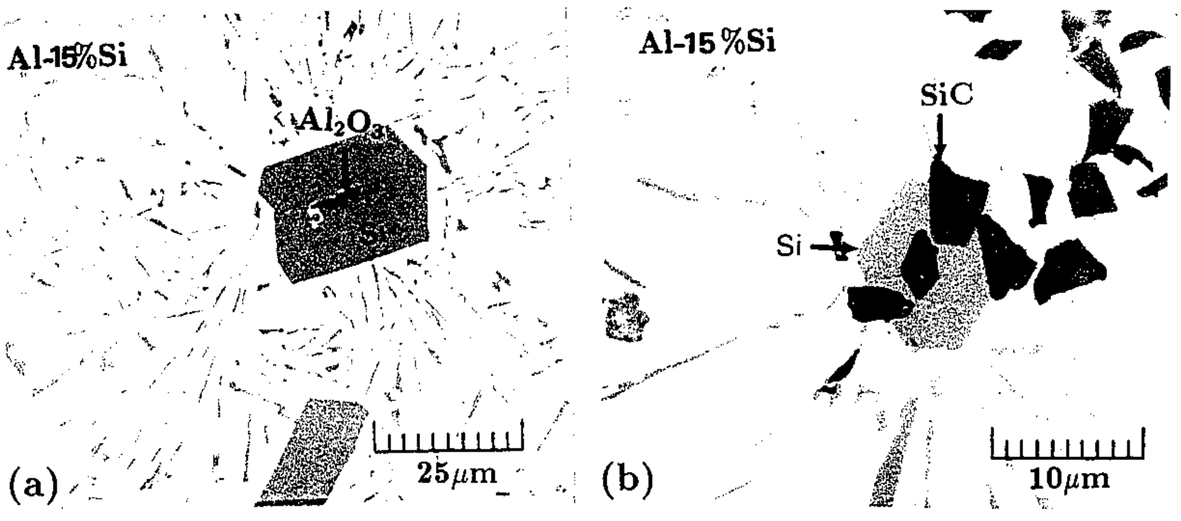

Fig. 3.40 Behaviour of Al_2O_3 and SiC Inclusions in Al-15%Si Alloy (Cooling Rate ~ 0.1 ^{0}C/s), (H_2= 0.24 cc/ 100 g).

The particle engulfment phenomenon in directionally solidified Al-15%Si alloy is shown in Fig. 3.41. It is evident from Fig. 3.41(b) that the growing Si S/L interface engulfs the SiC particles. The implication of particle pushing and engulfment phenomena on the porosity content in hypo and hypereutectic alloys is also quite clear from Fig. 3.22. Interestingly, the same alloy (Al-15%Si) exhibits different behaviour when the solidification characteristic is changed by varying the cooling rate as shown in Fig. 3.42. When primary dendrites are formed by increasing the cooling rate, the Al_2O_3 inclusions nucleate pores exactly as they would in a hypoeutectic alloy.

Besides pushing and engulfment, inclusions may also be mechanically trapped in the interdendritic space as shown in Fig. 3.35(b). The larger the particle the greater will be the tendency for it to be trapped. At the most, these inclusions will provide conditions for nucleation only for a very short period which may not be sufficient for the growth of a significant pore before the inclusions are exhausted as demonstrated in Fig. 3.43.

As discussed earlier, the cooling rate (*i.e.*, the growth velocity) which affects the entrapment tendency significantly, will ultimately affect the nucleation behaviour of the pores. The effect of cooling rate on the porosity content of alloys containing different

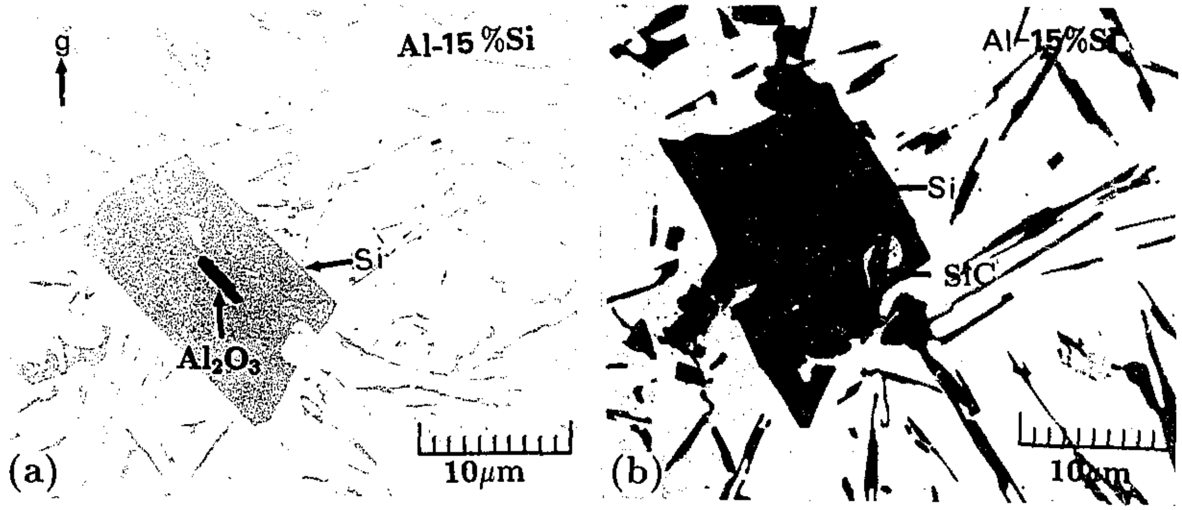

Fig. 3.41 Directionally Grown Al-15%Si Alloy Showing Engulfment of Inclusion Particles by Si Crystal (Growth Direction ⇓); (a) Al_2O_3 and (b) SiC.

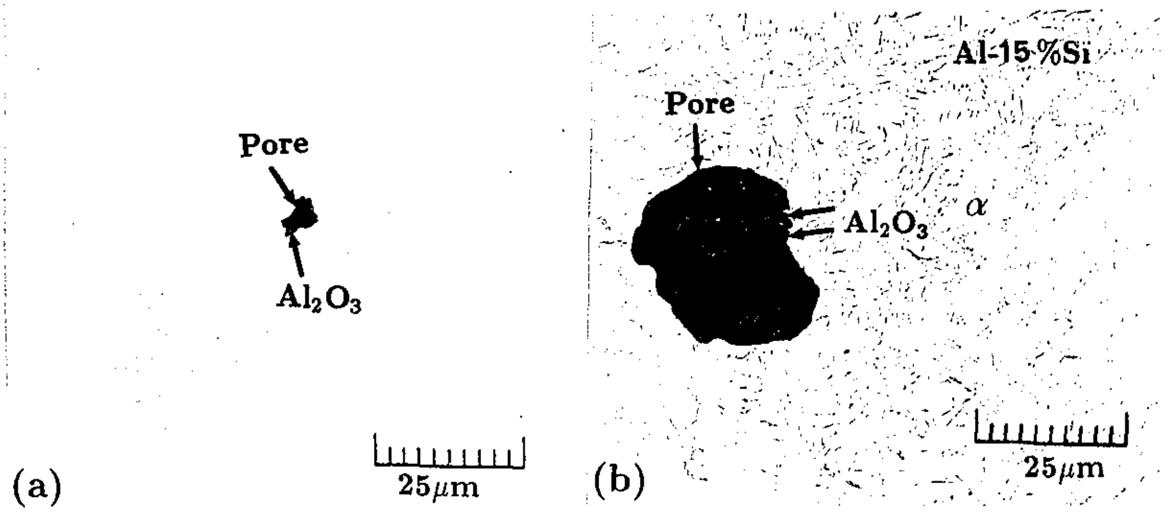

Fig. 3.42 Solidification of Hypereutectic (Al-15%Si) Alloy in Coupled Zone Leading to the Formation of Primary α-Dendrites (Cooling Rate~ 10 ^{0}C); (a) H_2=0.11 cc/100g and (b) H_2=0.24 cc/100g.

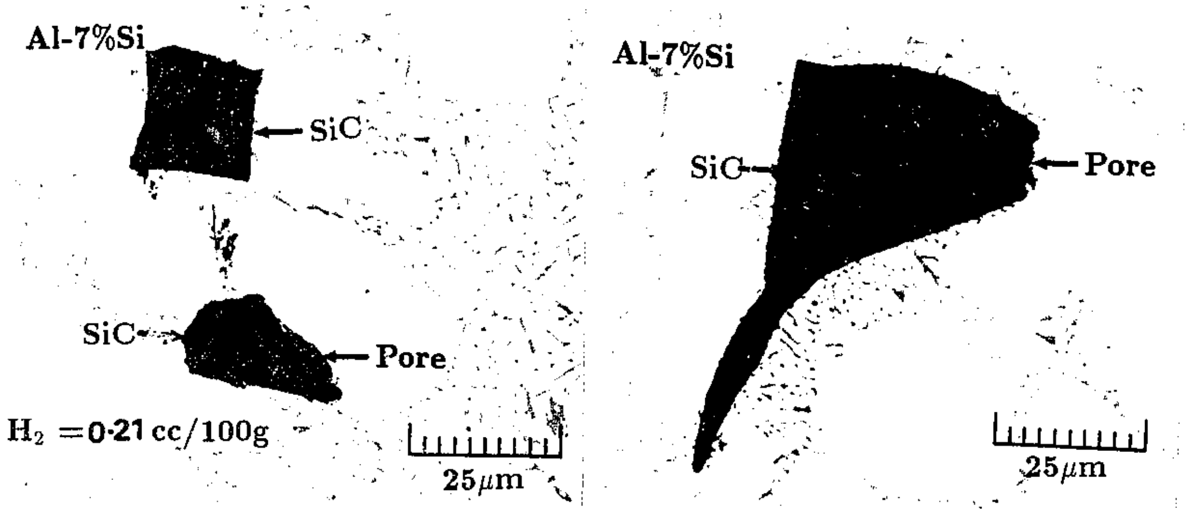

Fig. 3.43 Behaviour of 100 μ SiC Particles in A356 Alloy.

sizes of SiC inclusions is presented in Fig. 3.44. It is clear from Fig. 3.44 that as cooling rate increases the porosity content decreases. For example, in the case of 30-40μ SiC particle containing alloy (black bars) the porosity content falls from 0.5 area % to less than 0.1 area % as the cooling rate is increased from 0.1^0 C/s to 4.0^0 C/s. As expected, an increase in cooling rate should decrease the porosity content due to higher hydrogen retention in the solid. However, the effect is also in part due to the enhanced entrapment tendency of the inclusions with increasing cooling rates, which is evident if one considers the porosity content in the alloys containing 3-5 μ SiC particles (the grey bars). In this case the cooling rate does not affect the porosity content to the same extent as in the alloy with 30-40 μ SiC because the entrapment tendency is a strong function of the size of the particles (Eqn. [3.14]). Larger particles will be entrapped at an early stage reducing the number of nucleation sites whereas the smaller particles that are continuously pushed can act as active nucleants for a longer time *i.e.*, until the end of the local solidification time.

From the above discussion, it would appear that in castings, porosity can be reduced by creating conditions such that inclusions in the melt are exhausted as soon as possible by incorporation into the solid. A higher local solidification rate and low thermal gradient would enhance the entrapment tendency and thus may reduce the activity of

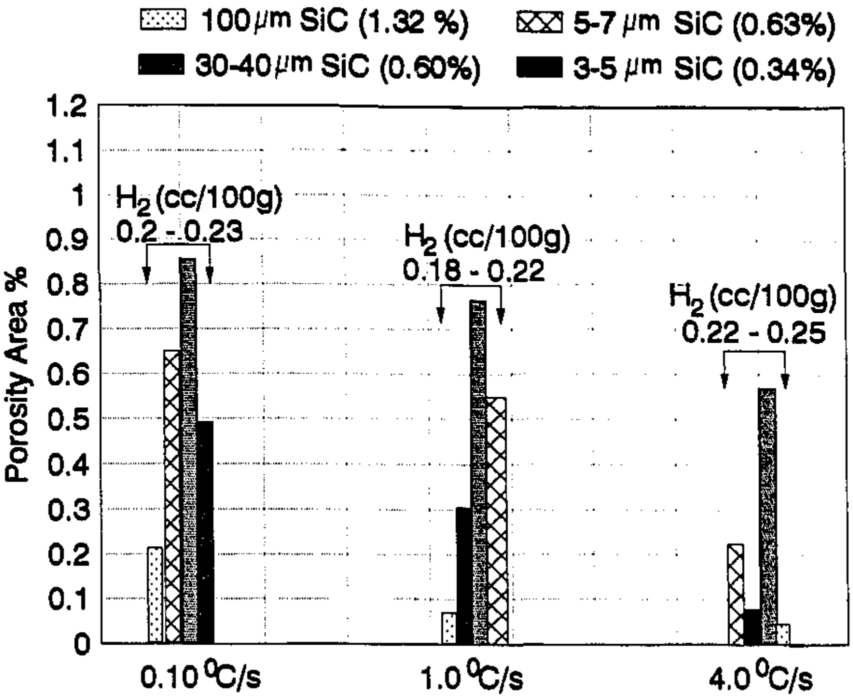

Fig. 3.44 Porosity Area % vs Cooling Rate in A356 Alloy.

the particle. Another alternative is surface energy modification of both the melt and the particles to enhance the engulfment tendency. It is clear from Chapter 2, that a slight change in the chemistry of the melt with respect to Ti content (0.01 %) changes the behaviour of TiB_2 particles drastically *i.e.*, they nucleate the α-Al and become exhausted within the solid. On the other hand, these particles in the absence of dissolved Ti are pushed by the S/L interface and consequently nucleate pores as is evident from Fig. 3.45. A very important industrial implication of the present experimental observation is that the TiB_2 particles which are added to the melt via master alloys for grain refinement can prove to be disasterous from the point of view of pore nucleation at a lower threshold hydrogen level, if the chemistry of the melt as well as the particles are not properly controlled. Fig 3.46(b) shows the formation of pores at TiB_2 particle clusters in a casting grain refined by Al-2.5%Ti-2.5%B master alloy.

Modification of surface energy of other particulates has been reported in the literature.[37] For example, the addition of trace amounts of magnesium to aluminum alloys containing alumina inclusions may improve the engulfment tendency be-

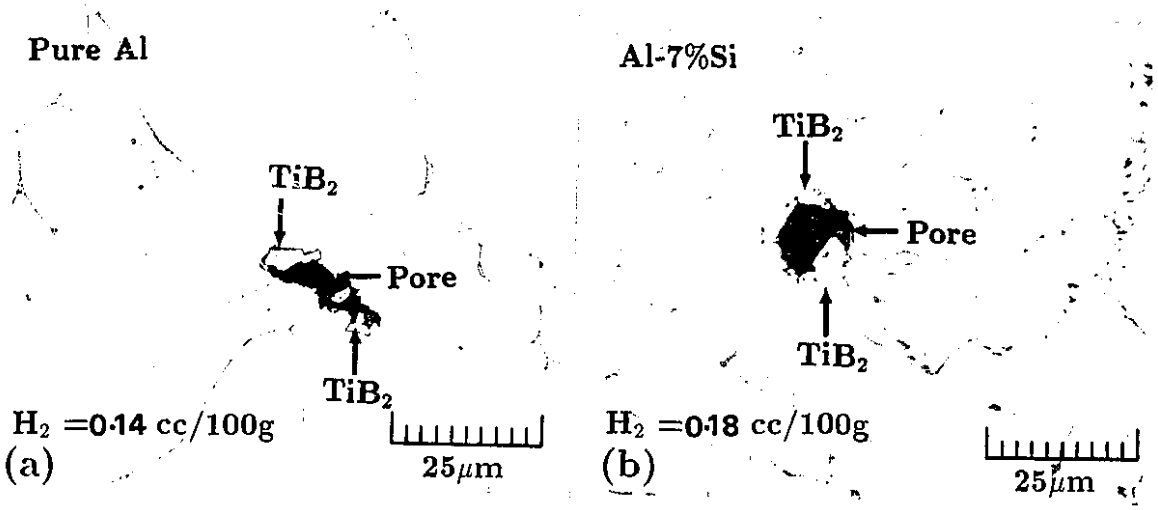

Fig. 3.45 Pore Nucleation at TiB_2 Particles; (a) Pure Al and (b) Al-7%Si Alloy.

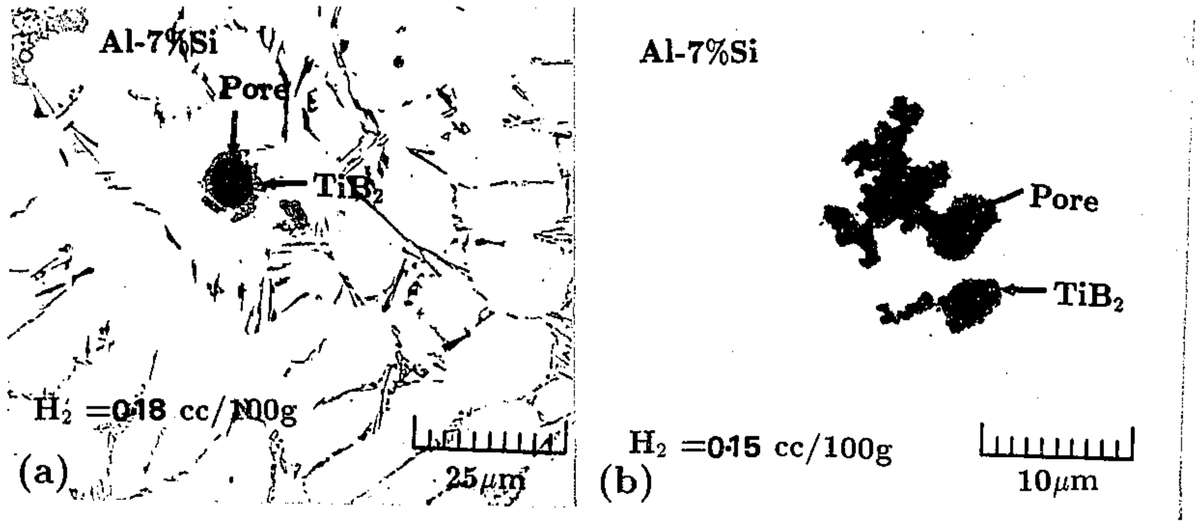

Fig. 3.46 Pore Nucleation at TiB_2 Clusters; (a) Directly Inoculated and (b) Added Through Al-2.5%-2.5%B Master Alloy.

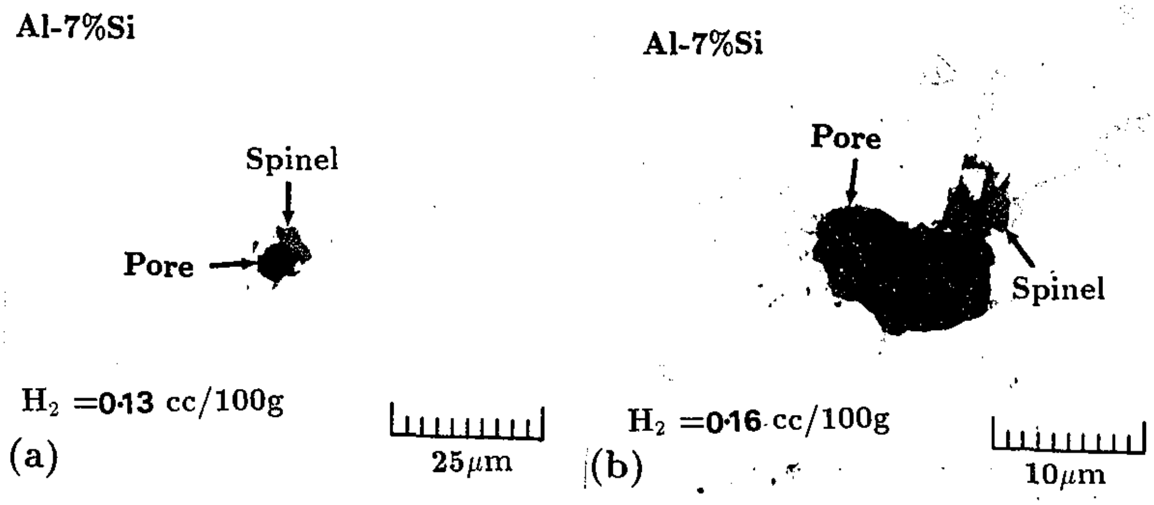

Fig. 3.47 Pore Nucleation at Spinel Particles; (a) Single Particulate and (b) Cluster.

cause of spinel layer formation on the surface, which is believed to have an enhanced wettability.[37] In the present study spinel particles were always rejected by the S/L interface and pores nucleated on them as shown in Fig. 3.47. Attempts to modify the behaviour of Al_2O_3 particles by the addition of Ti failed as reported in Chapter 2 (Fig. 2.33). Unfortunately, interfacial energy data, particularly between the solid and the particle, for many systems of interest are not available, and at present the theoretical prediction of the behaviour of many types of inclusions is not possible.

SrO and $Sr(OH)_2$ inclusions are found to be unstable in aluminum melts. Fig. 3.48 presents the microstructure of an Al-7%Si alloy after the addition of SrO and $Sr(OH)_2$. It appears that these oxides reduce to elemental Sr which subsequently reacts to form a complex compound of Sr(∼ 15%)-Al(∼40%)-Si(∼45%). In this figure the eutectic silicon is highly modified suggesting that elemental Sr is present in the melt. This was further verified by adding up to 2 % elemental Sr into an Al-7%Si alloy through binary Al-Sr master alloy. It was observed that similar compounds also formed with elemental Sr. This observation suggests that the oxides first dissociate into elemental Sr and the elemental Sr then combines to form the ternary compounds as shown in Fig 3.49. These particles were found to be engulfed completely by the α-Al, suggesting that the ternary compound of Al-Sr-Si nucleates α-Al. In other words they have a grain refining

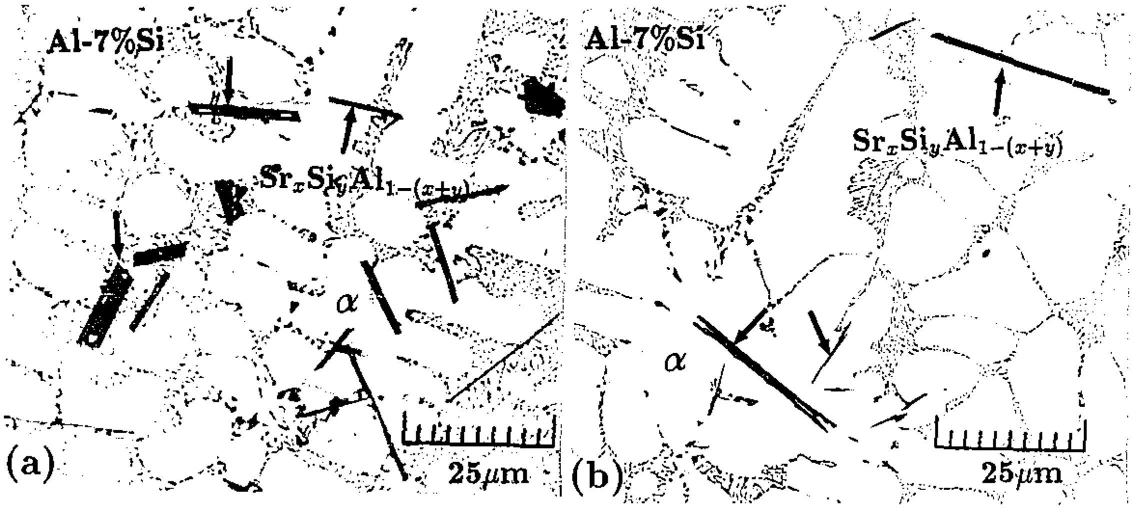

Fig. 3.48 Formation of Sr-Al-Si Compound; (a) SrO and (b) $Sr(OH)_2$.

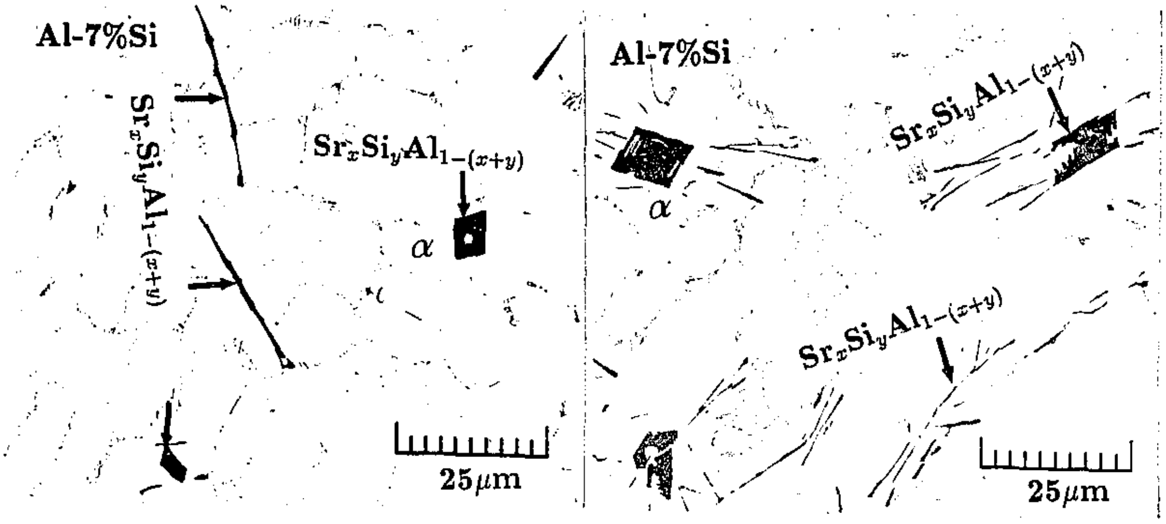

Fig. 3.49 Formation of Sr-Al-Si Compound by Elemental Sr Addition.

effect. The morphology of these particles varied with temperature of formation, but this aspect was not studied in detail. It is, however, clear that any oxide or hydroxide inclusions which may enter the melt as result of a modification treatment are unstable and consequently unable to act as pore nucleants.

3.6 Summary

An order of magnitude analysis is carried out to compare the pressure required to overcome the activation barrier for pore nucleation and the possibility of attaining such a pressure in a real casting. A novel theoretical approach to the mechanism of achieving this activation barrier in metallic systems is presented. The proposed mechanism is based on the behaviour of foreign particles at the advancing S/L interface. Mathematical analyses have been employed to predict the gas segregation and pressure drop in the gap between the particle and the S/L interface. The equations which arise are solved using experimental data available in the literature. The effect of particle properties and solidification parameters such as: wettability, density, thermal conductivity, solidification rate and morphology of S/L interface are discussed. To substantiate the mechanism, experimental verification and quantitative measurements are carried out by introducing different inclusions into aluminum melts. The implication of theoretical analysis and experimental findings on the heterogeneous nucleation mechanism of pores are summarized below.

Depending on the characteristics of the inclusions present:

- The particle behaviour map (Fig. 3.6), can be used to identify the type of inclusions responsible for pore nucleation.
- It is the net interfacial energy between inclusions, solid and liquid ($\Delta\sigma_0 = \Delta\sigma_{ps} - \Delta\sigma_{pl}$), which determines the potency of the inclusion as a pore nucleant, rather than simply the interfacial energy between the inclusion and the liquid ($\Delta\sigma_{pl}$), as believed previously.
- Those inclusions which are easily engulfed by the solid are not harmful as far as

nucleation of pores is concerned.

- Inclusions that are pushed by the S/L interface can act as a potential barrier to the fluid flow and diffusion field at the S/L front during solidification.
- The pressure drop and enhanced gas pressure in the film region, arising because of the interaction of the S/L front with the inclusions, can overcome the fracture pressure.
- The embryonic bubble at the point of nucleation can withstand the surface tension force without collapsing, due to high gas pressure and viscous pressure drop in the film region.
- Al_2O_3 and SiC inclusions in hypoeutectic Al-Si alloys nucleate pores whereas in the case of hypereutectic alloys they nucleate the primary silicon phase, or they are engulfed by it.
- The behaviour of certain inclusions (*e.g.,* TiB_2) can be altered by slightly changing the chemistry of the melt.
- The properties of inclusions such as: density, thermal conductivity, size and shape also affect pore formation.
- The present mechanism also explains the effect of the solidification parameters such as freezing rate and temperature gradient on the pore nucleation process.
- Clusters of inclusions which may be a quite common occurance in normal casting alloys are more conducive to pore nucleation than is a single particle of equivalent volume.
- TiB_2 inclusions may be deleterious in that they nucleate pores.
- SrO and $Sr(OH)_2$ inclusions are unstable in aluminum melts. They form a ternary compound which has a grain refining effect rather than taking part in pore nucleation.

Chapter 4

General Conclusions and Suggestions

4.1 Conclusions

From the theoretical analysis and experimental findings presented in this thesis, considerable insight can be gained into many age old scientific questions and their industrial implications relating to the grain refinement practice and the problem of pore formation in solidification processing of aluminum, as outlined below.

Foreign substrates play a significant role, directly or indirectly, in each nucleation process (*i.e.*, grain or pore). For any systematic study on the behaviour of foreign substrates, it is essential to introduce the synthetic crystals of these substrates directly rather than generating them within the melt. Generation of these substrates within the melt by chemical reactions may completely alter their behaviour by changing the melt chemistry.

Direct injection of synthetic crystals under the melt by an inert gas stream, as described in this thesis, is a suitable method for introducing synthetic crystals while preserving their surface characteristics as well as the melt chemistry. A wide variety of inclusions can be added to aluminum and aluminum alloy melts using this technique of injection. Uniform distributions can be obtained in the melt even with particle sizes of the order of 2-5 μm, and particle recoveries are in the range of 30-90 percent depending on the inclusion type. Inclusions with melting points below the melt temperature can also be added by a simple modification to the apparatus.

Titanium diboride is a very stable phase within liquid aluminum and has a negligible solubility even in the absence of any dissolved Ti. TiB_2 crystals which are commonly believed to be the nuclei for α solid,[18,21,23,57] do not nucleate grains alone, invalidating the so called 'boride theory'.[18,19,21,23] On the other hand, they are pushed by the S/L interface to the grain boundary suggesting a high interfacial energy between α-Al and TiB_2.

In grain refining practice, TiB_2 plays an indirect role in grain nucleation. In the presence of dissolved Ti in the melt, TiB_2 provides a substrate for the precipitation of $TiAl_3$. The presence of TiB_2 crystals introduces an activity gradient in a homogeneous melt with respect to Ti, leading to segregation of Ti atoms to the TiB_2/melt interface. Due to the inhomogeneous distribution of Ti in such a system, a stable layer of $TiAl_3$ can be present at Ti contents far below the peritectic composition. On cooling, this interfacial $TiAl_3$ layer undergoes a peritectic reaction and thereby nucleating the solid. Thus, the mechanism of grain refinement by Al-Ti-B master alloy is a two step nucleation process.

The proposed 'duplex' nucleation mechanism can explain almost all experimentally observed phenomena in grain refining practice. The presence of excess Ti over the stoichimetry of TiB_2 is essential for the duplex nucleation process rather than its growth restricting purpose believed earlier.[53] On prolonged holding, the boride particles settle and cause loss of grain refinement which can be reversed by agitation of the melt. In the presence of impurities such as Zr, specific segregation of Zr will also take place on the TiB_2 substrate and its atomic size mismatch will hinder $TiAl_3$ formation and lead to poisoning of the seeds.

Boride particles with spherical morphology would presumably enhance the chance of exposing a suitable crystallographic plane for precipitation, whereas an elongated particle morphology may limit the probability and thus may prove to be a redundant site. In such a situation, even under a very strong activity gradient, attachment and formation of a crystal will not be possible. It is also possible that in the presence of many adjacent sites, the precipitation of $TiAl_3$ may not occur on all particles. This is because, once precipitation starts at one centre, atomic attachment on another centre adjacent to it may not be favourable compared to the further growth of the already existing nucleus. As a result, while one site becomes an effective nucleus, the others will be redundant and will be pushed into the grain boundary. However, when the bulk Ti concentration is high, presumably close to the peritectic, precipitation of $TiAl_3$ should be favourable on many nearby sites, and as a result more than one particle can be found within the grain.

In an Al-Si alloy having excess Ti over the stoichiometry of TiB_2, a ternary aluminide (Al-Ti-Si) is formed at the TiB_2/melt interface by similar processes to those described for Al. However, due to the drastic reduction in peritectic solidification temperature of the ternary system at higher Si content, refinement by Al-5Ti-1B is inefficient. The suggestion that the observed enhanced grain refinement of Al-Si alloys by Al-B master alloy is due to the heterogeneous nucleation of aluminum crystals on intermetallic AlB_2 particles in the melt[87] does not appear to be true. From the present study, it is confirmed that TiB_2 crystals alone do not nucleate α-Al in Al-Si alloys. In view of the close similarity in the crystal lattice of AlB_2 and TiB_2, direct nucleation on AlB_2 should not be feasible. The enhanced grain refinement by AlB_2, possibly occurs via the eutectic reaction present in the Al-B system.

The improved performance of Al-3Ti-3B master alloy over Al-5Ti-1B is presumably due to excess B present in solution, which forms a layer of AlB_2 at the TiB_2/melt interface. A near perfect epitaxy is expected between AlB_2 and TiB_2 due to their isomorphous structure. On cooling, this interfacial layer nucleates α-Al in a similar manner to that which occurs in the Al-B system *i.e.*, possibly via a eutectic reaction.

The mechanism of grain refinement by TiC is straight forward *i.e.*, α-Al nucleates directly on TiC particles. The existence of epitaxy on the surface of TiC enables direct nucleation, but the thermodynamic stability of TiC within liquid aluminum limits its potential as a grain refiner. The present experimental observation does not support the idea of spontaneous formation of TiC on the addition of Al-Ti master alloys to aluminum melts according to the original postulation of the 'carbide theory'. [21] Even if pre-prepared TiC is introduced into the melt, interfacial reactions leading to the formation of aluminum carbides and complex carbides are likely to occur almost instantaneously. In Al-Si alloys, TiC decomposes completely.

Particles whose presence within the solid is thermodynamically unfavourable *i.e.,* they neither nucleate the solid nor become engulfed, are pushed by the solid/liquid interface to the grain boundary. Particles which are pushed by the interface act as a barrier to the fluid flow and the diffusion field ahead of the interface. The kinetic considerations of the particle pushing process suggest that a finite separation must be maintained between the particle and the S/L interface and fluid must flow continuously into this region to compensate for the liquid that is exhausted in the solidification process. Consequently, the viscous pressure drop and gas segregation are enhanced in this thin film region.

A mathematical analysis to predict the particle behaviour, the viscous pressure drop, and the gas segregation in the gap between the particle and the S/L interface, shows that the activation barrier to bubble nucleation can be reached in a normal casting. The embryonic bubble at the point of nucleation can withstand the surface tension force without collapsing, due to high gas pressure and viscous pressure drop in the film region.

The particle and S/L interface interaction phenomena are particular to specific particle/melt combinations. Those inclusions which are easily engulfed by the solid are not harmful as far as nucleation of pores is concerned. Al_2O_3 and SiC inclusions in hypoeutectic Al-Si alloys nucleate pores whereas in the case of hypereutectic alloys they nucleate the primary silicon phase, or they are engulfed by it. The behaviour of certain inclusions (*e.g.,* TiB_2) can be altered by slightly changing the chemistry of the melt.

The model identifies the inclusions and casting conditions which are responsible for pore nucleation. The particle behaviour map (Fig. 3.6) can be used to identify the type of inclusions responsible for pore nucleation. It is the net interfacial energy between inclusions, solid and liquid ($\Delta\sigma_0 = \Delta\sigma_{ps} - \Delta\sigma_{pl}$), which determines the potency of the inclusion as a pore nucleant, rather than simply the interfacial energy between the inclusion and the liquid ($\Delta\sigma_{pl}$).[151] The properties of inclusions such as: density, thermal conductivity, size and shape also affect pore formation. Clusters of inclusions which may be quite a common occurance in normal casting alloys, are more conducive to pore nucleation than is a single particle of equivalent volume.

The fact that a small grain refiner addition is beneficial does not necessarily mean that additions beyond an optimum quantity, or additions that lead to formation of undesirable by-products will provide greater rewards. The grain nucleation process is indifferent to the presence of many foreign substrates whether intentional or natural, but the presence of almost all inclusions significantly influences the porosity formation in castings. TiB_2 inclusions, which are added for the beneficial effect of grain refinement can act as pore nucleants if the melt chemistry, as well as the particle chemistry and number density, is not properly controlled.

SrO and $Sr(OH)_2$ inclusions are unstable in aluminum melts. They form a ternary compound which has a grain refining effect rather than taking part in pore nucleation.

4.2 Suggestions for Future Study

The author feels that there are a few aspects which should be further investigated for a better view of some of the propositions made in this thesis. They are outlined below:

- The observation of nucleation of $TiAl_3$ on TiB_2, in the first nucleation step of the 'duplex' nucleation process necessitates the existence of epitaxy between them. At this time there is no crystallographic information regarding the existence of epitaxy between TiB_2 and $TiAl_3$. A TEM study on the three layer structure ($TiB_2 \Rightarrow TiAl_3 \Rightarrow \alpha$-Al) may be useful in identifying the plane of TiB_2 on which $TiAl_3$ grows preferentially. Once this information is available, some suggestion can be made as to the morphology of TiB_2 which would provide better refinement, and steps towards obtaining this morphology during the manufacture of master alloys may be taken.

- It is well known that the presence of Zr poisons grain refinement. It would be appropriate to add elemental Zr to aluminum melts already containing synthetic TiB_2 crystals and dissolved Ti to verify the behaviour of the particles. It would be also interesting to study the effect of Zr and TiB_2 crystals in the absence of Ti.
- Synthetic AlB_2 crystals should be introduced directly to pure Al as well as to an Al-Si alloy to verify its nucleating capability.
- A study of epitaxy between α-Al and AlB_2 in pure aluminum as well as in the presence of Si may resolve the mechanism of enhanced grain refinement by Al-B master alloy.
- TiC crystals should be introduced into other alloys besides Al-Si, to verify their stability and nucleating capability.

References

1. W. Kurz and D. J. Fisher: *Fundamentals of Solidification*, Trans Tech Publications, Switzerland, 1986, p.27.

2. J. Campbell: *Castings*, Butterworth-Heinemann Ltd, Oxford, England, 1991, p. 2.

3. J. Campbell: *"Pore Nucleation in Solidifying Metals"*, Joint Conf. on Solidification of Metals, Brighton, UK, 1967, pp. 1-20 .

4. S. N. Tiwari and J. Beech: *Met. Science*, 1978(Aug.), pp. 356-362.

5. Q. T. Fang and D. A. Granger: *Trans. AFS*, 1989, vol. 97, pp. 989-1000.

6. H. Fredriksson: *Metall. Trans.B*, 1976, vol. 7B, pp. 599-606.

7. P. K. Ghosh and S. Ray: *Trans. AFS*, 1988, vol. 96, pp. 775-782.

8. H. Shahani: *Scand. J. Metall.*, 1985, vol. 14, pp. 306-312.

9. H. Iwahori, K. Yonekura, Y. Yamamoto and M. Nakamura: *Trans. AFS*, 1990, vol. 98, pp. 167-173.

10. G. Laslaz and P. Laty: *Trans. AFS*, 1991, vol. 99, pp. 83-90.

11. E. L. Rooy: *Modern Casting*, 1992 (Sept.), pp. 34-36.

12. C. J. Simensen and G. Berg: *Aluminium*, 1980, vol. 56(5), pp. 335-340.

13. P. S. Mohanty, F. H. Samuel and J. E. Gruzleski: *Metall. Trans.A*, 1993, Vol. 24A, pp. 1845-1856.

14. P. S. Mohanty, F. H. Samuel and J. E. Gruzleski: *Int. Materials Reviews*, (accepted).

15. P. S. Mohanty, F. H. Samuel and J. E. Gruzleski: *Metall. Trans.B*, (93-368-B), (in Press).

16. P. S. Mohanty, F. H. Samuel and J. E. Gruzleski: *Proc. of CIM International symposium on Light Metal Processing and Applications*, Quebec City, Canada, Aug. 29-Sept. 2, 1993, pp. 273-282.

17. P. S. Mohanty, F. H. Samuel, J. E. Gruzleski and T. J. Kosto: *Light Metals*, 1994, (in press) .

18. M. Johnsson, L. Backerud and G. K. Sigworth: *Metall. Trans.A*, 1993, vol. 24A, pp. 481-491.

19. D. G. McCartney: *Int. Materials Rev.*, 1989, vol. 34(5), pp. 247-260.

20. J. Pearson and M. E. J. Birch: *J. Metals*, 1979, vol. 31(11), pp. 27-31.

21. A. Cibula: *J. Inst. Met.* , 1951-52, vol. 80, pp. 1-16.

22. M. M. Guzowski, D. A. Sentner and G. K. Sigworth: U. K. Patent, No. GB2162540A, 1986.

23. A. Cibula: *J. Inst. Met.* , 1949-50, vol. 76, pp. 321-360.

24. F. A. Crossley and L. F. Mondolfo: *Trans. AIME* (*J. of Metals*), 1951, vol. 191, pp. 1143-1148.

25. J. A. Marcantonio and L. F. Mondolfo: *Metall. Trans.* , 1971, vol. 2, pp. 465-71.

26. F. Lihl and J. Sagoschen: *Metall.*, 1957, vol. 11, pp. 179-189.

27. Y. Nakao: *J. Japan. Inst. Light Metals* , 1967, vol. 17, pp. 65-75.

28. Y. Nakao, T. Kobayashi and A. Okumura: *J. Japan. Inst. Light Metals* , 1970, vol. 20, pp. 163-75.

29. W. Thury: *Z. Metallkd*, 1955, vol. 65, pp. 488-90.

30. A. Banerji and W. Reif: *Metall. Trans.A*, 1985, vol. 16A, pp. 2065-68.

31. A. Banerji and W. Reif: *Metall. Trans.A*, 1986, vol. 17A, pp. 2127-2137.

32. A. Banerji and W. Reif: *Solidification Processing 1987*, London, The Institute of Metals, 1988, pp. 145-48.

33. P. Sahoo and M. J. Koczak: *Mater. Sci. & Eng.*, 1991, vol. A131, pp. 69-76.

34. P. Sahoo and M. J. Koczak: *Mater. Sci. & Eng.*, 1991, vol. A144, pp. 37-44.

35. L. Arnberg, L. Bȧckerud and H. Klang: *Met. Technol.*, 1982, vol. 9, pp. 7-13.

36. M. K. Surappa and P. K. Rohatgi: *Met. Technol.*, 1978, vol. 5, pp. 358.

37. P. K. Rohatgi, R. Asthana and S. Das: *Int. Materials Rev.*, 1986, vol. 31(3), pp. 115-139.

38. J. Boutin and C. E. Gallernault: *Internal Report No. AR-89/0028*, Alcan Int. Ltd., Arvida, Canada, July 1989.

39. E. E. Underwood: *Quantitative Stereology*, Addisson & Wesley, Reading, Mass., 1970.

40. *Engineering Materials Handbook*, ASM INTERNATIONAL, Metal Park, OH, 1986, vol. 4, p. 890.

41. *Metals Handbook*, 10th Edition, ASM INTERNATIONAL, Metal Park, OH, 1990, vol. 2, p. 1003.

42. *Encyclopedia of Glass, Ceramics and Cements*, John Wiley & Sons, Ed. Martin Grayson, New York, 1985, p. 14.

43. T. Shinoda, Hua Liu and Y. Mishima: *Mater. Sci. Engg.*, 1991, vol. A146, pp. 91-104.

44. D. M. Stefanescu, A. Moitra, S. Kacar and B. K. Dhindaw: *Metall. Trans.A*, 1990, vol. 21A, pp. 231-239.

45. G. A. Yasinskaya: *Poroshk. Metall.*, 1966, vol. 7(43), p. 53.

46. F. A. Badia and P. K. Rohatgi: *Trans. AFS*, 1969, vol. 77, p. 402.

47. P. K. Rohatgi, R. Asthana, R. N. Yadav and S. Ray: *Metall. Trans.A*, 1990, vol. 21A, pp. 2073-2082.

48. K. D. Watson, J. M. Toguri and R. W. Shaw: *CIM Conf. Proc.*, Ottawa, Canada, Aug. 18-21, 1991, vol. 24, pp. 119-27.

49. M. M. Guzowski, G. K. Sigworth and D. A. Sentner: *Metall. Trans.A*, 1987, vol. 18A, p. 603.

50. I. G. Davis, J. M. Dennis and A. Hellawell: *Metall. Trans.*, 1970, vol. 1, p. 275.

51. J. A. Marcantonio and L. F. Mondolfo: *J. Inst. Met.* , 1970, vol. 98, p. 23.

52. K. F. Kobayashi, S. Hashimoto and P. H. Shinghu: *Z. Metallkd*, 1983, vol. 74, p. 787.

53. I. Maxwell and A. Hellawell: *Acta Metall.*, 1975, vol. 23, p. 229.

54. I. Maxwell and A. Hellawell: *Acta Metall.*, 1975, vol. 23, p. 901.

55. I. Maxwell and A. Hellawell: *Metall. Trans.*, 1972, vol. 3, p. 1487.

56. J. Moriceau: *Mem. Sci. Rev. met.*, 1970, vol. 77, p. 787.

57. G. P. Jones and J. Pearson: *Metall. Trans.B*, 1976, vol. 7B, p. 223.

58. G. K. Sigworth: *Metall. Trans.A*, 1984, vol. 15A, p. 223.

59. A. A. R. Abdel-Hamid and F. Durand: *Metall. Trans.A*, 1986, vol. 17A, p. 349.

60. N. J. Finch: *Metall. Trans.*, 1972, vol. 3, p. 2709.

61. L. F. Mondolfo, S. Farooq and C. Tse: *Solidification Processing 1987*, The Institute of Metals, London, 1988, p. 133.

62. J. Cissé and G. F. Bolling: *J. Cryst. Growth*, 1972, vol. 13/14, p. 777.

63. M. E. Fine and J. G. Conley: *Metall. Trans.A*, 1990, vol. 21A, p. 2609.

64. R. A. Rapp and X. Zheng: *Metall. Trans.A*, 1991, vol. 22A, p. 3071.

65. H. Yokokawa *et al.*: *Metall. Trans.A*, 1991, vol. 22A, p. 3075.

66. J. C. Schuster, H. Nowotny and C. Vaccaro: *J. Solid State Chem.*, 1980, vol. 32, p. 213.

67. A. M. Sherman and C. McHugh: *Wear Mater.*, 1979, vol. 2, p. 156.

68. R. Mitra *et al.*: *MRS Symp. Proc.*, Fall Meeting, 1991, vol. 238, p. 1.

69. A. Jarfors, H. Fredriksson and L. Froyen: *Mater. Sci. Eng.*, 1991, vol. A135, p. 119.

70. A. J. Cornish: *Met. Science*, 1975, vol. 9, p. 477.

71. L. B äckerud: *Jernkontorets Ann.*, 1971, vol. 155, p. 422.

72. R. Kiusalaas and L. Bäckerud: *Solidification Processing 1987*, The Institute of Metals, London, 1988, p. 137.

73. F. Morimuni. *et al.*: Trans. Japan. Inst. Metals, 1977, vol. 41, p. 444.

74. R. Kiusalaas: *Chem. Comm. (Stockholm)*, 1986, p. 1.

75. C. D. Mayes, G. J. Tatlock and D. G. McCartney: *Proc. 12th Int. Cong. on "Electron Microscopy"*, Ed. L. D. Peachey and D. B. Williams, San Francisco, CA, 1990, vol. 4, p. 962.

76. G. P. Jones: *Solidification Processing 1987*, The Institute of Metals, London, 1988, p. 496.

77. G. P. Jones: *Proc. Int. Seminar on " Refining and alloying of liquid aluminium and ferro-alloys"*, Trondheim, Norway, 1985, p. 213.

78. G. P. Jones: *New ideas on the mechanism of heterogeneous nucleation in liquid aluminium*, NPL Report DMA(A) 19, 1983.

79. L. Bäckerud P. Gustafson and M. Johnsson: *Aluminium*, 1991, vol. 67(9), p. 910.

80. M. Vader and J. Noordegraaf: *Light Metals 1990*, Ed. C. M. Bickert, Metal. Soc. of AIME, 1990, p. 851.

81. M. Vader and J. Noordegraaf: *Light Metals 1988*, Ed. P. G. Campbell, Metal. Soc. of AIME, 1988, p. 937.

82. M. S. Lee and B. S. Terry: *Mater. Sci. Technol.*, 1991, vol. 7(7), p. 608.

83. C. D. Mayes, D. G. McCartney and J. Tatlock: *Mater. Sci. Technol.*, 1993, vol. 9(2), p. 97.

84. M. E. J. Birch and P. Fisher: *Solidification Processing 1987*, The Institute of Metals, London, 1988, p. 500.

85. H. T. Lu, L. C. Eang and S. K. Kung: *J. Chinese Foundryman's Assc.*, 1981, vol. 29, pp. 10-18.

86. G. K. Sigworth and M. M. Guzowski: *Trans. AFS*, 1985, vol. 93, pp. 907-912.

87. P. A. Tondel, G. Halvorsen and L. Arnberg: *Light Metals 1993*, Ed. S. K. Das, Metal. Soc. of AIME, 1993, p. 783.

89. D. Apelian and J. J. A. Cheng: *Trans. AFS*, 1986, vol. 94, pp. 797-808.

90. D. K. Young *et al.*: *Light Metals 1991*, Ed. E. L. Rooy, Metal. Soc. of AIME, 1991, p. 1115.

91. D. Hadlet, D. G. McCartney and S. R. Thistlethwaite: *Solidification Processing 1987*, The Institute of Metals, London, 1988, p. 141.

92. D. R. Uhlmann, B. Chalmers, and K. A. Jackson: *J. Appl. Phys.*, 1964, vol. 35(10), pp. 2986-2993.

93. D. M. Stefanescu and B. K. Dhindaw: *Metals Handbook*, ASM INTERNATIONAL, Metal Park, OH, 1988, vol. 15, pp. 142-147.

94. L. Bäckerud: *Int. Conf. on High Voltage Electron Microscopy*, Stockholm, April 1971.

95. S. E. Naess and O. Berg: *Z. Metallkd*, 1974, vol. 65, p. 599.

96. M. P. Seah and E. D. Hondros: *Proc. Roy. Soc. (London)*, 1973, vol. A335, p. 191.

97. K. F. Hulme and J. B. Mullin: *Phil. Mag.* , 1959, vol. 4, p. 1286.

98. A. Raman and K. Schubert: *Z. Metallkde*, 1965, vol. 56(1), p. 44.

99. M. K. Hoffneyer and J. H. Perepezko: *Light Metals 1991*, Ed. E. L. Rooy, Metal. Soc. of AIME, 1991, p. 1105.

100. W. V. Youdelis: *Met. Sci.*, 1975, vol. 9, p. 464.

101. W. V. Youdelis: *Met. Sci.*, 1978, vol. 12, p. 363.

102. W. V. Youdelis: *Met. Sci.*, 1979, vol. 13, p. 540.

103. W. V. Youdelis and C. S. Yang: *Met. Sci.*, 1980, vol. 13, p. 500.

104. W. V. Youdelis and D. R. Grekul: *Met. Sci.*, 1984, vol. 18, p. 464.

105. W. Reif and W. Schneider: *Z. Metallkde*, 1979, vol. 70, p. 396.

106. N. Eustathopoulos, J. C. Joud and P. Desre: *J. Mater. Sci.*, 1974, vol. 9, p. 1233.

107. Yu. V. Naidich and G. A. Kolesnichenko: *Surface Phenomena in Metallurgical Processes*, Ed. A. I. Belyaev,, Consultants Bureau, New York, 1965, p. 218.

108. Yu. V. Naidich, Yu. N. Chubashov, N.F. Ishchuk and V. P. Krasovskii: *Poroshk. Metall.*, 1983, vol. 6, pp. 67-69.

109. V. I. Kostikov, Yu. I. Koshelov, E. F. Filimonov, E. M. Tatievskaya and R. N. Ponkratova: *Poroshk. Metall.*, 1981, vol. 10, p. 79.

110. C. R. Manning, Jr. and T. B. Gurganus: *J. Amer. Ceram. Soc.*, 1969, vol. 52, p. 115.

111. L. F. Mondolfo: *Aluminium Alloys: stucture and properties*, Butterworths, London, 1976.

112. I. Cadoff and J. P. Nielson: *Trans. AIME* (*J. of Metals*), 1953, vol. 197, p. 248.

113. R. F. Carver, G. W. Boone and F. P Koch: *Light Metals 1990*, Ed. C. M. Bickert, Metal. Soc. of AIME, 1990, p. 845.

114. P. Fisher and G. T. Campbell: *Light Metals 1993*, Ed. S. K. Das, Metal. Soc. of AIME, 1993, p. 807.

115. G. K. Sigworth and C. Wang: *Trans. AFS*, 1992, vol. 100, (in press).

116. Q. T. Fang & D. A. Granger: *TMS Conf. Proc. on Light Metals*, Las Vegas, NV, Feb. 1989.

117. S. Minakawa, I. V. Samarasekera and F. Wineberg: *Metall. Trans.B*, 1985, vol. 16B, p. 823.

118. X. G. Chen and S. Engler: *Metall.*, 1991, vol. 45(10), p. 995.

119. C. E. Ransley and D. E. J. Talbot: *Z. Metallkd.*, 1955, vol. 46, p. 328.

120. E. L. Rooy: *Modern Casting*, 1992 (Oct.), pp. 32-34.

121. G. K. Sigworth and C. Wang: *Metall. Trans.B*, 1993, vol. 24B, pp. 349-364.

122. L. W. Garber: *Met. Techn.*, 1980, vol. 7(10), p. 428.

123. C. E. Ransley and H. Neufeld: *J. Inst. Met.*, 1948, vol. 74, p. 599.

124. W. R. Opie and N. J. Grant: *Trans. AIME* (*J. of Metals*), 1950, vol. 188, p. 1237.

125. D. E. J. Talbot: *Int. Materials Rev.*, 1975, vol. 20, pp. 166-184.

126. W. Eichenauer *et al.*: *Z. Metallkd.*, 1961, vol. 52, p. 682.

127. D. E. J. Talbot and P. N. Anyalebechi: *Mater. Sci. Techn.*, 1988, vol. 4, p. 1.

128. R. Y. Lin and M. Hoch: *Metall. Trans.A*, 1989, vol. 20A, p. 1785.

129. B. R. Deoras and V. Kondic: *Foundry Trade J.*, 1956, p. 361.

130. K. J. Brondyke and P. D. Hess: *Trans. AIME* (*J. of Metals*), 1964, vol. 230, p. 1542.

131. Q. T. Fang, P. N. Anyalebechi, R. J. O'Malley and D. A. Granger: *Solidification Processing, 1989*, The Institute of Metals, London, 1990.

132. G. K. Sigworth and C. Wang: *Metall. Trans.B*, 1993, vol. 24B, pp. 365-377.

133. D. R. Irani and V. Kondic: *Trans. AFS*, 1969, vol. 77, p. 208.

134. W. S. Pellini: *Trans. AFS*, 1953, vol. 62, p. 61.

135. O. Prabhakar and K. V. K. Nehru: *Foundry Trade J.*, 1974 (Feb.), p. 231.

136. T. R. Rajeevan, R. K. Srikantakumara and M. R. Seshadri: *Trans. AFS*, 1975, vol. 83, p. 551.

137. R. M. Pillai, V. Panchanathan and U. D. Mallya: *Trans. AFS*, 1978, vol. 86, p. 103.

138. M. H. Khan and V. Kondic: *Brititsh Foundryman*, 1979, vol. 72(10), p. 221.

139. Y. Shinada and S. Nishi: *J. Jpn. Inst. Light Met.*, 1980, vol. 30(6), p. 317.

140. M. Imabayashi, M. Ichimura and Y. Kanno: *Trans. Jpn. Inst. Met.*, 1983, vol. 24(2), p. 93.

141. W. R. Roberts and V. Kondic: *Trans. AFS*, 1962, vol. 70, p. 577.

142. K. Hashihura and M. Komatsu: *J. Jpn. Inst. Light Met.*, 1966, vol. 16(6), p. 14.

143. J. Campbell: *AFS Cast Metals Res. J.*, 1969, vol. 5(1), p. 1.

144. D. Apelian, M. C. Flemings and R. Mehrabian: *Metall. Trans.*, 1974, vol. 5, p. 2533.

145. N. Streat and F. Weinberg: *Metall. Trans.B*, 1976, vol. 7B, p. 417.

146. K. Murakami, A. Shiraishi and T. Okamoto: *Acta Metall.*, 1983, vol. 31(9), p. 1417.

147. D. R. Poirier: *Metall. Trans.B*, 1987, vol. 18B, p. 245.

148. C. Y. Liu, K. Murakami and T. Okamoto: *Mater. Sci. Techn.*, 1989, vol. 5(11), p. 1148.

149. K. Chinnathambi and O. Prabhaker: *Trans. AFS*, 1981, vol. 89, p. 455.

150. B. Chalmers: *"Principles of Solidification"*, John Wiley, London, UK, 1964, pp. 186.

151. J. C. Fisher, *J. Appl. Phys.*, 1948, vol. 19, pp. 1062-1067.

152. J. Campbell, *"The Solidification of Metals"*, ISI Publication No. 110, London, UK, 1968, pp. 19-26.

153. E. J. Whittenberger and F. N. Rhines: *Trans. AIME (J. of Metals)*, 1952, vol. 223, p. 409.

154. W. D. Walther, C. M. Adams and H. F. Taylor: *Trans. AFS*, 1956, vol. 64, p. 658.

155. S. Engler and K. Gockman: *Aluminium*, 1974, vol. 50(11), p. 712.

156. M. Blander and J. L. Katz: *AIChE, J.*, 1975, vol. 21(5), p. 833.

157. J. P. Hirth, G. M. Pound and G. R. St. Pierre: *Metall. Trans.B*, 1976, vol. 7B, p. 599.

158. J. E. Gruzleski, P. M. Thomas and R. A. Entwistle: *British Foundryman.*, 1978, vol. 71(4), p. 69.

159. J. Pötschke: *Arch. Eisenhuttenwesens*, 1979, vol. 50(7), p. 277.

160. P. M. Wilt: *J. Colloid Interface Sci.*, 1986, vol. 112(2), p. 530.

161. D. R. Poirier, K. Yeum and A. L. Maples: *Metall. Trans.A*, 1987, vol. 18A, p. 1979.

162. Z. Wang and S. G. Bankoff: *Int. J. Multiphase Flow*, 1991, vol. 17(4), p. 425.

163. H. Fredriksson and I. Svensson: *Metall. Trans.*, 1970, vol. 1, p. 939.

164. J. Campbell: *Trans. AIME (J. of Metals)*, 1968, vol. 242, pp. 264-267.

165. J. Campbell: *Trans. AIME (J. of Metals)*, 1968, vol. 242, pp. 268-271.

166. G. Drossel, R. Mai and O. Liesenberg: *Giessereitechnik*, 1981, vol. 27(6), p. 167.

167. W. Eichenauer *et al.*: *Z. Metallkd.*, 1974, vol. 65(10), p. 649.

168. G. K. Sigworth: *Metall. Trans.B*, 1982, vol. 13B, p. 447.

169. H. Shahani and H. Fredriksson, *Scand. J. Metall.*, 1985, vol. 14, pp. 316-320.

170. R. L. Coble and M. C. Flemings, *Metall. Trans.*, 1972, vol. 2, pp. 409-415.

171. R. Mehrabian, M. Keane and M. C. Flemings, *Metall. Trans.*, 1970, vol. 1, pp. 1209-1220.

172. T. S. Piwonka and M. C. Flemings: *Trans. AIME* (*J. of Metals*), 1966, vol. 236, p. 1157.

173. D. Ji, J. Lecomte-Beckers and L. Habraken: *Metall. Rep. CRM No.1059*, June, 1982.

174. K. Kubo and R. D. Phelke: *Metall. Trans.B*, 1985, vol. 16B, p. 359.

175. K. Kubo and R. D. Pehlke, *Trans. AFS*, 1986, vol. 94, pp. 753-756.

176. M. Simpson, M. Yerebaken and M. C. Flemings: *Metall. Trans.A*, 1985, vol. 16A, p. 1687.

177. H. Iwahori, K. Yonekura, Y. Sugiyama, Y. Yamamoto and M. Nakamura: *Trans. AFS*, 1985, vol. 93, p. 443.

178. C. Y. Liu, K. Murakami and T. Okamoto: *Acta Metall.*, 1986, vol. 34(1), pp. 151-166.

179. S. Shivkumar, D. Apelian and J. Zou: *Trans. AFS*, 1990, vol. 98, p. 897.

180. J. D. Zhu and I. Ohnaka: *Conf. Proc. on Modeling of Castings, Welding and Advanced Solidification Technologies* , Davos, Switzerland, 1990.

181. J. Ampuero, A. F. Hoadley and M. Rappaz: *Conf. Proc. on Modeling of Castings, Welding and Advanced Solidification Technologies*, Davos, Switzerland, 1990.

182. J. Zou, K. Tynelius, S. Shivkumar and D. Apelian: *Production and Electrolysis of Light Metals*; 29th Annual Conf. of Metallurgists of CIM, Hamilton, Ontario,Canada, 1990.

183. I. J.Chiou, and H. L. Tsai: *Trans. AFS*, 1990, vol. 98, p. 823.

184. Y. W. Lee, E. Chang and C. F. Chieu: *Metall. Trans.B*, 1990, vol. 21B, p. 715.

185. Y. W. Lee, E. Chang and C. F. Chieu: *Mater. Sci. Engg.*, 1990, vol. A124, p. 233.

186. C. R. Loper, Jr. and T. E. Prucha: *Trans. AFS*, 1990, vol. 98, pp. 845-853.

187. H. Huang, A. V. Lodhia and J. T. Berry: *Trans. AFS*, 1990, vol. 98, pp. 547-552.

188. E. N. Pan, C. S. Lin and C. R. Loper, Jr.: *Trans. AFS*, 1990, vol. 98, p. 735.

189. J. Ampuero, Ch. Charbon, A. F. Hoadley and M. Rappaz: *TMS Conf. Proc. on Light Metals*, New Orleans, LA, USA, Feb., 1991.

190. T. Yoda, Y. Sugiyama, and M. Nakamura: *J. Jpn. Inst. Light Met.*, 1981, vol. 31(10), p. 637.

191. M. Nakamura em et al.: *J. Jpn. Inst. Light Met.*, 1982, vol. 32(3), p. 129.

192. S. D. Pathak and O. Prabhakar: *Trans. AFS*, 1984, vol. 92, p. 671.

193. E. Niyama, T. Uchida, M. Morikawa and S. Saito: *Am. Foundrymen's Soc. Int. Cast. Met. J.*, 1981, vol. 6(2), pp. 16-22.

194. E. Niyama, T. Uchida, M. Morikawa and S. Saito: *Am. Foundrymen's Soc. Int. Cast. Met. J.*, 1981, vol. 7(3), pp. 52-63.

195. S. Kitaoka and K. Nishina: *Proc. of CIM International symposium on Light Metal Processing and Applications*, Ottawa, Canada, 1991, pp. 435-448.

196. P. M. Thomas and J. E. Gruzleski, *Metall. Trans.B*, 1978, vol. 9B, pp. 139-141.

197. J. P. Hirth and G. M. Pound: *Condensation and Evaporation*, Pergamon Press, Oxford, 1963.

198. D. Turnbull and J. C. Fisher: em J. Chem. Phys., 1949, vol. 17(1), pp. 71-73.

199. N. P. Allen: *J. Inst. Metals*, 1932, vol. 49, pp. 317-346.

200. M. Berthelot: *Ann. Chim.*, 1850, vol. 30, p. 232.

201. R. S. Vincent and G. H. Simmons: *Proc. Phys. Soc. (London)*, 1943, pp. 376-382.

202. L. J. Briggs: *J. Appl. Phys.*, 1950, vol. 21, pp. 721-722.

203. G. M. Lewis: *Proc. Phys. Soc. (London)*, 1961, vol. 71, p. 133.

204. G. A. Carlson: *J. Appl. Phys.*, 1975, vol. 46(9), pp. 4069-4070.

205. K. I. Ohsasa, T. Takahashi and K. Kobori: *J. Japan Inst. Met.*, 1988, vol. 52(10), pp. 1006-1011.

206. J. Pötschke and V. Rogge: *J. Cryst. Growth*, 1989, vol. 94, p. 726.

207. R. Sashikumar, T. R. Ramamohan and B. C. Pai: *Acta Metall.*, 1989, vol. 37(7), p. 2085.

208. G. F. Bolling and J. Cissé: *J. Cryst. Growth*, 1971, vol. 10, p. 56.

209. R. R. Gilpin: *J. Colloid Interface Sci.*, 1972, vol. 68(2), p. 235.

210. D. M. Stefanescu, B. K. Dhindaw, S. A. Kacar and A. Moitra: *Metall. Trans.A*, 1988, vol. 19A, p. 2847.

211. D. Shangguan and D. M. Stefanescu: *Metall. Trans.B*, 1991, vol. 22B, p. 385.

212. D. Shangguan, S. Ahuja and D. M. Stefanescu: *Metall. Trans.A*, 1992, vol. 23A, p. 669.

213. D. M. Stefanescu, F. Rana, A. Moitra and S. Kacar: "*Solidification of Metal Matrix Composites*", Ed. P. K. Rohtagi, The Minerals, Metals and Materials Society, 1990, pp. 77-89.

214. I. Jin and D. J. Lloyd: *Proc. Int. Conf.*, Montreal, PQ, Canada, Sept. 17-29, 1990, Eds., J. Masounave and F. G. Hamel, ASM International, Metals Park, OH, 1990.

215. P. K. Trojan: *Metals Handbook*, ASM INTERNATIONAL, Metal Park, OH, 1985, vol. **9**, pp. 89-97.

216. R. A. Flinn and P. K. Trojan: *Engineering Materials and Their Applications*, 3rd Edition, Houghton-Mifflin, 1986.

217. S. Z. Lu and A. Hellawell: *Metall. Trans.A*, 1987, vol. 18A, p. 1721.

218. D. Argo and J. E. Gruzleski: *Trans. AFS*, 1988, vol. 96, p. 65.

219. M. Garat, G. Laslaz, S. Jacob, P. Meyer, P. H. Guerin and R. Adam: Presented at AFS Conf. Milwaukee, WI, 1992.

220. J. R. Denton and J. A. Spittle: *Mater. Sci. Techn.*, 1985, vol. 1, p. 305.

221. J. E. Gruzleski, N. Handiak, H. Campbell and B. Closset: *Trans. AFS*, 1986, vol. 94, p. 147.

222. F. C. Dimayuga, N. Handiak and J. E. Gruzleski: *Trans. AFS*, 1988, vol. 96, p. 83.

223. H. Uto, H. Kambe, S. Kitaoka, U. Honma and S. Oya: *J. Jpn. Inst. Light Met.*, 1990, vol. 40(6), p. 439.

224. J. Golcoechea, C. Garcia-Cordovilla, E. Louis and A. Pamies: *J. Mater. Sci*, 1992, vol. 27, pp. 5247-52.

225. D. Emadi, J. E. Gruzleski and J. M. Toguri: *Metall. Trans.B*, 1993, vol. 24B, pp. 1055-1063.

226. H. Jacobi: *Information Symposium, Casting and Solidification of Steel*, IPC Science and Technology Press Ltd., Engalnd, 1977, vol. 1, p. 111.

Appendix

Hydrogen Balance in the Film

Particles which are pushed by the interface act as a barrier to the fluid flow and the diffusion field ahead of the interface. The kinetic considerations of the particle pushing process suggest that a finite separation must be maintained between the particle and the S/L interface, and fluid must flow continuously into this region to compensate for the liquid that is exhausted in the solidification process. The constituent balance of the melt can be obtained by estimating the volume of liquid solidified per unit time which equals to the volume of liquid flow into the gap as represented by spherical coordinates shown in Fig. .1. The volume of liquid that solidifies per unit time is given by

$$F_s V_s = \pi[(R+h)sin\theta]^2 V_s \tag{A.1}$$

The same volume of melt which flows per unit time into the gap $h(\theta)$ and is given by

$$F_l V_l = 2\pi h[(R+\frac{1}{2}h)sin\theta]V_l \tag{A.2}$$

where F_s is the surface area of the interface, V_s is identical to solidification velocity V, F_l is the cross section of the film and V_l is liquid velocity. Now the flow balance equation can be represented as:

$$\pi[(R+h)sin\theta]^2 V = 2\pi h[(R+\frac{1}{2}h)sin\theta]V_l \tag{A.3}$$

Similarly, the balance for hydrogen can be obtained by considering hydrogen penetrating the gap $h(\theta)$ per unit time with the concentration $C_{\theta,H}$ and the portion of

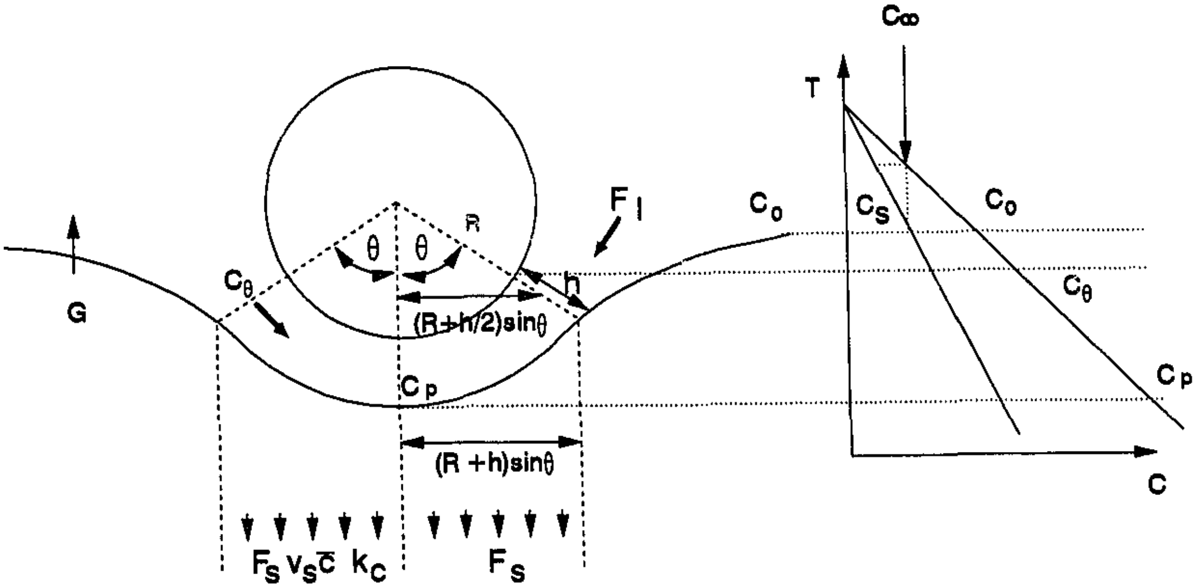

Fig. A.1 Particle in the Concentration Field.[159]

the concentration disappearing as a result of crystallization which can be expressed as

$$\pi[(R+h)sin\theta]^2V\bar{C}_Hk_e = 2\pi h[(R+\frac{1}{2}h)sin\theta](V_lC_H + D_H\frac{1}{R+\frac{1}{2}h}\frac{\delta C_H}{\delta\theta}) \tag{A.4}$$

where k_e is the equilibrium partition coefficient of hydrogen between solid and liquid, D_H is the diffusion coefficient of hydrogen in liquid aluminum, and C_H is the hydrogen concentration in the film. Over the gap width, h, the concentration is regarded as being constant. $\bar{C}_H$ is the integral mean of the concentrations over the gap width, which is defined as:

$$\bar{C}_H = \frac{\int_0^\theta h(1+\frac{h}{R}+\frac{h^2}{3R^2})C_Hsin\theta d\theta}{\int_0^\theta h(1+\frac{h}{R}+\frac{h^2}{3R^2})sin\theta d\theta} \tag{A.5}$$

Combining Eqns. (.3) and (.4), the differential equation for hydrogen segregation can be written as:

$$\frac{dC_H}{d\theta} = \frac{(R+h)^2Vsin\theta(\bar{C}_Hk_e - C_H)}{2D_Hh} \tag{A.6}$$

Glossary

C_d	Concentration of hydrogen at d_c (cc/100g)
C_H	Hydrogen concentration in the liquid (cc /100g)
C_0	Initial hydrogen concentration (cc /100g)
C_{ref}	Reference concentration (cc/100g)
d_c	Critical separation at $\theta = 0$ (m)
D_H	Diffusion coefficient of hydrogen (m^2/s)
f_H	Activity coefficient of hydrogen in liquid metal
G_l	Thermal gradient in liquid (^{0}C/m)
G_h	Thermal gradient behind the particle (^{0}C/m)
$h(r)$	Width of the film (m)
k_p	Thermal conductivity of particle (W/mK)
k_l	Thermal conductivity of liquid (W/mK)
k_{pl}	Ratio of thermal conductivity of particle and liquid
P_r	Reference pressure (atm.)
P_d	Pressure at d_c (atm.)
ΔP	Shrinkage pressure drop (atm.)
R_s	Radius of curvature of S/L front (m)
r_i	Initial radius of curvature of bubble in crevice (m)
r_b	Radius of curvature of the stable bubble (m)
r^*	Critical radius of curvature of the bubble in crevice (m)
T_m	Melting point (K)
T_1	Temperature on outside of particle (K)
T_o	Temperature along the centre of particle (K)
ΔT	Freezing range of the alloy (K)
V	Growth velocity (m/s)
V_c	Critical velocity (m/s)
ρ_p	Density of particle (kg/m^3)
ρ_l	Density of liquid (kg/m^3)
$\Delta\sigma_0$	$\sigma_{ps} - \sigma_{pl}$, Net interfacial energy (N/m)
γ	A constant which relates primary dendrite arm spacing to cooling rate
β	Volumetric shrinkage ratio